AD________________

Award Number: W81XWH-10-1-0836

TITLE: Challenges of Zinc-Specific Transrectal Fluorescence Tomography to Detect Prostate Cancer

PRINCIPAL INVESTIGATOR: Anqi Zhang
Daqing Piao Ph.D.

CONTRACTING ORGANIZATION: Oklahoma State University
Stillwater, OK 74078-5031

REPORT DATE: December 2013

TYPE OF REPORT: Annual Summary

PREPARED FOR: U.S. Army Medical Research and Materiel Command
Fort Detrick, Maryland 21702-5012

DISTRIBUTION STATEMENT: Approved for Public Release;
Distribution Unlimited

REPORT DOCUMENTATION PAGE

Form Approved
OMB No. 0704-0188

1. REPORT DATE December 2013	**2. REPORT TYPE** Annual Summary	**3. DATES COVERED** 15 September 2010 – 14 September 2013

4. TITLE AND SUBTITLE

Challenges of Zinc-Specific Transrectal Fluorescence Tomography to Detect Prostate Cancer

5a. CONTRACT NUMBER

5b. GRANT NUMBER
W81XWH-10-1-0836

5c. PROGRAM ELEMENT NUMBER

6. AUTHOR(S)

Anqi Zhang
Daqing Piao

E-Mail: daqing.piao@okstate.edu

5d. PROJECT NUMBER

5e. TASK NUMBER

5f. WORK UNIT NUMBER

7. PERFORMING ORGANIZATION NAME(S) AND ADDRESS(ES)

Oklahoma State University
Stillwater, OK 74078-5031

8. PERFORMING ORGANIZATION REPORT NUMBER

9. SPONSORING / MONITORING AGENCY NAME(S) AND ADDRESS(ES)
U.S. Army Medical Research and Materiel Command
Fort Detrick, Maryland 21702-5012

10. SPONSOR/MONITOR'S ACRONYM(S)

11. SPONSOR/MONITOR'S REPORT NUMBER(S)

12. DISTRIBUTION / AVAILABILITY STATEMENT
Approved for Public Release; Distribution Unlimited

13. SUPPLEMENTARY NOTES

14. ABSTRACT

This project studied the challenges of trans-rectal FDOT of negative-contrast targets relating to zinc-specific fluorophore. (1). Algorithms to enable trans-rectal FDOT reconstruction are developed, and synthetic FDOT study are performed to assess how sensitive the trans-rectal fluorescence measurement is to a ñegative-contrastòfluorescence target. (2). A novel geometric-sensitivity-difference method is introduced to improve target depth localization for trans-rectal fluorescence diffuse optical tomography. (3) A novel analytical approach has been developed to quantifying the diffuse photon propagation in an outward-imaging geometry that idealizes transrectal optical imaging. (4) Numerical studies have demonstrated that and detecting a target of negative-contrast in the trans-rectal prostate-imaging geometry is especially challenging. (5) Experimental woks are conducted to test the feasibility of TRUS-coupled FDOT of tissue phantoms containing target of positive or negative fluorescent contrast over the background. (6) A routine is developed to use sparsely 2D TRUS images to synthesize the 3D prostate profile to improve the image reconstruction.

15. SUBJECT TERMS
Prostate cancer, zinc, diffuse optical tomography, fluorescence diffuse optical tomography.

16. SECURITY CLASSIFICATION OF:			**17. LIMITATION OF ABSTRACT**	**18. NUMBER OF PAGES**	**19a. NAME OF RESPONSIBLE PERSON** USAMRMC
a. REPORT U	**b. ABSTRACT** U	**c. THIS PAGE** U	UU	113	**19b. TELEPHONE NUMBER** *(include area code)*

TABLE OF CONTENTS

Appendices (publications)

1. INTRODUCTION

1.1 Objective

The *long-term objective* of this research is to develop an imaging technology for detecting prostate cancer based on trans-rectal fluorescence diffuse optical tomography (FDOT) of zinc-specific fluorescent marker. The *specific aims* of this research are to evaluate the challenges unique to trans-rectal FDOT of zinc-specific fluorescence probe, and to assess the strategies of overcoming these challenges in clinically-relevant application settings.

1.2 Background

Zinc is a well-established metabolic marker of prostate cancer [1]. Benign prostate tissues secrete zinc in the form of $Zn_3Citrate_2$, and zinc has a concentration of approximately 10mM in prostatic fluid. In cancerous prostate tissue the zinc secretion ceases, resulting in five to ten folds of reduced level of zinc in the associated prostatic fluid. It is thus hypothesized that a fluorescence reagent with the affinity to zinc will be loaded up more by the tissue containing more free zinc, and much less in cancerous prostatic tissue, generating a ñreverse-uptakeò of the fluorescent probe. Subsequently, a fluorescence optical imaging approach for detecting prostate cancer based on a zinc-specific fluorescent probe has to be able to recover a target (or targets) of interest that has a weaker fluorescence than the background does. Such ñ*reverse-uptake*ò or ñ*negative-contrast*ò case is projected to be more challenging than the conventional FDOT cases [2-12] of which the task is to reconstruct a strong fluorescence target (or targets) within a weakly-fluorescent background. This project aims to identify and characterize the challenges associated with trans-rectal FDOT of target with a ñnegative contrastò over the background fluorescence.

1.3 Specific aims

The specific tasks of this project are to perform: **Task 1**: Conduct synthetic study on FDOT of fluorescence-strong targets within a weak background and FDOT of fluorescence-weak targets within a strong background. **Task 2**: Develop image processing techniques to extract spatial prior from TRUS for 3-D FEM model generation. **Task 3**: Perform relevant experimental investigation. These tasks are equivalent to the following aims: (A) to study algorithms to enable trans-rectal FDOT reconstruction, and to develop methods to assess how sensitive the trans-rectal fluorescence measurement is to a ñnegative-contrastò fluorescence target in comparison to a positive-contrast fluorescence target; (B) to experimentally evaluate the feasibilities or challenges of trans-rectal FDOT of ñnegative-contrastò fluorescence; (C) to develop procedures for extracting the spatial information from imagery of trans-rectal ultrasound as the spatial constraint information to improve trans-rectal DOT/FDOT image reconstruction.

1.4 Overview of the outcomes of this project

This project has resulted in six journal publications, two referred full-length proceeding papers, and nine short-papers and abstracts in conferences. This project has trained two pre-doctoral fellows to completing doctoral degrees and continuing to pursue academic paths. The original trainee PI, Mr. Guan Xu, after completing his doctoral degree, accepted a post-doctoral position in the University of Michigan Medical School. The current trainee PI, Mr. Anqi Zhang, after completing his doctoral degree, accepted a post-doctoral position in the Johns Hopkins University. In the following body section, we report the key results not yet peer-review-published and refer the peer-reviewed results to the attached copies of the publications.

2. BODY

2.1 Synthetic FDOT study of "negative-contrast" with spatial *prior*

A. Region-wise reconstruction to simultaneously recover emission-band optical properties and the fluorescence yield under spatial prior for negative contrast case in continuous-wave FDOT

The region-based reconstruction following a hierarchical algorithm we developed previously [13] is simulated in the geometry shown in Fig. 1(a). The imaging domain is a cube of 80mmĬ 80mmĬ 80mm. Substructures are segmented according to the presumed spatial *prior*. The optical array includes 7 sources and 7 detectors, arranged in parallel rows at the bottom of the imaging geometry, based on an experimental trans-rectal optical applicator available to this project. Figure 1(b)-(f) show the optical properties assignment. The optical properties in the excitation bands are assigned following the values shown in Table 1. The fluorescence quantum efficiency is set to 0.5 for all regions. The reconstruction initial values are set as: μ_{am} =0.01, μ'_{sm} =1 and $\eta\mu_{af}$ =0.0001. Table.1 compares the assigned values and the reconstructed values. Note that the scattering coefficients at excitation and emission wavelengths ($\mu'_{sx,m} = 1/(3ĀD_{x,m}) - \mu_{ax,m}$) are shown instead of showing the diffusion coefficient at excitation and emission wavelengths ($D_{x,m}$). As Table 1 indicates, although the reconstructed values do not agree exactly with the set values, the relative positive or negative contrasts among the regions are accurately identified.

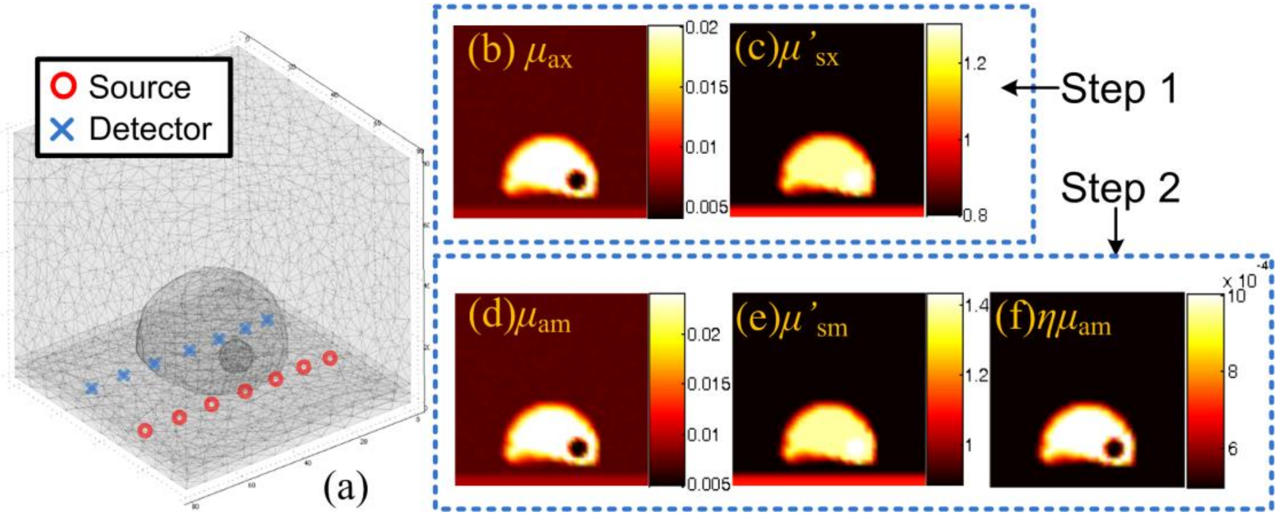

Fig.1 Simulation geometry and procedures with an innovative region-wise reconstruction algorithm. (a) Simulation geometry; (b)-(d) μ_{ax} and μ'_{sx} distribution, reconstruction parameters in the step 1; (d)-(f) μ_{am} /μ'_{sm}/$\eta\mu_{af}$ distribution, reconstruction parameters in the step 2.

Table 1 Comparison between the set values and the reconstruction results.
Note: The optical properties in excitation band is assumed as known, only the unknown parameters in the second step (Fig.10 (d)-(f)) are recovered here.

	regions	μ_{am} / mm^{-1}	μ'_{sm} / mm^{-1}	μ_{am} / mm^{-1}	μ'_{sm} / mm^{-1}	μ_{af} / mm^{-1}
Set values	peripheral tissue	0.006	0.8	0.0072	0.88	0.001
	prostate	0.02	1.25	0.0240	1.375	0.002
	rectum	0.008	1	0.0096	1.1	0.001
	tumor	0.004	1.3	0.0048	1.43	0.001
Reconstructed values	peripheral tissue	-	-	0.0072	0.88	0.001
	prostate	-	-	0.0259	1.23	0.0024
	rectum	-	-	0.0094	1.11	0.0010
	tumor	-	-	0.0027	1.22	0.0020

B. Piece-wise FDOT reconstruction of negative-contrast in fluorophore uptake

We also investigated the performance of piece-wise reconstruction in the negative contrast FDOT scenario and implemented the geometric-sensitivity-difference (GSD) reconstruction method [J8, C6] that will be discussed in the section 2, in planar reflectance geometry.

A few preliminary simulations indicate that the minimum source-detector distance (20mm) of our previous optical array could limit the depth resolution. Therefore, a modified optical array arrangement shown in Fig. 2(a) is used for the simulations study. As is shown in Fig. 2(a), the optical array has eleven sources and ten detectors. The sources and detectors are interspersedly positioned. The minimum source-detector distance in this geometry is thereby 10mm, and the sagittal and lateral extensions of the entire optical array are 60mm and 20mm, respectively.

Simulations include the examinations of the depth and longitudinal sensitivity of the imaging geometries. The FEM mesh includes 6466 nodes and 33591 elements. The background optical properties are assigned as μ_{ax} =0.01, μ'_{sx} =1, μ_{am} =0.012, μ'_{sm} =1.1 and $\eta\mu_{\mathrm{af}}$ =10^{-4}. A 7.5mm radius spherical blob is assigned as the heterogeneity. The optical properties of the blob are μ_{ax} =0.02, μ'_{sx} =1.1, μ_{am} =0.264, μ'_{sm} =1.32 and $\eta\mu_{\mathrm{af}}$ =10^{-5} (fluorophore uptake contrast ratio between the background and target is 10:1). In all the following simulations, we assume that the absorption and scattering properties of the targets are accurately determined and only the fluorescence yield is to be recovered.

The first set of simulations compares the target depth localization in image reconstruction with conventional and geometric differential approaches. The target is positioned at the middle of the sagittal plane. The center depth of the target varies from 5mm to 17mm at a step size of 3mm. Fig. 2(b) shows the reconstruction results with both the conventional method and the GDS method. It can be observed that similar to the endoscopic circular imaging geometry, the GDS method outperforms the conventional method in this planar optical array imaging geometry.

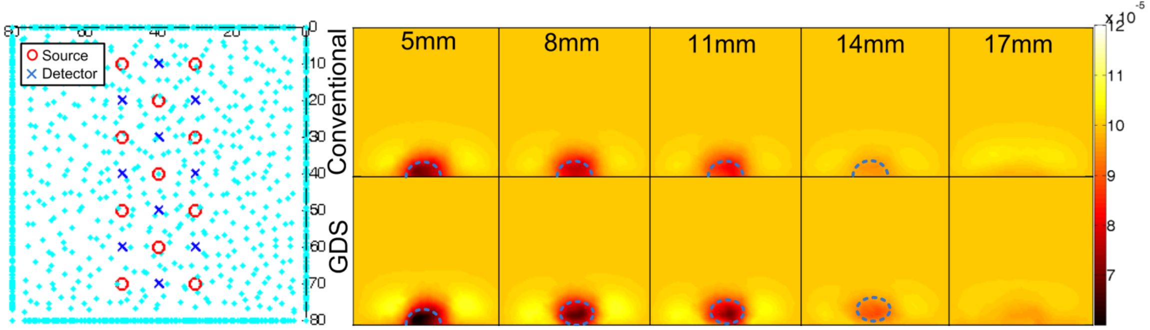

(a) Optical array geometry (b) Simulation results with varied target depth

Fig.2 Optical array geometry used in piece-wise simulation study. The numbers at the top of each column in (b) indicated the actual center-to-bottom depths of the targets

The second set of simulations examines the longitudinal target location variation. The target is embedded at the center depth of 14mm and moved along the sagittal middle plane from 15mm to 40mm from the left boundary of the imaging domain at a step size of 5mm. The reconstruction results are shown in Fig.3.

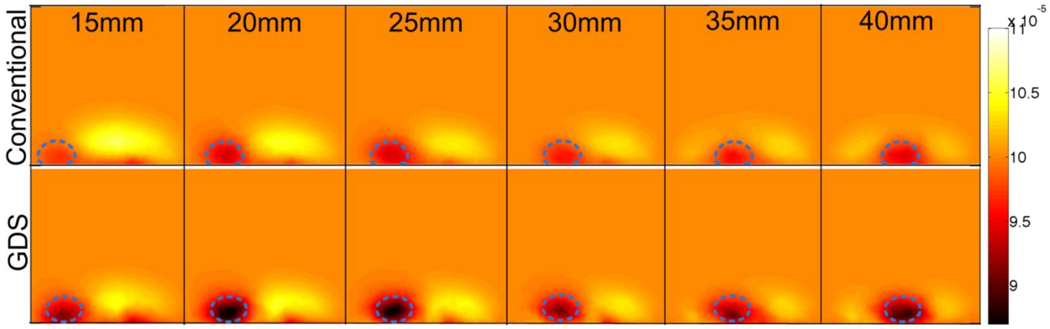

Fig.3 Piece-wise simulation results with varied target longitudinal position variation in sagittal-middle plane of the imaging geometry.

2.2 A novel geometric-sensitivity-difference method to improve target depth localization for trans-rectal fluorescence diffuse optical tomography [J8, C6]

Fluorescence diffuse optical tomography (FDOT) reconstruction based on reflectance measurements only is subjected to incorrect localization of the object depth when no prior information of the object is available. Depth-localization of an object of fluorescence contrast in an axial outward imaging geometry as applying to trans-rectal imaging of the prostate is particularly challenging, due to the significant variation of the sensitivity of the surface fluorescence measurement upon the depth of the object as associated with each pair of excitation source and detector. An important contribution of this project is a new algorithm of improving the target depth-localization in the case when the sensitivity dependence upon the depth varies significantly. We introduced a geometric-sensitivity-difference (GSD) algorithm that is shown to improve object depth-localization in both DOT [J8] and FDOT [C6]. The GSD method optimizes the data-model fit based on the paired measurements corresponding to two pairs of source-detector that share either the source or the detector, in comparison to the conventional method that optimizes the data-model fit based on the unpaired measurements corresponding to individual pairs of source-detector. The GSD method is shown to improve the depth-localization of an object with either a positive or negative fluorescence contrast over the background. The case of the object having a negative contrast of fluorescence over the background is specifically related to FDOT of zinc-specific fluorophore for prostate cancer detection since free-zinc concentration in cancerous tissue is known to be substantially lower than in normal tissue.

2.3 Systematic analytical and numerical evaluation of the photon propagation patterns associated with trans-rectal DOT and FDOT [J5-J7]

This project has also contributed to a new theoretical approach to a unified treatment of photon diffusion, at both excitation and emission wavelengths, in geometries containing long cylindrical tissue-applicator interface [J4-J7]. We have examined steady-state fluorescence photon diffusion in a homogenous medium that contains a homogenous distribution of fluorophores, and is enclosed by a ñconcaveò circular cylindrical applicator or is enclosing a ñconvexò circular cylindrical applicator, both geometries being infinite in the longitudinal dimension. The analytics and finite-element method are used to examine the changing characteristics of the fluorescence-wavelength photon-fluence rate and the ratio (sometimes called the Born ratio) of it versus the excitation-wavelength photon-fluence rate, with respect to the line-of-sight sourceïdetector distance. The analysis is performed for a source and a detector located on the mediumïapplicator interface and aligned either azimuthally or longitudinally in both concave and convex geometries. When compared to its steady-state counterparts on a semi-infinite mediumï applicator interface with the same line-of-sight sourceïdetector distance, the fluorescence-wavelength photon-fluence rate reduces faster along the longitudinal direction and slower along the azimuthal direction in the concave geometry, and conversely in the convex geometry. However, the Born ratio increases slower in both azimuthal and longitudinal directions in the concave geometry and faster in both directions in the convex geometry, respectively, when compared to that in the semi-infinite geometry.

2.4 Change to steady-state fluorescence measurement by a target of positive or negative contrast with respect to otherwise homogenous distribution of fluorophore

We have studied the changes to steady-state fluence at the emission wavelength as well as the Born ratio when the otherwise homogenous medium contains a target of fluorescence contrast, either positive or negative, over the background. We consider the following simplified configurations of the fluorescence target with respect to the source-detector positions: (1) the fluorescence target and the source-detector pair are all at the same **azimuthal** plane of a ***concave*** geometry with the source and the detector symmetric to the target; (2) the fluorescence target and the source-detector pair are all at the same **azimuthal** plane of a ***convex*** geometry with the source and the detector symmetric to the target; (3) the fluorescence target and the source-detector pair are all at the same **sagittal** plane of a ***concave*** geometry with the source and the detector symmetric to the target; (4) the fluorescence target and the source-detector pair are all at the same **sagittal** plane of a ***convex*** geometry with the source and the detector symmetric to the target; and these four configurations are compared against the case wherein the fluorescence target and the source-detector pair are all at the same **normal** plane of a ***semi-infinite*** geometry with the source and the detector symmetric to the target.

The FEM meshes of (1), (2) are illustrated with respect to a semi-infinite case in Fig. 4, and those of (3), (4) are illustrated with respect to a semi-infinite case in Fig. 5. In all these cases, the anomaly is set as a sphere with 6mm radius, and the center of the anomaly is 7mm away from the applicator interface. The radius of the cylindrical applicator is $R = 2\,cm$. The background optical parameters are $\mu_{ax} = 0.025\,cm^{-1}$, $\mu_{aem} = 0.025\,cm^{-1}$, $\mu'_{sx} = 10\,cm^{-1}$ and $\mu'_{sem} = 10\,cm^{-1}$. For positive contrast fluorescent anomaly, the absorption coefficient of at excitation wavelength of the anomaly is $\mu_{afl\_anomaly} = 0.1\,cm^{-1}$ and the background fluorophore is $\mu_{afl\_background} = 0.05\,cm^{-1}$. The fluorescence yield is $\eta = 0.1$. For negative contrast fluorescent anomaly, the absorption coefficient of at excitation wavelength of the anomaly is $\mu_{afl\_anomaly} = 0.05\,cm^{-1}$ and the background fluorophore is $\mu_{afl\_background} = 0.1\,cm^{-1}$. These optical parameters for both case-azi and case-longi are summarized in Table 2.

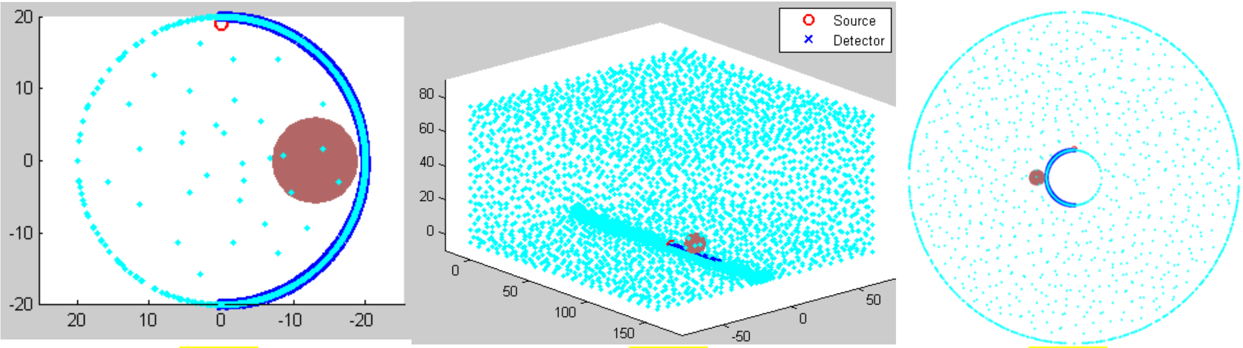

(A) (B) (C)

Figure 4. FEM imaging volume for case-azi. Detectors are aligned along the azimuth plane on the applicatorôs interface. (A) ***concave*** geometry, (B) semi-infinite geometry, (C) ***convex*** geometry.

Table 2. Optical parameters used for evaluating the change to florescent measurement by an anomaly

			background fluorescence $\mu_{afl\_background}$ (cm^{-1})	anomaly fluorescence $\mu_{afl\_anomaly}$ (cm^{-1})
Set 1	positive contrast	Case-azi	0.05	**0.1**
Set 2	negative contrast	Case-azi	**0.1**	0.05
Set 3	positive contrast	Case-longi	0.05	**0.1**
Set 4	negative contrast	Case-longi	**0.1**	0.05

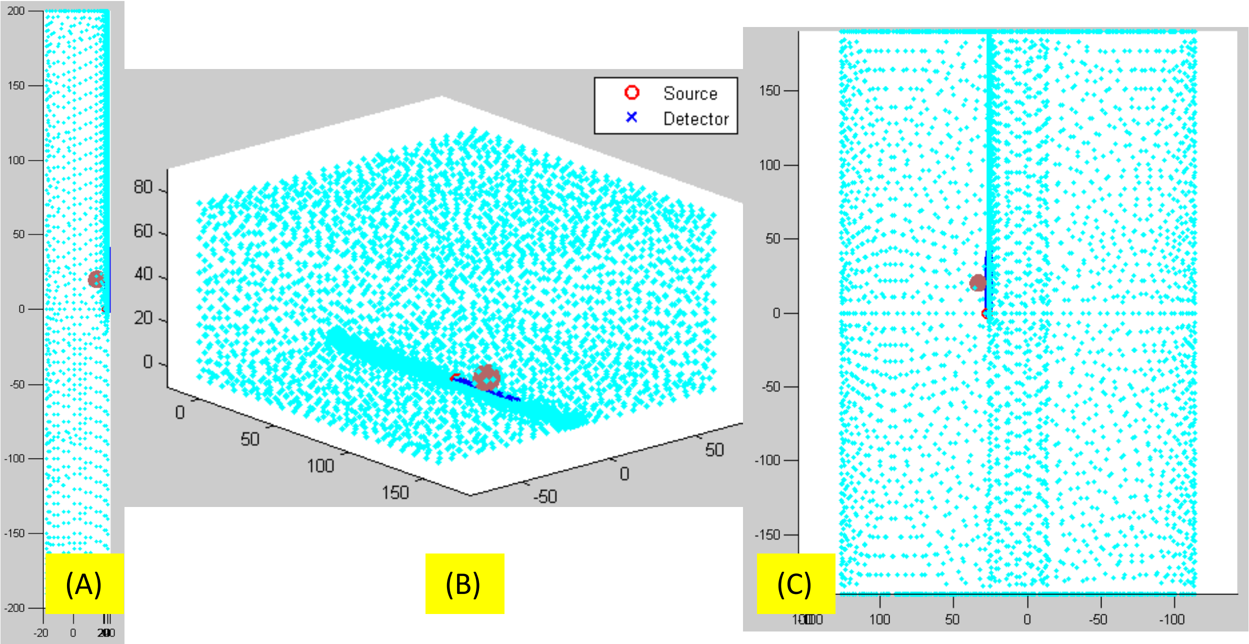

Figure 5. FEM imaging volume for case-longi. Detectors are aligned longitudinally with same azimuth angle on the applicatorôs interface. (A) ***concave*** geometry, (B) semi-infinite geometry, (C) ***convex*** geometry.

The simulation results for case-azi of both concave and convex geometries are illustrated in Figs. 6 as following: (A) shows the emission-fluence at the positive-contrast case, (B) is the Born ratio correspondence of (A), (C) shows the emission-fluence at the negative-contrast case, (D) is the Born ratio correspondence of (C). Figure 7 is the case-longi counterpart of Fig. 6. In all sub-plots of Figs. 6 and 7, the results corresponding to the anomaly (plotted by solid lines) are compared to the cases without the anomaly (plotted by dashed lines), to show the changes to the emission-fluence by the introduction of the target at the set parameters.

Figure 6 demonstrates that fluorescence measurement along the azimuthal direction is significantly more challenging in the convex geometry than in the concave geometry. Fig. 7 demonstrates that fluorescence measurement along the longitudinal direction is slightly more challenging in the convex geometry than in the concave geometry. Both figures show that a negative-contrast target is much more challenging to detect, regardless of the concave or convex geometry and the case-azi or case-longi configuration. *Therefore, we can anticipate that, trans-rectal FDOT of negative-contrast target faces the lowest signal sensitivity to the target property*.

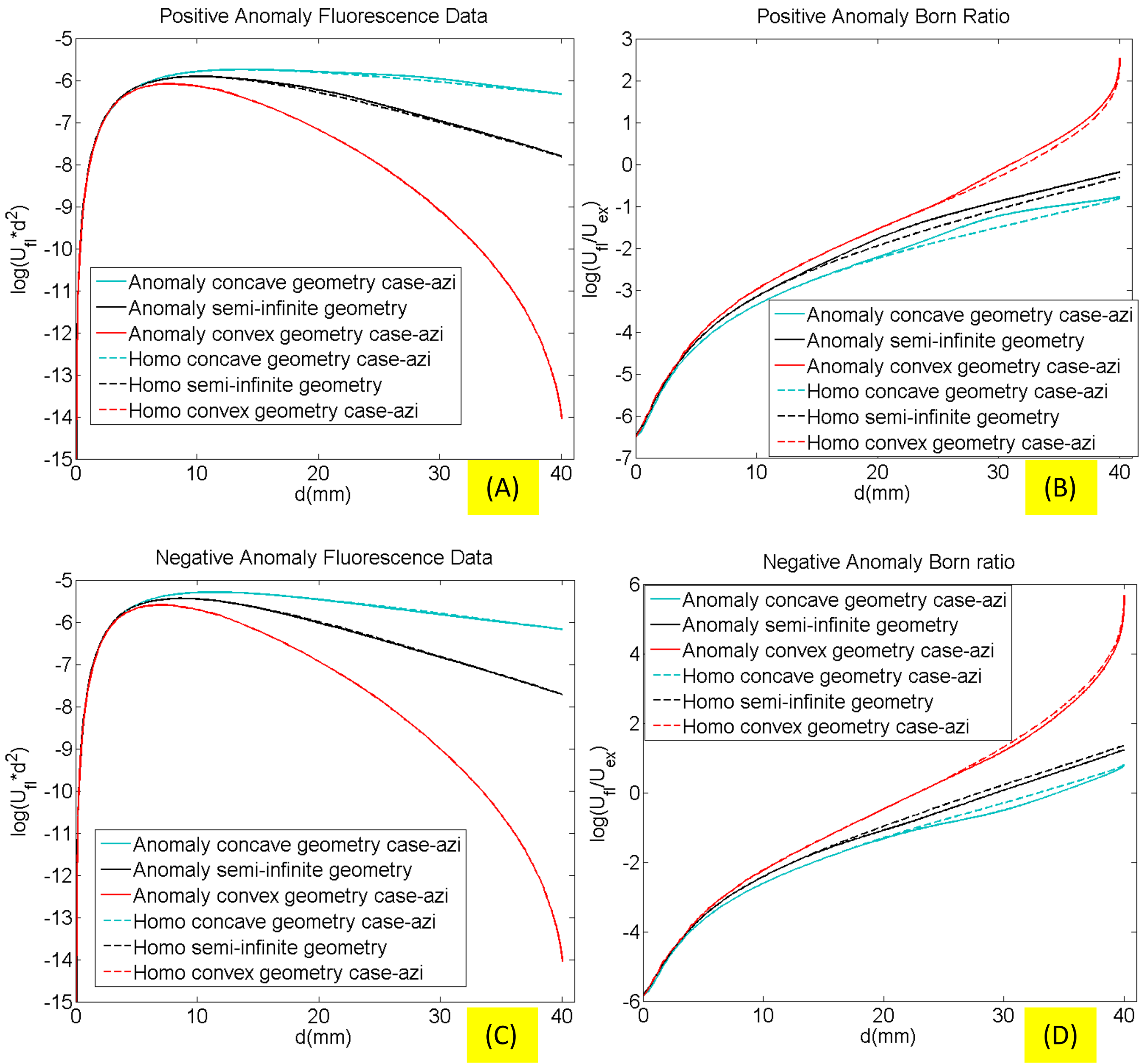

Figure 6. The comparisons of the change of fluorescent measurement due to an anomaly with fluorescence contrast in ***concave***, ***convex*** and semi-infinite geometry in case-azi. (A) The change in fluorescence data due to a positive contrast anomaly. (B) The change in Born ratio due to a positive contrast anomaly. (C) The change in fluorescence data due to a negative contrast anomaly. (D) The change in Born ratio due to a negative contrast anomaly. It is indicated that the fluorescent measurement is less sensitive to negative contrast anomaly than positive contrast anomaly and Born ratio is more sensitive to the anomaly inclusion than only the fluorescent data.

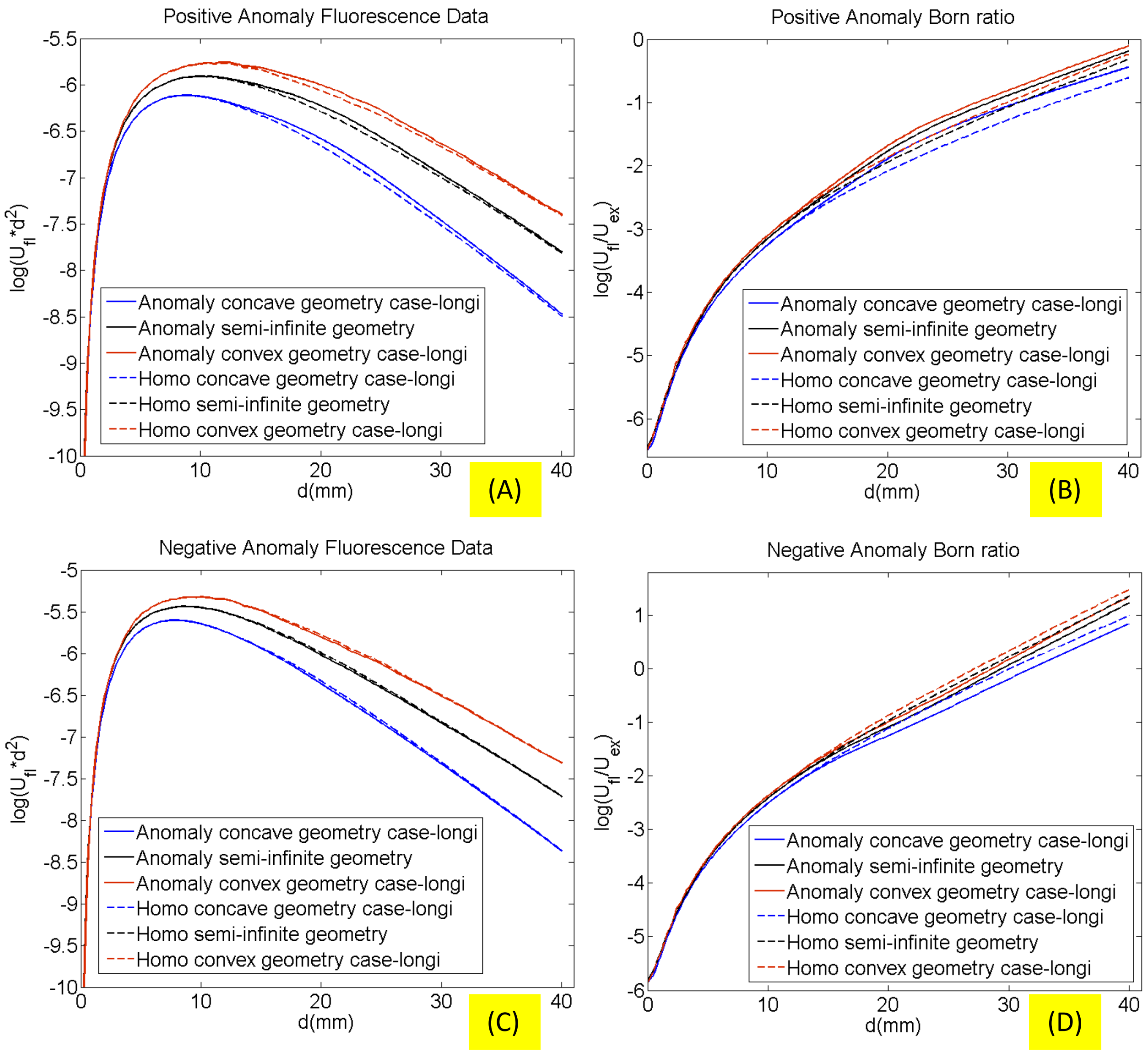

Figure 7. The comparisons of the change of fluorescent measurement due to an anomaly with fluorescence contrast in ***concave***, ***convex*** and semi-infinite geometry in case-longi. (A) The change in fluorescence data due to a positive contrast anomaly. (B) The change in Born ratio due to a positive contrast anomaly. (C) The change in fluorescence data due to a negative contrast anomaly. (D) The change in Born ratio due to a negative contrast anomaly. It is indicated that the fluorescent measurement is less sensitive to negative contrast anomaly than positive contrast anomaly and Born ratio is more sensitive to the anomaly inclusion than only the fluorescent data.

2.5 Experimental trans-rectal FDOT Measurement

The previous numerical analyses have clearly indicated that we should not become very optimistic about the outcome of reconstructing a target of negative contrast over the background fluorescence, particularly in trans-rectal geometry. To examine the feasibility of trans-rectal FDOT of negative-contrast target, we modified our trans-rectal ultrasound (TRUS)-coupled near-infrared (NIR) DOT system [14] for FDOT measurement. The NIR applicator coupled to TRUS transducer has 7 source channels and 7 detector channels. However, one detector channel within the applicator was out of order, likely due to aged adhesive that de-coupled or misaligned the micro-optics, leaving only 6 working channels for the detection of light from the tissue.

In terms of the system modification, as schematically shown in Fig. 8, an excitation laser diode at 705nm is coupled sequentially into the seven source channels through a fiber switch system. This 705nm laser diode is used to excite the indocyanine green (ICG) in the following phantom experiments to facilitate the measurement of the emission signals using the spectrometer of the system. For light excitation at each source channel, the six detector channels transmit the remitted signal at both the excitation (at 705nm) and the emission (centered at 785nm) to the spectrometer. The detection using a spectrometer allows separating the emission band from the excitation wavelength without a filtering scheme, for acquisition by a CCD, as long as the excitation wavelength has minimal overlapping with the emission spectra of ICG. Longer excitation wavelength (i.e., around 760nm) may be used to more effectively excite the fluorescence of ICG, however, the need to use a long-pass filter to block the excitation wavelength compromises the total emission power of the ICG.

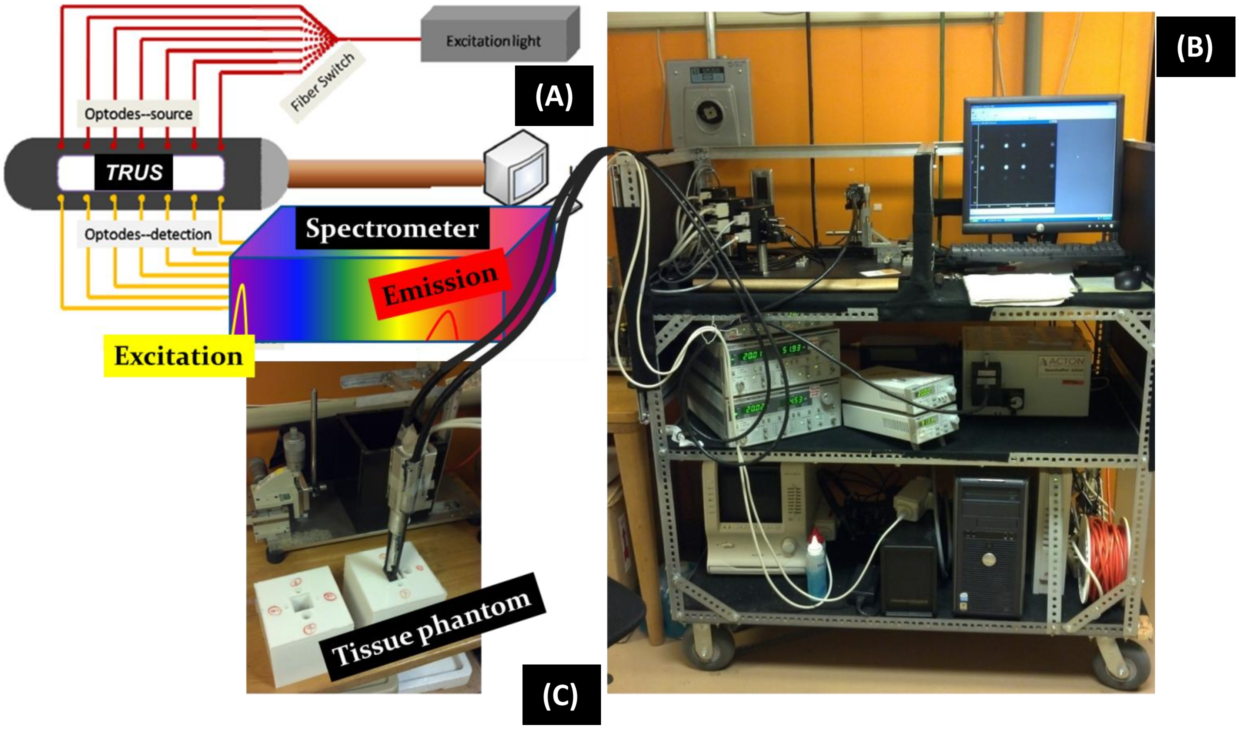

Figure 8. TRUS-coupled FDOT system. (A) System configuration. (B) The photograph of the system. (C) The applicator placed in a tissue phantom for positive-contrast test.

To simulate a target with positive-contrast of fluorescence over the background, we utilized silicon-based tissue phantoms (a collaborative development [C9]), the ones photographed in Fig. 8. The fluorescence target was a cylinder (1.4cm in diameter and approximately 4cm in length) filled with ICG concentration of 8 εM, which was embedded in the non-fluorescent homogeneous background enclosing the TRUS-coupled FDOT applicator, and was 3mm away from the optical probe and in the middle-sagittal plane. To simulate a target with negative contrast of fluorescence over the background, we developed a liquid phantom with a background ICG concentration of 8 εM, and embedded a non-fluorescent solid cylindrical phantom (1.5cm in diameter and 2.5cm in length), placed 5mm away from the optical probe and orthogonal to the middle-sagittal plane. The center locations of the targets at the two experiments were similar, as illustrated by the TRUS image of Fig. 9. The image was shown upward from the TRUS-NIR applicator, i.e., the position of the applicator was at the lower edge of the shown TRUS image.

The two sets of experiments, as one placed a target of fluorescence over a background of no-fluorescence, and the other embedded a target of no-fluorescence within a background of fluorescence, represent virtually the best-scenario cases in terms of the target-to-background contrast. The two cases, though not comprehensive, should reveal the potential of using tans-rectal FDOT to reconstruct a positive-contrast target or a negative-contrast target. It can be observed from the reconstructed results shown in Fig. 9 that, the contrast and size of the positive-contrast target were much more realistically recovered than those of the negative-contrast target. There negative-contrast target was ambiguous within a background of fluorescence that was strongly heterogeneous. *The shown difficulty of recovering a target with strongly negative-contrast of fluorescence agrees with the numerical analyses in terms of the sensitivity of FDOT measurement to the target with a positive or negative contrast to the background*.

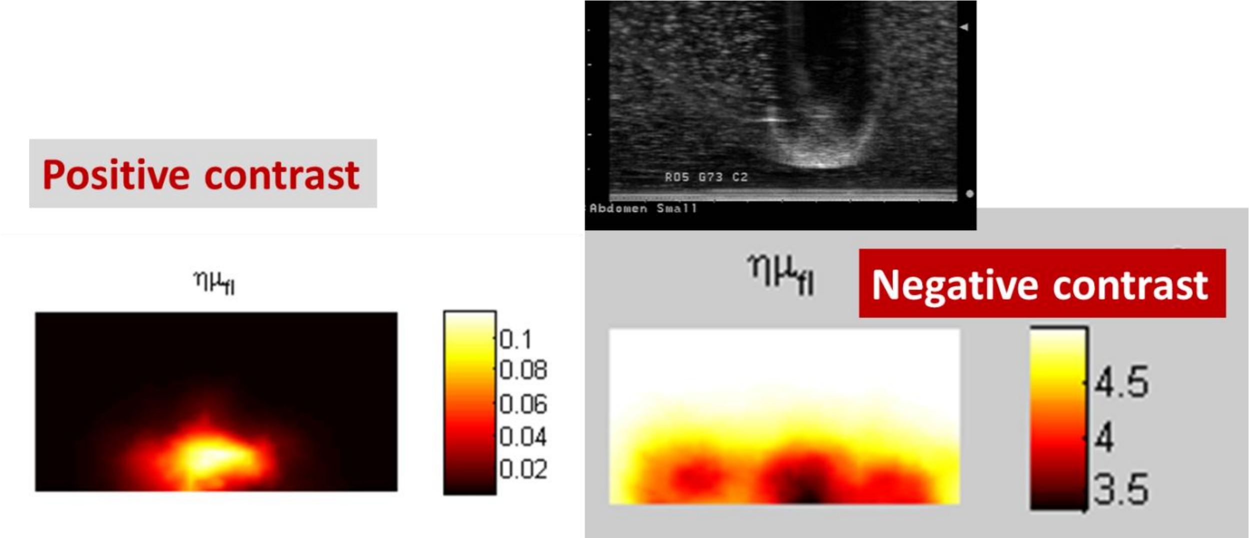

Figure 9. TRUS-coupled FDOT measurement. Top panel: a TRUS image of the negative-contrast tissue phantom. Lower left: the reconstructed image for the target having a positive-contrast of fluorescence over the background. Lower right; the reconstructed image for the target to have a negative-contrast of the fluorescence over the background.

2.6 Using 3D prostate profile extracted from sparsely positioned 2D TRUS images as the spatial constraint information to improve trans-rectal DOT image reconstruction

The TRUS axial images taken at different longitudinal positions are aligned according to one sagittal TRUS image to synthesize the approximate 3D profile of a prostate, as shown in Fig. 10. We use this prostate mesh as a spatial prior for NIR reconstruction by generating a mesh having a homogenous background region and a prostate region. The NIR image reconstruction uses a 3-dimensional mesh representing 80 x 40 x 70 mm^3 using different optical properties for prostate mesh and homogeneous background mesh. The Õ$_a$ value for nodes of homogeneous mesh is 0.008 mm^{-1} whereas, that for nodes of prostate profile mesh is 0.02 mm^{-1}

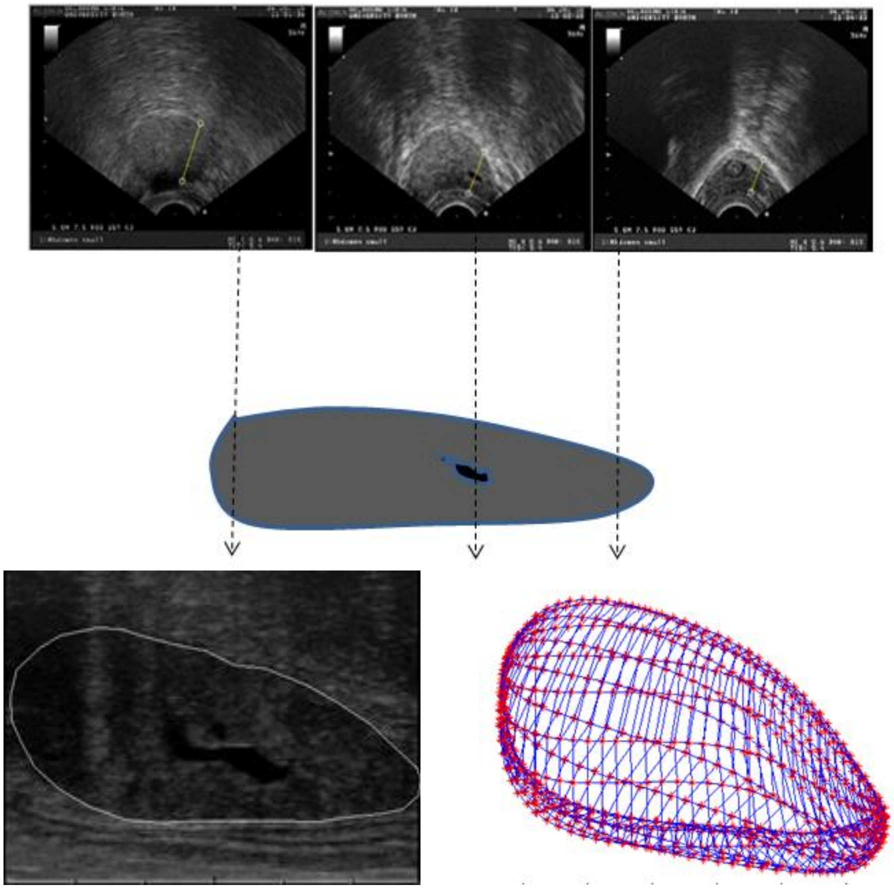

Figure 10 Several axial TRUS images are aligned using one sagittal image to extract the approximate 3D profile of the prostate to use as a spatial prior that are expected to improve reconstruction outcome.

The potential benefit of implementing the prostate profile as a spatial prior to trasnrectal DOT image reconstruction is illustrated in Fig. 11 for a right-lobe and Fig. 12 for a left-lobe, of a previous canine subject [15] that was developed in another project.

Baseline: Before TVT injection in a prostate, at baseline, in the left prostatic lobe, a large cystic lesion was observed. It showed highly elevated [Hb$_T$] and hypoxic for reconstruction with and without spatial prior. Right lobe of the prostate showed homogeneously weak [Hb$_T$] and S$_t$O$_2$

contrast except for some part which shows strong [Hb_T] and hyper-oxic region. The hyperoxic region is believed to be because of the intra-vascular tissue.

Right Lobe: After TVT injection in near-cranial-edge of the right lobe, the development of hypo-echoic mass in the middle-aspect of right lobe became evident on US by day 28. By day-49, the mass in the middle aspect of the right lobe which is marked as T_1 and T_2 turned to be an echoic and bi-lobular structure with shadowing at its caudal aspect. The larger dorsal-cranial-mass T_1 had unremarkable [Hb_T] contrast for both with and without spatial prior reconstructions. However, S_tO_2 marked a very strong response for mass T_1 in reconstruction with the spatial prior which was not very well developed in the reconstruction without using spatial prior. The smaller ventral-caudal-mass T_2 had strongly-marked S_tO_2 contrast for both the cases and weakly increased [Hb_T]. The necropsy performed at the end of 63 days showed the presence of tumors T_1, T_2, T_3 which matches our results of hypoxic region.

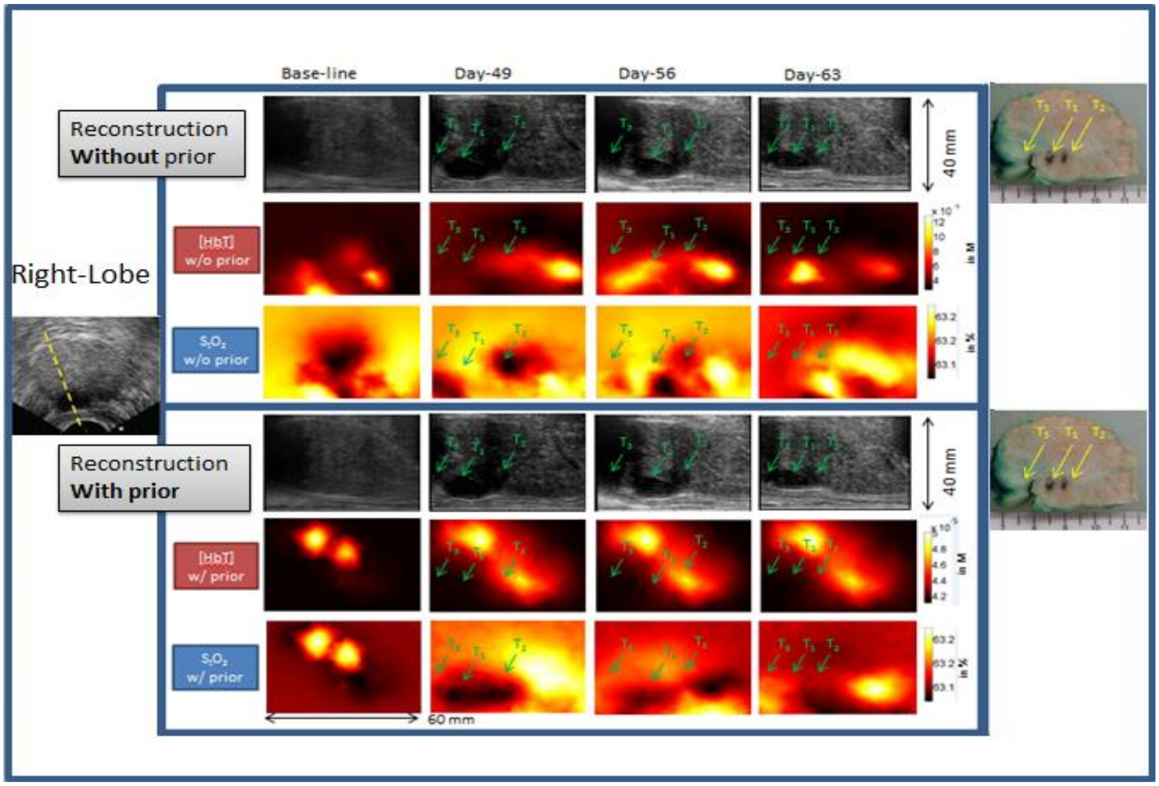

Figure 10 Image dimension: 60 mm x 40 mm (cranial-caudal x dorsal-ventral). Images were acquired at base-line, day-49, day-56 and day-63 after the injection, for grey-scale US, [Hb_T] and S_tO_2 (for reconstruction with and without using a spatial prior), at right-mid-sagittal plane across the planed TVT injection site as well as a later developed tumor mass (marked by the dashed line across the axial US image in the lower panel for the right-lobe). The prostate after necropsy was performed is in the right corner. The dashed line at the dorsal edge of the US images indicates the actual location of the NIR sensors at approximately 3 mm ventral to the surface of the US transducer. C indicates cyst; T indicates tumor.

By day-56, T_1 started regressing and reduced slightly in size on US with echoic reverberation artifact, the hyperoxic focus of it becoming larger, more intense and the [Hb_T] contrast of it remaining undetectable for reconstruction without spatial prior. For reconstruction using spatial prior, T_1 showed hypoxic region comparatively less strong than that for day-49 which is in correspondence with regressed tumor. T_2 was unremarkable on US except for the shadowing hypo-echoic region at the caudal aspect of the previously-indicated mass, the focus of it appearing as slightly hypoxic and having significantly increased [Hb_T] for reconstruction with spatial prior. Reconstruction without spatial prior showed highly hypoxic response with slightly increased [Hb_T].

By day-63, T1 remained unchanged in size on US with reduced echoic reverberation artifact, and the caudal aspect of the T2-indicating region became heterogeneously hypo-echoic without shadowing. The extended region corresponding to T1 & T2 was mostly anoxic-like, and only weak hyper-[HbT] contrast was observed in the indicated T2 mass.

Left Lobe: By day-49 the cystic lesion remained similar in NIR appearances to that in base-line. On Doppler US the blood flow was observed in areas ventral to the cystic lesion. On Doppler US the blood flow was observed in areas ventral to the cystic lesion. The cystic lesion showed strongly elevated [Hb_T] throughout the 63 days of this study for reconstruction using spatial prior in correspondence with the Doppler. However, no consistent feature in the proximity of the cystic lesion indicating lesion-wise blood flow was observed. By day-49, a response at the cystic lesion was highly hypoxic and the shape of the cystic lesion is somewhat visible and both were comparative in size to the ultrasonographically delineated lesion. However, for reconstruction without the spatial prior, cystic lesion showed elevated [Hb_T] similar to that with a spatial prior but, it was shown hyper-oxic in corresponding S_tO_2 map.

By day-56, it presented strong heterogeneously elevated [Hb_T] of which the gross profile resembled the hypoxic profile of the cystic lesion in base-line and day-49. Near that location the corresponding NIR image revealed a cluster of hyper-[Hb_T] region, but the center of which seemed displaced slightly cranially with respect to that of US hypo-echoic mass. The region of strong heterogeneously elevated [Hb_T] was associated with weak heterogeneous hyper-oxia for reconstruction with spatial prior. For reconstruction without spatial prior, cystic lesion was shown highly hypoxic and slightly elevated [Hb_T].

By day-63, the cystic lesion appeared as having weak lesion-wise hyper-[Hb_T] and heterogeneous hyper-oxic interior for reconstruction without using spatial prior whereas, for reconstruction using spatial prior, cystic lesion sows hypoxic interior. The leaked TVT cells from right lobe started to grow in the left lobe in early weeks. In week 4, the tumor mass became big volume at caudal to prostate. By day-63, a hypo-echoic mass with shadowing and Doppler flow-signal in its caudal aspect was noticed at the cranial-dorsal edge of the left lobe and was seemingly confined within the prostatic capsule which is marked by T_4. At the indicated position of T_4 mass, a hypoxic region of approximately 10 mm in longer axis was seen on S_tO_2 image with weak hyper-[Hb_T] contrast for reconstruction without spatial prior. The same T_4 mass was shown highly hypoxic and weak [Hb_T] for reconstruction with spatial prior. Retrospectively on day-56, the T_4 mass was shown smaller on US with shadowing, and at its dorsal aspect weak [Hb_T] and S_tO_2 contrast were noticed. From all these observations, it can be said that the NIR images reconstructed and displayed at the mid-sagittal plane correlate with TRUS images. The hyper-contrast region of [Hb_T] is correlated with the hypo-echoic region in TRUS images indicating the tumor mass. The necropsy result post 63 days indicates the presence of tumor T_4 was recognized by NIR which did not show up in TRUS images.

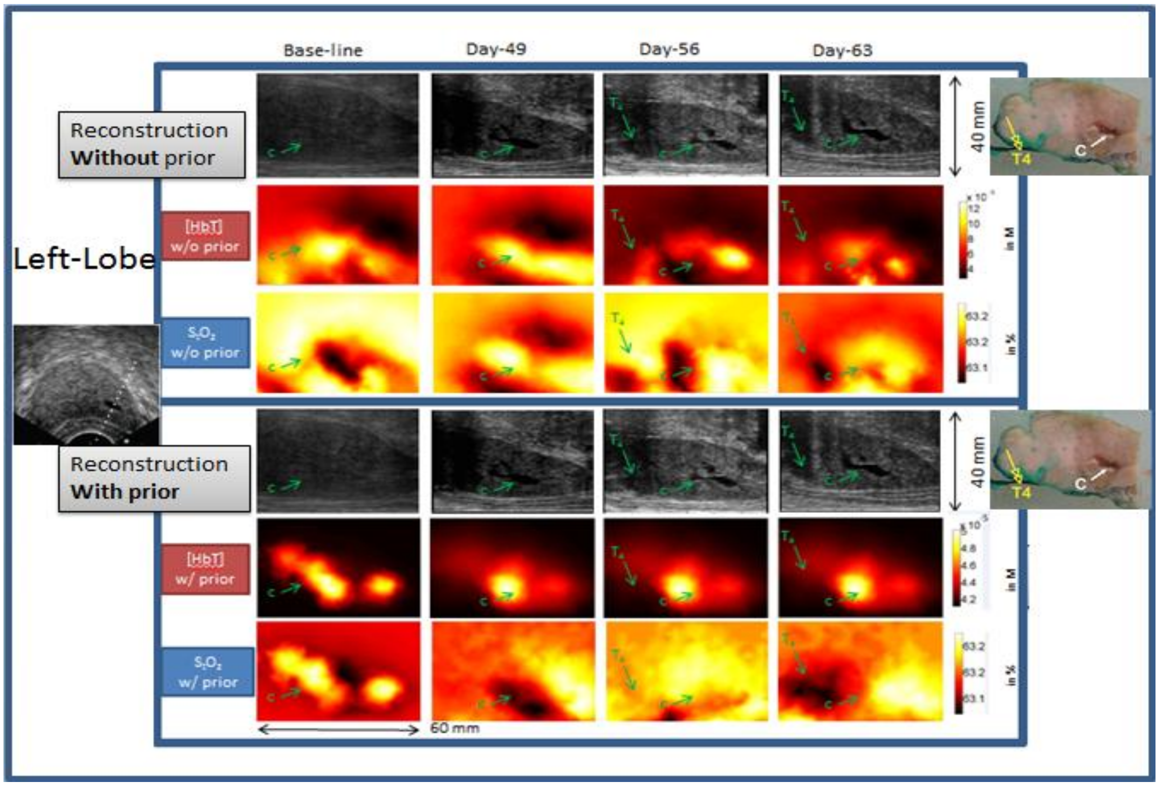

Figure 11 Image dimension: 60 mm x 40 mm (cranial-caudal x dorsal-ventral). Images were acquired at base-line, day-49, day-56 and day-63 after the injection, for grey-scale US, [Hb_T] and S_tO_2 (for reconstruction with and without using a spatial prior), at left-mid-sagittal plane across the cyst (marked by the dotted line across the axial US image in the upper panel for the left-lobe) The prostate after necropsy was performed is in the right corner. The dashed line at the dorsal edge of the US images indicates the actual location of the NIR sensors at approximately 3 mm ventral to the surface of the US transducer. C indicates cyst; T indicates tumor.

3. KEY RESEARCH ACCOMPLISHMENTS

This project has the accomplished the following tasks related to the challenges and feasibilities of trans-rectal FDOT of ñnegative-contrastò zinc-fluorescence for prostate imaging:

- Algorithms to enable trans-rectal FDOT reconstruction are developed, and synthetic FDOT study are performed to assess how sensitive the trans-rectal fluorescence measurement is to a ñnegative-contrastò fluorescence target in comparison to a positive-contrast fluorescence target.

- A novel geometric-sensitivity-difference method is introduced to improve target depth localization for trans-rectal fluorescence diffuse optical tomography

- A novel analytical approach has been developed to quantifying the diffuse photon propagation in an outward-imaging geometry that idealizes transrectal optical imaging. This analytical approach is also the first of its kind that applies to both outward-imaging and in-ward imaging through a cylindrically-shaped medium-applicator interface.

- Numerical studies have demonstrated that DOT/FDOT measurements is less sensitive to a negative-contrast target than to a positive-contrast target, and detecting a target of negative-contrast in the trans-rectal prostate-imaging geometry is especially challenging.

- Experimental woks are conducted to test the feasibility of TRUS-coupled FDOT of tissue phantoms containing target of positive or negative fluorescent contrast over the background. "Negative-contrast" target is found very challenging to reconstruct.

- A routine is developed to use sparsely positioned axial TRUS images and one sagittal TRUS image to synthesize the 3D prostate profile, which when used as the spatial constraint information is shown to improve the interpretation of the reconstructed image with respect to the histological or gross necropsy findings.

4. REPORTABLE OUTCOMES

The research has lead to the following reportable outcomes.

Journal publications

[J1] Xu G, Piao D, Dehghani H, ñThe utility of direct-current as compared to frequency domain measurement in spectrally-constrained diffuse optical tomography toward cancer imaging,ò ***Technol Cancer Res Treat***.; 10(5):403-16 (2011).

[J2] Xu G, Piao D, ñFeasibility of rapid near-infrared diffuse optical tomography by sweptspectral-encoded sequential light delivery,ò ***Proc. SPIE*** 7896, 78961W (2011).

[J3] Xu G, Piao D, Dehghani H, ñSpectral a priori to spatial a posteriori in continuous-wave image reconstruction in near-infrared optical tomography,ò ***Proc. SPIE*** 7892, 78920D (2011).

[J4] Piao D, Zhang A, Yao G, Xu G, Daluwatte C, Bunitng CF, Jiang Y, Pogue BW, ñWhen is spiral straight?ò, ***Optics & Photonics News***, 22(12): 24, (2011). ñOptics in 2011ò special issue (peer-reviewed).

[J5] Zhang A, Piao D, Bunting CF, ñPhoton diffusion in a homogeneous medium bounded externally or internally by an infinitely long circular cylindrical applicator. III. Synthetic-stuy of continous-wave photon fluence rate along unique spiral-paths,ò ***Journal of the Optical Society of America, A***, 29(4): 545-558 (2012).

[J6] Zhang A, Piao D, ñPhoton diffusion in a homogeneous medium bounded externally or internally by an infinitely long circular cylindrical applicator. IV. Frequency-domain analysis,ò ***Journal of the Optical Society of America, A***, 29(7): 1445-1458 (2012).

[J7] Piao D, Zhang A, Xu G, ñPhoton diffusion in a homogeneous medium bounded externally or internally by an infinitely long circular cylindrical applicator. V. Steady-state Fluorescence,ò ***Journal of the Optical Society of America,*** A, 30(4): 791-805 (2013).

[J8] XU G, Piao D, ñA geometric-differential-sensitivity based algorithm improves object depth-localization for diffuse optical tomography in a circular-array outward-imaging geometry,ò ***Medical Physics***, 40(1): 013101 (2013), 18 pages.

Conference proceeding papers

[C1] Xu G, Piao D, ñChallenges of and new configurations toward fluorescence diffuse optical tomography of zinc-specific biomarker for prostate cancer detectionò, poster presentation in ***2nd Innovative Minds in Prostate Cancer Today (IMPaCT) Conference*** for research funded by the Department of Defense (DOD) Prostate Cancer Research Program (PCRP), Mar. 09-11, 2011, Orlando, FL. Paper PC094694-1920.

[C2] Xu G, Piao D, ñNear-infrared diffuse optical tomography based on a wavelength-swept light sourceò ***Research Symposium 2011, Oklahoma State University***. The presentation was selected to the First-place of oral presentations in Biomedical Science.

[C3] Xu G, Piao D, ñA Geometric-differential-sensitivity based reconstruction algorithm improves target-depth localization for trans-lumenal outward-imaging diffuse optical tomography,ò Optical Society of America, ***Biomedical Topical Meetings*** (BIOMED), Paper BTu2A, Apr. 29-May 02, 2012, Miami, FL.

[C4] Piao D, ñTime-domain photon diffusions evaluated on concave and convex cylindrical medium-applicator interfaces show opposite trends of the time to reaching the peak-fluence rate----An analytic model,ò Optical Society of America, ***Biomedical Topical Meetings*** (BIOMED), Paper BTu3A.67, Apr. 29-May 02, 2012, Miami, FL.

[C5] Zhang A, Piao D, ñEffects of heterogeneity to continuous-wave photon remission along unique straight-line equivalent spiral-paths on a long cylindrical medium-applicator interface,ò Optical Society of America, ***Biomedical Topical Meetings*** (BIOMED), Paper BTu3A.69, Apr. 29-May 02, 2012, Miami, FL.

[C6] Tokala KT, Piao D, Xu G, ñImproving the object depth-localization in fluorescence diffuse optical tomography in an axial outward imaging geometry using a geometric-sensitivity-difference method,ò ***Saratov Fall Meetings*** (SFMô13), Saratov, Russia, Sep. 25-28, 2013. [Internet invited lecture].

[C7] Palande D, Piao D, ñtrans-rectal near-infrared optical tomography reconstruction of a regressing experimental tumor in a canine prostate by using the prostate shape profile synthesized from sparse 2-dimensional trans-rectal ultrasound images,ò ***Saratov Fall Meetings*** (SFMô13), Saratov, Russia, Sep. 25-28, 2013. [Internet report].

[C8] Zhang A, Piao D "Normalized Born ratio of steady-state fluorescence in concave- and convex- shaped infinitely long cylindrical medium geometries,ò ***SPIE International Symposium on Biomedical Optics***, Feb. 02-07, 2013, San Francisco, CA. Paper 8578-40.

[C9] He J, Weersink RA, Veilleux I, Zhang A, Piao D, Trachtenberg J, Wilson BC, "Development of transrectal diffuse optical tomography combined with 3D-transrectal ultrasound Imaging to monitor the photocoagulation front during interstitial photothermal therapy of primary focal prostate,ò ***SPIE International Symposium on Biomedical Optics***, Feb. 02-07, 2013, San Francisco, CA. Paper 8578-56.

5. CONCLUSIONS

In conclusion, this project has completed the original scopes of the work and resulted in additional discoveries that have substantially advanced our understanding of the challenges pertinent to trans-rectal FDOT of negative-contrast fluorescence probe based on zinc-specific fluorophores. This project has also successfully trained two pre-doctoral fellows who are pursuing academic paths.

REFERENCES

1. V. Zaichick, T. Sviridova, and S. Zaichick, "Zinc concentration in human prostatic fluid: Normal, chronic prostatitis, adenoma and cancer," International Urology and Nephrology **28**, 687-694 (1996).
2. J.S. Reynolds, T.L. Troy, R.H. Mayer, A.B. Thompson, D.J. Waters, K.K. Cornell, P.W. Snyder, and E.M. Sevick-Muraca, ñImaging of spontaneous canine mammary tumors using fluorescent contrast agents,ò Photochem. Photobiol. **66**, 87-94 (1999).
3. S. Achilefu, R. Dorshow, J. Bugaj, and R. Rajagopalan, ñNovel receptor-targeted fluorescent contrast agent for in vivo tumor imaging,ò Invest. Radiol. **35**, 479-485 (2000).
4. E. Kuwana and E.M. Sevick-Muraca, ñFluorescence lifetime spectroscopy for pH sensing in scattering media,ò Anal. Chem. **75**, 4325-4329 (2003).
5. A. Godavarty, M.J. Eppstein, C.Y. Zhang, S. Theru, A.B. Thompson, M. Gurfinkel, and E.M. Sevick-Muraca, ñFluorescence-enhanced optical imaging in large tissue volume using a gain-modulated ICCD camera,ò Phys. Med. Biol. **48**, 1701-1720 (2003).
6. V. Ntziachristos, J. Ripoll, L.V. Wang, and R. Weissleder, ñLooking and listening to light: the evolution of whole-body photonic imaging,ò Nat. Biotech. **23**, 13-20 (2005).
7. A. Corlu, R. Choe, T. Durduran, M.A. Rosen, M. Schweiger, M.D. Schnall, and A.G. Yodh, ñThree-dimansional in vivo fluorescence diffuse optical tomography of breast cancer in humans,ò Opt. Express **15**, 6696-6716 (2007).
8. J. Tian, J. J. Bai, X.-P. Yan, S.-L. Bao, Y.-H. Li, W. Liang, and X. Yang, ñMultimodality molecular imaging,ò IEEE Trans. Med. Biol. Mag. **27**, 48-57 (2008).

9. A. Hagen, D. Grosenick, and R. Macdonald, ñLate-fluorescence mammography assesses tumor capillary permeability and differentiates malignant from benign lesions,ò Opt. Express **17**, 17016-17033 (2009).

10. S. van de Ven, A.J. Wiethoff, T. Nielsen, B. Brendel, M. van der Voort, R. Nachabe, M. van de Mark, M. van Beek, L. Nakker, L. Fels, S. Elias, P. Luijten, and W. Mali, ñA novel fluorescent imaging agent for diffuse optical tomography of the breast: first clinical experience in patients,ò Mol. Imaging Biol. **12**, 343-348 (2010).

11. F. Gao, J. Li, L.-M. Zhang, P. Poulet, H.-J. Zhao, and Y. Yamada, ñSimultaneous fluorescence yield and lifetime tomography from time-resolved transmittances of a small-animal-stimulating phantom,ò Appl. Opt. **49**, 3163-3172 (2010).

12. A. Leproux, M. van der Voort, M.B. van der Mark, R. Harbers, S.M.W.Y. van de Ven, and T.G. Van Leeuwen, ñOptical mammography combined with fluorescence imaging: lesion detection using sactterplots,ò Biomed. Opt. Express **2**, 1007-1020 (2011).

13. Xu G, Bunting CF, Dehghani H, Piao D, ñA hierarchical spatial prior approach for prostate image reconstruction in trans-rectal optical tomography,ò International Symposium on Biomedical Optics, San Jose, CA, Jan. 24-29, 2009. Proceedings of SPIE, Vol. 7171, Paper #71710S

14. Jiang Z, Piao D*, Bartels KE, Holyoak GR, Ritchey JW, Ownby CL, Rock K, Slobodov G, ñTransrectal ultrasound-integrated spectral optical tomography of hypoxic progression of a regressing tumor in a canine prostate,ò Technology in Cancer Research and Treatment, 10(6): 519-531 (2011).

Technology in Cancer Research and Treatment
ISSN 1533-0346
Volume 10, Number 5, October 2011

The Utility of Direct-Current as Compared to Frequency Domain Measurements in Spectrally-Constrained Diffuse Optical Tomography Toward Cancer Imaging

www.tcrt.org

Guan Xu[1]
Daqing Piao, Ph.D.[1]*
Hamid Dehghani, Ph.D.[2]

[1]School of Electrical and Computer Engineering, Oklahoma State University, Stillwater, OK, USA
[2]School of Computer Science, The University of Birmingham, Birmingham, UK

This work investigates, by means of analytical and simulation studies, the performance of spectrally-constrained image reconstruction in Continuous-Wave or Direct-Current (DC) and Frequency Domain (FD) near-infrared optical tomography. A recent analytic approach for estimating the accuracy of target recovery and the level of background artifact for optical tomography at single wavelength, based on the analysis of parametric reconstruction uncertainty level (PRUL), is extended to spectrally-constrained optical tomography. The analytical model is implemented to rank three sets of wavelengths that had been used as spectral *prior* in an independent experimental study. Subsequent simulation appraises the recovery of oxygenated hemoglobin (HbO), deoxygenated hemoglobin (Hb), water (H_2O), scattering amplitude (A), and scattering power (b) using DC-only, DC-excluded FD, and DC-included FD, based on the three sets of wavelengths as the spectral *prior*. The simulation results support the analytic ranking of the performance of the three sets of spectral *priors*, and generally agree with the performance outcome of DC-only versus that of DC-excluded FD and DC-included FD. Specifically, this study indicate that: 1) the rank of overall quality of chromophore recovery is Hb, H_2O, and HbO from the highest to lowest; and in the scattering part the A is always better recovered than b. This outcome does suggest that the DC-only information gives rise to unique solution to the image reconstruction routine under the given spectral *prior*. 2) DC-information is not-redundant in FD-reconstruction, as the artifact levels of DC-included FD reconstruction are always lower than those of DC-excluded FD. 3) The artifact level as represented by the noise-to-contrast-ratio is almost always the lowest in DC-only, leading to generally better resolution of multiple targets of identical contrasts over the background than in FD. However, the FD could outperform DC in the recovery of scattering properties including both A and b when the spectral *prior* is less optimal, implying the benefit of phase-information in scattering recovery in the context of spectrally-constrained optical tomography.

Key words: Optical tomography; Image reconstruction; Spectral *prior*; Frequency-domain; Continuous-wave.

Introduction

Multi-spectral near infrared optical tomography aims to reconstruct pathologically-relevant optical heterogeneities in biological tissue from information

---

Abbreviations: Diffuse Optical Tomography (DOT); Parametric Reconstruction Uncertainty Level (PRUL); Direct-Current (DC); Continuous-Wave (CW); Frequency Domain (FD); Alternate Current (AC); PHase Shift (PHS); Contrast to Noise Ratio (CNR); Noise to Contrast Ratio (NCR); Oxygenated Hemoglobin (HbO); Deoxygenated Hemoglobin (Hb).

*Corresponding author:
Dr. Daqing Piao, Ph.D.
E-mail: daqing.piao@okstate.edu

obtained over a spectrum of light (1-5). The technique utilizes measurements at multiple wavelengths (5) to decompose the spectrally variant tissue optical properties such as absorption and reduced scattering coefficients into spectrally invariant chromophore concentrations and spectrally insensitive scattering properties such as scattering power and scattering amplitude (2). Although discussions remain over the uniqueness of optical tomography reconstruction by single wavelength Continuous-Wave (CW) or Direct-Current (DC) measurements (6-7), the unique solution to optical tomography reconstruction based on spectrally-constrained DC measurement has been demonstrated by Corlu *et al.* (2). Further studies based on DC measurements have been reported for imaging of breast (2-3, 8-9), prostate (10), brain function (11), small animal (12), *etc.*, and the spectrally-constrained DC-based reconstruction is shown to be more robust than the spatially-constrained single-wavelength DC-based reconstruction in recovering the optical heterogeneities (13). In recent studies (14-15), Wang *et al.* implemented broadband frequency domain (FD) measurements to multispectral optical tomography reconstruction. The studies concluded that increasing the bandwidth of FD measurements improves reconstruction results. In their subsequent studies, Wang *et al*. integrated the FD detection with DC (16-17) measurements to further expand the effective spectral bandwidth for reconstruction. The successful outcome of such FD/DC complemented approach, nonetheless, underlines a more fundamental inquiry, that is, under the same spectral-constraint, how DC based reconstruction performs with respect to FD based reconstruction. Intuitively, one might expect FD reconstruction to outperform DC reconstruction in all aspects owing to the extra phase information. However, such consideration has neither been confirmed nor negated, for which direct comparison of DC and FD reconstructions under the same context of spectral-constraint is necessary. For non-spectrally-constrained optical tomography, or optical tomography at single-wavelength, our previous study (18) investigated three conditions of reconstruction: 1) DC-only; 2) DC-excluded FD, *i.e.* utilizing only the modulation amplitude (AC) and phase shift (PHS); and 3) DC-included FD, *i.e.* including DC, AC and PHS. It is revealed that the DC-only reconstruction, despite the less accurate estimation of the target optical properties, presents higher Contrast-to-Noise-Ratio (CNR) than the FD reconstruction does, thereby potentially better resolves the targets in certain noisy circumferences. It is also demonstrated that with spatial-*prior*, DC-only reconstruction is essentially equivalent to FD reconstructions, and without spatial-*prior*, DC-included FD reconstruction generally outperforms DC-excluded FD reconstruction. Will spectrally-constrained reconstruction have similar outcome?

The study in (18) introduced an analytic model to estimate the translation of uncertainties in the measurements to the uncertainties in the reconstructed images, namely parameter-recovery-uncertainty-level (PRUL). This current study aims to evaluate the PRULs in spectrally-constrained optical tomography reconstruction. Specifically, we explore the PRULs of the concentrations of several important NIR chromophores, including oxygenated hemoglobin (HbO), deoxygenated hemoglobin (Hb), and water, and scattering parameters such as scattering amplitude and scattering power. The PRUL analyses are for the measurements of DC-only, DC-excluded FD, and DC-included FD, as did with the study in (18), even though other configurations of DC/FD measurements could be employed (19). The PRUL analyses are, essentially, to quantify the gradients of the chromophore concentrations and scattering components with respect to DC or FD measurement components. This study seeks to derive the wavelength-specific gradients of the chromophore concentrations and scattering components with respect to the optical properties in DC or FD measurements, which are then to be integrated with the gradients of the optical properties with respect to DC or FD measurements previously analyzed in (18) to reach the complete expressions of PRULs in multi-spectral measurements.

A practical issue arises in spectrally-constrained optical tomography is the selection of optimal set of wavelengths given the choices of doing so in the system integration. The optimization approaches demonstrated by Corlu *et al.* (2, 8) and Eames *et al.* (20) are similar as both methods compare the residue and condition numbers of numerically approximated sensitivity matrices derived for each set of the wavelength combinations. This current work proposes a novel method of optimizing the wavelength selection for spectrally-constrained optical tomography reconstruction based on the PRUL analyses. As the gradients in PRULs are formatively equivalent to the sensitivity matrices, the new method is shown to optimize the wavelength selection as effectively as Corlu's and Eames' methods do, but at much lower computational load.

The PRUL analyses under spectral-constraint as well as the newly proposed method for spectral-*prior* optimization are examined by synthetic studies in a 2-dimensional circular imaging geometry resembling an applicator enclosing the medium (3, 20). The synthetic studies are to recover targets each of which possesses only one independent contrast, and to resolve two closely positioned targets of identical studied properties. Evaluation criteria include the recovered target properties and the noise-to-contrast-ratio (NCR). In this study, NCR is defined as, opposed to CNR, the absolute levels of the background artifacts normalized by the target-to-background contrast, therefore a lower NCR is preferred.

It is well-known that multi-spectral optical tomography reconstruction can be implemented in two ways. A conventional "indirect" method first reconstructs wavelength-specific absorption and scattering distributions and then deduces the chromophore concentrations and scattering components (9). While a "direct" spectrally-constraint method integrates the spectral information into the sensitivity matrices to directly recover the chromophore concentrations and scattering parameters (2-4, 8, 13-14, 20-22). Note that the efficacies of both methods are ultimately bounded by the determination of the gradient of the spectrally variant optical properties with respect to the chromophore concentrations and scattering parameters. However, as the direct method has less unknown values than the indirect method does, the inverse problem in the direct method is better conditioned. Therefore it is well expected (2-4, 8, 13, 21) that the direct method outperforms the indirect method in terms of CNR and inter-parameter cross-talk, should the amount of the wavelengths be sufficient for recovering the unknown parameters. In light of this, the "direct" reconstruction method is adopted in the simulations of this study for multi-spectral optical tomography reconstruction.

The rest of the paper is structured to the following sections for the comparison of DC, DC-excluded FD, and DC-included FD measurements under the same spectral-constraint: analytical derivation of the PRULs, numerical implementation of the derived PRULs, ranking of the spectral-*priors* being implemented for the PRUL analyses, and finite-element-based simulation to validate the preceding numerical evaluations. The simulation study will demonstrate that: 1) the ranking of the wavelength sets given by the analytical approach is correct; 2) the rankings of the overall quality of chromophore recovery and the scattering property given by the analytical approach are correct; 3) DC-information is not-redundant in FD-reconstruction; 4) for less desirable spectral *prior,* the phase in FD gives more robust recovery of the scattering properties.

Parameter Recovery Uncertainty Level (PRUL) in Multi-spectral Measurement

General Expression of the PRUL

For a field point at a distance d from the source in an infinite homogenous diffusive medium, we define $U_{DC}(d, \lambda)$, $U_{AC}(d, \lambda)$ and $\Phi(d, \lambda)$ as the wavelength-specific DC, AC and phase measurands. For two field points located d_1 and d_2 from the source, the differences in their DC, AC, and phase-shift denoted by $\delta(\lambda)$, $a(\lambda)$ and $\varphi(\lambda)$, respectively, can be expressed as (18, 19):

$$\delta(\lambda) = \ln\left(\frac{d_2}{d_1}\frac{U_{DC}(d_2,\lambda)}{U_{DC}(d_1,\lambda)}\right) = -\rho \cdot \sqrt{\frac{\mu_a(\lambda)}{D(\lambda)}} = -\rho \cdot k_{DC} \quad \text{[1-DC]}$$

$$\begin{aligned} a(\lambda_i) &= \ln\left(\frac{d_2}{d_1}\frac{U_{AC}(d_2,\lambda)}{U_{AC}(d_1,\lambda)}\right) \\ &= -\rho \cdot \sqrt{\frac{\mu_a(\lambda)}{2D(\lambda)}\left(\sqrt{1+\frac{\omega^2}{v^2\mu_a^2(\lambda)}}+1\right)} = -\rho \cdot k_{AC} \quad \text{[1-AC]} \end{aligned}$$

$$\begin{aligned} \phi(\lambda) &= \Phi(d_2,\lambda) - \Phi(d_1,\lambda) \\ &= \rho \cdot \sqrt{\frac{\mu_a(\lambda)}{2D(\lambda)}\left(\sqrt{1+\frac{\omega^2}{v^2\mu_a^2(\lambda)}}-1\right)} = \rho \cdot k_{PHS} \quad \text{[1-PHS]} \end{aligned}$$

where $\rho = |d_1 - d_2|$, ω is the angular modulation frequency, v is the speed of light in the medium, and

$$\mu_a(\lambda) = \sum_i \log(10)\varepsilon_i(\lambda)\, c_i \text{ (the "log" denotes the natural logarithm)} \quad [2\text{-}\mu_a]$$

$$\mu_s'(\lambda) = A\lambda^{-b} \quad [2\text{-}\mu_s']$$

$$D(\lambda) = \{3[\mu_a(\lambda) + \mu_s'(\lambda)]\}^{-1} \quad [2\text{-}D]$$

are the absorption, reduced scattering and diffusion coefficients of the medium, respectively. In equation [2], $\varepsilon_i(\lambda)$ is the extinction coefficient of chromophore i at wavelength λ (23), A is the scattering amplitude and b is the scattering power (3, 8).

The standard deviations, denoted by σ_δ, σ_a and σ_φ, respectively, of the differences of the measurands δ, a and φ, in fact represent the measurement uncertainties (18, 19). The translation of the measurement uncertainties into variations in the reconstructed spectrally-constrained optical properties may be modeled by

$$\begin{aligned} \sigma_{x_j} &= \sqrt{\left(\frac{\partial x_j}{\partial M(\lambda)}\right)^2 \cdot \sigma^2_{M(\lambda)}} \\ &= \left|\frac{\partial x_j}{\partial \mu(\lambda)} \cdot \frac{\partial \mu(\lambda)}{\partial M(\lambda)}\right| \cdot \sigma_{M(\lambda)} = \left|\frac{\partial x_j}{\partial \mu(\lambda)}\right| \cdot \sigma_{\mu(\lambda)} \end{aligned} \quad [3]$$

where x represents the set of chromophore concentrations, scattering amplitude and scattering power, M represents the set of δ, a and φ, and $\mu(\lambda)$ represents the set of absorption and reduced scattering coefficients. Note that the $\sigma_{\mu(\lambda)}$ has already been given in Tables II and IV of (18), so only $\partial x/\partial \mu$ needs to be derived in this study.

The PRULs of Chromophore Concentration

By expressing equation [2-μ_a] in matrix form as following:

$$\begin{bmatrix}\mu_a(\lambda_1)\\ \mu_a(\lambda_2)\\ \vdots\\ \mu_a(\lambda_m)\end{bmatrix}_{m\times1} = \log(10)\cdot\begin{bmatrix}\varepsilon_1(\lambda_1) & \varepsilon_2(\lambda_1) & \dots & \varepsilon_n(\lambda_1)\\ \varepsilon_1(\lambda_2) & \varepsilon_2(\lambda_2) & \dots & \varepsilon_n(\lambda_2)\\ \vdots & \vdots & \ddots & \vdots\\ \varepsilon_1(\lambda_m) & \varepsilon_2(\lambda_m) & \dots & \varepsilon_n(\lambda_m)\end{bmatrix}_{m\times n}\times\begin{bmatrix}C_1\\ C_2\\ \vdots\\ C_n\end{bmatrix}_{n\times1}$$

one has the gradient of chromophore concentration with respect to the absorption coefficients as:

$$\begin{aligned}\frac{\partial\vec{c}_{n\times1}}{\partial(\vec{\mu}_a)_{m\times1}} &= \log^{-1}(10)\cdot\left[(\vec{\varepsilon}^T)_{n\times m}\vec{\varepsilon}_{m\times n}\right]^{-1}(\vec{\varepsilon}^T)_{n\times m}\\ &= \begin{bmatrix}\frac{\partial c_1}{\partial\mu_a(\lambda_1)} & \frac{\partial c_1}{\partial\mu_a(\lambda_2)} & \cdots & \frac{\partial c_1}{\partial\mu_a(\lambda_m)}\\ \frac{\partial c_2}{\partial\mu_a(\lambda_1)} & \frac{\partial c_2}{\partial\mu_a(\lambda_2)} & \cdots & \frac{\partial c_2}{\partial\mu_a(\lambda_m)}\\ \vdots & \vdots & \ddots & \vdots\\ \frac{\partial c_n}{\partial\mu_a(\lambda_1)} & \frac{\partial c_n}{\partial\mu_a(\lambda_2)} & \cdots & \frac{\partial c_n}{\partial\mu_a(\lambda_m)}\end{bmatrix}_{n\times m}\end{aligned}\tag*{[5]}$$

Combining equation [5] with σ_{μ_a} found in (18), the PRUL of the chromophore concentration becomes:

$$(\vec{\sigma}_c)_{n\times1} = \left|\frac{\partial\vec{c}_{n\times1}}{\partial(\vec{\mu}_a)_{m\times1}}\right|_{n\times m}\cdot\left(\vec{\sigma}_{\mu_a(\lambda)}\right)_{m\times1}\tag*{[6]}$$

The PRULs of Scattering Amplitude and Scattering Power

Take the logarithm of equation [2-μ_s'] as

$$\log\mu_s' = \log A + (-b)\log\lambda\tag*{[7]}$$

and convert equation [7] to the matrix form of:

$$\begin{bmatrix}\log[\mu_s'(\lambda_1)]\\ \log[\mu_s'(\lambda_2)]\\ \cdots\\ \log[\mu_s'(\lambda_m)]\end{bmatrix}_{m\times1} = \begin{bmatrix}1 & \log\lambda_1\\ 1 & \log\lambda_2\\ \cdots & \cdots\\ 1 & \log\lambda_m\end{bmatrix}_{m\times2}\times\begin{bmatrix}\log A\\ (-b)\end{bmatrix}_{2\times1}\tag*{[8]}$$

one has:

$$\begin{aligned}\left(\frac{\partial\log A}{\partial\log\mu_s'(\lambda_i)}\right)_{1\times m} &= \frac{1}{m\sum_{i=1}^{m}\log^2(\lambda_i)-\left[\sum_{i=1}^{m}\log(\lambda_i)\right]^2}\\ \text{[4]}\qquad &\times\left(\begin{bmatrix}\sum_{i=1}^{m}\log^2(\lambda_i)-\log(\lambda_1)\sum_{i=1}^{m}\log(\lambda_i)\\ \sum_{i=1}^{m}\log^2(\lambda_i)-\log(\lambda_2)\sum_{i=1}^{m}\log(\lambda_i)\\ \cdots\\ \sum_{i=1}^{m}\log^2(\lambda_i)-\log(\lambda_m)\sum_{i=1}^{m}\log(\lambda_i)\end{bmatrix}^T\right)_{1\times m}\end{aligned}\tag*{[9]}$$

$$\begin{aligned}\left(\frac{\partial b}{\partial\log\mu_s'(\lambda_i)}\right)_{1\times m} &= \frac{1}{m\sum_{i=1}^{n}\log^2(\lambda_i)-\left[\sum_{i=1}^{n}\log(\lambda_i)\right]^2}\\ &\times\left(\begin{bmatrix}\sum_{i=1}^{m}\log(\lambda_i)+m\cdot\log(\lambda_1)\\ \sum_{i=1}^{m}\log(\lambda_i)+m\cdot\log(\lambda_2)\\ \cdots\\ \sum_{i=1}^{m}\log(\lambda_i)+m\cdot\log(\lambda_m)\end{bmatrix}^T\right)_{1\times m}\end{aligned}\tag*{[10]}$$

The PRULs of scattering amplitude and scattering power are then expressed by:

$$\begin{aligned}\sigma_A &= \left|\frac{\partial A}{\partial\log A}\cdot\frac{\partial\log A}{\partial\log\mu_s'(\lambda)}\cdot\frac{\partial\log\mu_s'(\lambda)}{\partial\mu_s'(\lambda)}\right|\cdot\sigma_{\mu_s'(\lambda)}\\ &= A\cdot\left|\frac{\partial\log A}{\partial\log\mu_s'(\lambda)}\right|\cdot\frac{\sigma_{\mu_s'(\lambda)}}{\mu_s'(\lambda)}\end{aligned}\tag*{[11]}$$

$$\begin{aligned}\sigma_b &= \left|\frac{\partial b}{\partial\log\mu_s'(\lambda)}\cdot\frac{\partial\log\mu_s'(\lambda)}{\partial\mu_s'(\lambda)}\right|\cdot\sigma_{\mu_s'(\lambda)}\\ &= \left|\frac{\partial b}{\partial\log\mu_s'(\lambda)}\right|\cdot\frac{\sigma_{\mu_s'(\lambda)}}{\mu_s'(\lambda)}\end{aligned}\tag*{[12]}$$

where ($\sigma_{\mu s'(\lambda)}/\mu_s'(\lambda)$) was available in (18).

Qualitative Evaluation of the PRULs Between Scattering Amplitude and Scattering Power

A qualitative evaluation of equations [11] and [12] can estimate which one, between scattering amplitude and scattering power, is less prone to measurement uncertainties. Neglecting the common factor $\sigma_{\mu s'(\lambda)}/\mu_s'$ in equations [11] and [12] as well as the equal denominators in equations [9] and [10], only the elements in the $1 \times m$ matrices in equations [9] and [10] are to be compared. Within the NIR spectral range between 0.6μm and 1μm, *i.e.*, $\lambda \in [0.6,1]$ with the unit of μm, one has $-1 \leq \log(\lambda_i) \leq 0 \leq \log^2(\lambda_i) \leq 1$ for the first term in each element and thus

$$\Sigma\log(\lambda_i) < 0 < \Sigma\log^2(\lambda_i) \qquad [13]$$

For the second terms of $-\log(\lambda_m)\cdot\Sigma\log(\lambda_i)$ and $m\cdot\log(\lambda_m)$, apparently $m > -\Sigma\log(\lambda_i) > 0$ and thus

$$m\cdot\log(\lambda_m) < -\log(\lambda_m)\cdot\Sigma\log(\lambda_i) < 0 \qquad [14]$$

Summing the inequalities [13] and [14] leads to

$$|\Sigma\log(\lambda_i) + m\cdot\log(\lambda_m)| > |\Sigma\log^2(\lambda_i) - \log(\lambda_m)\cdot\Sigma\log(\lambda_i)| \qquad [15]$$

which implies that the PRULs of the scattering power should exceed that of scattering amplitude, or the scattering power is more prone to noise than the scattering amplitude is.

Numerical Evaluation of PRULs in Multi-spectral Measurement

Sets of Spectral-prior Used for PRUL Evaluation

We implemented the 3 sets of wavelengths used in (8) as the spectral-*prior* for quantitative analyses of PRULs in multi-spectral measurements. Each of the spectral-*prior* sets contains 5 wavelengths as shown in Figure 1 and Table I. The set 1 expands 186 nm from 740 nm to 926 nm. The set 2 expands 240 nm from 650 nm to 890 nm. The set 3 expands 280 nm, the broadest among the three, from 650 nm to 930 nm. Note that the three wavelength sets are not chosen arbitrarily, in fact, under the caliber introduced in (8) one of them, the set 3, forms an optimal set, so they are considered suitable for demonstrating the prominent cases of spectral-*prior*. Note that the spectra in Figure 1 follow the chromophore absorption spectra used in (2, 8), which are based on the study of Prahl (23).

Criteria of Wavelength Optimization in the Context of Minimizing PRULs

Wavelength optimization for spectrally-constrained optical tomography would naturally reduce the uncertainties in the reconstruction. One approach to optimize the wavelengths is to have a greater set of denominators in equations [5], [9] and [10]. For the scattering aspect in equations [9] and [10], several random attempts show that the value of $\left| m\sum_{i=1}^{m}\log^2(\lambda_i) - \left[\sum_{i=1}^{m}\log(\lambda_i)\right]^2 \right|$ stays in a narrow range of [0.1, 1]. However, for equation [5], the determinant of $\varepsilon^T\varepsilon$ varies in several orders depending upon the wavelengths, which is however not unexpected because the similarities between the row-vectors in matrix ε could induce rank deficiency. Corlu *et al.* (2, 8) and Eames *et al.* (22) indicated such issue of rank deficiency and recommended to construct the sensitivity matrix with small residual numbers. From another perspective, however, one could associate the determinant of a matrix with the area bounded by the row-vectors of the matrix. This suggests that maximizing the determinant of the matrix $\varepsilon^T\varepsilon$ will likely decrease the similarities among the row-vectors in the matrix ε and minimize its rank deficiency. The study in (22) also indicates that within the sensitivity matrix, less variation among the sub-matrices with respect

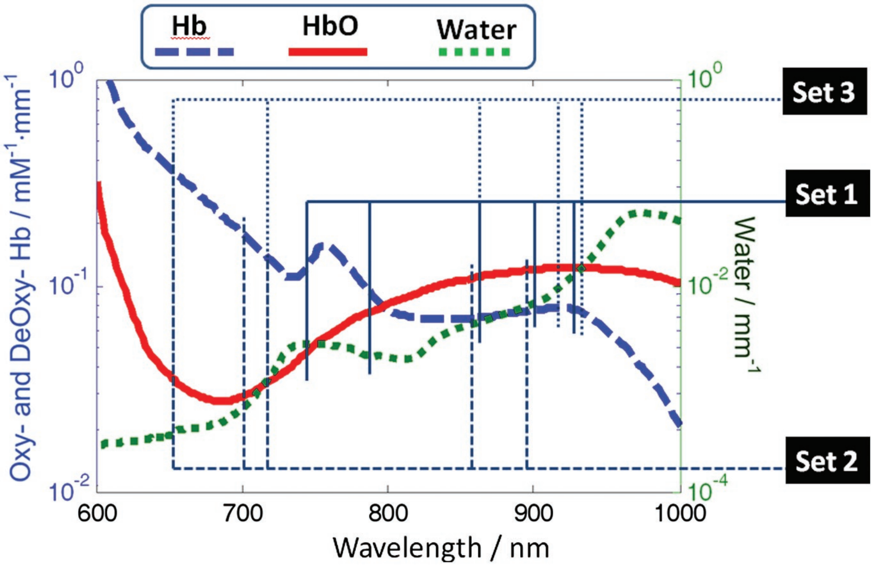

Figure 1: Illustration of the wavelength sets, which were used in an independent experimental study (8), employed for this study. The set 1 expands 186 nm from 740 nm to 926 nm. The set 2 expands 240 nm from 650 nm to 890 nm. The set 3 expands 280 nm from 650 nm to 930 nm. The spectra in Figure 1 follow the chromophore absorption spectraused in (2, 8), which are based on the same study by Prahl (23).

Table I
Wavelength sets to be examined and comparison of PRULs evaluation with the analytical solutions.

		Absorption Part		Scattering Part	
Sets	Wavelengths/nm	Determinant of denominator: ($\varepsilon^T\varepsilon$)	Standard deviation of extinction coefficients dev(ε)	Determinant of denominator	Standard deviation of $\partial x/\partial M(\lambda)$
(2)	650,700,716,860,890	2.58e-7	388.0	0.37	0.67
(1)	740,788,866,902,926	8.18e-7	63.7	0.18	1.03
(3)	650,716,866,914,930	1.30e-5	63.8	0.53	0.45

to each category of reconstruction parameters (such as chromophore concentrations and scattering parameters) renders more favorable reconstruction. This study thereby includes the magnitude uniformity of $\partial x/\partial M$ in equation (3) as one of the criteria for wavelength optimization.

Optimization methods in (2, 8, 20, 22) appraise the residue and condition numbers of sensitivity matrix that includes $n_{\text{source-detector-pair}} \times n_{\text{measurement-wavelength}} \times n_{\text{nodes}}$ terms. The method introduced in this study examines equations [5], [11] and [12], and the total evaluation number is $n_{\text{source-detector-pair}} \times n_{\text{measurement-wavelength}}$, which is n_{nodes} times less in the computation load needed than the methods introduced in (2, 8, 20, 22). Table I illustrates the outcome when applying our criteria to the three sets of spectral-*prior*, after neglecting the common terms $|\partial\mu(\lambda)/\partial M(\lambda)|\cdot\sigma_{M(\lambda)}$ in equation [3]. Since the optimization is in favor of large denominator of the determinant and small variation among the gradient values, the set 3 stands out as the best. The set 1 significantly outperforms the set 2 in absorption part, whereas the set 2 moderately outperforms the set 1 in scattering part. The overall ranking among the three sets of spectral-*prior* is thus (3, 1, 2), which agrees with the results in (8).

Quantitative Evaluations of Relative PRULs

To quantitatively evaluate the PRULs in equations [6], [11] and [12], we assign the background chromophore concentrations and scattering parameters as (22): $C_{HbO} = C_{Hb} = 0.01$ mM, $C_{H2O} = 40\%$ and A = b = 1. The preset properties of the anomaly are approximately two-folds of those assigned to the background, as: $C_{HbO\_anom} = 0.023$ mM, $C_{Hb\_anom} = 0.023$ mM, $C_{H2O\_anom} = 80\%$, $A_{anom} = 2$, and $b_{anom} = 2$. The relative uncertainties of all measurement differences are assumed as 1% (19), that is: $\frac{\sigma^2_{\delta(\lambda)}}{\delta^2(\lambda)} = \frac{\sigma^2_{a(\lambda)}}{a^2(\lambda)} = \frac{\sigma^2_{\phi(\lambda)}}{\phi^2(\lambda)} = (1\%)^2$. Besides, for the range of wavelengths and modulation frequency commonly utilized in optical tomography, one could approximate $\frac{a^2(\lambda)+\phi^2(\lambda)}{a^2(\lambda)-\phi^2(\lambda)} = \left(\sqrt{1+\frac{\omega^2}{\nu^2\mu_a^2(\lambda)}}\right)$ as 1. With these necessary pre-conditioning, Table II shows the quantitative evaluations of PRULs in equations [6], [11] and [12], and normalizes the PRULs by the pre-set contrasts of the anomaly. Such normalized values relate to the Noise-to-Contrast Ratios (NCR) in the reconstruction. In Table II, the absolute NCRs are further normalized by those of DC-only in each column, the absorption part is further normalized by NCRs of the hemoglobin in each row, and the scattering part is normalized by NCRs of the scattering amplitude in each row. Such normalizations more explicitly indicate the rankings of NCR among three measurement conditions for each reconstruction parameter.

From the Row-wise Norm. in Table II, one would expect that DC reconstruction has the least NCRs and accordingly, the least relative uncertainties in the reconstruction. One would also expect that including DC measurements in FD at several cases does not necessarily increase the reconstruction NCRs. Based on the Column-wise Norm. in Tables II, one would also expect that for the three sets of wavelengths, $NCR_{C\_Hb} < NCR_{C\_H2O} < NCR_{C\_HbO}$ for the absorption aspect and $NCR_A < NCR_b$ for the scattering aspect.

Simulation Studies

Synthetic Model and Geometry

The synthetic study is based on NIRFAST package (24). The forward model computes photon diffusion at each wavelength by:

$$\left(-\frac{\mu_a(\vec{r},\lambda)}{D(\vec{r},\lambda)} + \frac{i\omega}{\nu D(\vec{r},\lambda)}\right)U(\vec{r},\omega,\lambda) + \nabla^2 U(\vec{r},\omega,\lambda) = -\frac{S(\vec{r},\omega,\lambda)}{D(\vec{r})} \quad [16]$$

where $U(\vec{r},\omega,\lambda)$ is the photon fluence of wavelength λ at frequency ω (for DC simply assigning $\omega = 0$) for position $\vec{r}$, and $S(\vec{r},\omega,\lambda)$ is the source term. The Robin type boundary condition is assigned as:

$$U(\vec{r}_0,\omega) - 2DA\hat{n}_0 \cdot \nabla U(\vec{r}_0,\omega) = 0 \quad [17]$$

where $\vec{r}_0$ denotes the boundary node; A is the coefficient accounting for the refractive index mismatch; and $\hat{n}_0$ is the

Table II

Analytical evaluation of parameter reconstruction uncertainty levels normalized by target contrasts (NCRs).

		HbO/mM			Hb/mM			H_2O/%			A			b		
Sets	Measurement	Abs.	Column-wise Norm.	Row-wise Norm.	Abs.	Column-wise Norm.	Row-wise Norm.	Abs.	Column-wise Norm.	Row-wise Norm.	Abs.	Column-wise Norm.	Row-wise Norm.	Abs.	Column-wise Norm.	Row-wise Norm.
(1)	DC	0.044	1	2.0	0.022	1	1	0.030	1	1.4	0.010	1	1	0.053	1	5.2
	AC + PHS	0.062	1.41	2.0	0.031	1.41	1	0.042	1.41	1.4	0.015	1.41	1	0.075	1.41	5.2
	DC + AC + PHS	0.107	2.45	2.0	0.054	2.45	1	0.072	2.45	1.4	0.015	1.41	1	0.075	1.41	5.2
(2)	DC	0.127	1	9.4	0.014	1	1	0.126	1	9.3	0.011	1	1	0.037	1	3.3
	AC + PHS	0.180	1.41	9.4	0.019	1.41	1	0.179	1.41	9.3	0.016	1.41	1	0.052	1.41	3.3
	DC + AC + PHS	0.311	2.45	9.4	0.033	2.45	1	0.310	2.45	9.3	0.016	1.41	1	0.052	1.41	3.3
(3)	DC	0.054	1	5.4	0.010	1	1	0.032	1	3.2	0.008	1	1	0.031	1	3.9
	AC + PHS	0.076	1.41	5.4	0.014	1.41	1	0.046	1.41	3.2	0.011	1.41	1	0.044	1.41	3.9
	DC + AC + PHS	0.132	2.45	5.4	0.025	2.45	1	0.080	2.45	3.2	0.011	1.41	1	0.044	1.41	3.9

outgoing normal vector. The sensitivity or Jacobian matrix is constructed according to the measurands (18) as:

$$J = \begin{bmatrix} DC \\ AC \\ PHS \end{bmatrix} = \begin{bmatrix} \frac{\partial \ln U_{DC}(\lambda_1)}{\partial x} & \frac{\partial \ln U_{DC}(\lambda_2)}{\partial x} & \cdots & \frac{\partial \ln U_{DC}(\lambda_m)}{\partial x} \\ \frac{\partial \ln |U_{AC}(\lambda_1)|}{\partial x} & \frac{\partial \ln |U_{AC}(\lambda_2)|}{\partial x} & \cdots & \frac{\partial \ln |U_{AC}(\lambda_m)|}{\partial x} \\ \frac{\partial \Phi_{AC}(\lambda_1)}{\partial x} & \frac{\partial \Phi_{AC}(\lambda_2)}{\partial x} & \cdots & \frac{\partial \Phi_{AC}(\lambda_m)}{\partial x} \end{bmatrix} \quad [18]$$

where *x* represents the parameters to be reconstructed, including chromophore concentrations and scattering amplitude and scattering power.

Figure 2 shows a circular geometry with the medium enclosed by a ring-applicator of 86 mm in diameter (3, 18, 20, 22). 16 optodes are evenly distributed along the circumference, and each optode functions sequentially as the source with the other 15 optodes being the detection channels. As a two-dimensional optode array is simulated and all the targets are assumed centering on the plane of the optode array, two-dimensional finite-element-method (FEM) simulation is used in this study (25). The imaging geometry is discretized into 3418 finite-elements with 1785 nodes. All the simulations used 30 × 30 pixel basis for reconstruction. The reconstruction routines stop as the change of the projection error falls below 2%.

The optical properties employed in the simulations are identical to those used for Tables II, and an anomaly could have one or multiple contrasts of the properties. Two sets of simulations are conducted. One set simulates five targets with independent contrasts, and the other set studies two closely positioned targets of identical properties. White noise at 1% is added to the forward data before applying the Levernberg-Marquardt algorithm as the inverse solver.

Simulation Results

Reconstructing Targets with Independent Contrasts

The set targets are five 8 mm-radius contrast-regions located 25 mm away from the center of the geometry with 0.4π angular separation, as shown in the column set of Figure 3. Each of the five regions differs from the rest

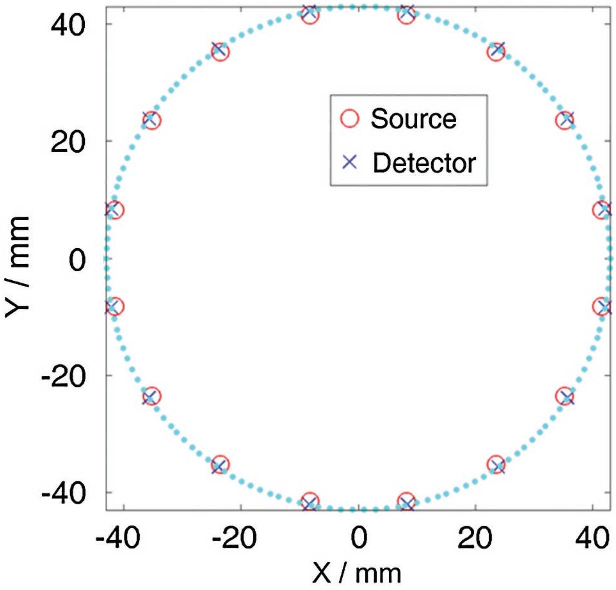

Figure 2: Simulation geometry. The FEM mesh has a radius of 43 mm and includes 1785 nodes and 3418 elements.

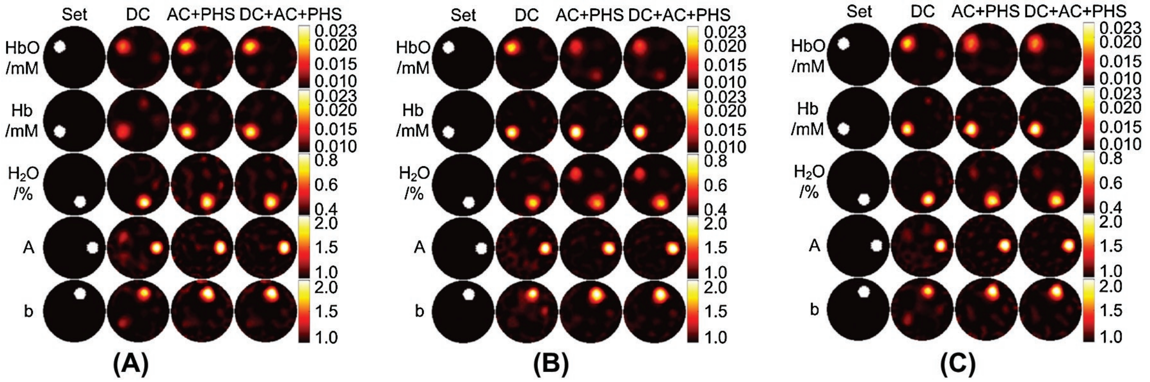

Figure 3: Synthetic study on five targets with independent contrasts in image geometry shown in Figure 2. (**A**)(**B**)(**C**) are the results for the wavelength sets (1)(2)(3) in Table I, respectively. (**A**) Second best: slight cross-coupling between HbO/A and between Hb/b recovery in column DC. (**B**) Worst: Severe cross-coupling between HbO and H_2O. (**C**) Best: minimal cross-coupling and target underestimation. Note: target overestimation is not visible because of uniform color bars. Look for absolute values in Table III.

in its contrast. Figure 3 shows the reconstruction results for the three sets of spectral-*prior*, and Table III demonstrates the maximum values of each variable within the target regions and the percentage error of the contrast. In terms of the overall accuracy quantified in the Table III and the artifact visualized in the Figure 3, the set 3 shown in Figure 3(C) outperforms the other two. Next to the set 3 is the set 1 shown in Figure 3(A), wherein the DC reconstruction underestimates HbO and Hb yet overestimates A and b due to cross-coupling. The set 2 shown in Figure 3(B) is the least accurate, specifically in FD reconstruction, as it has the highest level of cross-coupling between the HbO and H_2O concentrations.

Table IV lists the NCRs of the reconstruction results in Figure 3, that is, the standard deviations (σ_x) of the reconstructed background values normalized by the maximum target contrasts. The σ_x values are calculated by excluding the areas co-centric to the targets but with the radii twice as those of the target regions. Similar to those in Table II, the NCRs in Table IV are normalized by those of DC-only in each column. Similarly in each row of Table IV, the absorption part is normalized by NCRs of the Hb and the scattering part is normalized by NCRs of the A. The row-wisely normalized NCRs in Table IV unanimously show $NCR_{C\_Hb} < NCR_{C\_H2O} < NCR_{C\_HbO}$ for the absorption part and $NCR_A < NCR_b$ for the scattering part, which agree with those predicted in Table II. For column-wisely normalized NCRs, in the sets 1 and 3, both Table II and IV indicate that the ratio of AC + PHS over DC stays within the range of [1, 2]. The artifact levels of DC + AC + PHS reconstruction are shown always lower than those of AC + PHS and sometimes lower than those of DC. Similar observations were reported in (18), and collectively they conclude that DC component is indeed not-redundant in FD measurements, therefore neglecting DC would

Table III

Target accuracy in Figure 3.

	Data	HbO/mM		Hb/mM		H_2O/%		A		b	
		Abs.	Err./%	Abs.	Err./%	Abs.	Err./%	Abs.	Err./%	Abs.	Err./%
	Set Values	2.3e-2		2.3e-2		0.80		2.0		2.0	
(1)	DC	1.7e-2	−46	1.6e-2	−55	0.82	5	2.2	21	1.9	−9
	AC + PHS	2.0e-2	−23	2.3e-2	−2	0.81	2	2.4	39	2.3	30
	DC + AC + PHS	2.0e-2	−24	2.2e-2	−6	0.80	0.4	2.3	34	2.2	23
(2)	DC	2.0e-2	−21	2.4e-2	4	0.72	−21	2.4	40	2.1	7
	AC + PHS	1.6e-2	−56	2.6e-2	24	0.67	−33	2.3	26	2.1	6
	DC + AC + PHS	1.7e-2	−48	2.7e-2	27	0.69	−27	2.2	23	2.1	10
(3)	DC	2.0e-2	−25	2.3e-2	1	0.83	8	2.3	33	1.9	−11
	AC + PHS	1.8e-2	−42	2.5e-2	16	0.78	−6	2.4	45	2.2	19
	DC + AC + PHS	1.8e-2	−39	2.5e-2	18	0.77	−8	2.4	39	2.2	17

Table IV
Absolute and normalized NCRs of the images in Figure 3.

Sets	Measurement	HbO/mM			Hb/mM			H_2O/%			A			b		
		Abs.	Column-wise Norm.	Row-wise Norm.	Abs.	Column-wise Norm.	Row-wise Norm.	Abs.	Column-wise Norm.	Row-wise Norm.	Abs.	Column-wise Norm.	Row-wise Norm.	Abs.	Column-wise Norm.	Row-wise Norm.
(1)	DC	0.066	1	1.3	0.052	1	1	0.039	1	0.7	0.022	1	1	0.051	1	2.3
	AC + PHS	0.072	1.6	2.1	0.035	1.4	1	0.066	1.7	1.9	0.038	2.0	1	0.057	1.6	1.5
	DC + AC + PHS	0.058	1.2	1.8	0.033	1.3	1	0.049	1.2	1.5	0.032	1.6	1	0.047	1.3	1.4
(2)	DC	0.048	1	1.4	0.033	1	1	0.063	1	1.9	0.028	1	1	0.043	1	1.5
	AC + PHS	0.054	0.6	2.2	0.025	0.9	1	0.049	0.7	2.0	0.025	0.8	1	0.037	0.9	1.5
	DC + AC + PHS	0.049	0.7	2.1	0.023	0.9	1	0.047	0.7	2.0	0.027	0.8	1	0.036	0.9	1.3
(3)	DC	0.049	1	1.9	0.026	1	1	0.040	1	1.5	0.026	1	1	0.038	1	1.5
	AC + PHS	0.072	1.1	1.6	0.044	2.0	1	0.047	1.0	1.1	0.024	1.0	1	0.050	1.8	2.1
	DC + AC + PHS	0.052	0.9	1.6	0.033	1.5	1	0.037	0.8	1.1	0.020	0.8	1	0.040	1.4	2.0

degrade the accuracy of FD reconstruction. In the set 2, the NCRs are slightly lower in FD than in DC-only. This implies that FD measurement is more robust in case of less desirable spectral-*prior*.

Resolving Two Closely Positioned Identical Targets

In Figure 4, two identical targets of 8-mm in radius are embedded 25 mm from the center and the angular separation between the targets is $\pi/4$. Each target has all five contrast properties as previously defined. Figure 4 indicates that DC seems to be comparable to FD in the estimation of Hb, A, and b, but underestimates the concentration of Hb and H_2O as comparing to FD. To explicitly compare how well the targets are resolved, the parameter contours along the concentric circle of the imaging geometry and across the targets (marked with gold dotted loops in Figure 4) are plotted in Figure 5. Figures 4 and 5 show that even though the absolute properties of the target are the least accurate in DC reconstruction, the two targets are seemed better resolved in DC than in FD. Table V lists the ratios of target-to-valley contrast over target-to-background contrast (both contrasts are illustrated in the upper-left subfigure of Figure 5). Larger ratios indicate better identification of the targets. It is shown that, except for the cases of possessing the contrast of "A", the targets are always resolved more clearly in DC than in FD.

Comparison of $\mu_a(\lambda)$ *and* $\mu_s'(\lambda)$

Since the sensitivity matrices of multi-spectral NIR tomography are derived from that of single-wavelength optical tomography, the reconstruction results of $\mu_a(\lambda)$ and $\mu_s'(\lambda)$ could also be insightful to the evaluation of the reconstruction performance. In this section, the analytical model of

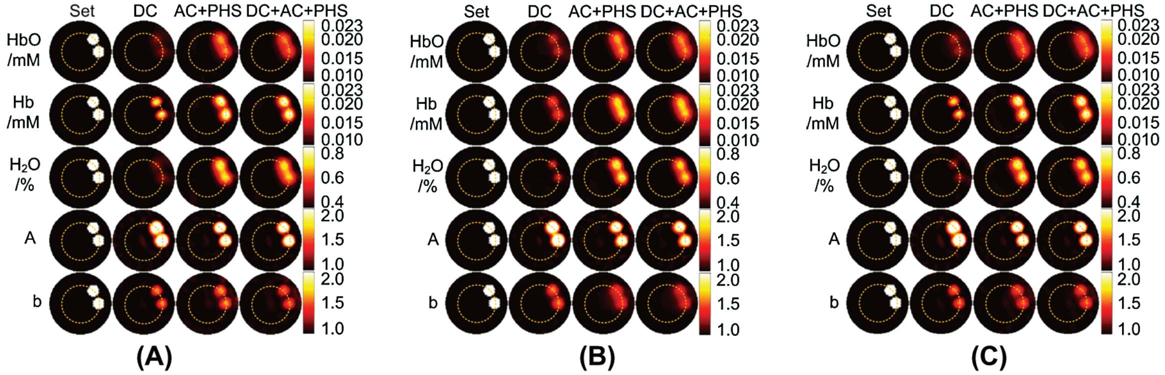

Figure 4: Synthetic study on two targets with all five parameter contrasts in image geometry shown in Figure 2. (**A**)(**B**)(**C**) are the results for the wavelength sets (1)(2)(3) in Table I, respectively. Cross-coupling are severe in all reconstructed parameters. (**A**) Second best: targets are inseparable in H_2O distribution recovery by FD reconstructions. (**B**) Worst: targets are inseparable in Hb and b distribution recovery by FD reconstructions. (**C**) Best: targets are separated in all cases.

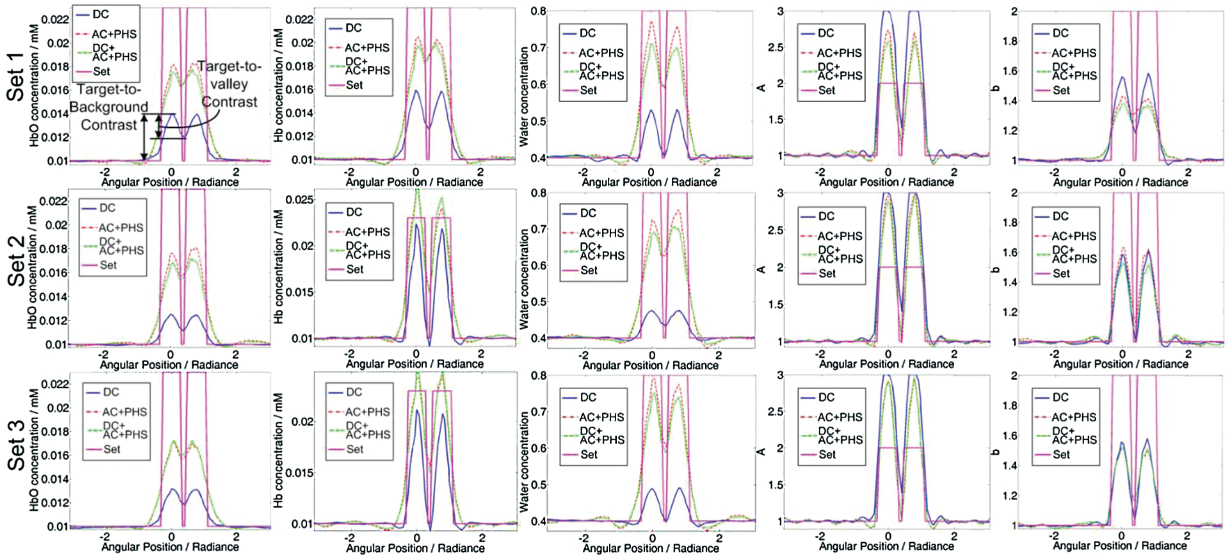

Figure 5: Parameter contour plots along the gold dash lines in Figure 4. The upper left subfigure denotes the target-to-valley contrast and target-to-background contrast. DC reconstruction shows relatively deeper contrast valleys between the targets for most cases.

$\sigma_{\mu a(\lambda)}$ and $\sigma_{\mu s'(\lambda)}$ will be compared to $\sigma_{\mu a(\lambda)}$ and $\sigma_{\mu s'(\lambda)}$ derived from synthetic studies. However, there is difference between the PRUL calculations of $\sigma_{\mu a(\lambda)}$ and $\sigma_{\mu s'(\lambda)}$ in analytical model and in simulation. For analytical model, the calculations of $\sigma_{\mu a(\lambda)}$ and $\sigma_{\mu s'(\lambda)}$ involve evaluating $\mu_a(\lambda)$ and $\mu_s'(\lambda)$ in equation [2] with the preset simulation parameters and substituting $\mu_a(\lambda)$ and $\mu_s'(\lambda)$ values into Table II and IV in (18). Whereas for simulation, $\mu_a(\lambda)$ and $\mu_s'(\lambda)$ values are not recovered explicitly in the reconstruction under spectral-*prior*, therefore, the PRULs of the recovered parameters need to be reversely projected to $\sigma_{\mu a(\lambda)}$ and $\sigma_{\mu s'(\lambda)}$, by:

$$(\vec{\sigma}_{\vec{\mu}_a(\lambda)})_{m\times 1} = \left|\frac{\partial \vec{\mu}_a(\lambda)_{m\times 1}}{\partial(\vec{c})_{n\times 1}}\right|_{m\times n} \times (\vec{\sigma}_c)_{n\times 1} \quad [19]$$

$$= \log(10)\cdot(\vec{\varepsilon})_{m\times n} \times (\vec{\sigma}_c)_{n\times 1}$$

and

$$\left(\sigma_{\mu_s'(\lambda)}\right)_{m\times 1} = \sqrt{\left(\frac{\partial \mu_s'(\lambda)}{\partial A}\right)^2_{m\times 1}\cdot\sigma_A^2 + \left(\frac{\partial \mu_s'(\lambda)}{\partial b}\right)^2_{m\times 1}\cdot\sigma_b^2} \quad [20]$$

$$= \left(\sqrt{(\lambda^{-b}\cdot\sigma_A)^2 + (-A\lambda^{-b}\cdot\log\lambda\cdot\sigma_b)^2}\right)_{m\times 1}$$

Analytical and simulated values of $\sigma\mu_a(\lambda)$ and $\sigma\mu_s'(\lambda)$ are plotted verses the wavelengths in Figure 6 (A) and (B) respectively. The curve shapes agree between the analytical predictions and reconstruction results, yet the relative magnitudes of the curves differ slightly. In the analytical prediction, the uncertainties always follow the relationship of $\sigma_{\mathrm{DC}} < \sigma_{\mathrm{AC+PHS}} \leq \sigma_{\mathrm{DC+AC+PHS}}$ for both $\mu_a(\lambda)$ and $\mu_s'(\lambda)$. In simulation study, one has $\sigma_{\mu a(\lambda)\_\mathrm{DC}} < \sigma_{\mu a(\lambda)\_\mathrm{DC+AC+PHS}} \leq \sigma_{\mu a(\lambda)\_\mathrm{AC+PHS}}$. However, for $\sigma_{\mu s'}(\lambda)$ in Figure 6 (B), DC reconstruction is not always advantageous than FD. Such outcome is in no doubt related to the phase information residing in FD as that gives an additional dimension to unveil the separate contributions of $\mu_a(\lambda)$ and $\mu_s'(\lambda)$ to the photon fluence. When phase information is employed, however, $\sigma_{\mu s'(\lambda)\_\mathrm{DC+AC+PHS}} < \sigma_{\mu s'(\lambda)\_\mathrm{AC+PHS}}$ stands for all cases, indicating that DC information is not redundant in FD.

Table V
Comparison of target separation in Figure 5.

	Data	HbO	Hb	H_2O	A	b
(1)	DC	0.76	0.56	0.98	0.81	0.68
	AC + PHS	0.15	0.18	0.47	0.93	0.27
	DC + AC + PHS	0.36	0.15	0.35	0.87	0.30
(2)	DC	0.54	1.07	0.57	0.80	1.01
	AC + PHS	0.25	0.65	0.31	1.01	0.80
	DC + AC + PHS	0.20	0.67	0.21	0.97	0.85
(3)	DC	0.42	1.06	1.01	0.81	0.93
	AC + PHS	0.19	0.61	0.46	0.99	0.67
	DC + AC + PHS	0.18	0.66	0.52	0.99	0.70

Note: Data are calculated as the ratio of the target-to-valley contrast over target-to-background contrast (target-to-valley contrast over and target-to-background contrast are illustrated respectively, in Figure 5 subfigure Set 1, Column HbO).

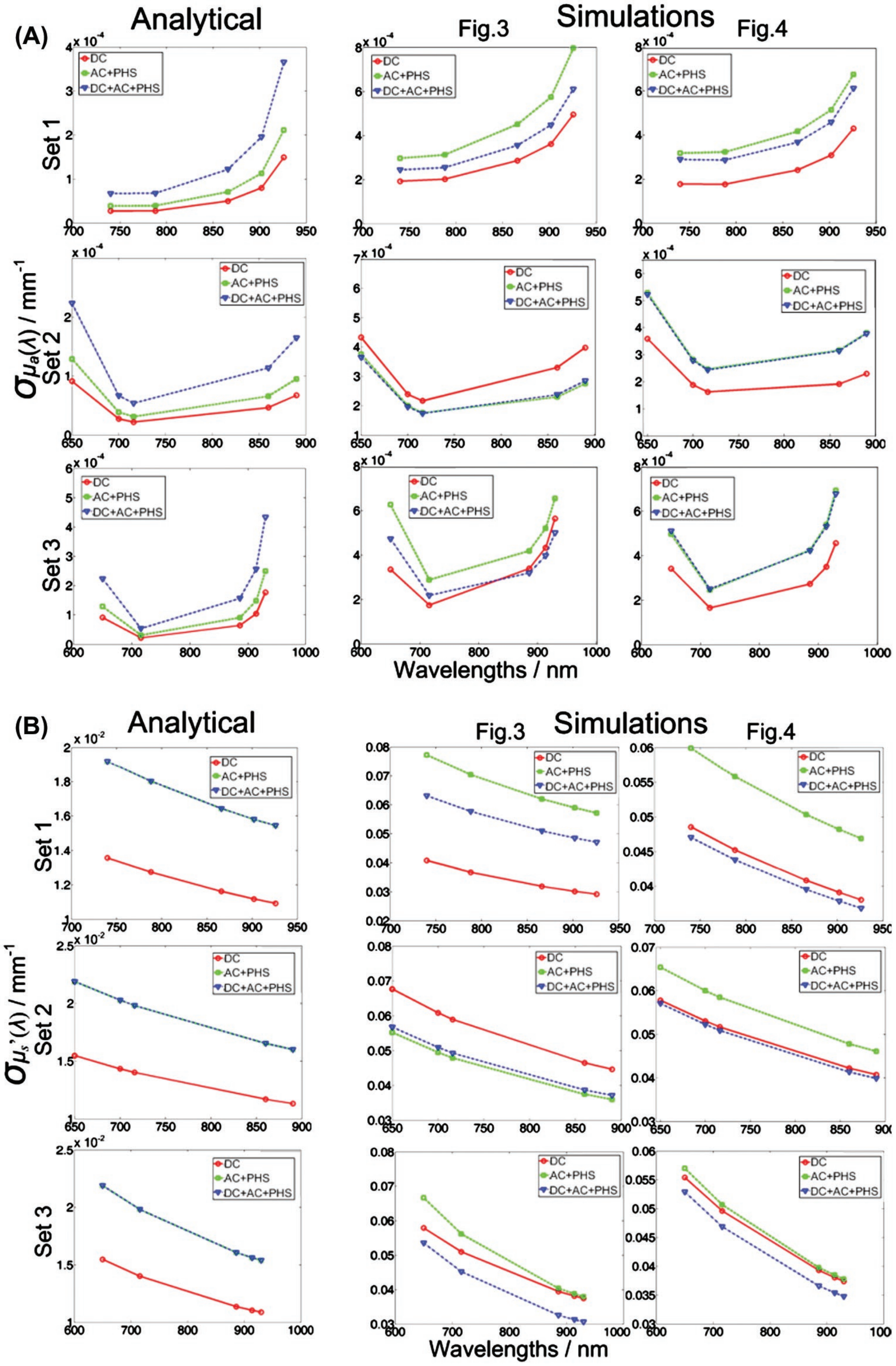

Figure 6: Comparison between the artifact levels in absorption and scattering coefficients at each wavelength. Curve shapes of analytical model and synthetic studies agree in all cases. (**A**) Absorption coefficients comparison. DC reconstructions show least background artifact levels. DC + AC + PHS at most cases outperforms AC + PHS. (**B**) Scattering coefficients comparison. DC reconstructions does not necessarily show least background artifact levels. DC + AC + PHS at most cases outperforms AC + PHS.

Discussions

The analytical model is derived under the condition of infinite medium, in which the measurements defined in equation [1] are linear with respect to ρ. However, the circular imaging geometry possesses a boundary and can be approximated at best as a semi-infinite medium. The solution of photon diffusion in a semi-infinite geometry generally utilizes an image source with respect of an extrapolated boundary (26). Boas derived an approximation solution to photon diffusion in the semi-infinite geometry in (27) under the condition that the source-detector distance is much larger than the diffusion path length. The equation is rewritten following the notations of this study:

$$U(\vec{r},\omega)=\frac{vS(\vec{r}',\omega)e^{ikd}}{4\pi Dd^2}\left[-4ik(z_b{}^2+z_b z_{tr})\right] \qquad [21]$$

where ω is the angular modulation frequency, $U(\vec{r},\omega)$ is the photon fluence detected at position $\vec{r}$, $S(\vec{r}',\omega)$ is the light source at $\vec{r}'$, $d=|\vec{r}'-\vec{r}|$ is source-detector distance, z_b is the distance of the extrapolated boundary to the physical boundary, $z_{tr}=(\mu_s')^{-1}$ is the diffusion path length, and k is the wave number of the photon fluence:

$$k_{\mathrm{CW}} = ik_{\mathrm{DC}} \qquad [22\text{-CW}]$$

$$k_{\mathrm{FD}} = ik_{\mathrm{AC}} - k_{\mathrm{PHS}} \qquad [22\text{-FD}]$$

where k_{DC} k_{AC} and k_{PHS} are defined in equation [1]. Note that the factor $\left[-4ik(z_b{}^2+z_b z_{tr})\right]$ in [21] is constant, therefore one has the following linear relationship between $\log\left[d^2\cdot U\left(\vec{r},\omega\right)\right]$ and d:

$$\begin{aligned}\log[d^2\cdot U_{CW,FD}(\vec{r},\omega)] &= ik_{CW,FD}d+\log\left(\frac{vS(\vec{r}',\omega)}{4\pi D}\right)\\ &\quad +\log[-4ik_{CW,FD}(z_b^2+z_b z_{tr})]\end{aligned} \qquad [23]$$

Following equation [1] we define the difference between $\ln(d^2\cdot U(d))$ measured at d_1 and d_2 away from the source as:

$$\begin{aligned}\delta &= \log[d_1^2\cdot U_{CW}(d_1)]-\log[d_2^2\cdot U_{CW}(d_2)] \qquad [24\text{-CW}]\\ &= \left|d_1-d_2\right|\cdot ik_{CW} = -\rho\cdot k_{DC}\end{aligned}$$

$$\begin{aligned}\alpha+i\phi &= \log[d_1^2\cdot U_{FD}(d_1)]-\log[d_2^2\cdot U_{FD}(d_2)] \qquad [24\text{-FD}]\\ &= \left|d_1-d_2\right|\cdot ik_{FD} = -\rho\cdot k_{AC}+\rho\cdot ik_{PHS}\end{aligned}$$

and the expressions of δ, α and ϕ are consistent with those in equation [1] and [24]. Therefore, the outcomes derived under infinite medium conditions are applicable to geometries with semi-infinite boundaries.

The PRUL analyses introduced in (18) actually implicated the uniqueness of the solutions of DC only reconstruction in multi-spectral NIR tomography. Previous studies (28-29) suggested that in a homogenous medium, the product of $\mu_a(\lambda)$ and $D(\lambda)$ can be considered as a constant function of the surface diffuse reflectance of the medium as:

$$\left[\mu_a\cdot D\right]=K\left(R_\infty\right) \qquad [25]$$

Taking equation [25] into consideration, $\mu_a(\lambda)$, $D(\lambda)$ and $\mu_s'(\lambda)$ can be independently expressed as (18):

$$\mu_a(\lambda)\big|_{DC}=\sqrt{K(R_\infty(\lambda))}\cdot\frac{\delta(\lambda)}{\rho} \qquad [26.1]$$

$$D(\lambda)\big|_{DC}=\sqrt{K(R_\infty(\lambda))}.\frac{\rho}{\delta(\lambda)} \qquad [26.2]$$

$$\begin{aligned}\mu_s'(\lambda)\big|_{DC} &= \frac{1}{(3D(\lambda))}-\mu_a(\lambda)\big|_{DC}\\ &= \left(\frac{1}{3\sqrt{K(R_\infty(\lambda))}}-\sqrt{K(R_\infty(\lambda))}\right)\cdot\frac{\delta(\lambda)}{\rho}\end{aligned} \qquad [26.3]$$

If the DC optical tomography measurement lacks $K(R_\infty)$, equation [26] may become under-determined and thereby inter-parameter cross-coupling may exist. Under spectral-*prior*, however, the $\sqrt{K(R_\infty(\lambda))}$ term could be eliminated and subsequently the cross-coupling be reduced. By combining equations [26.1] and [26.3] and substituting into equations [2-μ_a] and [2-μ_s'], the DC measurement becomes the function of only the absorption chromophore concentrations and scattering parameters as:

$$\begin{aligned}\frac{\delta^2(\lambda)}{\rho^2} &= 3\mu_a(\lambda)(\mu_a(\lambda)+\mu_s'(\lambda)) \qquad [27]\\ &= 3\cdot\sum_i\varepsilon_i(\lambda)c_i\cdot\left(\sum_i\varepsilon_i(\lambda)c_i+A\lambda^{-b}\right)\end{aligned}$$

Therefore one can decouple the unknown values once measurements at sufficient number of wavelengths are available. This agrees with the observation in this and several previous studies that DC reconstruction with spectral-*prior* successfully resolves the target, as evidenced in Figures 3. Interestingly, as is shown in Figures 4, even in the FD reconstruction the intrinsic cross-coupling problem becomes significant when multiple contrasts are assigned to the same location (21). As fewer measurement components in DC reconstruction facilitate less system noise in the inverse problem, the level of background artifacts could actually be lower in DC reconstruction.

The PRUL analyses of both multi-spectral reconstruction parameters and the optical properties have been shown reliable. The method of ranking the spectral-*prior* based on PRUL sets conforms to the recommendation by (8) at desirably less computation load. However, there is still disagreement between the analytical prediction and simulation results due to the approximation in analytic modeling and smoothing effect in synthetic studies. For example, since the analytical model only accounts for the perturbations in the measurement, it is predicted that DC-excluded FD will outperform DC-included FD, yet the simulation shows the contrary. Such aberrations actually explain that extra information in DC components has balanced the excessive reconstruction uncertainties and made DC + AC + PHS a better choice than AC + PHS for FD reconstruction.

Using the three sets of wavelengths experimented in an independent prior work, this study investigated two aspects of the spectral *prior*: (1) for a given spectral *prior*, which among the chromophore concentrations (HbO, Hb, and H_2O) or between the scattering properties (A and b) is recovered at lower (hence better) noise-to-contrast-ratio, regardless of using DC or FD reconstruction; (2) for a given spectral *prior*, which measurement information among DC, DC-excluded FD, and DC-included FD leads to better quantification or resolution of the target(s).

For the first above-mentioned aspect of spectral *prior*, it is shown, from both numerical estimation based on the introduced analytical approach and simulation, that the rank of overall quality of chromophore recovery is Hb, H_2O, and HbO from the highest to lowest; and in the scattering part the A is always better recovered than b. This finding, on the other hand, demonstrates that the DC-only information results in unique solution to the image reconstruction routine, under adequate (not necessarily optimal) spectral *prior*.

The second above-mentioned aspect of spectral *prior* actually gives rise to two important observations that were not widely appreciated previously: whether DC information is redundant in FD reconstruction, and how DC-only reconstruction compares with DC-excluded or DC-included FD reconstruction. It is shown in this study that, the artifact levels of DC + AC + PHS, or DC-included FD, reconstruction are always lower than those of AC + PHS, or DC-excluded FD. Therefore one should expect that the DC component is indeed not-redundant in FD measurements, and neglecting DC degrades the contrast-to-noise-ratio of FD reconstruction. In terms of DC-only reconstruction versus FD reconstruction (including DC-excluded or DC-included), the DC-only does lead to less accurate quantification of the absolute investigated properties of the target comparing to what FD provides. However, multiple targets of identical contrasts over the background are resolved almost always more clearly by DC-only than by FD reconstruction, except for the targets possessing the contrast of "A". Such salient features owe to the least level of artifacts in DC-only reconstruction associated with an optimal spectral *prior*, similar to what was demonstrated with single-band reconstruction (18). In the case of a less desirable spectral-*prior*, however, the FD could outperform DC in the recovery of scattering properties including both A and b, implying that the addition of phase-information helps the less desirable spectral *prior* resolve the scattering properties more robustly.

Conclusions

A PRUL analysis model has been applied to multispectral optical tomography and used to evaluate the outcome of three sets of wavelength for spectrally-constrained optical tomography reconstruction. Simulations in an external-imaging geometry are conducted to appraise the predictions given by the introduced analytical methods. Both numerical and simulation analyses demonstrate that the rank of overall quality of chromophore recovery is Hb, H_2O, and HbO from the highest to lowest; and in the scattering part the A is always better recovered than b. The DC-only information gives rise to unique solution to the image reconstruction routine under the given spectral *prior*. It is further shown that, DC-information is beneficial to FD-reconstruction, as the artifact levels of DC + AC + PHS, or DC-included FD, reconstruction are always lower than those of AC + PHS, or DC-excluded FD. The artifacts level as represented by the noise-to-contrast-ratio is almost always the least in DC-only, leading to generally better resolution of multiple targets of identical contrasts over the background than in FD. However, FD could outperform DC in the recovery of scattering properties including both A and b when the spectral *prior* is less optimal, implying the benefit of phase-information in scattering recovery in the context of spectrally-constrained optical tomography.

Acknowledgements

This work has been supported in part by the Prostate Cancer Research Program of the U.S. Army Medical Research Acquisition Activity (USAMRAA) through grants #W81XWH-07-1-0247 and #W81XWH-10-1-0836.

References

1. Tromberg, B. J., Pogue, B. W., Paulsen, K. D., Yodh, A. G., Boas, D. A., Cerussi, A. E. Assessing the future of diffuse optical imaging technologies for breast cancer management. *Medical Physics 35*, 2443-2451 (2008).
2. Corlu, A., Durduran, T., Choe, R., Schweiger, M., Hillman, E. M. C., Arridge, S. R., Yodh, A. G. Uniqueness and wavelength optimization in continuous-wave multispectral diffuse optical tomography. *Opt Lett 28*, 2339-2341 (2003).
3. Srinivasan, S., Pogue, B. W., Jiang, S., Dehghani, H., Paulsen, K. D. Spectrally constrained chromophore and scattering near-infrared

tomography provides quantitative and robust reconstruction. *Appl Opt 44*, 1858-1869 (2005).

4. Li, A., Zhang, Q., Culver, J. P., Miller, E. L., Boas, D. A. Reconstructing chromosphere concentration images directly by continuous-wave diffuse optical tomography. *Opt Lett 29*, 256-258 (2004).
5. Jobsis, F. F. Noninvasive, infrared monitoring of cerebral and myocardial oxygen sufficiency and circulatory parameters. *Science 198*, 1264-1267 (1977).
6. Bastian, H. On uniqueness in diffuse optical tomography. *Inverse Problems 25*, 055010 (2009).
7. Arridge, S. R., Lionheart, W. R. B. Nonuniqueness in diffusion-based optical tomography. *Opt Lett 23*, 882-884 (1998).
8. Corlu, A., Choe, R., Durduran, T., Lee, K., Schweiger, M., Arridge, S. R., Hillman, E. M. C., Yodh, A. G. Diffuse optical tomography with spectral constraints and wavelength optimization. *Appl Opt 44*, 2082-2093 (2005).
9. McBride, T. O., Pogue, B. W., Poplack, S., Soho, S., Wells, W. A., Jiang, S., Osterberg, U. L., Paulsen, K. D. Multispectral near-infrared tomography: a case study in compensating for water and lipid content in hemoglobin imaging of the breast. *Journal of Biomedical Optics 7*, 72-79 (2002).
10. Jiang, Z., Piao, D., Holyoak, G. R., Ritchey, J. W., Bartels, K. E., Slobodov, G., Bunting, C. F., Krasinski, J. S. Trans-rectal Ultrasound-coupled Spectral Optical Tomography of Total Hemoglobin Concentration Enhances Assessment of the Laterality and Progression of a Transmissible Venereal Tumor in Canine Prostate. *Urology 77*, 237-242 (2011).
11. Jones, P. B., Shin, H. K., Boas, D. A., Hyman, B. T., Moskowitz, M. A., Ayata, C., Dunn, A. K. Simultaneous multispectral reflectance imaging and laser speckle flowmetry of cerebral blood flow and oxygen metabolism in focal cerebral ischemia. *Journal of Biomedical Optics 13*, 044007 (2008).
12. Xu, H., Springett, R., Dehghani, H., Pogue, B. W., Paulsen, K. D., Dunn, J. F. Magnetic-resonance-imaging-coupled broadband near-infrared tomography system for small animal brain studies. *Appl Opt 44*, 2177-2188 (2005).
13. Brooksby, B., Srinivasan, S., Jiang, S., Dehghani, H., Pogue, B. W., Paulsen, K. D., Weaver, J., Kogel, C., Poplack, S. P. Spectral priors improve near-infrared diffuse tomography more than spatial priors. *Opt Lett 30*, 1968-1970 (2005).
14. Wang, J., Davis, S. C., Srinivasan, S., Jiang, S., Pogue, B. W., Paulsen, K. D. Spectral tomography with diffuse near-infrared light: inclusion of broadband frequency domain spectral data. *Journal of Biomedical Optics 13*, 041305-041310 (2008).
15. Wang, J., Jiang, S., Paulsen, K. D., Pogue, B. W. Broadband frequency-domain near-infrared spectral tomography using a mode-locked Ti:sapphire laser. *Appl Opt 48*, D198-D207 (2009).
16. Wang, J., Pogue, B. W., Jiang, S., Paulsen, K. D. Near-infrared tomography of breast cancer hemoglobin, water, lipid, and scattering using combined frequency domain and cw measurement. *Opt Lett 35*, 82-84 (2010).
17. Wang, J., Jiang, S., Li, Z., diFlorio-Alexander, R. M., Barth, R. J., Kaufman, P. A., Pogue, B. W., Paulsen, K. D. *In vivo* quantitative imaging of normal and cancerous breast tissue using broadband diffuse optical tomography. *Medical Physics 37*, 3715-3724 (2010).
18. Xu, G., Piao, D., Bunting, C. F., Dehghani, H. Direct-current-based image reconstruction versus direct-current included or excluded frequency-domain reconstruction in diffuse optical tomography. *Appl Opt 49*, 3059-3070 (2010).
19. Fantini, S., Franceschini, M., Fishkin, J. B., Barbieri, B., Gratton, E. Quantitative determination of the absorption spectra of chromophores in strongly scattering media: a light-emitting-diode based technique. *Appl Opt 33*, 5204-5213 (1994).
20. Eames, M. E., Wang, J., Pogue, B. W., Dehghani, H. Wavelength band optimization in spectral near-infrared optical tomography improves accuracy while reducing data acquisition and computational burden. *Journal of Biomedical Optics 13*, 054037-054039 (2008).
21. Li, C., Grobmyer, S. R., Chen, L., Zhang, Q., Fajardo, L. L., Jiang, H. Multispectral diffuse optical tomography with absorption and scattering spectral constraints. *Appl Opt 46*, 8229-8236 (2007).
22. Eames, M. E., Dehghani, H. Wavelength dependence of sensitivity in spectral diffuse optical imaging: effect of normalization on image reconstruction. *Opt Express 16*, 17780-17791 (2008).
23. Prahl, S. A. Optical absorption of hemoglobin. *http://omlc.ogi.edu/spectra/hemoglobin/* (1999). Accessed on May 22, 2011.
24. Dehghani, H., Eames, M. E., Yalavarthy, P. K., Davis, S. C., Srinivasan, S., Carpenter, C. M., Pogue, B. W., Paulsen, K. D. Near infrared optical tomography using NIRFAST: Algorithm for numerical model and image reconstruction. *Communications in Numerical Methods in Engineering 25*, 711-732 (2009).
25. Hebden, J. C., Veenstra, H., Dehghani, H., Hillman, E. M. C., Schweiger, M., Arridge, S. R., Delpy, D. T. Three-dimensional time-resolved optical tomography of a conical breast phantom. *Appl Opt 40*, 3278-3287 (2001).
26. Fantini, S., Franceschini, M. A., Gratton, E. Semi-infinite-geometry boundary problem for light migration in highly scattering media: a frequency-domain study in the diffusion approximation. *J Opt Soc Am B 11*, 2128-2138 (1994).
27. Boas, D. A. Diffusion photon probes of structral and dynamical properties of turbid media: theory and biomedical applications. *Ph.D dissertation* (University of Pennsylvania, Philadelphia, Pennsylvania, 2000).
28. Jacques, S. L. Reflectance spectroscopy with optical fiber devices and transcutaneous bilirubinometers. *Biomedical Optical Instrumentation and Laser-Assisted Biotechnology 12* (1996).
29. Fabbri, F., Franceschini, M. A., Fantini, S. Characterization of Spatial and Temporal Variations in the Optical Properties of Tissuelike Media with Diffuse Reflectance Imaging. *Appl Opt 42*, 3063-3072 (2003).

Received: May 22, 2011; Revised: August 7, 2011;
Accepted: August 8, 2011

Feasibility of rapid near-infrared diffuse optical tomography by swept-spectral-encoded sequential light delivery

Guan Xu, Daqing Piao,*
School of Electrical and Computer Engineering, Oklahoma State University, Stillwater, OK, USA, 74078
Daqing.piao@okstate.edu

ABSTRACT

We investigate the feasibility of rapid near infrared diffuse optical tomography by spectrally-encoded sequential light delivery using wavelength-swept source. The wavelength-swept light beam is dispersed by a spectrometer to form "swept-spectral-encoded" light beam which scans linearly across the exit window of the spectrometer and delivers sequential illumination to linearly bundled source fibers. A data acquisition rate of 0.5 frame/second is reached from a 4mW 830nm swept-source and a 20mm-diameter transverse-imaging intra-lumenal applicator with 7 source and 8 detector channels placed in a liquid phantom. Higher rate of data acquisition is achievable with more powerful wavelength-swept source or in a smaller imaging regime. This new configuration is intended for being implemented in rapid fluorescence diffuse optical tomography by enabling sequential source-channel-encoded excitations of fluorophores.

Keywords: biomedical optics, tomography, medical imaging

1. INTRODUCTION

Near-infrared optical tomography has demonstrated high functional contrast in imaging applications for cancer detection [1-3] and assessing disorders of extremity [4-5], functional status of brain [6] and hemodynamics of small animals [7-8]. Compared to other imaging modalities such as X-ray computed tomography and ultrasound imaging, NIR optical tomography usually is implemented at relatively slower rate of data acquisition due to the need of source-encoding in differentiating the origin of light diffused through scattering-dominant biological tissue.

Several methods have been used for source-decoding in NIR optical tomography. One of the method being implemented widely is by mechanically switching the light illumination among the source channels [1-2, 5], which ensures the sole-source illumination necessary to maximizing the signal dynamic range, but it could have potential issues such as reliability and repeatability if high-speed is desired. Frequency-multiplexing can in principle render real-time data acquisition, but the cross-channel suppression of weak signal by stronger signal is difficult to overcome. Recent studies have implemented digitally-controlled source-channeling coupled with frequency-multiplexing [9] to reach higher speed in DOT data acquisition.

One configuration of source-encoding in DOT leading to the first video-rate DOT imaging acquisition has been based upon the principle of spectral-encoding of the source channels. The spectral-encoded DOT has been demonstrated by discrete-spectral-encoding using multiple laser diodes (LD) with individual temperature and current control for each LD [10], and spread-spectral-encoding using a broad-band light source [11]. The configuration using multiple LDs demonstrates higher acquisition rate (approximately 30Hz), but the inter-channel frequency-hopping and uncorrelated channel-wise intensity fluctuation limit the accuracy of the system in resolving smaller dynamic changes of tissue optical properties. The configuration using a broad-band light-source for spread-spectral-encoding overcomes the issues of cross-channel frequency-hopping and intensity fluctuation because of the use of different spectral components from the same source, which resulted in much higher sensitivity to dynamic changes of tissue optical properties. One drawback of spread-spectral-encoding using single broadband light source is the potential overlapping of the spectrum of each source-channel with the neighboring source-channel when using imperfect optics [11], which may require deconvolution to remove the effect of spectral and intensity cross-talk.

Wavelength-swept light source is widely utilized in spectral-domain optical coherent tomography [12], and is recently implemented for spectrally-encoded detection of surface profile of a subject [13]. This work demonstrates the use of wavelength-swept light source in DOT applications by a configuration of swept-spectral-encoded sequential light delivery. Some advantages of this approach over previously demonstrated source-sequencing techniques are

Optical Tomography and Spectroscopy of Tissue IX,
Edited by Bruce J. Tromberg, Arjun G. Yodh, Mamoru Tamura, Eva M. Sevick-Muraca, Robert R. Alfano,
Proc. of SPIE Vol. 7896, 78961W · © 2011 SPIE · CCC code: 1605-7422/11/$18 · doi: 10.1117/12.874349

demonstrated, by phantom experiments, as: 1) the spectrally and temporally encoded source channeling facilitates rapid non-mechanical switching; 2) sole-source illumination eliminatess the cross-coupling problem seen in spectral-encoding based on a broadband light source. Temporally independent source illumination can also couple with CCD gain control to allow adaptive CCD exposure to the range of signals specific to one source-channel.

This paper also applied a recently developed analytic model of endoscopic imaging geometry to the reconstruction process. It is well-known that most of the system calibration in DOT image reconstruction involves fitting the numerically solved light propagation to the experimental measurements. Most of contemporary studies seem to utilize the analytical model for planar semi-infinite photon diffusion [14] during the first step of data calibration. Such approach demonstrates its robustness in many frequency domain systems, in which the gradients of the measurement components are considered in the analytical fitting process. However, as to the continuous wave systems, since multiple optical properties cannot be strictly decoupled by merely utilizing the attenuation of light signal intensity, the accurate fitting to the absolute intensity is also required. Therefore, more accurate analytical model specified for the applicator geometry of each imaging system are desired, which, for the particular case of this study targeted for endo-rectal imaging using a circular cylindrical applicator a new model is derived and validated by Zhang et al[15]. This geometry-specific analytic model is expected to provide more accurate estimation of the optical properties of homogeneous medium during the initial step of data calibration as it improves the data-model match.

This paper discusses the structure of the system and presents experimental results based on phantom for assessment of system performance as well as demonstrating the use of geometry-specific analytic model for data calibration.

2. METHODS AND MATERIALS

2.1 Principles of swept-spectral-encoding

The principle of swept-spectral-encoding is illustrated in Fig. 1(a). As is shown, the source light with swepting wavelengths is dispersed by spectrometer #1 and sequentially coupled to the fiber channels linearly arranged at the output plane of spectrometer #1. Therefore, the sweeping source light appears similar to a broadband light, and a spectral-encoding of the source illumination similar to the one reported in [11] is achieved. At the detection end, spectrometer #2 decodes the light signals for CCD acquisition, as is shown in Fig.1 (b) (with 1200 groove/mm grating) and Fig.1(c) (with 600 groove/mm grating).

The detection signals corresponding to each source channel are acquired independently in time, *per se*, by spectral as well as temporal encoding represented by equ(1):

$$\mathbf{Loop}(\boldsymbol{t=1:m})\text{: }\{\boldsymbol{D}(\boldsymbol{t})_{n\times 1}=(\boldsymbol{W}_{m\times n})^{T}\times \boldsymbol{T}(\boldsymbol{t})_{m\times m}\times \boldsymbol{Spec}_{m\times m}\times \boldsymbol{S}_{m\times 1}\} \tag{1}$$

where ***t*** is the time-slot of wavelength-sweeping controlled by PC; ***D*(*t*)** is the detector signal at time ***t***, ***W*** is the weight matrix or sensitivity matrix of the imaging geometry; ***T(t)*** is the diagonal matrix representing the time-encoding,

$$\boldsymbol{T}(\boldsymbol{t})(\boldsymbol{i,i})=\begin{cases}1 & i=t\\ 0 & i\neq t\end{cases};\boldsymbol{Spec}=\begin{bmatrix}\lambda_1 & \lambda_2 & \cdots & \lambda_3\\ \lambda_1 & \lambda_2 & \cdots & \lambda_3\\ \vdots & \vdots & \ddots & \vdots\\ \lambda_1 & \lambda_2 & \cdots & \lambda_3\end{bmatrix}$$ is the spectral encoding matrix.

The synchronization mechanism between the swept source and CCD is shown in Fig.1(a). Controlled by the PC, the source -sweeping stops when the maximum source power is coupled to designated source channel, followed by the CCD exposure. Therefore, for one imaging cycle, image acquisition number equals to the number of source channels (illustrated in Fig.1(d)). Such design facilities the temporal separation of the light spots at the detection end despite the spatial overlapping.

2.2 System configuration

A Superlum wavelength-swept light source is used. It has 4mW output power and scans in the range of 838nm to 858nm at an increment of 0.05nm. The wavelength stability is ±2.5pm per five hours. The source light is pigtailed by a single-mode fiber and collimated by an aspherical lens of 4.51mm focal length. The collimated source light is coupled to a spectrometer #1 (SpectroPro 500i, Princeton Instrument). The 1200 groove per mm grating and 500mm path length of the spectrometer expands the 20nm spectral range of the source light to approximately 15mm span at the output plane of the spectrometer, where linearly arranged 1mm-diameter fibers deliver the sequentially coupled light to the imaging applicator. At the detection end, a CCD camera (ACTON PIXIS 512) with 12.3mm×12.3mm imaging area and a 300mm focal-length spectrometer #2 (SpectroPro 2300i, Princeton Instrument) is integrated for signal acquisition. The source-sweeping and CCD data acquisition are synchronized by a data acquisition card (National Instrument) using LabView (National Instrument). Limited by the source power, a minimum exposure time of 170ms is required and an extra 150ms CCD readout time is necessary before sweeping the source light to the next source channel. Therefore for each channel approximately 320ms is required, which is equivalent to 0.5 frames per second. This frame rate can be improved with stronger source.

The experiment validation utilizes a two dimensional circular endoscopic imaging geometry previously studied by our group[16]. As is shown in Fig. 2, the 8 source channels and 8 detector channels are evenly interspersed around the perimeter of the 20mm-diameter probe. However, one source channel (marked in Fig.2(c)) is discarded because of its significantly low coupling efficiency due to fabrication defect. The actual experimental system is shown in Fig.3.

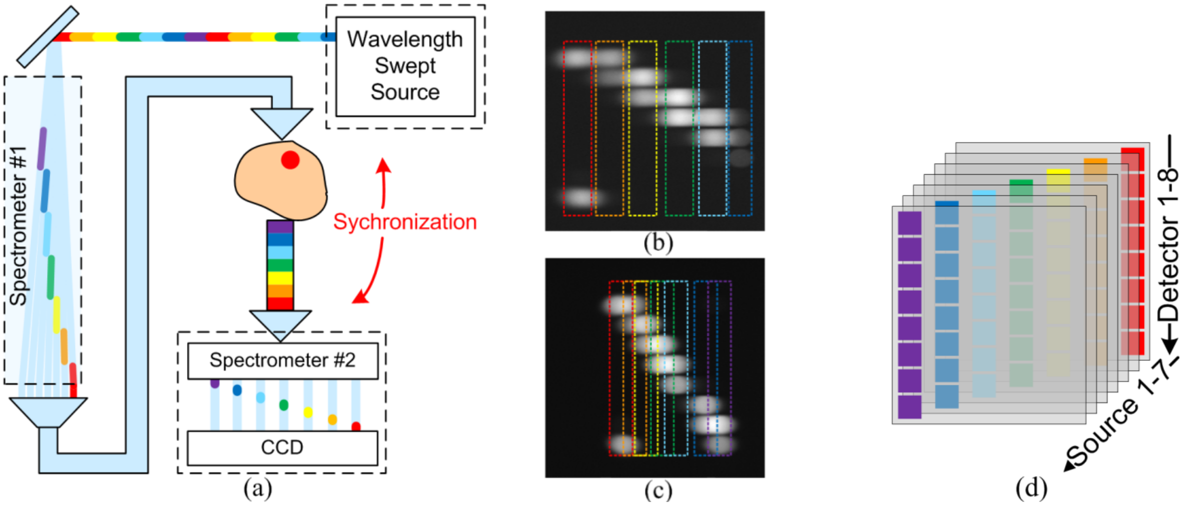

Fig. 1 Principle of swept-spectral-encoding
(a) System schematics (b) Spectral encoding mode 1200 grooves / mm
(c) Spectral encoding mode 600 grooves / mm (d) Spectral and temporal encoding mode

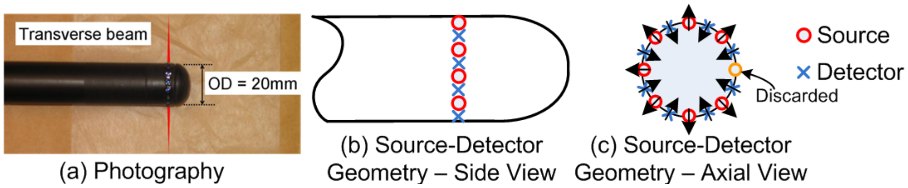

(a) Photography (b) Source-Detector Geometry – Side View (c) Source-Detector Geometry – Axial View

Fig.2 A circular endoscopic imaging geometry

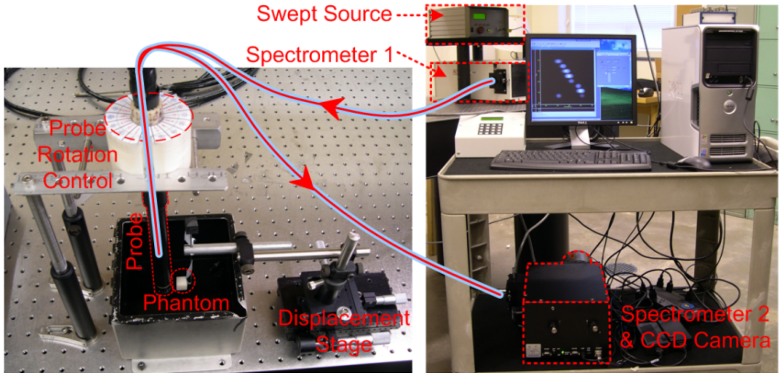

Fig.3 Experiment system constructed

2.3 Examples of signals

With the exposure time and source power described above, the signal intensity detected by the 16-bit CCD camera is in the range of maximum 60000 to minimum 1000. The background count of CCD is approximately 700. One set of images are captured by submerging the probe into 1% intralipid solution. Figure 4(a) shows the images acquired after subtracting dark background. By averaging through the region of interest in the center part of the light spots as seen in Fig.4(b), the extracted data points are used for calibration and reconstruction (Fig.4(c)).

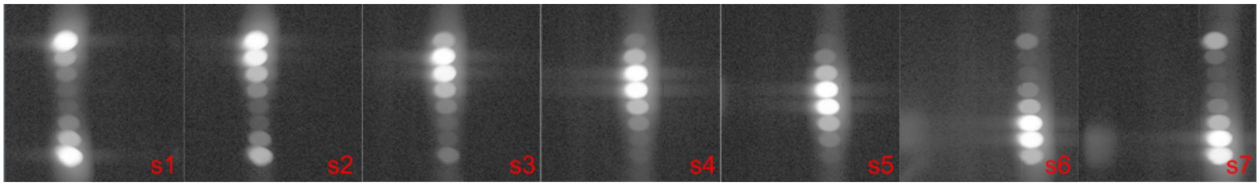

(a) Data spots captured by CCD camera

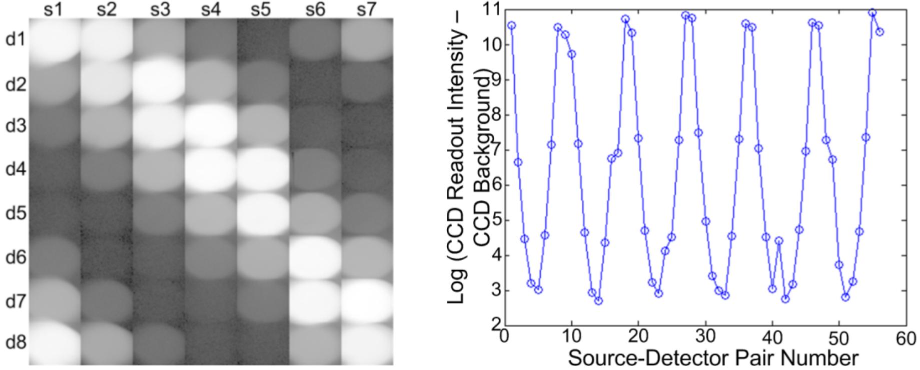

(b) Cropped data spots and center average

(c) Extracted measurement intensities

Fig. 4 Raw data processing

2.4 Calibration methods

In this study, the calibration algorithm searches for the offset values between the experimental data, analytical and numerical model in log scale. A bulk 1% intralipid solution with μ_a= 0.0023 mm^{-1} and μ_s'=1mm^{-1} is used in the calibration process. The calibration involves 2 stages: 1) estimation of the optical properties of homogeneous medium with analytical model and; 2) offset between the experimental data and the numerical model.

For the analytical fitting process, many studies use the linear model for semi-infinite homogenous turbid media [14]. However, such model does not accurately represent the light transportation pattern in cylindrical geometry, as is shown in Fig.7(a). Zhang et al [15] have proposed and validated an analytical model for such cylindrical geometry:

$$\Psi=\frac{S}{2\pi^2 D}\int_0^\infty dk\left\{\sum_{m=0}^{\infty}\varepsilon_m I_m(k_{eff}R_0)K_m[k_{eff}(R_0+R_a)]\left\langle 1-\frac{K_m(k_{eff}R_0)}{I_m(k_{eff}R_0)}\frac{I_m[k_{eff}(R_0-R_b)]}{K_m[k_{eff}(R_0-R_b)]}\right\rangle\cos[m(\varphi-\varphi')]\right\} \tag{2}$$

Where S is the source intensity; D=1/(3(μ_a+μ_s')) is diffusion coefficient; R_0 is the probe radius; R_a=1/ μ_s',is the scattering distance of the imaged medium; ε_m is 2 for m≠0 and 1 for m=0; I_m and K_m are the modified Bessel function of the first and second kind; k_{eff} is the attenuation coefficient; φ and φ' are the angular coordinate of detector and source, respectively. For the evaluation of the model, since the equation consists of infinite series, approximation is applied by cutting off the series at the 60th terms. Such approximation is computationally efficient but introduces discontinuity in the function evaluation, which the commonly used gradient based fitting algorithms does not allow. A heuristic random optimization approach [17] is thus integrated into the analytical calibration process. Since 1) the absolute values are fitted; 2) the duration of the analytical model evaluation increases proportionally to the number of sampling points; and 3) calibration process bases on homogeneous medium, the analytical model is evaluated only at the source-detector separations found in the experimental geometry as shown in Fig. 2. Therefore, only 4 data points are evaluated in each round fitting iteration.

It can be observed that S value is independent of the integral in Equ (2), and in log scale, it is an amplitude bias of the analytical model, which is found to bring in large projection error in the fitting process and might destabilize the searching for other parameters. To suppress such instability, the algorithm first minimizes the log(S) value and starts the overall parametric search, then the result (Fig.5(a) red curve) of which is assigned to the FEM model as the initial guess of the second calibration stage. It can be clearly observed from Fig 7(a) that the algorithm recognized the larger light intensity attenuation in a nonlinear pattern by correcting the μ_a initial guess of 0.005mm^{-1} to 0.0029 mm^{-1}.

The numerical fitting stage integrates finite element method on the ring geometry shown in Fig.2(c), which is disretized to a finite element mesh with 872 nodes and 1620 elements uniformly distributed in the imaging domain. The numerical calibration also starts from searching for the optimum amplitude bias, which is subsequently optimized along with the optical properties of numerical model. And the final model fitting converged to the optical properties of μ_a=0.0023mm^{-1} and μ_s'=0.8982, of which the μ_s' part could be more accurate if analytical model and measurements in frequency domain are available.

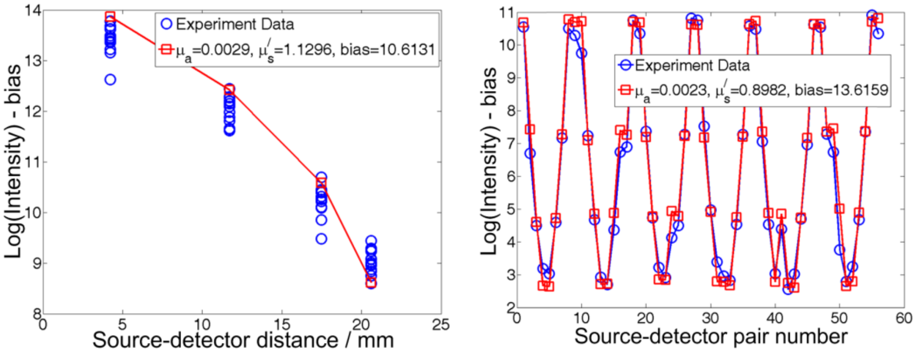

(a)Analytical model calibration (b) Numerical model calibration

Fig. 5 Data calibration

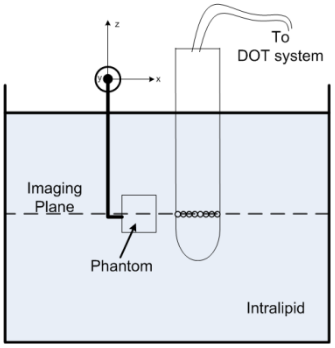

Fig 6 Experiment setup

3. RESULTS ON PHANTOM IMAGING

The performance of this system configuration is evaluated by using liquid and solid phantoms.

3.1 Experiments setup

As is shown in Fig.3 and Fig.6(a), the axial-imaging cylindrical probe was submerged in a tank of 10×10×5 cubic-inch that filled with intralipid. The inner wall of the tank was painted black. The solid phantom targets to be imaged were fabricated from a black plastic material, which was to mimic infinite absorption contrast of the target inclusion over the background intralipid solution, and a phantom with μ_a= 0.0056 mm^{-1} and μ_s'=1.03 mm^{-1}. The sizes of the cubic-shape solid phantom ranged from 5mm to 15 mm. The targets were aligned initially at the imaging plane of the probe and displaced by translation or rotation stages to positions of examination.

3.2 Experiment results

Four sets of experiments were conducted to examine system sensitivity on 1) the size, (Fig. 7(a)); 2) the radial position (Fig. 8(a)); 3) the azimuthal direction (Fig. 9(a)) of the inclusion; and 4) multiple inclusions (Fig. 10(a)).

The first set of results is derived from experiments with target with varied sizes and materials embedded at side-to-probe distance of 5mm. As is expected and demonstrated by the results in Fig.9(b), the reconstructed absorption properties of black plastic materials obviously exceed the solid tissue phantoms. For all five target sizes, the targets made with black plastic were recovered at the same azimuthal location although the recovered volumes decrease with respect to those of the actual targets. For the targets fabricated from solid tissue phantom, the recovered absorption contrast fades as the target volume decreases and background artifacts overwhelms the targets with volumes less than 10×10×10 mm^3.

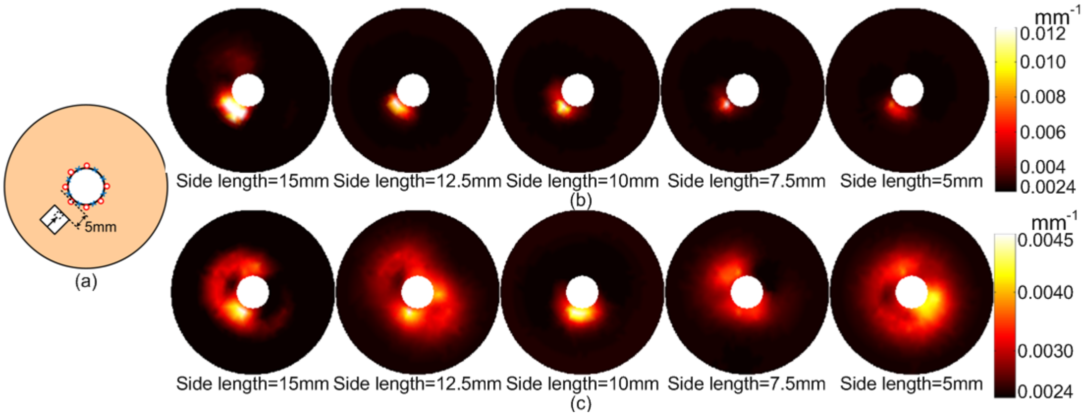

Fig. 7 Experiment on system resolution on inclusion size. (a) Target location and size illustration (b) Reconstruction results on black plastic targets. (c) Reconstruction results on synthetic phantom targets

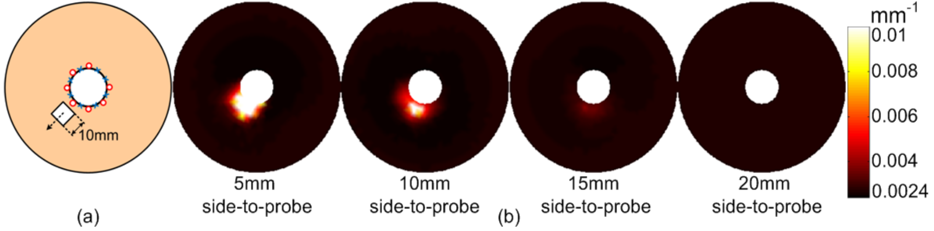

Fig. 8 Experiment on system sensitivity along radial direction
(a) Target location and size illustration (b) Reconstruction results on 10×10×10mm^3 black plastic targets embed at 3mm depth

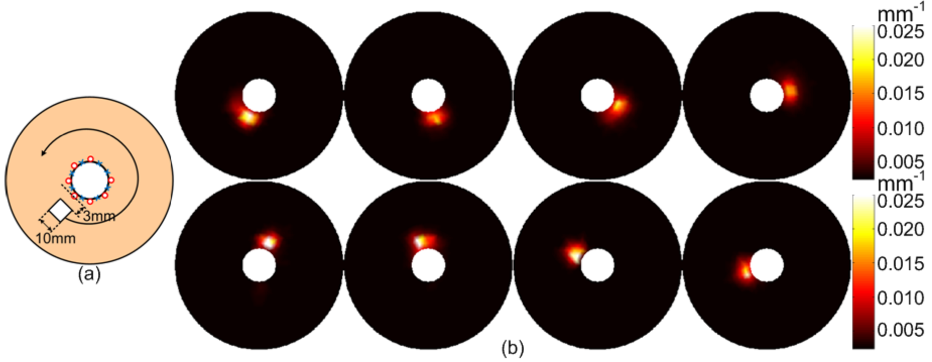

Fig. 9 Experiment on system sensitivity along azimuthal direction
(a) Target location and size illustration (b) Reconstruction results on 10×10×10mm^3 black plastic targets

The second set of experiments examines the system sensitivity along the radial direction. A 10×10×10 mm^3 cube fabricated from black plastic was imaged at side-to-probe distances from 0mm to 15mm (equivalent center depths of 5mm to 20mm). Fig.8(b) shows the recovered absorption distributions. Results indicated that 1) the target could not be recovered beyond 15mm depth; 2) the recovered volume decreased as the depth increased; and 3) similar to experiment shown in Fig.9. Further, all of the target centers were recovered closer to the probe due to the non-uniform sensitivity of the imaging geometry in the radial direction.

However, it is expected that the reconstruction sensitivity should be uniform along the azimuthal direction of the probe in the image plane. Therefore, in the third set of experiments, the 10×10×10 mm^3 black target is embedded 3mm away from the probe and rotated along the azimuthal direction, as is shown in Fig.9(a). Approximately constant target volume and optical properties can be observed in Fig.9(b) as foreseen, and since the targets locate at the most sensitive region of the imaging geometry, all the target depths are desirably recovered.

The fourth set of experiments examine the system capacity of recovering multiple inclusions. Two 7.5×7.5×7.5 mm^3 black cubes were used in this case in consideration that the dimensions of larger targets limit their center separation and smaller targets are more difficult to be resolved. The two targets are both embedded 2mm away from the probe (center depth = 2+7.5/2= 5.75 mm) at different angular positions with respect to the probe, as is shown in the Fig.10(a). Reconstruction results are shown in Fig.10(b).

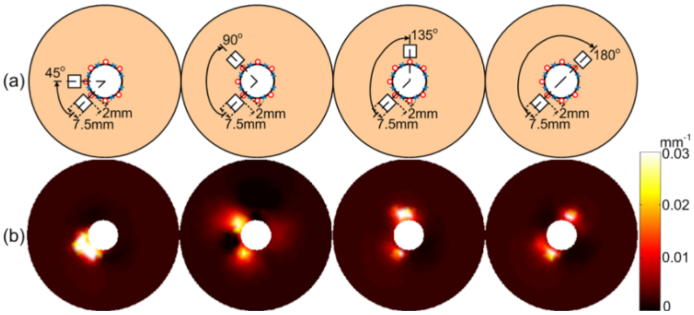

Fig. 10 Experiment on recovery of multiple targets
(a) Target location and size illustration (b) Reconstruction results

It can be observed that for the predetermined depth, angular separation beyond 90 degrees can be recovered accurately by the system. However, at 45 degree separation, the system cannot resolve the gap between the targets and indicates a large light absorbing blob at the correct location. Such result is expected, because the minimum angular separation of two neighboring sources is 45 degree and the signal intensity received by the detector between the two source channels could be substantially reduced by the two targets located in the dominant light propagation path tracing to the detector channel. Hence for the limited source-detector pair in this imaging geometry, reconstruction algorithm recognize the two sources and one detector channel within the 45 degree range as being blocked by one large light absorbing blob.

4. DISCUSSIONS AND FURTURE WORKS

The four sets of experimental evaluations demonstrated the feasibility of DOT using this novel configuration of swept-spectral encoding. It seems that the in most experiments conducted above the rectangular contour of the phantoms was recovered. The ability of such profile-identification may relate to the element geometries of the finite element mesh used in reconstruction algorithm, but similar level of profile-identification was not seen in previous studies wherein identical mesh structures were used [16]. The most likely explanation of such gain in the imaging outcome is that the temporal and spectral encoding of the source light fundamentally reduces the source channel crosstalk between source channels, improving the imaging resolution of a predetermined imaging geometry.

Moreover, with the 4mW source power and 170ms exposure time, targets with center depth up to 20mm (Fig.8) can be detected. Although the previously reported broad-band spectral encoding system possesses higher total power level (20mW), the average power coupled to each source channel could be on the same level as or even lower than the system constructed in this study. The 0.5 frame per second data requisition rate can be readily improved given a stronger wavelength-swept source.

The calibration of the homogenous data with analytical model is proved to be effective and accurate in the circular geometries, although fitting experimental data to the approximately evaluated model could be computationally intensive and impracticable with the gradient based algorithms. The more exhaustive heuristic random optimization approach [17] is implemented in two stages to the calibration process, which is validated by the experimental results. However, the analytical model utilized in this study is limited to steady-state measurement, which is known less accurate in estimating the scattering properties. More accurate calibration may need measurements and models in frequency domain.

Prospectively, this configuration of swept-spectral-encoded sequential source illumination can be extended for rapid fluorescence optical tomography[18], as the source channel for the fluorescence excitation could be differentiated by the temporal encoding of the source channels out of sequential spectral-encoding. Works are planned to validate the use the configuration for fluorescence optical tomography.

5. CONCLUSION

A novel near infrared tomography configuration based on wavelength swept light source is constructed. A data acquisition rate of 0.5 frame per second is demonstrated, which can be improved with more powerful light source. This source-sequencing configuration based on wavelength-swept source can be extended to rapid fluorescence optical tomography.

ACKNOWLEDGEMENT

This work has been supported in part by the Prostate Cancer Research Program of the U.S. Army Medical Research Acquisition Activity (USAMRAA) through grants #W81XWH-07-1-0247 and #W81XWH-10-1-0836.

REFERENCES

[1] Pogue, B., et al., "Instrumentation and design of a frequency-domaindiffuse optical tomography imager for breast cancer detection," Opt. Express 1(13), 391-403(1997)
[2] Huang, M., et al., "Simultaneous Reconstruction of Absorption and Scattering Maps with Ultrasound Localization: Feasibility Study Using Transmission Geometry," Appl. Opt. 42(19), 4102-4114(2003)
[3] Jiang, Z., et al., "Trans-rectal ultrasound-coupled near-infrared optical tomography of the prostate, Part II: Experimental demonstration," Opt. Express 16(22), 17505-17520(2008)
[4] Andreas, H.H. and et al., "Sagittal laser optical tomography for imaging of rheumatoid finger joints," Physics in Medicine and Biology 49(7),1147(2004)
[5] Yuan, Z., et al., "Tomographic x-ray--guided three-dimensional diffuse optical tomography of osteoarthritis in the finger joints," Journal of Biomedical Optics 13(4), 044006-10(2008)
[6] Boas, D.A. and A.M. Dale, "Simulation study of magnetic resonance imaging-guided cortically constrained diffuse optical tomography of human brain function," Appl. Opt. 44(10), 1957-1968(2005)
[7] Pogue, B.W. and K.D. Paulsen, "High-resolution near-infrared tomographic imaging simulations of the rat cranium by use of a priori magnetic resonance imaging structural information," Opt. Lett. 23(21), 1716-1718(1998)
[8] Hielscher, A.H., "Optical tomographic imaging of small animals," Current Opinion in Biotechnology 16(1), 79-88(2005)
[9] White, B.R. and J.P. Culver, "Phase-encoded retinotopy as an evaluation of diffuse optical neuroimaging," NeuroImage 49(1), 568-577(2010)
[10] Piao, D., et al., "Video-rate near-infrared optical tomography using spectrally encoded parallel light delivery," Opt. Lett. 30(19), 2593-2595(2005)
[11] Piao, D. and B.W. Pogue, "Rapid near-infrared diffuse tomography for hemodynamic imaging using a low-coherence wideband light source," Journal of Biomedical Optics 12(1), 014016-12(2007)
[12] Choma, M., et al., "Sensitivity advantage of swept source and Fourier domain optical coherence tomography," Opt. Express 11(18), 2183-2189(2003)
[13] Strupler, M., et al., "Rapid spectrally encoded fluorescence imaging using a wavelength-swept source," Opt. Lett. 35(11), 1737-1739(2010)
[14] Fantini, S., et al., "Quantitative determination of the absorption spectra of chromophores in strongly scattering media: a light-emitting-diode based technique," Appl. Opt. 33(22), 5204-5213(1994)
[15] Zhang, A., et al., "Photon diffusion in a homogeneous medium bounded externally or internally by an infinitely long circular cylindrical applicator. I. Steady-state theory," J. Opt. Soc. Am. A 27(3), p. 648-662(2010)
[16] Piao, D., et al. "Near-infrared optical tomography: endoscopic imaging approach," Proceeding SPIE 6431, 643103-1(2007)
[17] Li, J. and R. Russell Rhinehart, "Heuristic random optimization," Computers & Chemical Engineering 22(3), 427-444(1998)
[18] Lee, J. and E.M. Sevick-Muraca, "Three-dimensional fluorescence enhanced optical tomography using referenced frequency-domain photon migration measurements at emission and excitation wavelengths," J. Opt. Soc. Am. A 19(4), 759-771(2002)

“Spectral *a priori*” to “spatial *a posteriori*” in continuous-wave image reconstruction in near-infrared optical tomography

Guan Xu,[a] Daqing Piao,[a]* Hamid Dehghani [b]
[a]School of Electrical and Computer Engineering, Oklahoma State University, Stillwater, OK, USA
[b]University of Birmingham, Birmingham, UK

* School of Electrical and Computer Engineering, Oklahoma State University, Stillwater, OK 74078
(Phone: 405-744-5250; FAX: 405-744-9198; e-mail: daqing.piao@okstate.edu)

ABSTRACT

This work examines the robustness of spectral *prior* to continuous-wave based, with respect to frequency domain based, image reconstruction for unique recovering of chromophores and scattering property distributions. An analytical model for parametric uncertainty in recovering optical property is derived, which afterwards is implemented for optimized selection of wavelengths and quality estimation of the image. Simulation results agree with the theoretical predictions in the following aspects: 1) the proposed analytical model is capable of selecting the optimal set of wavelengths for CW-based spectral reconstruction; 2) with sufficient number of wavelengths, DC-only reconstruction can resolve the concentrations of several important chromophores and scattering parameters, with the accuracy and background artifact level equivalent to those by DC-excluded or DC-included frequency-domain reconstructions; and 3) including DC in frequency-domain reconstruction generally improves reconstruction outcome as compared to when neglecting DC.

Keywords: multi-spectral, optical tomography, image reconstruction

1. INTRODUCTION

The outcome of functional imaging of near-infrared (NIR) optical tomography [1-2] depends upon the information obtained over a spectrum of light. A conventional technique of spectral optical tomography reconstruction is to reconstruct the wavelength-specific absorption and scattering properties first, then to derive the concentrations of tissue chromophores and distributions of the scatterers. An alternative technique of spectral optical tomography reconstruction utilizes *a priori* knowledge of the absorption and scattering spectra of tissue compositions within the NIR range to modify the inverse problem to directly recover the chromophore concentrations and scattering parameters including scattering power and amplitude. Such alternative technique, which is commonly stated as “spectral-*prior*” method, has been demonstrated by a number of studies [1-2]. The most successful demonstration[2] of spectral-*prior* method has been in coupling with *a priori* knowledge of the spatial content of the tissue under frequency-domain imaging, in other words, the *spectral-prior* has been implemented along with *spatial-prior* in frequency-domain measurement.

An interesting question thereby arises, in regards to the outcome of spectral-*prior* without the availability of *spatial-prior*, that what the likelihood of recovering the spatially-resolved spectral information would be, given only continuous-wave measurement. Our study on multi-wavelength optical tomography without *spatial-prior* has shown that implementing the spectral-*prior* in DC measurements often results in spatial information being reconstructed in unexpected level of details. This observation is referred to as “spectral *a priori*” to “spatial *a posteriori*”, in other words it is the likelihood of accurately recovering spatially-resolved tissue absorption and scattering distribution from spectral reconstruction without spatial *prior*. The observation that spectrally-resolved measurements in DC lead to accurate spatially-resolved reconstruction, in our opinion, deserves further investigation. This study, as an initial exploration of the underlining mechanism, attempts to justify one derivative issue of such mechanism, specifically the reliability of recovering each unknown spectral variables including chromophore concentrations and scattering contributions under DC-based reconstruction. Based on the analytical approach demonstrated in our previous study [3], the analytical solution for multi-spectral optical tomography and the “parametric reconstruction uncertainty level” (PRUL) of each variable being reconstructed are derived, in a semi-infinite planar medium geometry. Such model provides quantitative means of estimating the relative errors among the parameters subjected to spectral reconstruction, with which the quality of spectral reconstruction may be better understood.

Multimodal Biomedical Imaging VI, edited by Fred S. Azar, Xavier Intes, Proc. of SPIE Vol. 7892,
78920D · © 2011 SPIE · CCC code: 1605-7422/11/$18 · doi: 10.1117/12.873462

In this study the analytical model is first implemented on the optimization of the wavelength sets for the spectral measurements. Studies [1, 4] have demonstrated selection of the optimum wavelengths for reliable recovery of chromophore concentrations and scattering parameters based on statistical investigation, by comparing numerically approximated sensitivity matrices derived from numerous possible wavelength combinations within the NIR spectrum, which is computationally intensive. In this paper, a novel method of optimizing the selection of wavelengths is investigated based on the PRUL model of multi-spectral optical tomography, which is found to be computationally less demanding.

The analytic model introduced in this work also supports the uniqueness of continuous-wave spectral optical tomography, which is an extension of the prediction made in our previous studies for single wavelength optical tomography [3]. The uniqueness of continuous-wave spectral optical tomography substantiated integrating more wavelengths in direct-current measurement to improve spectral reconstruction [1-2, 4-7]. As few studies have investigated the difference in performance between continuous wave and frequency domain spectral optical tomography, this study extends the approach of single-wavelength analysis in [3] to the analysis of spectral-*prior*, on measurement combinations of 1) continuous wave only (DC); 2) frequency domain measurements excluding direct-current components (AC+PHS); and 3) frequency domain measurements including direct-current (DC+AC+PHS), in the outcome of "spatial *a posteriori*" from "spectral *a priori*".

Finally, this study conduct numerical evaluations of synthetic models to examine the effect of "spectral *a priori*" on "spatial *a posterior*". The simulation studies demonstrate that, in agreement with the analytical predictions: 1) the proposed analytical model is capable of selecting the optimum set of wavelengths for spectral reconstruction; 2) with sufficient number of wavelengths for a given set of tissue chromophores, the DC-only reconstruction delivers spatially-resolved chromophore concentrations and scattering parameters with the accuracy and background artifact equivalent to that of AC+PHS and DC+AC+PHS; and 3)including DC in frequency-domain reconstruction generally improves reconstruction outcome more than neglecting DC.

2. THEORY

An earlier study [3] on the parametric-recovery-uncertainty-level (PRUL) has demonstrated an analytic approach of estimating the background artifact level in single-wavelength optical tomography reconstruction. The PRUL analysis in [3] adopted the analytic treatment originally introduced in [8], and in this study this analytic approach is extended to spectral reconstruction. For two field points separated from a source at distances of d_1 and d_2, respectively, in a homogenous diffusive medium, one has:

$$\begin{aligned}
\delta(\lambda) &= \ln\left(\frac{d_2}{d_1}\frac{U_{DC}(d_2,\lambda)}{U_{DC}(d_1,\lambda)}\right) = -\rho\cdot\sqrt{\frac{\mu_a(\lambda)}{D(\lambda)}} \\
\alpha(\lambda) &= \ln\left(\frac{d_2}{d_1}\frac{U_{AC}(d_2,\lambda)}{U_{AC}(d_1,\lambda)}\right) = -\rho\cdot\sqrt{\frac{\mu_a(\lambda)}{2D(\lambda)}\left(\sqrt{1+\frac{\omega^2}{v^2\mu_a^2(\lambda)}}+1\right)} \\
\phi(\lambda) &= \Phi(d_2,\lambda)-\Phi(d_1,\lambda) = \rho\cdot\sqrt{\frac{\mu_a(\lambda)}{2D(\lambda)}\left(\sqrt{1+\frac{\omega^2}{v^2\mu_a^2(\lambda)}}-1\right)}
\end{aligned} \tag{1}$$

where $U_{DC}(d, \lambda)$ $U_{AC}(d, \lambda)$ and $\Phi(d, \lambda)$ are the wavelength-specific amplitude of the direct-current modulated amplitude and phase of the modulation of the intensity measured at distance d from the source, respectively. In equ.(1) $\delta(\lambda)$ $\alpha(\lambda)$ and $\varphi(\lambda)$ are the attenuation of the direct-current (DC), the attenuation of the amplitude modulation (AC) and the phase shift (PHS) accordingly between two detectors placed d_1 and d_2 from the source, $\rho = |d_1 - d_1|$ is the distance between the two detectors, and ω is the angular modulation frequency. Also

$$\begin{aligned}
\mu_a(\lambda) &= \sum_i \varepsilon_i(\lambda)c_i, \\
\mu_s'(\lambda) &= A\lambda^{-b}, \\
D(\lambda) &= 1/3[\mu_a(\lambda)+\mu_s'(\lambda)]
\end{aligned} \tag{2}$$

are the absorption, scattering and diffusion coefficients of the medium at wavelength λ, respectively, where $\varepsilon_i(\lambda)$ is the extinction coefficient of chromophore i at λ and A is the scattering amplitude and b is the scattering power. The PRUL of the chromophore concentrations and the scattering amplitude/power can be derived by analysis of the propagation of uncertainty and chain rule of partial derivatives as:

$$\sigma_{x_j} = \sqrt{\left(\frac{\partial x_j}{\partial M(\lambda)}\right)^2 \cdot \sigma^2_{M(\lambda)}} = \left|\frac{\partial x_j}{\partial \mu(\lambda)} \cdot \frac{\partial \mu(\lambda)}{\partial M(\lambda)}\right| \cdot \sigma_{M(\lambda)} = \left|\frac{\partial x_j}{\partial \mu(\lambda)}\right| \cdot \sigma_{\mu(\lambda)} \tag{3}$$

where M represents the set of δ, α and φ for the measurement, and x represents the unknowns including derived concentrations of the chromophores, the scattering amplitude and the scattering power. The μ represents the absorption and scattering coefficients in general. Given the extensive analyses of the PRUL of μ_a and μ_s' in [3], the analytical solution of $\sigma_{\mu(\lambda)}$ given in table 2 and table 4 of [3] are directly integrated into equ. (3), with the $\partial x/\partial \mu$ being newly derived.

Equation (2) transforms to a matrix form of

$$\begin{bmatrix} \mu_a(\lambda) \\ \mu_a(\lambda) \\ \vdots \\ \mu_a(\lambda) \end{bmatrix}_{m\times 1} = \begin{bmatrix} \varepsilon_1(\lambda_1) & \varepsilon_2(\lambda_1) & \cdots & \varepsilon_n(\lambda_1) \\ \varepsilon_1(\lambda_2) & \varepsilon_2(\lambda_2) & \cdots & \varepsilon_n(\lambda_2) \\ \vdots & \vdots & \ddots & \vdots \\ \varepsilon_1(\lambda_m) & \varepsilon_2(\lambda_m) & \cdots & \varepsilon_n(\lambda_m) \end{bmatrix}_{m\times n} \times \begin{bmatrix} c_1 \\ c_2 \\ \vdots \\ c_n \end{bmatrix}_{n\times 1} \tag{4}$$

with which one has

$$\frac{\partial \vec{c}_{n\times 1}}{\partial(\vec{\mu}_a)_{m\times 1}} = [(\vec{\varepsilon}^T)_{n\times m}\vec{\varepsilon}_{m\times n}]^{-1}(\vec{\varepsilon}^T)_{n\times m} = \begin{bmatrix} \frac{\partial c_1}{\partial \mu_a(\lambda_1)} & \frac{\partial c_1}{\partial \mu_a(\lambda_2)} & \cdots & \frac{\partial c_1}{\partial \mu_a(\lambda_m)} \\ \frac{\partial c_2}{\partial \mu_a(\lambda_1)} & \frac{\partial c_2}{\partial \mu_a(\lambda_2)} & \cdots & \frac{\partial c_2}{\partial \mu_a(\lambda_m)} \\ \vdots & \vdots & \ddots & \vdots \\ \frac{\partial c_n}{\partial \mu_a(\lambda_1)} & \frac{\partial c_n}{\partial \mu_a(\lambda_2)} & \cdots & \frac{\partial c_n}{\partial \mu_a(\lambda_m)} \end{bmatrix}_{n\times m} \tag{5}$$

and then for the terms in PRUL of chromophore concentrations we have:

$$(\vec{\sigma}_c)_{n\times 1} = \left|\frac{\partial \vec{c}_{n\times 1}}{\partial(\vec{\mu}_a)_{m\times 1}}\right|_{n\times m} \cdot \left(\vec{\sigma}_{\mu_a(\lambda)}\right)_{m\times 1} \tag{6}$$

Note that the scattering power and amplitude are not linearly related as the chromophore concentrations are in equ. (2). The PRULs of these two variables are derived by firstly obtaining:

$$\log \mu_s' = \log A + (-b)\log \lambda \tag{7}$$

then converting equ. (7) to a matrix form of:

$$\begin{bmatrix} \log[\mu_s'(\lambda_1)] \\ \log[\mu_s'(\lambda_2)] \\ \cdots \\ \log[\mu_s'(\lambda_m)] \end{bmatrix}_{m\times 1} = \begin{bmatrix} 1 & \log \lambda_1 \\ 1 & \log \lambda_2 \\ \cdots & \cdots \\ 1 & \log \lambda_m \end{bmatrix}_{m\times 2} \times \begin{bmatrix} \log A \\ (-b) \end{bmatrix}_{2\times 1} \tag{8}$$

which gives the following result:

$$\left(\frac{\partial \log A}{\partial \log \mu_s'(\lambda_i)}\right)_{1\times m} = \frac{1}{m\sum_{i=1}^{m}\log^2(\lambda_i) - [\sum_{i=1}^{m}\log(\lambda_i)]^2} \cdot \left(\begin{bmatrix} \sum_{i=1}^{m}\log^2(\lambda_i) - \log(\lambda_1)\sum_{i=1}^{m}\log(\lambda_i) \\ \sum_{i=1}^{m}\log^2(\lambda_i) - \log(\lambda_2)\sum_{i=1}^{m}\log(\lambda_i) \\ \cdots \\ \sum_{i=1}^{m}\log^2(\lambda_i) - \log(\lambda_m)\sum_{i=1}^{m}\log(\lambda_i) \end{bmatrix}^T\right)_{1\times m} \tag{9}$$

$$\left(\frac{\partial b}{\partial \log \mu_s'(\lambda_i)}\right)_{1\times m} = \frac{1}{m\sum_{i=1}^{n}\log^2(\lambda_i) - [\sum_{i=1}^{n}\log(\lambda_i)]^2} \cdot \left(\begin{bmatrix} \sum_{i=1}^{m}\log(\lambda_i) + m\cdot\log(\lambda_1) \\ \sum_{i=1}^{m}\log(\lambda_i) + m\cdot\log(\lambda_2) \\ \dots \\ \sum_{i=1}^{m}\log(\lambda_i) + m\cdot\log(\lambda_m) \end{bmatrix}^T\right)_{1\times m} \tag{10}$$

The PRULs of scattering amplitude and power are finally expressed as:

$$\sigma_A = \left|\frac{\partial A}{\partial \log A}\cdot\frac{\partial \log A}{\partial \log \mu_s'(\lambda)}\cdot\frac{\partial \log \mu_s'(\lambda)}{\partial \mu_s'(\lambda)}\right|\cdot\sigma_{\mu_s'(\lambda)} = A\cdot\left|\frac{\partial \log A}{\partial \log \mu_s'(\lambda)}\right|\cdot\frac{\sigma_{\mu_s'(\lambda)}}{\mu_s'(\lambda)} \tag{11}$$

$$\sigma_b = \left|\frac{\partial b}{\partial \log \mu_s'(\lambda)}\cdot\frac{\partial \log \mu_s'(\lambda)}{\partial \mu_s'(\lambda)}\right|\cdot\sigma_{\mu_s'(\lambda)} = \left|\frac{\partial b}{\partial \log \mu_s'(\lambda)}\right|\cdot\frac{\sigma_{\mu_s'(\lambda)}}{\mu_s'(\lambda)} \tag{12}$$

Up to here, by substituting expressions in table 2 and 4 in [3] to equ.s (6) (11) and (12), all the PRUL equation for reconstruction variables in multi-spectral optical tomography are derived and a series of comparison and analysis will be conducted to reveal the intrinsic relationships between the reconstruction parameters. It should also be noted that since PRUL analysis is expressed in terms of the standard deviations, all comparisons will neglect common factors and consider only the absolute values of the equations.

Integrating the results of PRUL in the previous study, the uncertainty level of the parameters to be recovered can be quantitatively compared. Note that in equ. (5), the expression does not facilitate the normalization of σ_{μ_a} on the right hand side compared to the ($\sigma_{\mu_s'}/\mu_s$') terms in equ.s (9) and (10). Multiplication by μ_a values is thereby necessary when utilizing (σ_{μ_a}/μ_a) results.

It is desirable that the uncertainty values can be reduced by correctly selecting the wavelengths used in the system. One approach is to increase absolute value of the determinant of $\varepsilon^T\varepsilon$ in equ. (6) and $m\sum_{i=1}^{m}\log^2(\lambda_i)-[\sum_{i=1}^{m}\log(\lambda_i)]^2$ in equ.s (9) and (10) to reduce the overall absolute value of the PRULs. Several random attempts on the denominator terms will show that the values of $\left|m\sum_{i=1}^{m}\log^2(\lambda_i)-[\sum_{i=1}^{m}\log(\lambda_i)]^2\right|$ stay in a narrow range of [0,1] but the determinant of $\varepsilon^T\varepsilon$ varies in several orders depending on the selection of wavelengths. Such phenomenon is understandable because high similarity between the row vectors of the extinction coefficient matrix could induce rank deficiency, making its determinant close to zero or producing singular values in its pseudo-inverse, which reduces the accuracy of matrix inversion in equ. (4). Previous study [1] has shown such problems and recommended to construct sensitivity matrix with small residual numbers for improving the reliability of the inverse algorithm. From another perspective, the determinant of the matrix geometrically quantifies the volume in the space bounded by the row factors, therefore, larger divergence of the row vectors in extinction coefficients enclosures larger volumes in the vector space, which again supports the hypothesis that larger determinant of the $\varepsilon^T\varepsilon$ matrix ensures more accurate reconstruction.

Further, reference [4] indicates that the uniformity of the sensitivity matrix (∂x/∂ M(λ) in equ. (3)) is also desired for stable and accurate reconstruction. The criteria for wavelengths optimization in this study thereby also include the standard deviation of (∂x/∂ M(λ)) for each wavelength set and again the common terms $|\partial\mu(\lambda)/\partial M(\lambda)|\cdot\sigma_{M(\lambda)}$ is neglected in the quantitative evaluation.

This study is conducted for 3 sets of wavelength, each containing 5 wavelengths adopted from a previous literature [1], in the numerical evaluation of the analytical approach for recovering concentrations of oxygenated hemoglobin, deoxygenated hemoglobin, water, scattering power, and scattering amplitude, as is listed in table 1. Although the previous study [1] has shown that the wavelength selection method is capable of determining the optimum wavelength set and validated the method with simulations, it is difficult to rank the performance of the other two sets. In observation of Table 1 as well as the expectation to have larger denominator determinant and smaller variation among the sensitivity values, the performance ranking of the three wavelength sets can be predicted, from best to worst as: 3,1,2, which agrees with the simulations presented in[1]. Validations from more aspects will be shown later in this paper.

For the calculation of the PRULs in this study, the chromophore concentrations and scattering parameters are estimated as: C_{HbO}=C_{Hb}=0.01mM, C_{H_2O}=40% and A=b=1. It is also assumed that for all measurement types the relative uncertainties of the measurements are the same, that is: $\frac{\sigma^2_{\delta(\lambda)}}{\delta^2(\lambda)}=\frac{\sigma^2_{\alpha(\lambda)}}{\alpha^2(\lambda)}=\frac{\sigma^2_{\phi(\lambda)}}{\phi^2(\lambda)}$. Further, with a given set of wavelengths and a modulation frequency, equ.(1) implicitly determined the value of $\frac{\alpha^2(\lambda)+\phi^2(\lambda)}{\alpha^2(\lambda)-\phi^2(\lambda)}$ ($=\sqrt{1+\frac{\omega^2}{v^2\mu_a^2(\lambda)}}$), which is approximately 1 for all cases. With these approximations and preconditions in-place, equ.s (6) (11) and (12) can be evaluated and compared to simulation results later in this paper.

Table 1 Wavelength sets to be examined and comparison of the PRUL evaluation with the analytical solutions

Set	Wavelengths / nm	Absorption component		Scattering component	
		Determinant of denominator: $(\varepsilon^T\varepsilon)^{-1}$	Standard deviation of chromophores dev(ε)	Absolute value of denominator	Sensitivity standard deviation of scattering amplitude and power
1	740,788,866,902,926	8.18×10^{-7}	63.7	0.18	1.03
2	650,700,716,860,890	2.58×10^{-7}	388.0	0.37	0.67
3	650,716,866,914,930	1.30×10^{-5}	63.8	0.53	0.45

3. SIMULATIONS

Simulations are conducted to quantitatively examine the accuracy of the analytically derived predictions. Similar to [3], PRULs of three measurement types: DC, AC+PHS, DC+AC+PHS are calculated and compared.

3.1 Synthetic model

Forward model is carried out with Finite Element Method solution of photon diffusion at each wavelength[9]:

$$\left(-\frac{\mu_a(\vec{r},\lambda)}{D(\vec{r},\lambda)}+\frac{i\omega}{vD(\vec{r},\lambda)}\right)U(\vec{r},\omega,\lambda)+\nabla^2U(\vec{r},\omega,\lambda)=-\frac{S(\vec{r},\omega,\lambda)}{D(\vec{r})} \tag{13}$$

Where $U(\vec{r},\omega,\lambda)$ is the photon fluence of wavelength λ modulated to angular frequency ω (ω=0 for DC) at position $\vec{r}$ in phasor notation. $S(\vec{r},\omega,\lambda)$ is the source term. The Jacobian matrix is constructed according to the measurement type [3] as:

$$J=\begin{bmatrix}DC\\AC\\PHS\end{bmatrix}=\begin{bmatrix}\frac{\partial\ln U_{DC}(\lambda_1)}{\partial x} & \frac{\partial\ln U_{DC}(\lambda_2)}{\partial x} & \cdots & \frac{\partial\ln U_{DC}(\lambda_m)}{\partial x}\\ \frac{\partial\ln|U_{AC}(\lambda_1)|}{\partial x} & \frac{\partial\ln|U_{AC}(\lambda_2)|}{\partial x} & \cdots & \frac{\partial\ln|U_{AC}(\lambda_m)|}{\partial x}\\ \frac{\partial\Phi_{AC}(\lambda_1)}{\partial x} & \frac{\partial\Phi_{AC}(\lambda_2)}{\partial x} & \cdots & \frac{\partial\Phi_{AC}(\lambda_m)}{\partial x}\end{bmatrix} \tag{14}$$

where *x* represents the parameters to be reconstructed, including chromophore concentrations and scattering amplitude and scattering power. The Levernberg-Marquardt algorithm is implemented as the inverse solver.

A 43mm-radius circular geometry with 16 optode channels evenly distributed on its perimeter is used in this study for its relatively uniform sensitivity along the azimuthal direction with respect to the center of the circle. Each channel functions as source channel sequentially while others function as detector simultaneously. Background values of each reconstruction variables are assigned identical to those used in analytical calculation and the contrast of the anomaly are: C_{HbO_anom} =0.0023mM, C_{Hb_anom} = 0.0023mM, $C_{H_2O\_anom}$ =80% A_{anom}=2, and b_{anom}=2. Contrasts of each of the five variables are assigned to a set of five 8mm-radius targets, as is shown in Fig.1 columns Set. The targets locate 25 mm away from the center of the geometry with 0.4π angular separation. 1% randomly distributed noise is added to all forward data to simulate the perturbations in the actual measurement system.

3.2 Results

Fig.1 shows the reconstruction results and Table 2 demonstrates the maximum values of each variable within the target regions and the percentage error of the contrast. Comparisons in Fig. 1 and table 2 infer that the set 3 outperforms the other two in terms of the overall reliability of quantitative reconstruction and the crosstalk among the recovered variables. Next to the set 3 is set 1, which underestimates hemoglobin concentration and has higher level of crosstalk between hemoglobin and scattering parameters in DC reconstruction. The set 2 is the least accurate, producing severe crosstalk between the oxygenated hemoglobin and water concentration. Besides the comparison among the sets of wavelength, it is also noted that for most cases, DC reconstruction demonstrates the most accurate recovery of the targets when the target presents the contrast of only one parameter, and including DC measurement in frequency domain usually improve the estimation precision.

Further, table 3 lists the analytical PRULs and the reconstructed background artifact levels normalized by the absolute variable of the contrast being recovered, which is, in a more explicit way, the inverse of the contrast-noise-ratio. For more clarity in comparison, the noise to contrast (NCR) ratios are normalized by that of the deoxygenated hemoglobin for the absorptive chromophores and by that of the scattering amplitude for the scattering parameters.

Although the analytically estimated values of the noise to contrast ratios always exceed those calculated from the numerical simulations, the data unanimously shows that, $NCR_{c\_Hb} < NCR_{c\_HbO} < NCR_{C\_H_2O}$ for the absorption part and $NCR_A < NCR_b$ for the scattering part, both of which are in agreement with the previous hypotheses. The quantitative inaccuracy could relate to the smoothing effect of the piecewise reconstruction algorithm.

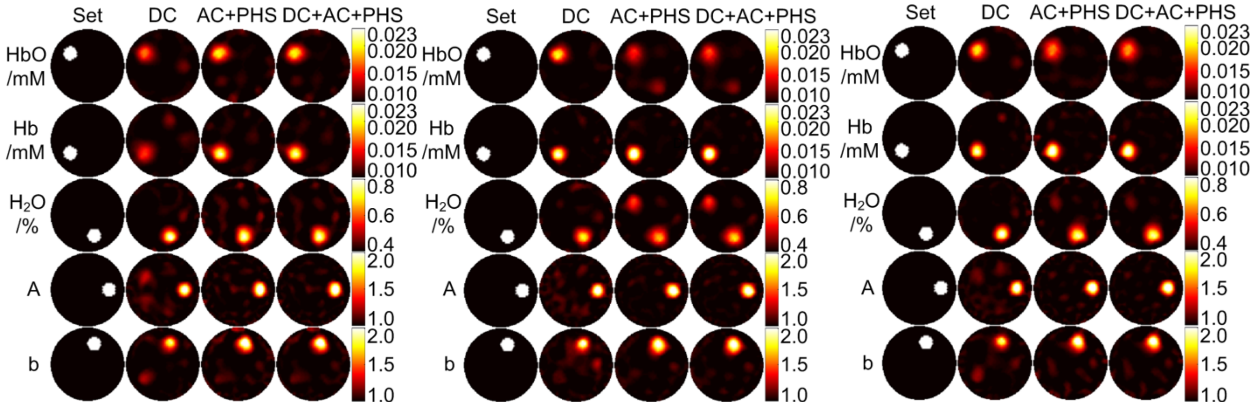

(a) (b) (c)

Fig.1Synthetic study on targets with independent contrast

Table 2 Target accuracy comparison

Data		HbO / mM		Hb / mM		H2O / %		A		b	
		Abs.	Err. / %	Abs.	Err. / %	Abs.	Err. / %	Abs.	Err. / %	Abs.	Err. / %
Set Values		2.3E-2		2.3E-2		0.80		2.0		2.0	
(1)	DC	1.7E-2	-46	1.6E-2	-55	0.82	5	2.2	21	1.9	-9
	AC+PHS	2.0E-2	-23	2.3E-2	-2	0.81	2	2.4	39	2.3	30
	DC+AC+PHS	2.0E-2	-24	2.2E-2	-6	0.80	0.4	2.3	34	2.2	23
(2)	DC	2.0E-2	-21	2.4E-2	4	0.72	-21	2.4	40	2.1	7
	AC+PHS	1.6E-2	-56	2.6E-2	24	0.67	-33	2.3	26	2.1	6
	DC+AC+PHS	1.7E-2	-48	2.7E-2	27	0.69	-27	2.2	23	2.1	10
(3)	DC	2.0E-2	-25	2.3E-2	1	0.83	8	2.3	33	1.9	-11
	AC+PHS	1.8E-2	-42	2.5E-2	16	0.78	-6	2.4	45	2.2	19
	DC+AC+PHS	1.8E-2	-39	2.5E-2	18	0.77	-8	2.4	39	2.2	17

Table 3 Comparison between the PRULs and the background artifact levels normalized by variable contrast

Set		Measurement	HbO / mM		Hb / mM		H2O / %		A		b	
			Abs.	Norm.	Abs.	Norm.	Abs.	Norm.	Abs.	Norm.	Abs.	Norm.
(3)	Ana.	DC	5.38	5.40	1.00	1	3.24	3.26	0.79	1	3.10	3.91
		AC+PHS	7.61	5.40	1.41	1	4.59	3.26	1.12	1	4.39	3.91

		DC+AC+PHS	13.17	5.40	2.44	1	7.94	3.26	1.12	1	4.39	3.91
	Sim.	DC	0.0489	1.89	0.0258	1	0.0395	1.53	0.0260	1	0.0381	1.46
		AC+PHS	0.0716	1.62	0.0443	1	0.0466	1.05	0.0242	1	0.0498	2.06
		DC+AC+PHS	0.0521	1.58	0.0328	1	0.0367	1.12	0.0203	1	0.0404	1.99

4. DISCUSSIONS AND CONCLUSION

The predictions made by a novel analytical PRUL model regarding spectral *a priori* leading to spatial *a posteriori* is supported by the results from simulation. The wavelength ranking method shows agreement with previous study, with much less computational intensity. The PRUL values qualitatively estimates the background artifact level of the DC and frequency domain reconstructions, although neglecting DC components in DC+AC+PHS induces explainable aberration. Comparisons on both the multi-spectral tomography reconstruction PRULs and the projected absorption and scattering reconstruction PRULs support the reliability of the model predictions. However, quantitative inaccuracy still exists in the comparisons, which could be attributed to the approximation and smoothing effect of the inverse algorithm.

An interesting observation is that different from the study in [3], the DC reconstruction with spectral *prior* has quite desirable reconstruction outcome. This should relate to the expectation that sufficient wavelength components will impose the outcome as a result of the uniqueness of DC multispectral tomography, with minimized cross-coupling among the parameters to be recover. Moreover, fewer measurement components facilitate less system noise in the inverse problem and thereby generate less background artifacts, improving the overall DC reconstruction quality. As to frequency domain reconstruction, although DC component could contribute to excessive reconstruction uncertainty, its extra information has actually balanced the negative effect and made DC+AC+PHS a better choice.

ACKNOWLEDGEMENT

This work has been supported in part by the Prostate Cancer Research Program of the U.S. Army Medical Research Acquisition Activity (USAMRAA) through grants #W81XWH-07-1-0247 and #W81XWH-10-1-0836.

REFERENCES

[1] Corlu, A., et al., "Diffuse optical tomography with spectral constraints and wavelength optimization," Appl. Opt. 44(11), 2082-2093 (2005)

[2] Srinivasan, S., et al., "Spectrally constrained chromophore and scattering near-infrared tomography provides quantitative and robust reconstruction," Appl. Opt. 44(10), 1858-1869 (2005)

[3] Xu, G., et al., "Direct-current-based image reconstruction versus direct-current included or excluded frequency-domain reconstruction in diffuse optical tomography," Appl. Opt. 49(16), 3059-3070 (2010)

[4] Eames, M.E., et al., "Wavelength band optimization in spectral near-infrared optical tomography improves accuracy while reducing data acquisition and computational burden," Journal of Biomedical Optics 13(5), 054037-9 (2008)

[5] Li, C., et al., "Multispectral diffuse optical tomography with absorption and scattering spectral constraints," Appl. Opt. 46(34), 8229-8236 (2007)

[6] Jones, P.B., et al., "Simultaneous multispectral reflectance imaging and laser speckle flowmetry of cerebral blood flow and oxygen metabolism in focal cerebral ischemia," Journal of Biomedical Optics 13(4), 044007 (2008)

[7] Xu, H., et al., "Magnetic-resonance-imaging-coupled broadband near-infrared tomography system for small animal brain studies," Appl. Opt. 44(11), 2177-2188 (2005)

[8] Fantini, S., et al., "Quantitative determination of the absorption spectra of chromophores in strongly scattering media: a light-emitting-diode based technique," Appl. Opt. 33(22), 5204-5213 (1994)

[9] Dehghani, H., et al., "Near infrared optical tomography using NIRFAST: Algorithm for numerical model and image reconstruction," Communications in Numerical Methods in Engineering 25(6), 711-732 (2009)

When Is Spiral Straight?

Daqing Piao, Anqi Zhang, Gang Yao, Guan Xu, Chathuri Daluwatte,
Charles F. Bunting, Yuhao Jiang and Brian W. Pogue

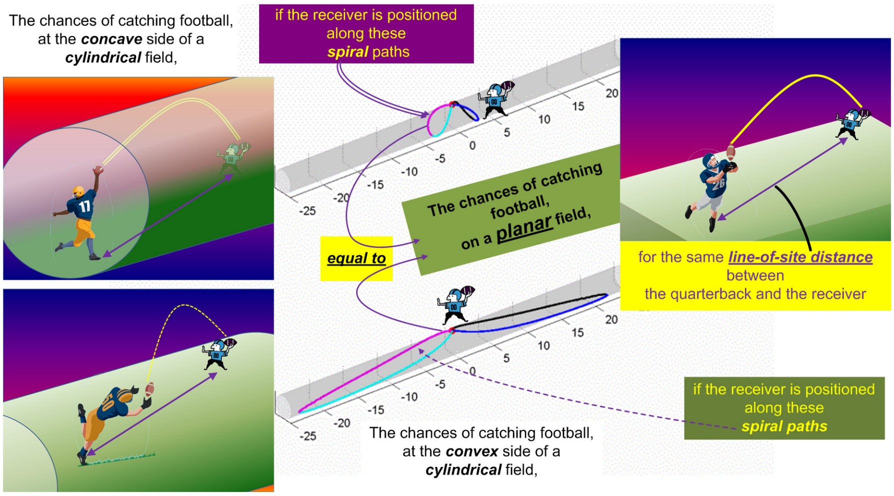

The trajectory of a photon in a medium is analogous to that of a football: Catching the ball is comparable to scattering/absorption of the photon, and the partial bouncing of the ball on a grass field compares with partial absorption on a tissue-applicator interface. We therefore compare the photon remission associated with a concave tissue applicator interface as the chance of catching a football between a quarterback and a wide receiver playing inside a cylindrical field (left-upper inset). Conversely, photon remission associated with a convex tissue-applicator interface correlates to the chance of catching a football between a quarterback and a receiver outside a cylindrical field (left-lower inset). The odds of catching a ball along a unique set of spiral paths on concave or convex field are equal to that along a straight line on a regular planar field (right-upper inset), for the same line-of-sight yards between the thrower and the receiver.

Diffusion occurs for many types of particles or energy transfer in scattering media. Accurate measurement of diffusion is needed to probe the properties of associated media and predict processes.[1]

Nondestructive characterization of diffusion is often done through surface measurements, in which the particle or energy for transport is launched into the medium, and the measured diffuse remission is compared against a model-predicted value. There are rigorous models of photon diffusion associated with various shapes of applicator-tissue interface;[2] however, direct numerical implementation of these analytic entities is daunting. For this reason, alternative numerical approaches, such as the finite element method, are frequently used.

For photon diffusion in noninvasive biological imaging applications, arguably the simplest geometry approximated is that of an infinite planar volume of tissue interfaced with an infinite planar applicator—such is a “semi-infinite” geometry. In practice, however, one commonly encounters configurations that could be idealized by either a concave geometry, wherein the photon probes the regime inner to a cylindrical tissue-applicator interface, or a convex geometry, wherein the photon probes the regime outside a cylindrical tissue-applicator interface.

We introduced novel analytical treatment of steady-state photon diffusion in concave and convex geometries.[3] Our approach, validated by experiments,[4] accurately quantified photon remission along the azimuthal and longitudinal directions with respect to a photon-launching position in idealized concave and convex geometries. In the concave geometry, photon remission along the azimuthal (or longitudinal) direction is found to be greater (or smaller) than that along a straight line on a semi-infinite interface, given the same line-of-sight source-detector distance.

The trends in the convex geometry are opposite. These findings project naturally to the existence of a set of spiral paths on a concave or convex interface, along which photon remission is modeled by the simplest form of describing remission along a straight line on a semi-infinite interface versus the same line-of-sight source-detector distance.[5] Such interesting phenomenon as a spiral/straight equivalence pattern of diffuse photon remission, as shown in the figure, might exist in other regimes, and it may provoke simple sensing strategies to accurately probe the associated medium with challenging geometries. ◭

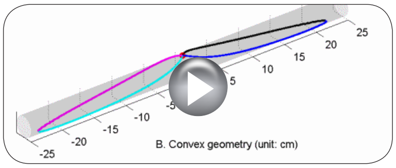

Visit www.opnmagazine-digital.com to view the video that accompanies this article.

D.Piao (daqing.piao@okstate.edu), A. Zhang, G.Xu and C.F. Bunting are with the School of Electrical and Computer Engineering, Oklahoma State University, Stillwater, Okla., U.S.A. G.Yao and C.Daluwatte are with the department of biological engineering, University of Missouri, Columbia, Mo. Y. Jiang is with the department of engineering and physics at the University of Central Oklahoma, Edmond, Okla., and B.W. Pogue is with the Thayer School of Engineering, Dartmouth College, Hanover, N.H.

References

1. A. Ishimaru. Appl. Opt. **28**, 2210-2215 (1989).
2. S.R. Arridge et al. Phys. Med. Biol. **37**(7), 1531-60 (1992).
3. A. Zhang et al. J. Opt. Soc. Am. A. Opt. Image. Sci. Vis. **27**(3), 648-62 (2010).
4. A. Zhang et al. J. Opt. Soc. Am. A. Opt. Image. Sci. Vis., **28**(2), 66-75 (2011).
5. A. Zhang et al. Opt. Lett. **36**(5), 654-6 (2011).

Photon diffusion in a homogeneous medium bounded externally or internally by an infinitely long circular cylindrical applicator. III. Synthetic study of continuous-wave photon fluence rate along unique spiral paths

Anqi Zhang, Daqing Piao* and Charles F. Bunting

School of Electrical and Computer Engineering, Oklahoma State University, Stillwater, Oklahoma 74078, USA
**Corresponding author: daqing.piao@okstate.edu*

Received September 28, 2011; revised November 30, 2011; accepted December 1, 2011;
posted December 1, 2011 (Doc. ID 155485); published March 22, 2012

This is Part III of the work that examines photon diffusion in a scattering-dominant medium *enclosed by* a "concave" circular cylindrical applicator or *enclosing* a "convex" circular cylindrical applicator. In Part II of this work Zhang *et al.* [J. Opt. Soc. Am. A **28**, 66 (2011)] predicted that, on the tissue-applicator interface of either "concave" or "convex" geometry, there exists a unique set of spiral paths, along which the steady-state photon fluence rate decays at a rate equal to that along a straight line on a planar semi-infinite interface, for the same line-of-sight source–detector distance. This phenomenon of steady-state photon diffusion is referred to as "straight-line-resembling-spiral paths" (abbreviated as "spiral paths"). This Part III study develops analytic approaches to the spiral paths associated with geometry of a large radial dimension and presents spiral paths found numerically for geometry of a small radial dimension. This Part III study also examines whether the spiral paths associated with a homogeneous medium are a good approximation for the medium containing heterogeneity. The heterogeneity is limited to an anomaly that is aligned azimuthally with the spiral paths and has either positive or negative contrast of the absorption or scattering coefficient over the background medium. For a weak-contrast anomaly the perturbation by it to the photon fluence rate along the spiral paths is found by applying a well-established perturbation analysis in cylindrical coordinates. For a strong-contrast anomaly the change by it to the photon fluence rate along the spiral paths is computed using the finite-element method. For the investigated heterogeneous-medium cases the photon fluence rate along the homogeneous-medium associated spiral paths is macroscopically indistinguishable from, and microscopically close to, that along a straight line on a planar semi-infinite interface.

OCIS codes: 170.3660, 170.5280, 170.6960.

1. INTRODUCTION

The diffusion process is used to describe many types of particles or energy transfer in scattering media, including photon propagation in biological tissue [1], charge-carrier conveyance in semiconducting material [2], and neutron navigation in a nuclear reactor [3]. The diffusion model also applies to observances such as harmonic mass-transport [4], modulated eddy current [5], thermal waves [6], and the still-controversial viscosity waves [7]. Accurate and accessible quantitation of diffusion is fundamental to probing the properties of associated media and predicting processes [8].

Characterization of the diffusion in a medium nondestructively is often done through surface measurements, in which the particle or energy for transport is launched into the medium, and then the measured diffuse fluence rate is compared against a model-predicted value. Numerical computation based on accurate analytic modeling of diffusion in a nondestructive probing configuration is nontrivial even for a homogeneous medium within a seemingly regular boundary. For the instances of interrogating biological tissue, one could easily find rigorous analytic models of photon diffusion in a homogeneous medium bounded by various shapes of applicator-tissue interface [9]. However, direct numerical implementation of these analytic entities for characterizing the diffusion is daunting; therefore alternative numerical approaches, including the Monte Carlo (MC) method [10], the finite-element method (FEM) [11], and the finite difference method [12], have been used.

In regard to photon diffusion for noninvasive biological imaging applications, arguably the simplest geometry approximated is that of an infinite planar volume of tissue interfaced with an infinite planar applicator—such is a "semi-infinite" geometry [13], of which the photon fluence rate between a source-detector pair on the interface is determined "straightforwardly" by the line-of-sight distance between the positions of a source and a detector [14] for a given set of associated optical properties. In practice, however, the imaging configurations commonly encountered could be idealized by either a "concave" geometry, wherein the photon probes the regime inner to a cylindrical tissue-applicator interface, or a "convex" geometry, wherein the photon probes the regime outside a cylindrical tissue-applicator interface. These three geometries of approximating the tissue-applicator interface are illustrated in Fig. 1(A). The photon fluence rate associated with any source-detector paths along the interface in either concave or convex geometry likely will differ from the fluence rate along a "straight" line on a semi-infinite interface for the same line-of-sight source–detector distance; however, analytic treatments

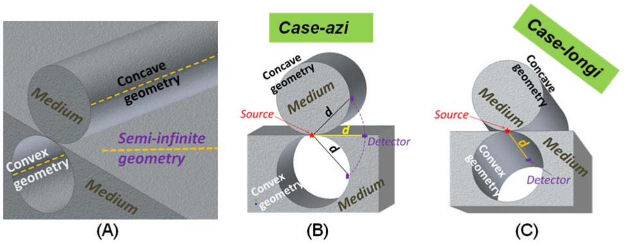

Fig. 1. (Color online) Three geometries of approximating the tissue-applicator interface are illustrated in (A). The geometries include a concave geometry representing the medium being enclosed by the circular cylindrical tissue-applicator interface, a convex geometry representing the medium enclosing the circular cylindrical tissue-applicator interface, and a semi-infinite geometry representing the medium interfacing with a planar applicator. For the concave and convex geometries, there are two specific directions for evaluating the photon fluence rate: a *case-azi* configuration shown in (B) that represents the case of having both source and detector on the same azimuthal plane, and a *case-longi* configuration shown in (C) that represents the case of having both source and detector on the same longitudinal line. In both (B) and (C) the line-of-sight distance between the source and the position of photon detection is denoted by *d*.

for both concave and convex geometries that can be conveniently translated to quantitative evaluations had been, to our knowledge, absent.

In Part I of this study [15] we introduced an analytic approach to steady-state photon diffusion in both concave and convex geometries of an infinitely long cylinder applicator. The analytic results to both concave and convex geometries are similar in the format, with the actual geometry accounted for by the differences in three aspects, including the sequence of the kinds of the modified Bessel functions in a term, the sequence of the terms with and without those modified Bessel functions, and the arguments of the modified Bessel functions containing the radial coordinates of the extrapolated boundary and the equivalent isotropic source.

For both concave and convex geometries, there are apparently two specific configurations for evaluating the photon fluence rate on the tissue-applicator interface: (1) a case-azi configuration as shown in Fig. 1(B), wherein the position of the photon launching into the tissue and the position of the detector are at the same *azimuthal* plane; (2) a case-longi configuration as shown in Fig. 1(C), wherein the position of the photon launching into the tissue and the position of the detector are at the same *longitudinal* plane. It is straightforward to appreciate that, as the radial dimension of either the concave or the convex geometry reaches infinity, both case-azi and case-longi configurations will become the case of a straight line on a semi-infinite interface.

For either the concave or the convex geometry of the radius at the order of centimeters, the photon fluence rates associated with both case-azi and case-longi configurations have been investigated, with respect to the fluence rate along a straight line on a semi-infinite interface, in Part II of this study [16]. The analytic solution to the photon diffusion equation for the idealized concave and convex geometries being demonstrated in Part I was first numerically evaluated and then validated against the FEM solution to the same photon diffusion equation, MC simulation, and experimental measurements, all made in geometries identical to the two idealized ones except with a finite length of the cylinder. For the concave geometry it is found that the photon fluence for the case-azi configuration decays slower than the photon fluence along a straight line on a semi-infinite interface, and the photon fluence for the case-longi configuration decays *faster* than the photon fluence along a straight line on a semi-infinite interface, for the same line-of-sight source–detector distance. Conversely, for the convex geometry it is found that the photon fluence for the case-azi configuration decays faster than the photon fluence along a straight line on a semi-infinite interface, and the photon fluence for the case-longi configuration decays *slower* than the photon fluence along a straight line on a semi-infinite interface, for the same line-of-sight source–detector distance. These findings suggest that on either a concave or a convex interface there exists a set of directions that are oblique to the azimuthal and longitudinal directions (thereby spirally shaped), along which the photon fluence decays at a rate equal to that along a straight line on a semi-infinite interface, for the same line-of-sight source–detector distance. Such a phenomenon, referred to as "straight-line-resembling-spiral paths" of the photon fluence rate associated with concave or convex geometry, was first rationalized in Part II of this study [16].

Note that the straight-line-resembling-spiral paths should not be exclusive to photon diffusion. As long as the energy or particle transfer undergoes diffusion loss in the medium, and the medium-applicator interface imposes "lossy" boundary conditions, the straight-line-resembling-spiral paths likely would occur for cylindrical interfacing cases.

Recently the straight-line-resembling-spiral paths of photon fluence rate (hereafter abbreviated as "spiral paths") associated with concave or convex geometries were demonstrated for homogeneous-medium conditions in [17]. In [17] the existence of such spiral paths was shown through analytic treatments for concave and convex geometries of large radii that rendered favorable analytic approximations, and through numerical methods for concave and convex geometries of smaller practical dimensions. A rigorous accounting of the approximation leading to the analytic representation of the shown spiral paths for concave or convex geometries of large radii, which was not included in [17] owing to the length limit, could shed light on the pattern of spiral paths found numerically for concave or convex geometry of smaller practical radii. As the spiral paths have been shown to exist in concave or convex geometries with homogeneous-medium conditions, it would also be interesting to question whether the spiral paths found for the homogeneous medium would hold for the same geometry if the medium contains heterogeneity. Such issues are among the topics of Part III of this study.

Part III of the study consists of the following sections: Section 2 details the approach leading to the analytic representation of the spiral paths for concave and convex geometries of large radius with homogeneous-medium conditions. Section 3 summarizes the numerical approach used in [17] to find the spiral paths for concave and convex geometries of smaller radius with homogeneous-medium conditions. Section 4 employs the Born approximation to analyze the perturbation introduced to the photon fluence rate by a single heterogeneity with contrast in absorption (μ_a) and reduced scattering (μ_s'). A mistake seen in analytic descriptions of some previous works regarding the sign associated with a scattering perturbation term is identified. Section 5 implements numerically the analytic results from Section 4 to the case of single heterogeneity with weak perturbation strength, to examine the photon fluence rate along the spiral paths identified for the otherwise homogeneous medium. Section 6 quantifies the effect of single heterogeneity of strong perturbation strength to the photon fluence rate along the spiral paths identified for the otherwise homogeneous medium, by the use of FEM. Both Secs. 5 and 6 limit the evaluations to the case of single heterogeneity aligned azimuthally with the spiral paths; however, four cases of the contrast of the heterogeneity are considered: (1) positive absorption contrast, (2) negative absorption contrast, (3) positive reduced-scattering contrast, and (4) negative reduced-scattering contrast. Section 7 discusses the dependence of the spiral paths upon the optical properties of the homogeneous medium as well as the radial dimension of the concave or convex geometry.

2. SPIRAL PATHS ASSOCIATED WITH CONCAVE AND CONVEX GEOMETRIES OF LARGE RADII

This section derives the analytic representation of the spiral paths for concave and convex geometries of a large radial dimension. We assume that the radial dimension is substantially greater than the source-detector distance, which is also much greater than the scattering path length. These assumptions are necessary to simplify the photon fluence to a form from which the analytic profile of the spiral paths could be reached.

The general case of a source and a detector located on the tissue-applicator interface is illustrated in Figs. 2(A) and 2(B), for concave and convex geometries, respectively. The tissue enclosed by the interface in the concave geometry or enclosing the interface in the convex geometry has an absorption coefficient μ_a, a reduced-scattering coefficient $\mu_s{}'$, a diffusion coefficient D, and an effective attenuation coefficient $k_0 = \sqrt{\mu_a/D}$. The radius of the infinitely long circular cylindrical interface is R_0; therefore, by cylindrical coordinates, the source with an intensity of S locates at $(R_0, 0, 0)$ and the detector locates at (R_0, ϕ, z). The line-of-sight distance between the source $(R_0, 0, 0)$ and the detector (R_0, ϕ, z) is denoted by d. The projection of d to the azimuthal plane or the projection of d perpendicular to the longitudinal axis of the cylindrical interface is denoted as $d_\perp = d \cdot \cos\alpha$, where α is the angle between d and $d_\perp$. The position of the detector with respect to the source can then be represented by $(\alpha, d_\perp)$. If keeping the source fixed at $(R_0, 0, 0)$ and increasing the radius R_0, the detector will eventually reach a plane that is tangential to the shown cylindrical interface and intersects with the interface at the longitudinal line crossing the source $(R_0, 0, 0)$. Such a plane forms the semi-infinite geometry limit of the concave or convex geometry [15].

A. Analytic Representation of the Spiral Paths Associated with Concave Geometry of Large Radii

Consider the concave geometry shown in Fig. 2(A). The source illuminating into the tissue at $(R_0, 0, 0)$ can be represented by an isotropic source at $(R_0 - R_a, 0, 0)$, where $R_a = 1/\mu_s'$. An extrapolated boundary in the imaginary "semi-infinite geometry" will be placed at $R_b = 2AD$, where A is a parameter determined by the refractive index mismatch across the tissue-applicator interface, outward from the source $(R_0, 0, 0)$. For the equivalent isotropic source at $(R_0 - R_a, 0, 0)$, its image source with respect to the extrapolated boundary of the imaginary "semi-infinite geometry" locates at $(R_0 + R_a + 2R_b, 0, 0)$.

Denote l_r as the distance from the detector (R_0, ϕ, z) to the equivalent "real" isotropic source at $(R_0 - R_a, 0, 0)$, and l_i as the distance from the detector (R_0, ϕ, z) to the "image" source $(R_0 + R_a + 2R_a, 0, 0)$ associated with the imaginary semi-infinite geometry. For $R_0 \gg d \gg R_a, R_b$, the photon fluence rate at the detector position can be expressed by [15]

$$\Psi = \frac{S}{4\pi D}\frac{e^{-k_0 l_r}}{l_r} - \frac{S}{4\pi D}\frac{e^{-k_0 l_i}}{l_i}\sqrt{\frac{R_0 + R_a + 2R_b}{R_0 - R_a}}, \qquad (1)$$

and we have

$$l_r = d\sqrt{\left[1 + \frac{R_a^2}{d^2} - \frac{R_a}{R_0}(\cos\alpha)^2\right]}, \qquad (2)$$

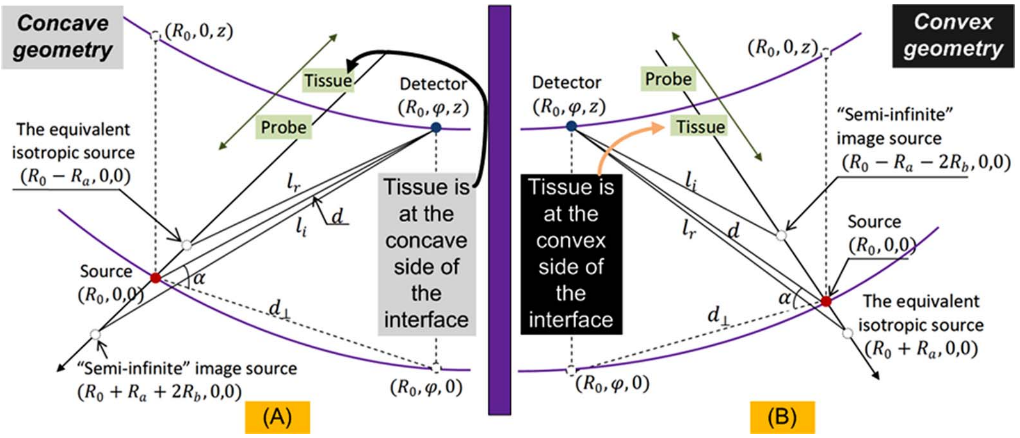

Fig. 2. (Color online) Notations and physical entities of concave or convex geometry for analytic evaluation of photon fluence rate associated with larger radius. (A) The tissue is at the concave side of the circular cylindrical tissue-applicator interface, so the equivalent isotropic source of the physical source that illuminates into the medium is located closer to the center axis than the physical source is. (B) The tissue is at the convex side of the circular cylindrical tissue-applicator interface, so the equivalent isotropic source of the physical source that illuminates into the medium is located farther from the center axis than the physical source is.

$$l_i = d\sqrt{\left[1 + \frac{(R_a + 2R_b)^2}{d^2} + \frac{R_a + 2R_b}{R_0}(\cos\,\alpha)^2\right]}. \tag{3}$$

Since

$$\sqrt{\frac{R_0 + R_a + 2R_b}{R_0 - R_a}} = \left(1 + 2\frac{R_a + R_b}{R_0 - R_a}\right)^{1/2} \approx 1 + \frac{R_a + R_b}{R_0 - R_a} \tag{4}$$

and for $d \gg R_a, R_b$ one has $k_0 d \gg 1$, so Taylor-series expansion gives

$$\frac{e^{-k_0 d\sqrt{1+\Delta}}}{d\sqrt{1+\Delta}} \approx \frac{e^{-k_0 d}}{d}\left[1 - \frac{1}{2}(k_0 d + 1)\Delta\right] \approx \frac{e^{-k_0 d}}{d}\left[1 - \frac{1}{2}(k_0 d)\Delta\right], \tag{5}$$

where $\Delta \ll 1$. Using Eqs. (2) to (5), Eq. (1) simplifies to

$$\begin{aligned}\Psi = \frac{S}{4\pi D}\frac{e^{-k_0 d}}{d}\Bigg\{&\left[1 - \frac{1}{2}k_0 d\left(\frac{R_a^2}{d^2} - \frac{R_a}{R_0}(\cos\,\alpha)^2\right)\right] \\ &- \left[1 - \frac{1}{2}k_0 d\left(\frac{(R_a + 2R_b)^2}{d^2} + \frac{R_a + 2R_b}{R_0}(\cos\,\alpha)^2\right)\right] \\ &\times\left(1 + \frac{R_a + R_b}{R_0 - R_a}\right)\Bigg\},\end{aligned} \tag{6}$$

which can be further derived to the form of (the derivation is detailed in Appendix A)

$$\frac{\partial \ln(\Psi \cdot d^2)}{\partial d} = -\left\{k_0 + \frac{1}{2k_0 R_b(R_0 - R_a)} - \left[\frac{2R_0 - R_a + 2R_b}{2R_0 R_b(R_0 - R_a)}\right]\cos\alpha \cdot d_\perp\right\}. \tag{7}$$

Equation (7) characterizes the decay rate of photon fluence along the direction defined by angle α, with respect to the line-of-sight source–detector distance d. For the case-longi configuration, the detector locates at $(R_0, 0, z)$, so $\alpha = \pi/2$ and $d_\perp = 0$, and then Eq. (7) becomes

$$\frac{\partial\,\ln(\Psi \cdot d^2)}{\partial d} = -\left[k_0 + \frac{1}{2k_0 R_b(R_0 - R_a)}\right]. \tag{8}$$

For the case-azi configuration, the detector locates at $(R_0, \phi, 0)$, so $\alpha = 0$ and $d_\perp = d$, and then Eq. (7) becomes

$$\frac{\partial\,\ln(\Psi \cdot d^2)}{\partial d} = -\left\{k_0 + \frac{1}{2k_0 R_b(R_0 - R_a)} - \left[\frac{2R_0 - R_a + 2R_b}{2R_0 R_b(R_0 - R_a)}\right]d\right\}. \tag{9}$$

The first term k_0 in the right-hand side of Eqs. (8) and (9) characterizes the decay rate of photon fluence along a straight line on a semi-infinite interface. It is clear by Eq. (8) that the photon fluence along the longitudinal direction on a concave interface decays faster than the photon fluence along a straight line on the semi-infinite interface. However, the decay rate of photon fluence (comparing to k_0) along the azimuthal direction on a concave interface as described by Eq. (9) is inexplicit owing to the two terms of opposite signs after k_0. It can be shown that the third term at the right-hand side of Eq. (9) is greater in magnitude than the second term for a general diffusion regime; therefore Eq. (9) actually accounts for the smaller decay rate of photon fluence along the azimuthal direction on a concave interface than that along a straight line on the semi-infinite interface.

From Eq. (7) it is straightforward to conclude that if the coordinates of the detector $(\alpha, d_\perp)$ with respect to the source satisfy the condition of

$$\cos\,\alpha = \frac{1}{k_0 d_\perp}\frac{R_0}{2R_0 - R_a + 2R_b}, \tag{10}$$

then the decay rate of photon fluence over the line-of-sight source–detector distance d on the concave interface is identical to that over the same d on the semi-infinite interface. Equation (10) implies that α changes as the detector displaces azimuthally away from the source.

B. Analytic Representation of the Spiral Paths Associated with Convex Geometry of Large Radii

Consider the convex geometry shown in Fig. 2(B). A source illuminating into the tissue at $(R_0, 0, 0)$ can be represented by an isotropic source at $(R_0 + R_a, 0, 0)$. An extrapolated boundary in the imaginary "semi-infinite geometry" will be placed at $R_b = 2AD$ inward from the source $(R_0, 0, 0)$. For the equivalent isotropic source at $(R_0 + R_a, 0, 0)$, its image source with respect to the extrapolated boundary of the imaginary "semi-infinite geometry" locates at $(R_0 - R_a - 2R_b, 0, 0)$.

Denote l_r as the distance from the detector (R_0, ϕ, z) to the equivalent "real" isotropic source at $(R_0 + R_a, 0, 0)$, and l_i as the distance from the detector (R_0, ϕ, z) to the "image" source $(R_0 - R_a - 2R_b, 0, 0)$ associated with the imaginary semi-infinite geometry. For $R_0 \gg d \gg R_a, R_b$, the photon fluence rate at the detector position can be expressed by [15]

$$\Psi = \frac{S}{4\pi D}\frac{e^{-k_0 l_r}}{l_r} - \frac{S}{4\pi D}\frac{e^{-k_0 l_i}}{l_i}\sqrt{\frac{R_0 - R_a - 2R_b}{R_0 + R_a}}, \tag{11}$$

and we have

$$l_r = d\sqrt{\left[1 + \frac{R_a^2}{d^2} + \frac{R_a}{R_0}(\cos\,\alpha)^2\right]}, \tag{12}$$

$$l_i = d\sqrt{\left[1 + \frac{(R_a + 2R_b)^2}{d^2} - \frac{R_a + 2R_b}{R_0}(\cos\,\alpha)^2\right]}. \tag{13}$$

Since

$$\sqrt{\frac{R_0 - R_a - 2R_b}{R_0 + R_a}} = \left(1 - 2\frac{R_a + R_b}{R_0 + R_a}\right)^{1/2} \approx 1 - \frac{R_a + R_b}{R_0 + R_a}, \tag{14}$$

using Eqs. (12) to (14) and (5), Eq. (11) simplifies to

$$\Psi=\frac{S}{4\pi D}\frac{e^{-k_0 d}}{d}\left\{\left[1-\frac{1}{2}k_0 d\left(\frac{R_a^2}{d^2}+\frac{R_a}{R_0}(\cos\alpha)^2\right)\right]\right.$$
$$\left.-\left[1-\frac{1}{2}k_0 d\left(\frac{(R_a+2R_b)^2}{d^2}-\frac{R_a+2R_b}{R_0}(\cos\alpha)^2\right)\right]\left(1-\frac{R_a+R_b}{R_0+R_a}\right)\right\}, \tag{15}$$

which can be further derived to the form of (the derivation is detailed in Appendix B)

$$\frac{\partial\ \ln(\Psi\cdot d^2)}{\partial d}=-\left\{k_0-\frac{1}{2k_0 R_b(R_0+R_a)}\right.$$
$$\left.+\left[\frac{2R_0+R_a-2R_b}{2R_0 R_b(R_0+R_a)}\right]\cos\,\alpha\cdot d_\perp\right\}. \tag{16}$$

Equation (16) characterizes the decay rate of photon fluence along the direction defined by angle α, with respect to the line-of-sight source–detector distance d. For the case-longi configuration, the detector locates at $(R_0, 0, z)$, so $\alpha = \pi/2$ and $d_\perp = 0$, and then Eq. (16) becomes

$$\frac{\partial\ \ln(\Psi\cdot d^2)}{\partial d}=-\left[k_0-\frac{1}{2k_0 R_b(R_0+R_a)}\right]. \tag{17}$$

For the case-azi configuration, the detector locates at $(R_0, \phi, 0)$, so $\alpha = 0$ and $d_\perp = d$, and then Eq, (16) becomes

$$\frac{\partial\ln(\Psi\cdot d^2)}{\partial d}=-\left\{k_0-\frac{1}{2k_0 R_b(R_0+R_a)}+\left[\frac{2R_0+R_a-2R_b}{2R_0 R_b(R_0+R_a)}\right]d\right\}. \tag{18}$$

The first term k_0 in the right-hand side of Eqs. (17) and (18) characterizes the decay rate of photon fluence along a straight line on a semi-infinite interface. It is clear by Eq. (17) that the photon fluence along the longitudinal direction on a convex interface decays slower than the photon fluence along a straight line on the semi-infinite interface. However, the decay rate of photon fluence (comparing to k_0) along the azimuthal direction on a convex interface described by Eq. (18) is inexplicit owing to the two terms of opposite signs after k_0. It can be shown that the third term at the right-hand side of Eq. (18) is greater in magnitude than the second term for the general diffusion regime; therefore Eq. (18) actually accounts for the greater decay rate of photon fluence along the azimuthal direction on a convex interface than that along a straight line on the semi-infinite interface.

From Eq. (16) it is straightforward to conclude that if the coordinates of the detector $(\alpha, d_\perp)$ with respect to the source satisfy the condition of

$$\cos\,\alpha=\frac{1}{k_0 d_\perp}\frac{R_0}{2R_0+R_a-2R_b}, \tag{19}$$

then the decay rate of photon fluence over line-of-sight source–detector distance d on the convex interface is identical to that over the same d on the semi-infinite interface. Equation (19) also implies that α changes as the detector is displaced azimuthally away from the source.

3. SPIRAL PATHS ASSOCIATED WITH CONCAVE AND CONVEX GEOMETRIES OF SMALL RADII

For concave or convex geometries of small radii, analytic derivation of the spiral paths could become much more complicated. Should an analytic approximation of the spiral paths be reached, the resulting profiles would likely be much more inaccurate owing to the approximation imposed by a smaller radial dimension. In [17], the spiral paths of concave or convex geometry of a smaller radial dimension were found numerically based on the general analytic results given in [15]. The method and the found spiral paths are summarized in Fig. 3. First, a uniform grid is established on the cylindrical interface, and the source is fixed at one node. A detector has three options of moving away from the source: along the azimuthal direction, along the longitudinal direction, and along the diagonal of the previous two directions. For each possible future location of the detector, the photon fluence rate at that position is compared with the case in the semi-infinite geometry for the same line-of-sight distance of the detector from the source. The position with the least difference of the evaluated photon fluence rate from the semi-infinite geometry is chosen as the next starting position of the detector. The trace of moving the detector on the interface forms the spiral paths. In both concave and convex geometries, the spiral paths have two lobes symmetric to the source location, and each lobe is symmetric with respect to a middle sagittal plane containing the source. The spiral paths are shown to contain four identical quadrants. The MC and FEM solution of photon diffusion confirmed that the decay rate of photon fluence along the spiral paths was indeed equal to that along a straight line on a semi-infinite interface [17].

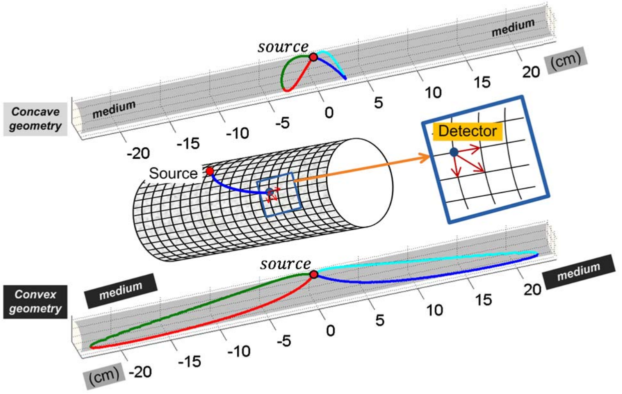

Fig. 3. (Color online) spiral paths for concave and convex geometries of centimeter-order radii are calculated based on analytic results derived in [15]. For a fixed source, a detector has three directions to move away from the source: along the azimuthal direction, along the longitudinal direction, and along the diagonal of the above two directions. For each possible future location of the detector, the photon fluence rate at that position is compared with the case in the semi-infinite geometry for the same line-of-sight distance of the detector from the source, and the position with the least difference in the evaluated photon fluence rate is the next starting position of the detector. The shown complete sets of the spiral profile for concave geometry (upper) and convex geometry (lower) are computed for a cylinder radius of $R_0 = 1.5$ cm and optical properties of $\mu_a = 0.02\ \mathrm{cm}^{-1}$, $\mu_s' = 5\ \mathrm{cm}^{-1}$, and $A = 1.86$.

4. PERTURBATION TO PHOTON FLUENCE RATE IN CONCAVE OR CONVEX GEOMETRIES—ANALYTIC TREATMENT

The spiral paths are demonstrated in concave and convex geometries for homogeneous-medium cases. However, it is questionable that the spiral paths associated with homogeneous-medium cases will hold for the medium containing heterogeneity. Practically, however, it may only be possible to examine the spiral paths in limited cases of medium heterogeneity. To facilitate the examination by analytic means, this section employs perturbation-based analysis to derive the general form of the photon fluence rate in concave or convex geometry that contains a single heterogeneity in an otherwise homogeneous medium.

We start with the equation of steady-state photon diffusion in an infinite medium as

$$\mu_a(\vec{r})\Psi(\vec{r}) - \nabla\cdot[D(\vec{r})\nabla\Psi(\vec{r})] = S(\vec{r}), \tag{20}$$

where $\Psi(\vec{r})$ is the photon fluence rate at position $\vec{r}$, and $S(\vec{r})$ is the source term. The optical heterogeneity to a homogeneous medium of absorption coefficient μ_{a0} and diffusion coefficient D_0 may be represented by

$$\mu_a(\vec{r}) = \mu_{a0} + \delta\mu_a(\vec{r}), \tag{21}$$

$$D(\vec{r}) = D_0 + \delta D(\vec{r}) \tag{22}$$

and the resulted photon fluence rate is expressed by

$$\Psi(\vec{r}) = \Psi_0(\vec{r}) + \Psi_{SC}(\vec{r}), \tag{23}$$

where $\Psi_0(\vec{r})$ is the photon fluence rate for homogeneous medium that satisfies the equation of

$$\mu_{a0}\Psi_0(\vec{r}) - D_0\nabla^2\Psi_0(\vec{r}) = S(\vec{r}) \tag{24}$$

and $\Psi_{SC}(\vec{r})$ represents a perturbation. By using Eqs. (21)–(23) we convert Eq. (20) to

$$\begin{aligned}&[\mu_{a0} + \delta\mu_a(\vec{r})][\Psi_0(\vec{r}) + \Psi_{SC}(\vec{r})]\\ &\quad - D_0\nabla^2[\Psi_0(\vec{r})\\ &\quad + \Psi_{SC}(\vec{r})] - \nabla\cdot\{\delta D(\vec{r})\cdot\nabla[\Psi_0(\vec{r}) + \Psi_{SC}(\vec{r})]\} = S(\vec{r}).\end{aligned} \tag{25}$$

Subtracting Eq. (24) from Eq. (25) leads to

$$\begin{aligned}D_0\nabla^2\Psi_{SC}(\vec{r}) - \mu_{a0}\Psi_{SC}(\vec{r}) = \delta\mu_a(\vec{r})[\Psi_0(\vec{r}) + \Psi_{SC}(\vec{r})] - \nabla\\ \cdot\{\delta D(\vec{r})\nabla[\Psi_0(\vec{r}) + \Psi_{SC}(\vec{r})]\}.\end{aligned} \tag{26}$$

For a weak heterogeneity [18,19], i.e.,

$$\Psi_{SC}(\vec{r}) \ll \Psi_0(\vec{r}), \tag{27}$$

Eq. (26) becomes

$$\begin{aligned}\nabla^2\Psi_{SC}(\vec{r}) - \frac{\mu_{a0}}{D_0}\Psi_{SC}(\vec{r}) = \frac{\delta\mu_a(\vec{r})}{D_0}\Psi_0(\vec{r}) - \frac{1}{D_0}\nabla\\ \cdot\{\delta D(\vec{r})\nabla\Psi_0(\vec{r})\}.\end{aligned} \tag{28}$$

The Green function of Eq. (28) satisfies the equation of

$$\nabla^2 G(\vec{r},\vec{r}\,') - \frac{\mu_{a0}}{D_0}G(\vec{r},\vec{r}\,') = -\delta(\vec{r}-\vec{r}\,'). \tag{29}$$

We denote the source location as $\vec{r}_s$, the heterogeneity location as $\vec{r}\,'$, and the detector location as $\vec{r}_d$. The photon fluence rate measured at $\vec{r}\,'$ associated with a source at $\vec{r}_s$ is denoted as $\Psi_0(\vec{r}\,',\vec{r}_s)$, and $G(\vec{r}_d,\vec{r}\,')$ in Eq. (29) represents the response at $\vec{r}_d$ owing to an impulse at $\vec{r}\,'$.

We now consider a concave geometry of radius R_0 and the extrapolated boundary condition based on Part I of this study. For a directional source at $\vec{r}_s(R_0,\varphi_s,z_s)$ thereby an equivalent isotropic source at $\vec{r}_s(R_0-R_a,\varphi_s,z_s)$, and a heterogeneity at $\vec{r}\,'(\rho',\varphi',z')$ assuming that the heterogeneity locates deeper than R_a from the interface boundary, i.e., $\rho' < R_0 - R_a$, we have

$$\begin{aligned}\Psi_0(\vec{r}\,',\vec{r}_s) = \frac{S}{D}\frac{1}{2\pi^2}\int_0^\infty \mathrm{d}k\Bigg\{&\cos[k(z'-z_s)]\\ &\times\sum_{m=0}^\infty \varepsilon_m I_m(k_{\text{eff}}\rho')K_m[k_{\text{eff}}(R_0-R_a)]\\ &\cdot\left\langle 1 - \frac{I_m[k_{\text{eff}}(R_0-R_a)]}{K_m[k_{\text{eff}}(R_0-R_a)]}\frac{K_m[k_{\text{eff}}(R_0+R_b)]}{I_m[k_{\text{eff}}(R_0+R_b)]}\right\rangle\\ &\times\cos[m(\varphi'-\varphi_s)]\Bigg\},\end{aligned} \tag{30}$$

where I_m and K_m are the modified Bessel functions of the first and second kinds, respectively, $k_{\text{eff}} = \sqrt{k^2+k_0^2}$, and

$$\varepsilon_m = \begin{cases} 2 & m > 0 \\ 1 & m = 0 \end{cases}. \tag{31}$$

For the heterogeneity at $\vec{r}\,'(\rho',\varphi',z')$ and a detector at $\vec{r}_d(R_0,\varphi_d,z_d)$, note $\rho' < R_0$, we have

$$\begin{aligned}G(\vec{r}_d,\vec{r}\,') = \frac{1}{2\pi^2}\int_0^\infty \mathrm{d}k\Bigg\{&\cos[k(z_d-z')]\sum_{m=0}^\infty \varepsilon_m I_m(k_{\text{eff}}\rho')K_m(k_{\text{eff}}R_0)\\ &\cdot\left\langle 1 - \frac{I_m(k_{\text{eff}}R_0)\,K_m[k_{\text{eff}}(R_0+R_b)]}{K_m(k_{\text{eff}}R_0)\,I_m[k_{\text{eff}}(R_0+R_b)]}\right\rangle\cos[m(\varphi_d-\varphi')]\Bigg\}.\end{aligned} \tag{32}$$

Similarly we consider a convex geometry of radius R_0 and the extrapolated boundary condition. For a directional source at $\vec{r}_s(R_0,\varphi_s,z_s)$ thereby an equivalent isotropic source at $\vec{r}_s(R_0+R_a,\varphi_s,z_s)$, and a heterogeneity at $\vec{r}\,'(\rho',\varphi',z')$ assuming that the heterogeneity locates deeper than R_a from the interface boundary, i.e., $\rho' > R_0 + R_a$, we have

$$\Psi_0(\vec{r}',\vec{r}_s)=\frac{S}{D}\frac{1}{2\pi^2}\int_0^\infty \mathrm{d}k\Bigg\{\cos[k(z'-z_s)]\\ \times\sum_{m=0}^{\infty}\varepsilon_m I_m[k_{\mathrm{eff}}(R_0+R_a)]K_m(k_{\mathrm{eff}}\rho')\\ \cdot\left\langle 1-\frac{I_m[k_{\mathrm{eff}}(R_0-R_b)]}{K_m[k_{\mathrm{eff}}(R_0-R_b)]}\frac{K_m[k_{\mathrm{eff}}(R_0+R_a)]}{I_m[k_{\mathrm{eff}}(R_0+R_a)]}\right\rangle\\ \times\cos[m(\varphi'-\varphi_s)]\Bigg\}. \tag{33}$$

For the heterogeneity at $\vec{r}'(\rho',\varphi',z')$ and a detector at $\vec{r}_d(R_0,\varphi_d,z_d)$, note $\rho'>R_0$, we have

$$G(\vec{r}_d,\vec{r}')=\frac{1}{2\pi^2}\int_0^\infty \mathrm{d}k\Bigg\{\cos[k(z_d-z')]\\ \times\sum_{m=0}^{\infty}\varepsilon_m I_m(k_{\mathrm{eff}}R_0)K_m(k_{\mathrm{eff}}\rho')\\ \cdot\left\langle 1-\frac{I_m[k_{\mathrm{eff}}(R_0-R_b)]}{K_m[k_{\mathrm{eff}}(R_0-R_b)]}\frac{K_m(k_{\mathrm{eff}}R_0)}{I_m(k_{\mathrm{eff}}R_0)}\right\rangle\\ \times\cos[m(\varphi_d-\varphi')]\Bigg\}. \tag{34}$$

The solution to Eq. (28), representing the change to the photon fluence rate measured at $\vec{r}_d$ associated with a source at $\vec{r}_s$ by the heterogeneity at $\vec{r}'$, is then

$$\Psi_{SC}(\vec{r}_d,\vec{r}_s)=-\frac{1}{D_0}\iiint_V G(\vec{r}_d,\vec{r}')\delta\mu_a(\vec{r}')\Psi_0(\vec{r}',\vec{r}_s)\mathrm{d}^3r'\\ +\frac{1}{D_0}\iiint_V G(\vec{r}_d,\vec{r}')\nabla\cdot\{\delta D(\vec{r}')\nabla\Psi_0(\vec{r}',\vec{r}_s)\}\mathrm{d}^3r'. \tag{35}$$

In Eq. (35), the first term of integration is associated with the absorption heterogeneity, and the second term of integration is associated with the diffusion heterogeneity. Appendix C shows that the second term can be transformed, and by that transformation Eq. (35) changes to

$$\Psi_{SC}(\vec{r}_d,\vec{r}_s)=-\frac{1}{D_0}\iiint_V G(\vec{r}_d,\vec{r}')\delta\mu_a(\vec{r}')\Psi_0(\vec{r}',\vec{r}_s)\mathrm{d}^3r'\\ -\frac{1}{D_0}\iiint_V \delta D(\vec{r}')\nabla G(\vec{r}_d,\vec{r}')\cdot\nabla\Psi_0(\vec{r}',\vec{r}_s)\mathrm{d}^3r'. \tag{36}$$

It is worthwhile to notice that there is a mistake seen in analytic descriptions of some previous works similar in form to Eq. (36), such as Eq. (2) in [19] and Eq. (11.63) in [20], regarding the sign associated with the second term of integration. The detailed accounting in Appendix C shall clarify the "–" sign, rather than a "+" sign, associated with the second term of integration related to the diffusion heterogeneity.

For an inclusion of volume V and a uniform contrast over the background medium, we define the absorption strength of the inclusion with respect to the background medium as

$$\delta P_{\mu_a}=\frac{\|\delta\mu_a\bullet V\|}{\mu_{a0}} \tag{37}$$

and the scattering strength of the inclusion with respect to the background medium as

$$\delta P_D=\frac{\|\delta D\bullet V\|}{D_0}. \tag{38}$$

Equation (37) implies that the same level of absorption perturbation to the photon fluence rate could be caused by either a smaller anomaly with stronger absorption contrast or a larger anomaly with weaker absorption contrast. Equation (38) implies that the same level of scattering perturbation to the photon fluence rate could be caused by either a smaller anomaly with stronger scattering contrast or a larger anomaly with weaker scattering contrast. Then Eq. (36) becomes

$$\Psi_{SC}(\vec{r}_d,\vec{r}_s)=-\delta P_{\mu_a}\frac{\mu_{a0}}{D_0}G(\vec{r}_d,\vec{r}')\Psi_0(\vec{r}',\vec{r}_s)\\ -\delta P_D\nabla G(\vec{r}_d,\vec{r}')\cdot\nabla\Psi_0(\vec{r}',\vec{r}_s). \tag{39}$$

The gradient operator in Eq. (39) can be expanded in cylindrical coordinates as

$$\nabla G(\vec{r}_d,\vec{r}')\cdot\nabla\Psi_0(\vec{r}',\vec{r}_s)\\ =\left\{\left[\frac{\partial G(\vec{r}_d,\vec{r}')}{\partial\rho'}\right]\left[\frac{\partial\Psi_0(\vec{r}',\vec{r}_s)}{\partial\rho'}\right]\right.\\ +\left[\frac{1}{\rho'}\frac{\partial G(\vec{r}_d,\quad\times\vec{r}')}{\partial\varphi'}\right]\left[\frac{1}{\rho'}\frac{\partial\Psi_0(\vec{r}',\vec{r}_s)}{\partial\varphi'}\right]\\ \left.+\left[\frac{\partial G(\vec{r}_d,\vec{r}')}{\partial z'}\right]\left[\frac{\partial\Psi_0(\vec{r}',\vec{r}_s)}{\partial z'}\right]\right\}. \tag{40}$$

5. PERTURBATION TO PHOTON FLUENCE RATE BY A WEAK TARGET ALIGNED AZIMUTHALLY WITH THE SPIRAL PATHS —NUMERICAL EVALUATION BASED ON ANALYTIC TREATMENT

This section aims to evaluate the photon fluence rate along the spiral paths identified for homogeneous-medium cases, when the medium contains a weak heterogeneous inclusion whose center is aligned azimuthally with one location on the spiral paths. The perturbation analysis discussed in the previous section will be numerically implemented for the weak inclusion. For concave and convex geometries, the partial derivatives in Eq. (40) can be numerically approximated using a central difference scheme, after $\Psi_0(\vec{r}',\vec{r}_s)$ and $G(\vec{r}_d,\vec{r}')$ are quantified based on the numerical methods demonstrated in [15,16]. As the evaluation of spiral paths with inclusion in concave

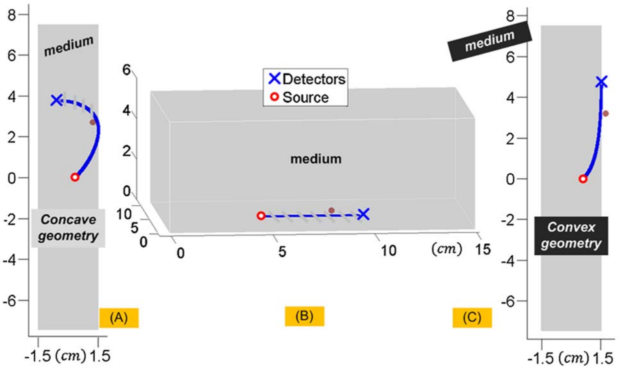

Fig. 4. (Color online) Position of the anomaly of weak perturbation strength in the otherwise homogeneous background medium. (A) Concave geometry, (B) semi-infinite geometry, (C) convex geometry.

Table 1. Four Sets of Optical Parameters for Evaluating the Change to Photon Fluence Rate by an Anomaly of Weak Contrast to the Background Medium

		Background μ_a(cm^{-1})	Background μ_s'(cm^{-1})	Anomaly μ_a(cm^{-1})	Anomaly μ_s'(cm^{-1})
Set 1	Positive μ_a contrast	*0.025*	10.0	0.05	10.0
Set 2	Positive μ_s' contrast	0.025	*10.0*	0.025	12.0
Set 3	Negative μ_a contrast	0.05	10.0	**0.025**	10.0
Set 4	Negative μ_s' contrast	0.025	12.0	0.025	**10.0**

or convex geometry has to involve evaluating the photon fluence rate along a straight line in a semi-infinite geometry with identical inclusion, the gradient operator in Eq. (39) will be expanded in Cartesian coordinates for the semi-infinite geometry, and the resulting partial derivatives will be found similarly by a central difference scheme.

We consider a spherical anomaly of 0.15 cm in radius and 0.25 cm in depth that is aligned with one quadrant of the spiral paths, as shown in Fig. 4. The position of the anomaly is chosen so that in the concave geometry [Fig. 4(A)] the azimuthal angle between the anomaly center and the source is $\pi/2$. In the semi-infinite geometry [Fig. 4(B)] and the convex geometry [Fig. 4(C)], the position of the anomaly is chosen such that the line-of-sight distance between the source and the projection of the anomaly center onto the straight line or spiral-path (hence the physical boundary) is kept the same as that in the concave geometry. Table 1 lists the four sets of optical parameters assigned to the single anomaly, which include positive μ_a, positive μ_s', negative μ_a, and negative μ_s' contrasts with respect to those of the background medium that is not necessarily identical in the four cases. The radii of both concave and convex applicators are set as 1.5 cm, and $A = 1.86$ is chosen.

The results of numerical evaluation based on the four cases of contrasts specified in Table 1 are given in Fig. 5. In each of the figure parts from 5(A) to 5(D), the photon fluence rates are compared among four configurations: (1) along a straight line on the semi-infinite interface for homogeneous medium, which is used as the reference; (2) along a straight line on the semi-infinite interface with the anomaly; (3) along the spiral profile on the concave interface with the anomaly; (4) along the spiral profile on the convex interface with the anomaly. The photon fluence curves for the four configurations are shown indistinguishable at the macroscopic scale near the 5 cm range for d. To examine the microscopic differences of the photon fluence curves, the curves corresponding to a 0.1 cm range of d and centering at the azimuthal coordinate of the anomaly are magnified as the inset in each figure part. Under the magnification, it is found that (1) the photon fluence curves associated with the anomaly are clearly distinguished from the reference; (2) the photon fluence curves associated with the anomaly of absorption contrast are still indistinguishable among the three geometries; and (3) the

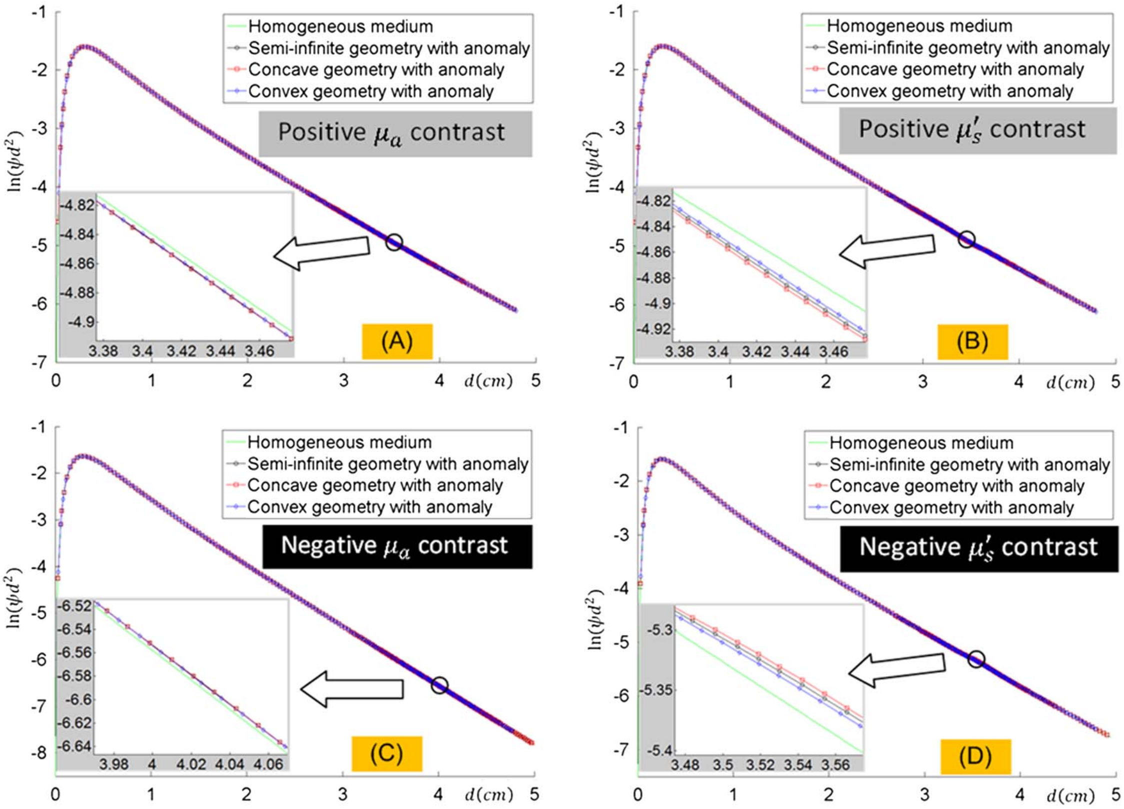

Fig. 5. (Color online) Photon fluence rate when one weak anomaly resides in the otherwise homogeneous background medium. The anomaly possesses (A) positive μ_a contrast, (B) positive μ_s' contrast, (C) negative μ_a contrast, and (D) negative μ_s' contrast over the background. The shown curves of photon fluence are plotted for (1) along a straight line on semi-infinite interface of homogeneous medium, (2) along a straight line on semi-infinite interface having the anomaly aligned with the straight line, (3) along the spiral profile on concave interface having the anomaly aligned with the spiral profile, and (4) along the spiral profile on convex interface having the anomaly aligned with the spiral profile.

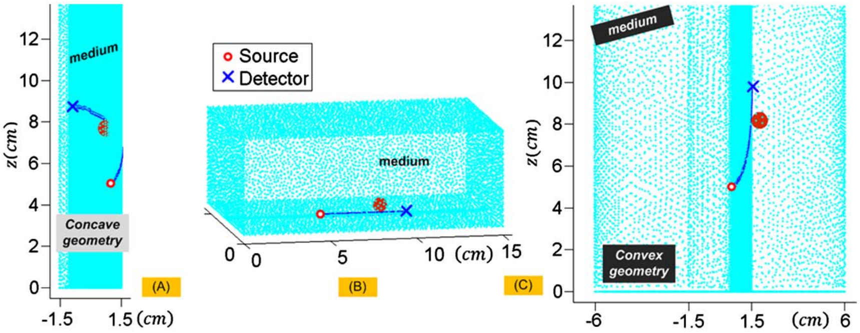

Fig. 6. (Color online) Finite-element discretization of the imaging domain and the position of the anomaly with strong perturbation strength. (A) Concave geometry, (B) semi-infinite geometry, and (C) convex geometry.

photon fluence curves associated with the anomaly of scattering contrast are distinguishable among the three geometries, with the curves of concave and convex geometries locating very close to and at the opposite sides of the curve of semi-infinite geometry.

6. CHANGE TO PHOTON FLUENCE RATE BY A STRONG TARGET ALIGNED AZIMUTHALLY WITH THE SPIRAL PATHS—NUMERICAL EVALUATION BASED ON FINITE-ELEMENT METHOD

As the perturbation analysis becomes increasingly inaccurate for increasing contrast strength of the anomaly, FEM computation based on a software package of near infrared fluorescence and spectral tomography (NIRFAST) [21] is implemented to evaluate the photon fluence rate along the spiral paths when a strong anomaly resides in the medium.

The FEM meshing domain is illustrated in Figs. 6(A), 6(B), and 6(C) for concave, semi-infinite, and convex geometries, respectively. In the concave geometry, the meshing volume is a cylinder of 14 cm in height and 1.5 cm in radius, which is discretized into 76620 nodes and 349697 tetrahedral elements. The surface containing the spiral profile is set with higher node density. In the semi-infinite geometry, the meshing volume is a rectangle of $15 \times 11 \times 5.5$ cm^3, which is discretized into 88941 nodes and 496211 elements. The straight line for evaluating the photon fluence rate is set with higher node density. In the convex geometry, the meshing domain is the volume between two concentric cylinders of 15 cm in height, with 1.5 cm inner radius and 6 cm outer radius. The meshing volume is discretized into 83312 nodes and 437039 tetrahedral elements. The surface containing the spiral profile is set with denser nodes.

Table 2. Four Sets of Optical Parameters Used for Evaluating the Change to Photon Fluence Rate by an Anomaly of Strong Contrast to the Background Medium

	Background μ_a(cm^{-1})	Background μ_s'(cm^{-1})	Anomaly μ_a(cm^{-1})	Anomaly μ_s'(cm^{-1})
Set 1 Positive μ_a contrast	*0.025*	10.0	0.1	10.0
Set 2 Positive μ_s' contrast	0.025	*10.0*	0.025	20.0
Set 3 Negative μ_a contrast	0.1	10.0	**0.025**	10.0
Set 4 Negative μ_s' contrast	0.025	20.0	0.025	**10.0**

We consider a spherical anomaly of 0.4 cm in radius and 0.5 cm in depth that is aligned azimuthally with one quadrant of the spiral paths. The positions of the anomaly in concave, semi-infinite, and convex geometries are chosen following the same rules as in Section 5. Table 2 lists the four sets of optical parameters assigned to the single anomaly, which include positive μ_a, positive μ_s', negative μ_a, and negative μ_s' contrasts with respect to those of the background medium that is not necessarily identical in the four cases. The four sets of anomaly defined in Table 2 have approximately 57 times of positive absorption strength, 57 times of positive scattering strength, 28 times of negative absorption strength, and 95 times of negative scattering strength, respectively, of the ones defined in Table 1, when counting the difference in volume.

The results of FEM simulation based on the four cases of contrasts as specified in Table 2 are given in Fig. 7. In each of the figure parts from 7(A) to 7(D), the photon fluence rates are compared among four configurations as with Fig. 5. At the macroscopic scale near the 5 cm range for d, the photon fluence curves for the three geometries with the anomaly are distinguished from the reference except for negative μ_a contrast; however, the photon fluence curves for the three geometries with the anomaly are nearly indistinguishable. At the microscopic level similar to that in Fig. 5, the photon fluence curves of the concave and convex geometries are very close to and at the opposite sides of the curve of semi-infinite geometry, for anomaly of either absorption or scattering contrast.

7. DISCUSSION

Our previous studies have suggested and demonstrated the existence of spiral paths in the concave and convex geometries for homogeneous-medium conditions. As stated earlier, the spiral paths refer to the equivalence of a unique set of directions on the concave and convex interfaces to a straight line on a semi-infinite interface, in terms of the decay rate of photon fluence with respect to the line-of-sight distance between a source and a detector positioned for probing a homogeneous medium. Such equivalence of the spiral directions in concave or convex geometries to a straight line in a semi-infinite geometry may very well be limited to only the specific set of parameters. For concave and convex geometries of large radii, Eqs. (10) and (19) represent the spiral paths by means of the angle α. It is unmistakable that α is a function of R_0, and α should also be affected by R_a and R_b, which collectively are determined by the optical properties of medium and tissue-applicator interface. It is therefore

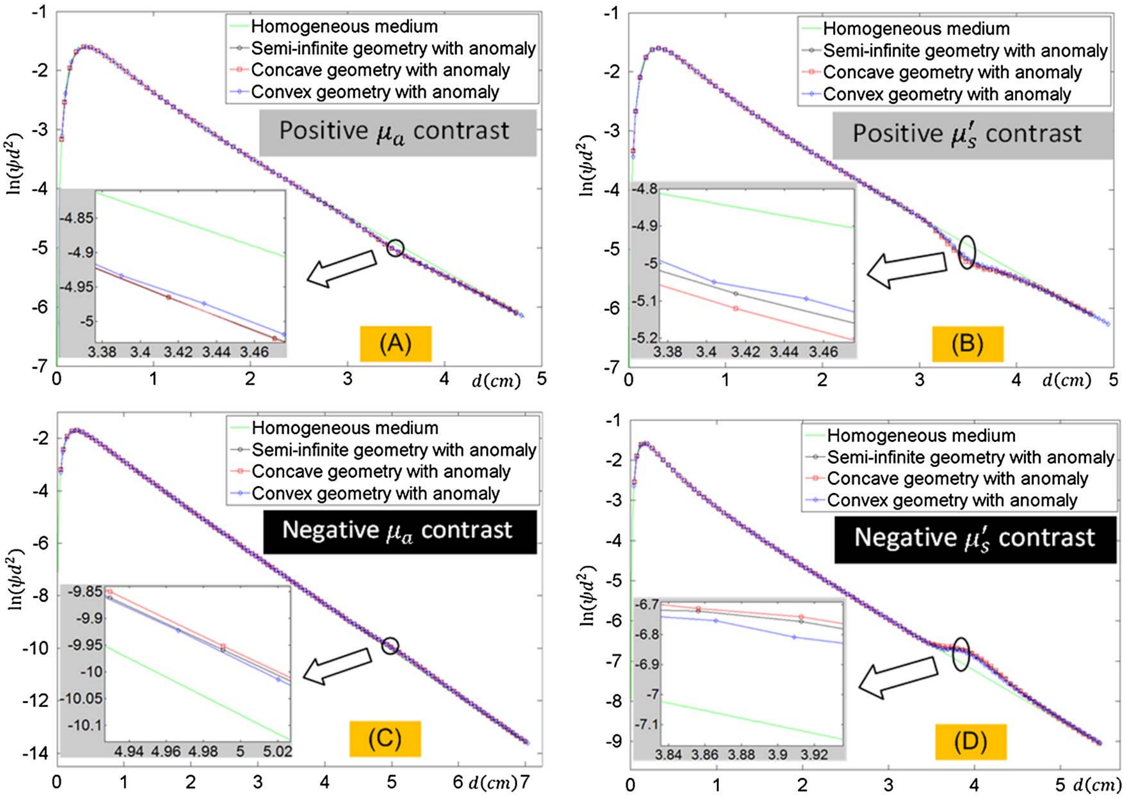

Fig. 7. (Color online) Photon fluence rate when one strong anomaly resides in the otherwise homogeneous background medium. The anomaly possesses (A) positive μ_a contrast, (B) positive μ_s' contrast, (C) negative μ_a contrast, and (D) negative μ_s' contrast over the background. The shown curves of photon fluence are plotted for (1) along a straight line on semi-infinite interface of homogeneous medium, (2) along a straight line on semi-infinite interface having the anomaly aligned with the straight line, (3) along the spiral profile on concave interface having the anomaly aligned with the spiral profile, and (4) along the spiral profile on convex interface having the anomaly aligned with the spiral profile.

imperative to examine the actual profile of spiral paths associated with different geometric and optical parameters.

Figure 8 investigates the spiral paths associated with different sets of geometric and optical parameters. Since the four limbs of the spiral paths in both concave and convex geometries are symmetric with regard to the midsagittal plane containing the source, only one quadrant of the spiral paths is to be investigated. The spiral paths found for concave geometry are grouped in the left column and for convex geometry in the right column. The set of baseline parameters are $R_0 = 1.5$ cm, $A = 1.86$, $\mu_a = 0.025\ \text{cm}^{-1}$, and $\mu_s' = 10\ \text{cm}^{-1}$, and each of the plots from 8(A) to 8(H) has one parameter differing from the baseline parameters. Specifically, 8(A) and 8(B) correspond to changing radius from 1, 1.5, to 2 cm; 8(C) and 8(D) correspond to changing the value of the A parameter from 1, 1.86, to 2.82; 8(E) and 8(F) correspond to changing μ_a from 0.025, 0.05, to 0.1 cm^{-1}; and 8(G) and 8(H) correspond to changing μ_s' from 5, 10, to 20 cm^{-1}. The most salient feature observed from Fig. 8 is that the spiral profile develops much deeper into the z direction in the convex geometry than in the concave geometry, for the otherwise identical set of parameters. The value of the A parameter seems to have little effect on the profile of spiral paths in both geometries. The spiral profile is shown to relate to other parameters; however, it is affected considerably less in convex geometry than in concave geometry.

As this study has also investigated whether the spiral paths found for the homogeneous medium specific to a given set of optical parameters would be valid for the same geometry if the medium contains heterogeneity, two observations are noted. At the macroscopic scale, the photon fluence curves for the three geometries associated with the anomaly are nearly indistinguishable from each other even for the strong anomaly considered, indicating that the spiral paths is a good approximation macroscopically. At a sufficiently detailed microscopic scale, the photon fluence curves for the three geometries associated with the anomaly do become separated; however, the photon fluence curves of the concave and convex geometries seem to locate at the opposite sides of the curve of semi-infinite geometry. As the numerical evaluation based on the analytic treatment involves summing modified Bessel functions of finite orders, and the FEM is implemented at finite resolution of the elements, limited precision is expected for the numerical results shown, as expressed by the slight oscillatory behavior of the curves associated with concave or convex geometries visible at microscopic scales. The deviation of the photon fluence curve of concave or convex geometry from that of semi-infinite geometry may be related to the slight variance of the spiral paths with respect to the actual optical properties, indicating that the spiral paths could be considered a good approximation to a straight line, but it is not identical to a straight line in semi-infinite geometry. Apparently the deviation of the photon fluence curve of concave or convex geometry from that of semi-infinite geometry is to become smaller as the radial dimension of the concave or convex applicator is to be increased.

This study examined the change to photon fluence rate along the spiral paths of concave and convex geometries

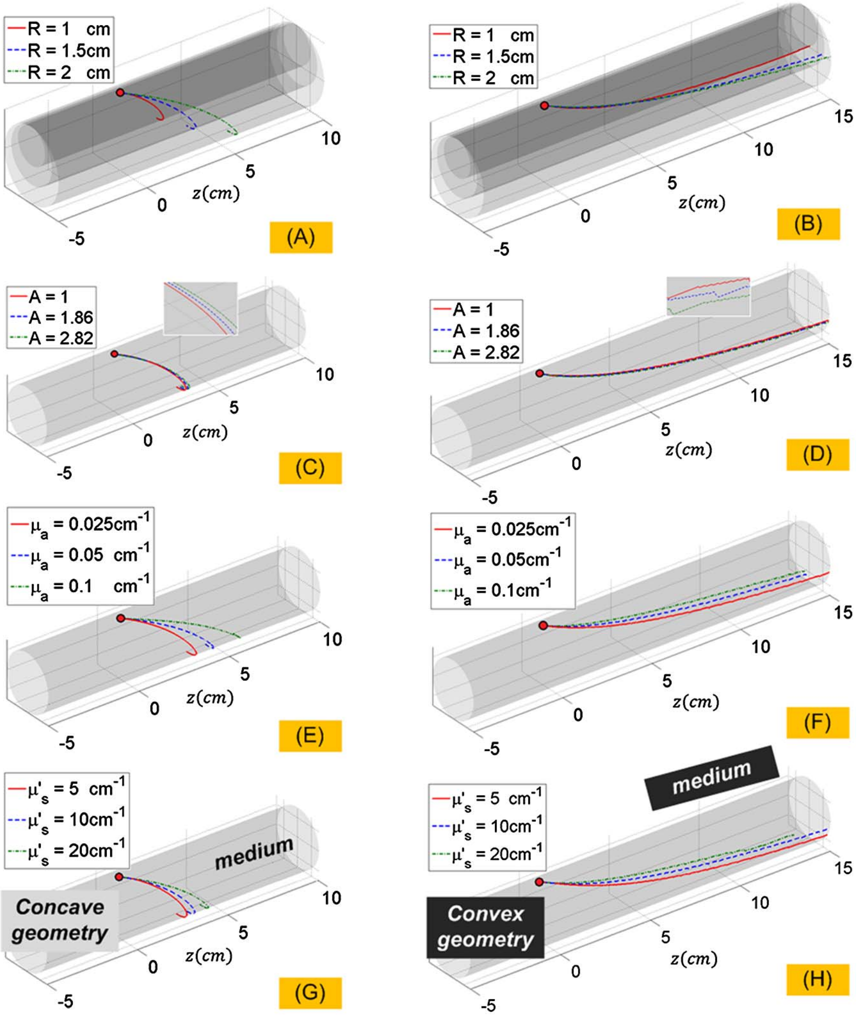

Fig. 8. (Color online) Spiral profiles of concave geometry (left column) and convex geometry (right column) found for different geometric parameters and optical properties. Each subplot illustrates the spiral profiles associated with the change of only one parameter with respect to a set of baseline parameters. The parameter to be changed in (A) and (B) is the radius of the cylindrical applicator. The parameter to be changed in (C) and (D) is the A value. The parameter to be changed in (E) and (F) is μ_a. The parameter to be changed in (G) and (H) is μ'_s.

identified for homogeneous medium cases when only one anomaly is introduced into the medium. The perturbation analysis, being linear in its nature, can in principle be applied to multiple anomalies. However, the results based on numerical implementation of the perturbation-based analytic approach will become increasingly inaccurate if anomalies with large volume or strong contrast are included owing to the nonlinearity between the photon fluence and μ_a or μ'_s. Certainly FEM would facilitate more accurate evaluation for multiple anomalies of various contrasts. This study is also specific to the case of having the only anomaly aligned azimuthally with the spiral paths. If the same anomaly is placed off from the position aligning with the spiral paths, the change to the photon fluence rate measured along the spiral paths by the anomaly is expected to be less than that shown in Figs. 5 and 7. In that case the photon fluence curves associated with the three geometries with the anomaly as studied in Figs. 4 and 6 will become less distinguishable. Therefore the approximation by spiral paths could become more accurate for an inclusion not aligned with the spiral paths than one aligned with the spiral paths.

8. CONCLUSIONS

This study continued the work of examining steady-state photon diffusion in a concave or convex geometry. The analysis in either of these two geometries has implications to diffuse optical sensing of externally applicable or internally applicable tissue medium. The study specifically complemented our previous prediction that, on the tissue-applicator interface of either concave or convex geometry there exists a unique set of spiral paths, along which the steady-state photon fluence rate decays at a rate equal to that along a straight line on a planar semi-infinite interface, for the same line-of-sight source–detector distance. This phenomenon, referred to as spiral paths, is demonstrated analytically for concave or convex geometry of large radial dimension, and numerically for concave or convex geometry of small radial dimension. This study also examined the spiral paths when the medium contained heterogeneity. Although the heterogeneity being investigated is limited to an anomaly with either positive or negative contrast of absorption or scattering coefficient over the background medium, by aligning the anomaly azimuthally with the spiral paths the anomaly has the maximum sensitivity to the change to photon fluence rate. For an anomaly of weak contrast strength the effect of it to the photon fluence rate along the spiral paths is calculated by a well-established perturbation analysis. Our revisiting of the perturbation analysis for numerical implementation in cylindrical coordinates helped identify a mistake appearing in similar analyses in some previous works. As the perturbation analysis is limited to weak-target cases, the change by an anomaly of strong contrast to the photon fluence rate along the spiral paths is instead computed by using FEM. For all investigated heterogeneous-medium cases the photon fluence rate along the homogeneous-medium associated spiral paths is macroscopically indistinguishable from that along a straight line on a semi-infinite interface, though microscopically the discrepancy is observed.

APPENDIX A: DERIVATION OF EQ. (7) FROM EQ. (6)

Equation (6) is rewritten here as

$$\Psi = \frac{S}{4\pi D}\frac{e^{-k_0 d}}{d}\left\{\left[1-\frac{1}{2}k_0 d\left(\frac{R_a^2}{d^2}-\frac{R_a}{R_0}(\cos\alpha)^2\right)\right]-\left[1-\frac{1}{2}k_0 d\left(\frac{(R_a+2R_b)^2}{d^2}+\frac{R_a+2R_b}{R_0}(\cos\alpha)^2\right)\right]\left(1+\frac{R_a+R_b}{R_0-R_a}\right)\right\}. \tag{A1}$$

Equation (A1) can be further simplified as

$$\begin{aligned}\Psi &= \frac{S}{4\pi D}\frac{e^{-k_0 d}}{d}\left[1-\frac{k_0 R_a^2}{2d}+\frac{k_0 R_a d}{2R_0}(\cos\alpha)^2-1+\frac{k_0(R_a+2R_b)^2}{2d}+\frac{k_0(R_a+2R_b)d}{2R_0}(\cos\alpha)^2-\frac{R_a+R_b}{R_0-R_a}+\frac{k_0(R_a+2R_b)^2}{2d}\frac{R_a+R_b}{R_0-R_a}\right.\\ &\quad\left.+\frac{k_0(R_a+2R_b)d}{2R_0}\frac{R_a+R_b}{R_0-R_a}(\cos\alpha)^2\right]\\ &= \frac{S}{4\pi D}\frac{e^{-k_0 d}}{d}\left[\frac{2k_0 R_b(R_a+R_b)}{d}+\frac{k_0(R_a+R_b)d}{R_0}(\cos\alpha)^2-\frac{R_a+R_b}{R_0-R_a}+\frac{k_0(R_a+2R_b)^2}{2d}\frac{R_a+R_b}{R_0-R_a}+\frac{k_0(R_a+2R_b)d}{2R_0}\frac{R_a+R_b}{R_0-R_a}(\cos\alpha)^2\right]\\ &= \frac{S}{2\pi D}\frac{e^{-k_0 d}}{d}\frac{k_0 R_b(R_a+R_b)}{d}\left[1-\frac{d}{2k_0 R_b(R_0-R_a)}+\frac{d^2}{2R_b R_0}(\cos\alpha)^2+\frac{(R_a+2R_b)d^2}{4R_b R_0(R_0-R_a)}(\cos\alpha)^2+\frac{(R_a+2R_b)^2}{4R_b(R_0-R_a)}\right].\end{aligned} \tag{A2}$$

Under the assumption that $R_0 \gg R_a, R_b, d$, based on Taylor expansion, Eq. (A2) can be approximated as

$$\Psi = \frac{S}{2\pi D}\frac{e^{-k_0 d}}{d}\frac{k_0 R_b(R_a+R_b)}{d}\exp\left\{-\frac{d}{2k_0 R_b(R_0-R_a)}+\left[\frac{d^2}{2R_b R_0}+\frac{(R_a+2R_b)d^2}{4R_b R_0(R_0-R_a)}\right](\cos\alpha)^2+\frac{(R_a+2R_b)^2}{4R_b(R_0-R_a)}\right\}. \tag{A3}$$

By multiplying both sides of Eq. (A3) with d^2, we have

$$\Psi d^2 = \frac{S}{2\pi D}k_0 R_b(R_a+R_b)e^{\frac{(R_a+2R_b)^2}{4R_b(R_0-R_a)}}\exp\left\{-k_0 d-\frac{d}{2k_0 R_b(R_0-R_a)}+\left[\frac{1}{2R_b R_0}+\frac{R_a+2R_b}{4R_b R_0(R_0-R_a)}\right](\cos\alpha)^2 d^2\right\}. \tag{A4}$$

Taking the natural logarithm, Eq. (A4) leads to

$$\ln(\Psi d^2) = -k_0 d-\frac{d}{2k_0 R_b(R_0-R_a)}+\left[\frac{1}{2R_b R_0}+\frac{R_a+2R_b}{4R_b R_0(R_0-R_a)}\right](\cos\alpha)^2 d^2+\ln\left[\frac{S}{2\pi D}k_0 R_b(R_a+R_b)\right]+\frac{(R_a+2R_b)^2}{4R_b(R_0-R_a)}. \tag{A5}$$

Taking the derivative with respect to d and substituting $d_\perp = d\cdot\cos\alpha$, Eq. (A5) leads to

$$\frac{\partial\ln(\Psi\cdot d^2)}{\partial d} = -\left\{k_0+\frac{1}{2k_0 R_b(R_0-R_a)}-\left[\frac{2R_0-R_a+2R_b}{2R_0 R_b(R_0-R_a)}\right]\cos\alpha\cdot d_\perp\right\}. \tag{A6}$$

APPENDIX B: DERIVATION OF EQ. (16) FROM EQ. (15)

Equation (15) is rewritten here as

$$\Psi = \frac{S}{4\pi D}\frac{e^{-k_0 d}}{d}\left\{\left[1-\frac{1}{2}k_0 d\left(\frac{R_a^2}{d^2}+\frac{R_a}{R_0}(\cos\alpha)^2\right)\right]-\left[1-\frac{1}{2}k_0 d\left(\frac{(R_a+2R_b)^2}{d^2}-\frac{R_a+2R_b}{R_0}(\cos\alpha)^2\right)\right]\left(1-\frac{R_a+R_b}{R_0+R_a}\right)\right\}. \tag{B1}$$

Equation (B1) can be further simplified as

$$\begin{aligned}\Psi &= \frac{S}{4\pi D}\frac{e^{-k_0 d}}{d}\left[1-\frac{k_0 R_a^2}{2d}-\frac{k_0 R_a d}{2R_0}(\cos\alpha)^2-1+\frac{k_0(R_a+2R_b)^2}{2d}-\frac{k_0(R_a+2R_b)d}{2R_0}(\cos\alpha)^2+\frac{R_a+R_b}{R_0+R_a}-\frac{k_0(R_a+2R_b)^2}{2d}\frac{R_a+R_b}{R_0+R_a}\right.\\ &\quad\left.+\frac{k_0(R_a+2R_b)d}{2R_0}\frac{R_a+R_b}{R_0+R_a}(\cos\alpha)^2\right]\\ &= \frac{S}{4\pi D}\frac{e^{-k_0 d}}{d}\left[\frac{2k_0R_b(R_a+R_b)}{d}-\frac{k_0(R_a+R_b)d}{R_0}(\cos\alpha)^2+\frac{R_a+R_b}{R_0+R_a}-\frac{k_0(R_a+2R_b)^2}{2d}\frac{R_a+R_b}{R_0+R_a}+\frac{k_0(R_a+2R_b)d}{2R_0}\frac{R_a+R_b}{R_0+R_a}(\cos\alpha)^2\right]\\ &= \frac{S}{4\pi D}\frac{e^{-k_0 d}}{d}\frac{2k_0R_b(R_a+R_b)}{d}\left[1+\frac{d}{2k_0R_b(R_0+R_a)}-\frac{d^2}{2R_bR_0}(\cos\alpha)^2+\frac{(R_a+2R_b)d^2}{4R_bR_0(R_0+R_a)}(\cos\alpha)^2-\frac{(R_a+2R_b)^2}{4R_b(R_0+R_a)}\right].\end{aligned}\tag{B2}$$

Under the assumption that $R_0 \gg R_a, R_b, d$, based on Taylor expansion, Eq. (B2) can be approximated as

$$\Psi = \frac{S}{4\pi D}\frac{e^{-k_0 d}}{d}\frac{2k_0R_b(R_a+R_b)}{d}\exp\left\{\frac{d}{2k_0R_b(R_0+R_a)}+\left[-\frac{d^2}{2R_bR_0}+\frac{(R_a+2R_b)d^2}{4R_bR_0(R_0+R_a)}\right](\cos\alpha)^2-\frac{(R_a+2R_b)^2}{4R_b(R_0+R_a)}\right\}.\tag{B3}$$

By multiplying both sides of Eq. (B3) with d^2, we have

$$\Psi d^2 = \frac{S}{2\pi D}k_0R_b(R_a+R_b)e^{-\frac{(R_a+2R_b)^2}{4R_b(R_0+R_a)}}\exp\left\{-k_0 d+\frac{d}{2k_0R_b(R_0+R_a)}+\left[-\frac{d^2}{2R_bR_0}+\frac{(R_a+2R_b)d^2}{4R_bR_0(R_0+R_a)}\right](\cos\alpha)^2\right\}.\tag{B4}$$

Taking the natural logarithm, Eq. (B4) leads to

$$\ln(\Psi d^2) = -k_0 d+\frac{d}{2k_0R_b(R_0+R_a)}+\left[-\frac{1}{2R_bR_0}+\frac{R_a+2R_b}{4R_bR_0(R_0+R_a)}\right](\cos\alpha)^2 d^2+\ln\left[\frac{S}{2\pi D}k_0R_b(R_a+R_b)\right]-\frac{(R_a+2R_b)^2}{4R_b(R_0+R_a)}.\tag{B5}$$

Taking the derivative with respect to d and substituting $d_\perp = d\cdot\cos\alpha$, Eq. (B5) leads to

$$\frac{\partial\ln(\Psi\cdot d^2)}{\partial d} = -\left\{k_0-\frac{1}{2k_0R_b(R_0+R_a)}+\left[\frac{2R_0+R_a-2R_b}{2R_0R_b(R_0+R_a)}\right]\cos\alpha\cdot d_\perp\right\}.\tag{B6}$$

APPENDIX C: DERIVATION OF EQ. (36) BY FOLLOWING THE APPROACH IN [18]

Equation (35) is rewritten here as

$$\Psi_{SC}(\vec r_d,\vec r_s) = -\frac{1}{D_0}\iiint_V G(\vec r_d,\vec r')\delta\mu_a(\vec r')\Psi_0(\vec r',\vec r_s)\mathrm{d}^3r'+\frac{1}{D_0}\iiint_V G(\vec r_d,\vec r')\nabla\cdot\{\delta D(\vec r')\nabla\Psi_0(\vec r',\vec r_s)\}\mathrm{d}^3r'.\tag{C1}$$

The second integration part can be expanded as

$$\iiint_V G(\vec r_d,\vec r')\nabla\cdot\{\delta D(\vec r)\nabla\Psi_0(\vec r,\vec r_s)\}\mathrm{d}^3r' = \iiint_V G(\vec r_d,\vec r')\nabla\delta D(\vec r)\cdot\nabla\Psi_0(\vec r,\vec r_s)\mathrm{d}^3r'+\iiint_V G(\vec r_d,\vec r')\delta D(\vec r)\nabla^2\Psi_0(\vec r,\vec r_s)\mathrm{d}^3r'.\tag{C2}$$

Applying Green's first identity $\iiint_V(\phi\nabla^2\psi+\nabla\phi\cdot\nabla\psi)\mathrm{d}^3x = \oiint_s(\phi\hat n\cdot\nabla\psi)\mathrm{d}^2a$, it can be seen that

$$\iiint_V G(\vec r_d,\vec r')\delta D(\vec r)\nabla^2\Psi_0(\vec r,\vec r_s)\mathrm{d}^3r' = \oiint_s(G(\vec r_d,\vec r')\delta D(\vec r)\hat n\cdot\nabla\Psi_0(\vec r,\vec r_s))\mathrm{d}^2a-\iiint_V\nabla[G(\vec r_d,\vec r')\delta D(\vec r)]\cdot\nabla\Psi_0(\vec r,\vec r_s)\mathrm{d}^3r'.\tag{C3}$$

The surface integral in the above derivation is eliminated because we have the freedom to choose the surface at infinity, where $G(\vec r_d,\vec r')$ decays to zero. Hence,

$$\begin{aligned}\iiint_V G(\vec r_d,\vec r')\delta D(\vec r)\nabla^2\Psi_0(\vec r,\vec r_s)\mathrm{d}^3r' &= -\iiint_V\nabla[G(\vec r_d,\vec r')\delta D(\vec r)]\cdot\nabla\Psi_0(\vec r,\vec r_s)\mathrm{d}^3r'\\ &= -\iiint_V G(\vec r_d,\vec r')\nabla\delta D(\vec r)\cdot\nabla\Psi_0(\vec r,\vec r_s)\mathrm{d}^3r'-\iiint_V\delta D(\vec r)\nabla G(\vec r_d,\vec r')\cdot\nabla\Psi_0(\vec r,\vec r_s)\mathrm{d}^3r'.\end{aligned}\tag{C4}$$

Substituting Eq. (C4) into Eq. (C2) leads to

$$\frac{1}{D_0}\iiint_V G(\vec r_d,\vec r')\nabla\cdot\{\delta D(\vec r)\nabla\Psi_0(\vec r,\vec r_s)\}\mathrm{d}^3r' = -\frac{1}{D_0}\iiint_V\delta D(\vec r)\nabla G(\vec r_d,\vec r')\cdot\nabla\Psi_0(\vec r,\vec r_s)\mathrm{d}^3r'.\tag{C5}$$

Substituting Eq. (C5) into Eq. (C1) leads to

$$\Psi_{SC}(\vec{r}_d,\vec{r}_s) = -\frac{1}{D_0}\iiint_V G(\vec{r}_d,\vec{r}')\delta\mu_a(\vec{r}')\Psi_0(\vec{r}',\vec{r}_s)\mathrm{d}^3r' - \frac{1}{D_0}\iiint_V \delta D(\vec{r}')\nabla G(\vec{r}_d,\vec{r}')\cdot\nabla\Psi_0(\vec{r}',\vec{r}_s)\mathrm{d}^3r'. \tag{C6}$$

ACKNOWLEDGMENT

This work has been supported in part by the Prostate Cancer Research Program of the U.S. Army Medical Research Acquisition Activity through grant #W81XWH-10-1-0836.

REFERENCES

1. A. Ishimaru, "Diffusion of light in turbid material," Appl. Opt. **28**, 2210–2215 (1989).
2. W. Jost, "Diffusion and electrolytic conduction in crystals (ionic semiconductors)," J. Chem. Phys. **1**, 466–475 (1933).
3. A. M. Weinberg and E. P. Wigner, *The Physical Theory of Neutron Chain Reactors* (University of Chicago Press, 1958).
4. D. L. Cummings, R. L. Reuben, and D. A. Blackburn, "The effect of pressure modulation on the flow of gas through a solid membrane: permeation and diffusion of hydrogen through nickel," Metall. Trans. A **15**, 639–648 (1984).
5. L. B. Felsen and N. Marcuvitz, *Radiation and Scattering of Waves* (Prentice-Hall, 1973).
6. E. A. Mason, R. J. Munn, and F. J. Smith, "Thermal diffusion in gases," in *Advances in Atomic and Molecular Physics* (Academic, 1966), pp. 33–91.
7. W. K. Hocking, S. Fukao, M. Yamamoto, T. Tsuda, and S. Kato, "Viscosity waves and thermal-conduction waves as a cause of 'specular' reflectors in radar studies of the atmosphere," Radio Sci. **26**, 1281–1303 (1991).
8. A. Mandelis, *Diffusion-Wave Fields: Mathematical Methods and Green Functions* (Springer-Verlag, 2001).
9. S. R. Arridge, M. Cope, and D. T. Delpy, "The theoretical basis for the determination of optical pathlengths in tissue: temporal and frequency analysis," Phys. Med. Biol. **37**, 1531–1560 (1992).
10. R. L. Barbour, H. Graber, R. Aronson, and J. Lubowsky, "Model for 3-D optical imaging of tissue," *Remote Sensing Science for the Nineties, IGARSS '90*, 1395–1399 (1990). http://ieeexplore.ieee.org/xpl/freeabs_all.jsp?isNumber=3531&arNumber=688761&isnumber=3531&arnumber=688761&tag=1
11. S. R. Arridge, M. Schweiger, M. Hiraoka, and D. T. Delpy, "A finite element approach for modeling photon transport in tissue," Med. Phys. **20**, 299–309 (1993).
12. A. H. Hielscher, R. E. Alcouffe, and R. L. Barbour, "Comparison of finite-difference transport and diffusion calculations for photon migration in homogeneous and heterogeneous tissues," Phys. Med. Biol. **43**, 1285–1302 (1998).
13. S. J. Madsen, B. C. Wilson, M. S. Patterson, Y. D. Park, S. L. Jacques, and Y. Hefetz, "Experimental tests of a simple diffusion model for the estimation of scattering and absorption coefficients of turbid media from time-resolved diffuse reflectance measurements," Appl. Opt. **31**, 3509–3517 (1992).
14. S. Fantini, M. A. Franceschini, and E. Gratton, "Semi-infinite-geometry boundary problem for light migration in highly scattering media: a frequency-domain study in the diffusion approximation," J. Opt. Soc. Am. B **11**, 2128–2138 (1994).
15. A. Zhang, D. Piao, C. F. Bunting, and B. W. Pogue, "Photon diffusion in a homogeneous medium bounded externally or internally by an infinitely long circular cylindrical applicator. I. Steady-state theory," J. Opt. Soc. Am. A **27**, 648–662 (2010).
16. A. Zhang, G. Xu, C. Daluwatte, G. Yao, C. F. Bunting, B. W. Pogue, and D. Piao, "Photon diffusion in a homogeneous medium bounded externally or internally by an infinitely long circular cylindrical applicator. II. Quantitative examinations of the steady-state theory," J. Opt. Soc. Am. A **28**, 66–75 (2011).
17. A. Zhang, D. Piao, G. Yao, C. F. Bunting, and Y. Jiang, "Diffuse photon remission along unique spiral paths on a cylindrical interface is modeled by photon remission along a straight line on a semi-infinite interface," Opt. Lett. **36**, 654–656 (2011).
18. S. R. Arridge, P. van der Zee, M. Cope, and D. T. Delpy, "Reconstruction methods for infra-red absorption imaging," Proc. SPIE **1431**, 204–215 (1991).
19. M. A. O'Leary, D. A. Boas, B. Chance, and A. G. Yodh, "Experimental images of heterogeneous turbid media by frequency-domain diffusing-photon tomography," Opt. Lett. **20**, 426–428 (1995).
20. L. V. Wang and H. Wu, *Biomedical Optics, Principles and Imaging* (Wiley, 2007).
21. H. Dehghani, M. E. Eames, P. K. Yalavarthy, S. C. Davis, S. Srinivasan, C. M. Carpenter, B. W. Pogue, and K. D. Paulsen, "Near infrared optical tomography using NIRFAST: algorithm for numerical model and image reconstruction," Commun. Numer. Methods Eng. **25**, 711–732 (2009).

Photon diffusion in a homogeneous medium bounded externally or internally by an infinitely long circular cylindrical applicator. IV. Frequency-domain analysis

Anqi Zhang and Daqing Piao*

School of Electrical and Computer Engineering, Oklahoma State University, Stillwater, Oklahoma 74078, USA
**Correspondence: daqing.piao@okstate.edu*

Received March 6, 2012; revised May 11, 2012; accepted May 14, 2012;
posted May 16, 2012 (Doc. ID 164299); published June 29, 2012

Part IV examines frequency-domain photon diffusion in a homogeneous medium enclosed by a "concave" circular cylindrical applicator or enclosing a "convex" circular cylindrical applicator, both geometries being infinite in the longitudinal dimension. The aim is to assess by analogical and finite-element methods the changes of AC amplitude, modulation depth, and phase with respect to the line-of-sight source–detector distance for a source and a detector located along the azimuthal or longitudinal direction on the concave or convex medium–applicator interface. By comparing to their counterparts along a straight line on a semi-infinite medium–applicator interface, for the same line-of-sight source–detector distance, it is found that: (1) the decay-rate of AC photon fluence is smaller along the azimuthal direction and greater along the longitudinal direction on the concave interface, (2) the decay-rate of AC photon fluence is greater along the azimuthal direction and smaller along the longitudinal direction on the convex interface, (3) the modulation depth along both azimuthal and longitudinal directions decays more slowly on the concave interface and faster on the convex interface, and (4) the phase along both azimuthal and longitudinal directions increases more slowly on the concave interface and faster on the convex interface.

OCIS codes: 170.3660, 170.5280, 170.6960.

1. INTRODUCTION

Modeling optical imaging of biological tissue located centimeters deep involves diffusion approximation to the radiative transport [1]. Although the semi-infinite geometry specific to placing the optodes on a planar medium–applicator interface is most widely studied, other geometries with the optodes on curved medium–applicator interface could be more relevant to imaging applications [2]. A "concave" geometry may resemble probing the diffusive medium at the "recessing" side of the cylindrical applicator, and a "convex" imaging geometry may represent probing the diffusive medium at the "bulging" side of the cylindrical applicator [3]. For the semi-infinite geometry with a homogeneous medium, the analytic solution to the photon diffusion is well studied [4] and has been applied widely to analyzing raw data measured from surface tissue applicators and for image reconstruction. For "concave" medium–applicator geometry there is a noticeable amount of studies of diffuse photon propagation within the geometry. Arguably all these approaches were based on the same methodology, i.e., the analytical Green's function is derived in the form of a sum of two terms that contain the analytical solution in the infinite medium plus a particular solution, specifically the one corresponding to an "image" source, allowing the global solution to satisfy the boundary condition. In terms of frequency-domain (FD) modeling, Arridge *et al.* [5] applied zero fluence boundary condition to derive the solutions for finite-length and infinite-length "concave" cylinder geometries, using Green's functions as well as their Laplace transforms similar to those demonstrated by Carslaw and Jaeger on heat conduction [6]. Pogue and Patterson [7] used the extrapolated boundary condition, which is considered more accurate than zero-boundary condition for tissue–applicator interface [8,9], to derive the solutions for a finite-length "concave" cylinder geometry. Da Silva *et al.* [10] also employed extrapolated boundary condition to study photon diffusion in finite-length "concave" cylindrical geometries. Recently, Liemert and Kienle [11,12] employed finite Hankel and cosine transforms to reach a solution of FD photon diffusion in the medium bounded by single or multilayered infinitely long "concave" cylinder. However, there is a lack of understanding regarding FD photon diffusion associated with "convex" medium–applicator geometry.

In the Part I study [13], we developed a theoretical framework to unify the treatment of continuous-wave (CW) photon remission on the medium–applicator interface of both "concave" and "convex" geometries with infinite longitudinal dimension. Solutions to the CW photon diffusion in the two geometries were derived based on the extrapolated boundary condition and expressed in terms of the first and second kinds of the modified Bessel functions. In the Part II study [14], the validity of the analytic treatment of Part I [13] in the diffusion regime was examined by means including finite-element method (FEM), Monte Carlo modeling, and experiments. It was found that in both "concave" and "convex" geometries the changes of CW photon fluence along the azimuthal and longitudinal directions showed opposite trends, in terms of the decay rate versus the line-of-sight source–detector distance with respect to that along a straight line on a semi-infinite medium–applicator interface for the same line-of-sight source–detector distance. It was predicted [14] and subsequently outlined in [15] and detailed in Part III [16] that there was a unique set of spiral paths on the medium–applicator interface in both concave and convex geometries of infinite longitudinal dimension, along which the decay-rate of CW photon fluence could be identical to that along a straight line on the semi-infinite medium–applicator interface, given the same line-of-sight source–detector distance and the same set of optical properties.

In this Part IV study, the methodology introduced in Part I for analysis of CW photon diffusion is extended to formulate a unified analysis of FD photon diffusion in both concave and convex geometries of infinite longitudinal dimension. Section 2 reviews the FD photon diffusion for infinite and semi-infinite geometries expressed in both spherical and cylindrical coordinates. Section 3 develops the cylindrical-coordinate solutions to FD photon diffusion in both "concave" and "convex" geometries, respectively. Section 4 generalizes the characteristics of FD photon diffusion along the azimuthal and longitudinal directions in concave and convex geometries, by assuming a large radius of the cylinder geometry that renders analytical approximations to be made. Section 5 presents numerical evaluations of FD photon fluence along the azimuthal and longitudinal directions with respect to the source–detector distance for concave and convex geometries of practical centimeter-order radius, based on FEM and analytical results. We demonstrate that the aforementioned spiral paths exist for the amplitude of AC fluence rate as well; however, they do not coincide with those for DC fluence rate. As long as the modulation depth and phase are concerned, no such spiral paths can be inferred.

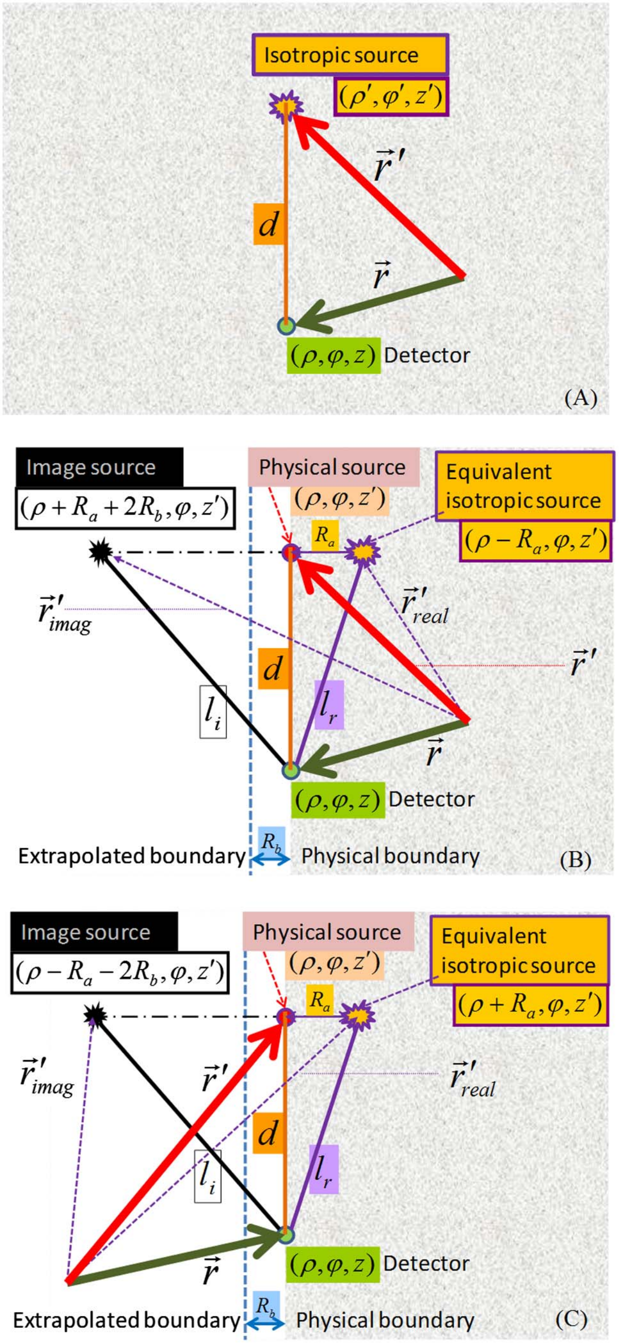

Fig. 1. (Color online) Illustrations of a medium of infinite geometry in (A) and a medium of semi-infinite geometry in (B) and (C). In the semi-infinite geometry the source and detector are positioned on the physical boundary of the medium, and it becomes convenient to assign the same radial and azimuthal coordinates to the source and detector.

2. FD ANALYSIS FOR INFINITE AND SEMI-INFINITE GEOMETRIES—RECOUNTING

We consider a scattering dominant medium with a diffusion coefficient $D = [3(\mu_a + \mu_s')]^{-1}$, where μ_a is the absorption coefficient and μ_s' is the reduced scattering coefficient. The locations of a detector $\vec{r}$ and a source $\vec{r}'$ are represented in cylindrical coordinates by (ρ, φ, z) and (ρ', φ', z'), respectively, for all medium geometries investigated in this study. A medium of infinite geometry is illustrated in Fig. 1(A), wherein the source is regarded as isotropic. A medium of semi-infinite geometry with the source and the detector located on the medium boundary is depicted in Fig. 1(B) for the coordinate origin located at the medium side or in Fig. 1(C) for the coordinate origin located at the opposite to the medium side. In the semi-infinite geometry, the source $\vec{r}'(\rho', \varphi', z')$ launches photon into the medium at an initial direction orthogonal to the medium–applicator interface and is represented by an equivalent "real" isotropic source at $\vec{r}'_{\text{real}}(\rho - R_a, \varphi, z')$ in Fig. 1(B) or $\vec{r}'_{\text{real}}(\rho + R_a, \varphi, z')$ in Fig. 1(C), where $R_a = 1/\mu_s'$ is the step size of transport scattering. The effect of medium–applicator interface on photon diffusion may be modeled by setting zero the photon fluence rate on an extrapolated boundary located $R_b = 2AD$ away from the physical boundary, where $A = (1 + R_{\text{eff}})/(1 - R_{\text{eff}})$, and R_{eff} is a coefficient [8,9] determined by the refractive index differences across the physical boundary. This boundary condition is accommodated by setting a negative "image" source of the "real" isotropic source, with respect to the extrapolated boundary, at $\vec{r}'_{\text{imag}}(\rho + R_a + 2R_b, \varphi, z')$ in Fig. 1(B) or $\vec{r}'_{\text{imag}}(\rho - R_a - 2R_b, \varphi, z')$ in Fig. 1(C). The distances from the detector to the "real" isotropic source $\vec{r}'_{\text{real}}$ and the "image" source $\vec{r}'_{\text{imag}}$ are denoted by l_r and l_i, respectively. The notations of l_r and l_i also apply to other studied medium geometries involving a boundary. In all studied geometries, the straight distance between the source and the detector, i.e., $d = |\vec{r} - \vec{r}'|$, is referred to as the "line-of-sight" source–detector distance, with respect to which the changing characteristics of photo fluence rate Ψ are to be evaluated among different geometries. Hereafter the "source–detector distance" stands for line-of-sight source–detector distance.

A FD source at $\vec{r}'$ is expressed as $S(\vec{r}', t) = \bar{S}(\vec{r}') + \tilde{S}(\vec{r}') \exp(i\omega t)$, where the overhead notations "–" and "~" represent DC and AC components, respectively, and ω is the angular frequency. Then the FD photon fluence rate at $\vec{r}$ is expressed by $\Psi(\vec{r}, t) = \bar{\Psi}(\vec{r}) + \tilde{\Psi}(\vec{r}) \exp(i\omega t)$. For a homogeneous medium, we have the following photon diffusion equations [1,2,4–9]:

$$\nabla^2\bar{\Psi}(\vec{r}) - \bar{k}_0\bar{\Psi}(\vec{r}) = -\frac{\bar{S}(\vec{r})}{D}; \qquad \nabla^2\tilde{\Psi}(\vec{r}) - \tilde{k}_0\tilde{\Psi}(\vec{r}) = -\frac{\tilde{S}(\vec{r})}{D}, \tag{2.0.1}$$

where $\bar{k}_0$ and $\tilde{k}_0$ are the effective attenuation coefficients of the medium to the DC and AC components, respectively, of photon fluence rate as

$$\bar{k}_0 = \sqrt{\frac{\mu_a}{D}}; \qquad \tilde{k}_0 = \tilde{k}_{\mathrm{amp}} + j\tilde{k}_{\mathrm{phi}} = \sqrt{\frac{\mu_a}{D} + \frac{i\omega}{Dc}}, \tag{2.0.2}$$

with c being the speed of light in the medium, and

$$\tilde{k}_{\mathrm{amp}} = \bar{k}_0\sqrt{\frac{1}{2}\left(\sqrt{1 + \left(\frac{\omega}{c\mu_a}\right)^2} + 1\right)};$$
$$\tilde{k}_{\mathrm{phi}} = \bar{k}_0\sqrt{\frac{1}{2}\left(\sqrt{1 + \left(\frac{\omega}{c\mu_a}\right)^2} - 1\right)} \tag{2.0.3}$$

A. Solutions in Spherical Coordinates to FD Photon Diffusion

1. *Source and Detector in an Infinite Medium Geometry*

For a source and a detector in a homogeneous medium of infinite geometry, the solutions to Eqs. (2.0.1) in spherical-coordinates are well-known to be

$$\bar{\Psi}_{\mathrm{inf}}\left(\vec{r}, \vec{r}'\right) = \frac{\bar{S}}{4\pi D}\frac{1}{|\vec{r} - \vec{r}'|}\exp\left(-\bar{k}_0|\vec{r} - \vec{r}'|\right), \tag{2.1.1.DC}$$

$$\tilde{\Psi}_{\mathrm{inf}}(\vec{r}, \vec{r}\prime) = \frac{\tilde{S}}{4\pi D}\frac{1}{|\vec{r} - \vec{r}'|}\exp\left(-\tilde{k}_{\mathrm{amp}}|\vec{r} - \vec{r}'|\right)\exp\left(-i\tilde{k}_{\mathrm{phi}}|\vec{r} - \vec{r}'|\right). \tag{2.1.1.AC}$$

2. *Source and Detector on a Semi-Infinite Medium–Applicator Interface*

For a source and a detector located on a semi-infinite boundary to a homogeneous medium, the solutions to Eqs. (2.0.1) in spherical coordinates may be derived based on the aforementioned extrapolated boundary condition as

$$\begin{aligned}\bar{\Psi}_{\mathrm{semi}} &= \bar{\Psi}_{\mathrm{real}}\left(\vec{r}, \vec{r}'_{\mathrm{real}}\right) + \bar{\Psi}_{\mathrm{imag}}\left(\vec{r}, \vec{r}'_{\mathrm{imag}}\right)\\ &= \frac{\bar{S}}{4\pi Dl_r}\exp\left(-\bar{k}_0 l_r\right) - \frac{\bar{S}}{4\pi Dl_i}\exp\left(-\bar{k}_0 l_i\right),\end{aligned} \tag{2.1.2.DC}$$

$$\begin{aligned}\tilde{\Psi}_{\mathrm{semi}} &= \tilde{\Psi}_{\mathrm{real}}\left(\vec{r}, \vec{r}'_{\mathrm{real}}\right) + \tilde{\Psi}_{\mathrm{imag}}\left(\vec{r}, \vec{r}'_{\mathrm{imag}}\right)\\ &= \frac{\tilde{S}}{4\pi Dl_r}\exp\left(-\tilde{k}_0 l_r\right) - \frac{\tilde{S}}{4\pi Dl_i}\exp\left(-\tilde{k}_0 l_i\right),\end{aligned} \tag{2.1.2.AC}$$

where we have

$$l_r = \sqrt{d^2 + R_a^2}; \qquad l_i = \sqrt{d^2 + (R_a + 2R_b)^2}, \tag{2.1.3}$$

as shown in Figs. 1(B) and 1(C). For the condition of $d \gg R_a, R_b$, Eq. (2.1.2) are approximated to

$$\bar{\Psi}_{\mathrm{semi}} = \frac{\bar{S}}{2\pi D}\left[\frac{1}{d^2}\exp(-\bar{k}_0 d)\right]\bar{k}_0 R_b(R_a + R_b), \tag{2.1.4.DC}$$

$$\begin{aligned}\tilde{\Psi}_{\mathrm{semi}} = {}& \frac{\tilde{S}}{2\pi D}\left[\frac{1}{d^2}\exp(-\tilde{k}_{\mathrm{amp}} d)\right]\left[\tilde{k}_{\mathrm{amp}} R_b(R_a + R_b)\right]\sqrt{1 + \left(\frac{\tilde{k}_{\mathrm{phi}}}{\tilde{k}_{\mathrm{amp}}}\right)^2}\\ &\times\exp\left\{-i\left[\tilde{k}_{\mathrm{phi}} d - \tan^{-1}\left(\frac{\tilde{k}_{\mathrm{phi}}}{\tilde{k}_{\mathrm{amp}}}\right)\right]\right\}.\end{aligned} \tag{2.1.4.AC}$$

B. Solutions in Cylindrical Coordinates to FD Photon Diffusion

1. *Source and Detector in an Infinite Medium Geometry*

The cylindrical-coordinate solution to the DC photon fluence rate associated with a source–detector pair in a homogeneous medium of infinite geometry has been solved in Part I [13] as follows:

$$\begin{aligned}\bar{\Psi}_{\mathrm{inf}}\left(\vec{r}, \vec{r}'\right) = {}& \frac{\bar{S}}{4\pi^2 D}\int_{-\infty}^{\infty} dk e^{ik(z-z')}\sum_{m=-\infty}^{\infty} I_m\left(\bar{k}_{\mathrm{eff}}\,\rho_<\right)\\ &\times K_m\left(\bar{k}_{\mathrm{eff}}\,\rho_>\right)e^{im(\varphi-\varphi')},\end{aligned} \tag{2.2.1.DC}$$

where I_m and K_m are the modified Bessel functions of the first and the second kinds, respectively,

$$\bar{k}_{\mathrm{eff}} = \sqrt{k^2 + \bar{k}_0^2}, \tag{2.2.2.DC}$$

and $\rho_<$ and $\rho_>$ indicate the smaller and larger radial coordinates of the source and the detector, respectively. Note that the format of $\bar{\Psi}_{\mathrm{inf}}(\vec{r}, \vec{r}')$ in Eq. (2.2.1.DC) is slightly different from the corresponding one in Eq. (2.1.13) in [13], in terms of the lower limits of the integration and the summation as well as the number in the denominator to the source term $\bar{S}$, as a result of using exponential terms with complex arguments versus using cosine terms only.

Based on the similarity between the DC and AC counterparts in Eqs. (2.0.1), one would appreciate that the cylindrical-coordinate solution to AC photon fluence rate in a homogeneous medium of infinite geometry must have a form similar to that of Eq. (2.2.1.DC) as

$$\tilde{\Psi}_{\mathrm{inf}}\left(\vec{r},\vec{r}'\right)=\frac{\tilde{S}}{4\pi^2 D}\int_{-\infty}^{\infty}dk e^{ik(z-z')}\sum_{m=-\infty}^{\infty}I_m\left(\tilde{k}_{\mathrm{eff}}\,\rho_<\right)\times K_m\left(\tilde{k}_{\mathrm{eff}}\,\rho_>\right)e^{im(\varphi-\varphi')}, \tag{2.2.1.AC}$$

where.

$$\tilde{k}_{\mathrm{eff}}=\sqrt{k^2+\tilde{k}_0^2}. \tag{2.2.2.AC}$$

According to Part I [13] and Jackson [17], the cylindrical-coordinates representation of $\bar{\Psi}_{\mathrm{inf}}(\vec{r},\vec{r}')$ in Eq. (2.2.1.DC) and the spherical-coordinate representation of $\tilde{\Psi}_{\mathrm{inf}}(\vec{r},\vec{r}')$ in Eq. (2.1.1.DC) are analytically identical. The said identity was also tested numerically in [13]. Similarly, we maintain that the cylindrical-coordinate representation of $\tilde{\Psi}_{\mathrm{inf}}(\vec{r},\vec{r}')$ in Eq. (2.2.1.AC) and the spherical-coordinates representation of $\tilde{\Psi}_{\mathrm{inf}}(\vec{r},\vec{r}')$ in Eq. (2.1.1.AC) are analytically identical and thereby interchangeable.

2. Source and Detector on a Semi-Infinite Medium–Applicator Interface

For completeness, we consider the cylindrical-coordinate solutions to photon diffusion in a homogeneous medium of semi-infinite geometry as that illustrated in Fig. 1(B). Between the radial coordinates of the detector $\vec{r}$ and the "real" isotropic source $\vec{r}'_{\mathrm{real}}$ we have $\rho_< = \rho - R_a$ and $\rho_> = \rho$. Between the radial coordinates of the detector $\vec{r}$ and the "image" source $\vec{r}'_{\mathrm{imag}}$ we have $\rho_< = \rho$ and $\rho_> = \rho + R_a + 2R_b$. Based on Eq. (2.1.2) and the interchangeability between Eqs. (2.2.1) and (2.1.1), the DC photon fluence rate at $\vec{r}$ due to $\vec{r}'_{\mathrm{real}}$ and $\vec{r}'_{\mathrm{imag}}$ may be expressed by

$$\begin{aligned}\bar{\Psi}_{\mathrm{semi}}&=\bar{\Psi}_{\mathrm{real}}\left(\vec{r},\vec{r}'_{\mathrm{real}}\right)+\bar{\Psi}_{\mathrm{imag}}\left(\vec{r},\vec{r}'_{\mathrm{imag}}\right)\\&=\frac{\bar{S}}{4\pi^2 D}\left\{\int_{-\infty}^{\infty}dk e^{ik(z-z'_{\mathrm{real}})}\sum_{m=-\infty}^{\infty}I_m\left[\bar{k}_{\mathrm{eff}}(\rho-R_a)\right]\right.\\&\quad\times K_m\left(\bar{k}_{\mathrm{eff}}\rho\right)e^{im(\varphi-\varphi'_{\mathrm{real}})}-\int_{-\infty}^{\infty}dk e^{ik(z-z'_{\mathrm{imag}})}\sum_{m=-\infty}^{\infty}I_m\left(\bar{k}_{\mathrm{eff}}\rho\right)\\&\quad\left.\times K_m\left[\bar{k}_{\mathrm{eff}}(\rho+R_a+2R_b)\right]e^{im(\varphi-\varphi'_{\mathrm{imag}})}\right\}\end{aligned} \tag{2.2.3.DC}$$

and accordingly the AC photon fluence rate by

$$\begin{aligned}\tilde{\Psi}_{\mathrm{semi}}&=\tilde{\Psi}_{\mathrm{real}}\left(\vec{r},\vec{r}'_{\mathrm{real}}\right)+\tilde{\Psi}_{\mathrm{imag}}\left(\vec{r},\vec{r}'_{\mathrm{imag}}\right)\\&=\frac{\tilde{S}}{4\pi^2 D}\left\{\int_{-\infty}^{\infty}dk e^{ik(z-z'_{\mathrm{real}})}\sum_{m=-\infty}^{\infty}I_m\left[\tilde{k}_{\mathrm{eff}}(\rho-R_a)\right]\right.\\&\quad\times K_m\left(\tilde{k}_{\mathrm{eff}}\rho\right)e^{im(\varphi-\varphi'_{\mathrm{real}})}\\&\quad-\int_{-\infty}^{\infty}dk e^{ik(z-z'_{\mathrm{imag}})}\sum_{m=-\infty}^{\infty}I_m\left(\tilde{k}_{\mathrm{eff}}\rho\right)\\&\quad\left.\times K_m\left[\tilde{k}_{\mathrm{eff}}(\rho+R_a+2R_b)\right]e^{im(\varphi-\varphi'_{\mathrm{imag}})}\right\}.\end{aligned} \tag{2.2.3.AC}$$

Alternatively, if the semi-infinite geometry is coordinated as the one in Fig. 1(C), we have

$$\begin{aligned}\bar{\Psi}_{\mathrm{semi}}&=\frac{\bar{S}}{4\pi^2 D}\left\{\int_{-\infty}^{\infty}dk e^{ik(z-z'_{\mathrm{real}})}\sum_{m=-\infty}^{\infty}I_m(\bar{k}_{\mathrm{eff}}\rho)\right.\\&\quad\times K_m\left[\bar{k}_{\mathrm{eff}}(\rho+R_a)\right]e^{im(\varphi-\varphi'_{\mathrm{real}})}-\int_{-\infty}^{\infty}dk e^{ik(z-z'_{\mathrm{imag}})}\\&\quad\times\sum_{m=-\infty}^{\infty}I_m\left[\bar{k}_{\mathrm{eff}}(\rho-R_a-2R_b)\right]\\&\quad\left.\times K_m\left(\bar{k}_{\mathrm{eff}}\rho\right)e^{im(\varphi-\varphi'_{\mathrm{imag}})}\right\}\end{aligned} \tag{2.2.3.DC*}$$

$$\begin{aligned}\tilde{\Psi}_{\mathrm{semi}}&=\frac{\tilde{S}}{4\pi^2 D}\left\{\int_{-\infty}^{\infty}dk e^{ik(z-z'_{\mathrm{real}})}\sum_{m=-\infty}^{\infty}I_m\left(\tilde{k}_{\mathrm{eff}}\rho\right)\right.\\&\quad\times K_m\left[\tilde{k}_{\mathrm{eff}}(\rho+R_a)\right]e^{im(\varphi-\varphi'_{\mathrm{real}})}-\int_{-\infty}^{\infty}dk e^{ik(z-z'_{\mathrm{imag}})}\\&\quad\times\sum_{m=-\infty}^{\infty}I_m\left[\tilde{k}_{\mathrm{eff}}(\rho-R_a-2R_b)\right]\\&\quad\left.\times K_m(\tilde{k}_{\mathrm{eff}}\rho)e^{im(\varphi-\varphi'_{\mathrm{imag}})}\right\}.\end{aligned} \tag{2.2.3.AC*}$$

3. FD ANALYSIS OF PHOTON DIFFUSION ASSOCIATED WITH "CONCAVE" AND "CONVEX" GEOMETRIES OF INFINITE LONGITUDINAL DIMENSION

A. Concave Geometry

The "concave" geometry as shown in Fig. 2(A) refers to a diffusive medium enclosed by an infinitely long cylindrical medium–applicator interface [13,14,16]. Given the radius of the cylinder as R_0, a detector $\vec{r}$ on the medium–applicator interface locates at (R_0,φ,z), and a directional source $\vec{r}'$ on the medium–applicator interface locates at (R_0,φ',z'). Based on the symmetry of the concave geometry, the directional source $\vec{r}'$ is to be modeled by a "real" isotropic source $\vec{r}'_{\mathrm{real}}$ located along the radial direction of the physical source and inwardly at a distance of $R_a = 1/\mu'_s$, i.e., at $(R_0 - R_a, \varphi', z')$. The extrapolated boundary is concentric with and at a radial distance of $R_b = 2AD$ away from the physical boundary [8,13]. Apparently as the radius R_0 reaches infinity the photon fluence rate associated with a source–detector pair on the medium–applicator interface of the concave geometry approaches that on the associated semi-infinite interface that is tangential to the concave interface at the source position, for the same source-detector distance. This characteristic serves as both the qualitative and quantitative calibers of the analytic solutions derived for the concave geometry.

Considering that Eqs. (2.2.1.DC) and (2.2.1.AC) are identical in their analytical forms except for the notations differentiating "DC" and "AC," the cylindrical-coordinate solutions to FD photon diffusion associated with optodes on the concave medium–applicator interface can be derived by following the approaches to the corresponding CW photon diffusion demonstrated in Part I [13]. The resulted DC photon fluence rate sensed by the detector $\vec{r}$ on the physical boundary of the concave geometry due to the physical source $\vec{r}'$ is

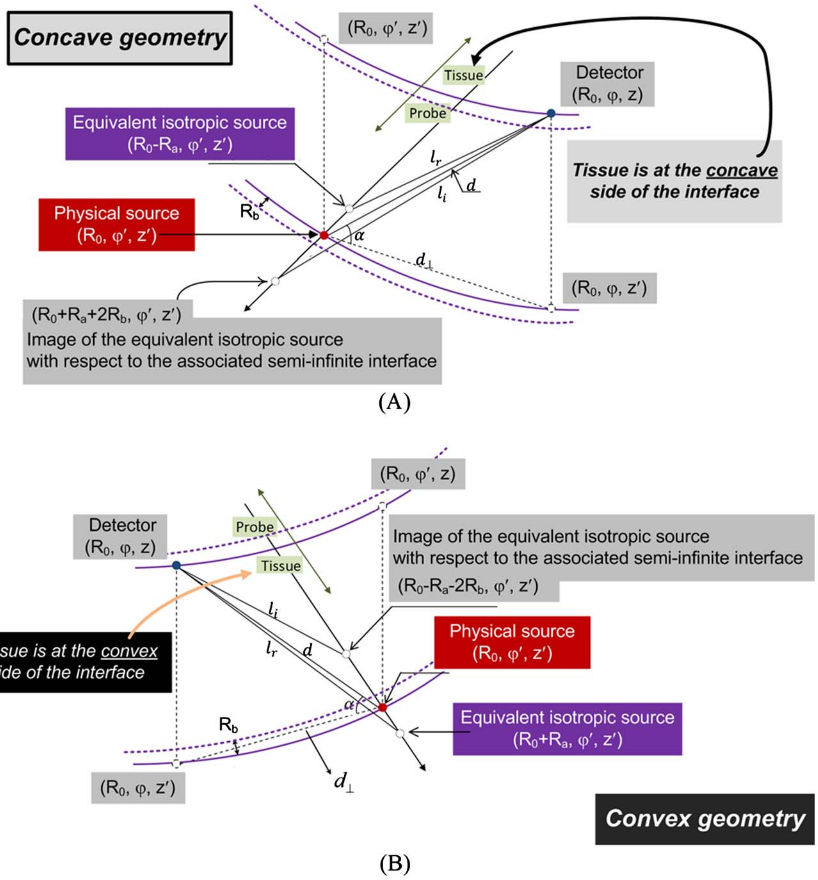

Fig. 2. (Color online) Configurations of (A) concave geometry and (B) convex geometry. The physical directional source and detector locate at the probe–tissue interface at (R_0, φ', z') and (R_0, φ, z) respectively. In concave geometry, the equivalent isotropic source locates inwardly at $(R_0 - R_a, \varphi', z')$. The image of the source with respect to the associated semi-infinite geometry locates at $(R_0 + R_a + 2R_b, \varphi', z')$. In convex geometry, the equivalent isotropic source locates outwardly at $(R_0 + R_a, \varphi', z')$. The image of the source with respect to the associated semi-infinite geometry locates at $(R_0 - R_a - 2R_b, \varphi', z')$.

$$\bar{\Psi}_{\text{conC}} = \frac{\bar{S}}{4\pi^2 D}\int_{-\infty}^{\infty} dk \left\{ \exp[ik(z-z')] \sum_{m=-\infty}^{\infty} I_m\left[\bar{k}_{\text{eff}}(R_0-R_a)\right] \times K_m\left(\bar{k}_{\text{eff}}R_0\right)\left\langle 1 - \frac{I_m(\bar{k}_{\text{eff}}R_0)}{K_m(\bar{k}_{\text{eff}}R_0)}\frac{K_m[\bar{k}_{\text{eff}}(R_0+R_b)]}{I_m[\bar{k}_{\text{eff}}(R_0+R_b)]}\right\rangle \times \exp[im(\varphi-\varphi')]\right\}, \tag{3.1.1.DC}$$

which has a slightly different format comparing to Eq. (3.1.5) in Part-I, and its AC counterpart is

$$\tilde{\Psi}_{\text{conC}} = \frac{\tilde{S}}{4\pi^2 D}\int_{-\infty}^{\infty} dk \left\{ \exp[ik(z-z')] \sum_{m=-\infty}^{\infty} I_m[\tilde{k}_{\text{eff}}(R_0-R_a)] \times K_m(\tilde{k}_{\text{eff}}R_0)\left\langle 1 - \frac{I_m(\tilde{k}_{\text{eff}}R_0)}{K_m(\tilde{k}_{\text{eff}}R_0)}\frac{K_m[\tilde{k}_{\text{eff}}(R_0+R_b)]}{I_m[\tilde{k}_{\text{eff}}(R_0+R_b)]}\right\rangle \times \exp[im(\varphi-\varphi')]\right\}. \tag{3.1.1.AC}$$

B. Convex Geometry

The "convex" geometry as shown in Fig. 2(B) refers to a diffusive medium enclosing an infinitely long cylindrical medium–applicator interface [13,14,16]. Given the radius of the cylinder as R_0, a detector $\vec{r}$ on the medium–applicator interface locates at (R_0, φ, z), and a directional source $\vec{r}'$ on the medium–applicator interface locates at (R_0, φ', z'). Based on the symmetry of the convex geometry, the directional source $\vec{r}$ is to be modeled by a "real" isotropic source $\vec{r}'_{\text{real}}$ located along the radial direction of the physical source and outwardly at a distance of $R_a = 1/\mu'_s$, i.e., at $(R_0 + R_a, \varphi', z')$. The extrapolated boundary is concentric with and at a radial distance of $R_b = 2AD$ inward from the physical boundary. Apparently as the radius R_0 reaches infinity the photon fluence rate associated with a source–detector pair on the medium–applicator interface of the convex geometry approaches that on the associated semi-infinite geometry interface that is tangential to the convex interface at the source position, for the same source–detector distance. This characteristic serves as both the qualitative and quantitative calibers of the analytic solutions derived for the concave geometry.

Considering again that Eqs. (2.2.1.DC) and (2.2.1.AC) are identical in their analytical forms except for the notations differentiating "DC" and "AC," the cylindrical-coordinate solutions to FD photon diffusion associated with optodes on the convex medium–applicator interface can be derived by following the approaches to the corresponding CW photon diffusion demonstrated in Part I. The resulted DC photon fluence rate sensed by the detector $\vec{r}$ on the physical boundary of the convex geometry due to the physical source $\vec{r}'$ is

$$\begin{aligned}\bar{\Psi}_{\mathrm{conV}} &= \bar{\Psi}_{\mathrm{real}}|_{\mathrm{phys}} + \bar{\Psi}_{\mathrm{imag}}|_{\mathrm{phys}}\\ &= \frac{\bar{S}}{4\pi^2 D}\int_{-\infty}^{\infty} dk\left\{\exp[ik(z-z')]\sum_{m=-\infty}^{\infty} I_m(\bar{k}_{\mathrm{eff}}R_0)\right.\\ &\quad\times K_m[\bar{k}_{\mathrm{eff}}(R_0+R_a)]\\ &\quad\times\left\langle 1-\frac{K_m(\bar{k}_{\mathrm{eff}}R_0)}{I_m(\bar{k}_{\mathrm{eff}}R_0)}\frac{I_m[\bar{k}_{\mathrm{eff}}(R_0-R_b)]}{K_m[\bar{k}_{\mathrm{eff}}(R_0-R_b)]}\right\rangle\\ &\quad\left.\times\exp[im(\varphi-\varphi')]\right\}, \end{aligned} \tag{3.2.1.DC}$$

which has a slightly different format comparing to Eq. (3.2.5) in Part I, and its AC counterpart is

$$\begin{aligned}\tilde{\Psi}_{\mathrm{conV}} &= \tilde{\Psi}_{\mathrm{real}}|_{\mathrm{phys}} + \tilde{\Psi}_{\mathrm{imag}}|_{\mathrm{phys}}\\ &= \frac{\tilde{S}}{4\pi^2 D}\int_{-\infty}^{\infty} dk\left\{\exp[ik(z-z')]\sum_{m=-\infty}^{\infty} I_m(\tilde{k}_{\mathrm{eff}}R_0)\right.\\ &\quad\times K_m[\tilde{k}_{\mathrm{eff}}(R_0+R_a)]\\ &\quad\times\left\langle 1-\frac{K_m(\tilde{k}_{\mathrm{eff}}R_0)}{I_m(\tilde{k}_{\mathrm{eff}}R_0)}\frac{I_m[\tilde{k}_{\mathrm{eff}}(R_0-R_b)]}{K_m[\tilde{k}_{\mathrm{eff}}(R_0-R_b)]}\right\rangle\\ &\quad\left.\times\exp[im(\varphi-\varphi')]\right\}. \end{aligned} \tag{3.2.1.AC}$$

4. ANALYTICAL PREDICTION OF THE CHARACTERISTICS OF FD PHOTON DIFFUSION VERSUS SOURCE–DETECTOR DISTANCE IN CONCAVE AND CONVEX GEOMETRIES OF LARGE RADIUS

To understand the generalized behavior of the FD photon diffusion versus source–detector distance in concave and convex geometries, we now consider that the radius of the concave or convex geometry is much greater than the source–detector distance that is also in the diffusion regime, i.e., we have assumed that $R_0 \gg d \gg R_a, R_b$. By using the spherical coordinate expression of the photon fluence rates given in Eq. (2.1.2), we can rewrite Eq. (3.1.1) for concave geometry (refer to Subsection 3.A.2 in Part I for the analytical means) as

$$\begin{aligned}\bar{\Psi}_{\mathrm{conC}} &= \left[\frac{\bar{S}}{4\pi D l_r}\exp(-\bar{k}_0 l_r)\right]\\ &\quad-\left[\frac{\bar{S}}{4\pi D l_i}\exp(-\bar{k}_0 l_i)\right]\sqrt{\frac{R_0+R_a+2R_b}{R_0-R_a}}, \end{aligned} \tag{4.1.DC}$$

$$\begin{aligned}\tilde{\Psi}_{\mathrm{conC}} &= \left[\frac{\tilde{S}}{4\pi D l_r}\exp(-\tilde{k}_{\mathrm{amp}} l_r)\right]\exp(-i\tilde{k}_{\mathrm{phi}} l_r)\\ &\quad-\left[\frac{\tilde{S}}{4\pi D l_i}\exp(-\tilde{k}_{\mathrm{amp}} l_i)\right]\sqrt{\frac{R_0+R_a+2R_b}{R_0-R_a}}\exp(-i\tilde{k}_{\mathrm{phi}} l_i). \end{aligned} \tag{4.1.AC}$$

The acute angle formed by $(\vec{r}-\vec{r}')$ and the azimuthal plane is α as shown in Fig. 2(A), and

$$\begin{aligned} l_r &= d\sqrt{\left[1+\frac{R_a^2}{d^2}-\frac{R_a}{R_0}(\cos\alpha)^2\right]};\\ l_i &= d\sqrt{\left[1+\frac{(R_a+2R_b)^2}{d^2}+\frac{R_a+2R_b}{R_0}(\cos\alpha)^2\right]}. \end{aligned} \tag{4.2}$$

Then based on the approach demonstrated in Part III [16], the DC and AC photon fluence rates expressed by Eq. (4.1) can be simplified to

$$\begin{aligned}\bar{\Psi}_{\mathrm{conC}} &= \frac{\bar{S}}{2\pi D}\frac{1}{d^2}\exp\left\{-\left[\bar{k}_0 d+\frac{d}{2\bar{k}_0 R_b(R_0-R_a)}\right.\right.\\ &\quad\left.\left.-\frac{2R_0-R_a+2R_b}{4R_0R_b(R_0-R_a)}(\cos\alpha)^2 d^2\right]\right\}\\ &\quad\times\exp\left[\frac{(R_0+2R_b)^2}{4R_b(R_0-R_a)}\right][\bar{k}_0 R_b(R_a+R_b)], \end{aligned} \tag{4.3.DC}$$

$$\begin{aligned}\tilde{\Psi}_{\mathrm{conC}} &= \frac{\tilde{S}}{2\pi D}\frac{1}{d^2}\exp\left\{-\left[\tilde{k}_{\mathrm{amp}} d+\frac{\tilde{k}_{\mathrm{amp}} d}{2(\tilde{k}_{\mathrm{amp}}^2+\tilde{k}_{\mathrm{phi}}^2)R_b(R_0-R_a)}\right.\right.\\ &\quad\left.\left.-\frac{2R_0-R_a+2R_b}{4R_0R_b(R_0-R_a)}(\cos\alpha)^2 d^2\right]\right\}\exp\left[\frac{(R_0+2R_b)^2}{4R_b(R_0-R_a)}\right]\\ &\quad\times\left[\sqrt{\tilde{k}_{\mathrm{amp}}^2+\tilde{k}_{\mathrm{phi}}^2}R_b(R_a+R_b)\right]\\ &\quad\times\exp\left\{-i\left[\tilde{k}_{\mathrm{phi}} d-\frac{\tilde{k}_{\mathrm{phi}} d}{2(\tilde{k}_{\mathrm{amp}}^2+\tilde{k}_{\mathrm{phi}}^2)R_b(R_0-R_a)}\right.\right.\\ &\quad\left.\left.-\tan^{-1}\left(\frac{\tilde{k}_{\mathrm{phi}}}{\tilde{k}_{\mathrm{amp}}}\right)\right]\right\}. \end{aligned} \tag{4.3.AC}$$

Similarly, we can rewrite Eq. (3.2.1) for convex geometry (refer to Subsection 3.B.2 in Part I) as

$$\begin{aligned}\bar{\Psi}_{\mathrm{conV}} &= \left[\frac{\bar{S}}{4\pi D l_r}\exp(-\bar{k}_0 l_r)\right]\\ &\quad-\left[\frac{\bar{S}}{4\pi D l_i}\exp(-\bar{k}_0 l_i)\right]\sqrt{\frac{R_0-R_a-2R_b}{R_0+R_a}} \end{aligned} \tag{4.4.DC}$$

$$\begin{aligned}\tilde{\Psi}_{\mathrm{conV}} &= \left[\frac{\tilde{S}}{4\pi D l_r}\exp(-\tilde{k}_{\mathrm{amp}} l_r)\right]\exp(-i\tilde{k}_{\mathrm{phi}} l_r)\\ &\quad-\left[\frac{\tilde{S}}{4\pi D l_i}\exp(-\tilde{k}_{\mathrm{amp}} l_i)\right]\sqrt{\frac{R_0-R_a-2R_b}{R_0+R_a}}\exp(-i\tilde{k}_{\mathrm{phi}} l_i). \end{aligned} \tag{4.4.AC}$$

Utilizing the acute angle α between $(\vec{r}-\vec{r}')$ and the azimuthal plane as shown in Fig. 2(B) and

$$\begin{aligned} l_r &= d\sqrt{\left[1+\frac{R_a^2}{d^2}+\frac{R_a}{R_0}(\cos\alpha)^2\right]};\\ l_i &= d\sqrt{\left[1+\frac{(R_a+2R_b)^2}{d^2}-\frac{R_a+2R_b}{R_0}(\cos\alpha)^2\right]}, \end{aligned} \tag{4.5}$$

the DC and AC photon fluence rates expressed by Eq. (4.4) can be simplified to

$$\bar{\Psi}_{\mathrm{conV}} = \frac{\bar{S}}{2\pi D}\frac{1}{d^2}\exp\left\{-\left[\bar{k}_0 d - \frac{d}{2\bar{k}_0 R_b(R_0+R_a)} + \frac{2R_0+R_a-2R_b}{4R_0R_b(R_0+R_a)}(\cos\alpha)^2 d^2\right]\right\} \times \exp\left[-\frac{(R_0+2R_b)^2}{4R_b(R_0+R_a)}\right][\bar{k}_0 R_b(R_a+R_b)] \quad \text{(4.6.DC)}$$

$$\tilde{\Psi}_{\mathrm{conV}} = \frac{\tilde{S}}{2\pi D}\frac{1}{d^2}\exp\left\{-\left[\tilde{k}_{\mathrm{amp}} d - \frac{\tilde{k}_{\mathrm{amp}} d}{2(\tilde{k}^2_{\mathrm{amp}}+\tilde{k}^2_{\mathrm{phi}})R_b(R_0+R_a)} + \frac{2R_0+R_a-2R_b}{4R_0R_b(R_0+R_a)}(\cos\alpha)^2 d^2\right]\right\}\exp\left[-\frac{(R_0+2R_b)^2}{4R_b(R_0+R_a)}\right] \times\left[\sqrt{\tilde{k}^2_{\mathrm{amp}}+\tilde{k}^2_{\mathrm{phi}}}R_b(R_a+R_b)\right] \times\exp\left\{-i\left[\tilde{k}_{\mathrm{phi}} d + \frac{\tilde{k}_{\mathrm{phi}} d}{2(\tilde{k}^2_{\mathrm{amp}}+\tilde{k}^2_{\mathrm{phi}})R_b(R_0+R_a)} - \tan^{-1}\left(\frac{\tilde{k}_{\mathrm{phi}}}{\tilde{k}_{\mathrm{amp}}}\right)\right]\right\}. \quad \text{(4.6.AC)}$$

Note that Eqs. (4.1)–(4.6) are formulated under the condition of $R_0 \gg d \gg R_a, R_b$, and with which we generalize the behavior of FD photon diffusion, in terms of the changes of DC and AC photon fluence rates with respect to the source-detector distance $d = |\vec{r} - \vec{r}'|$, in a homogeneous medium of infinite geometry as well as on the semi-infinite, concave, and convex medium–applicator interfaces bounding a homogeneous medium. The characteristics given in below are derived from the base equations of Eq. (2.1.1) for infinite geometry, Eq. (2.1.4) for semi-infinite geometry, Eq. (4.3) for concave geometry, and Eq. (4.6) for convex geometry.

A. Change of DC Photon Fluence Rate with Respect to d (Recounting)

1. Source and Detector in an Infinite Medium Geometry

In an infinite medium geometry, we have $\ln(\bar{\Psi}_{\mathrm{inf}} d)$ reducing versus d at a rate of $\bar{k}_0$ as

$$\frac{\partial \ln(\bar{\Psi}_{\mathrm{inf}} d)}{\partial d} = -\bar{k}_0. \quad \text{(4.DC.infi)}$$

2. Source and Detector on a Semi-Infinite Medium–Applicator Interface

On a semi-infinite interface, we have $\ln(\bar{\Psi}_{\mathrm{semi}} d^2)$ reducing versus d at a rate of $\bar{k}_0$ as

$$\frac{\partial \ln(\bar{\Psi}_{\mathrm{semi}} d^2)}{\partial d} = -\bar{k}_0. \quad \text{(4.DC.semi)}$$

3. Source and Detector on a Concave Medium–Applicator Interface with Large Radius

On a concave interface with larger radius, we have $\ln(\bar{\Psi}_{\mathrm{conC}} d^2)$ reducing versus d as [16]

$$\frac{\partial \ln(\bar{\Psi}_{\mathrm{conC}} d^2)}{\partial d} = -\left\{\bar{k}_0 + \frac{1}{2\bar{k}_0 R_b(R_0-R_a)} - \left[\frac{2R_0-R_a+2R_b}{2R_0R_b(R_0-R_a)}\right](\cos\alpha)d_\perp\right\}, \quad \text{(4.DC.conC)}$$

where $d_\perp = d\cos\alpha$ is the projection of d to the azimuthal plane. Along the longitudinal direction, termed *case-longi*, i.e., $\cos\alpha = 0$, we have

$$\left.\frac{\partial \ln(\bar{\Psi}_{\mathrm{conC}} d^2)}{\partial d}\right|_{\mathrm{longi}} = -\left[\bar{k}_0 + \frac{1}{2\bar{k}_0 R_b(R_0-R_a)}\right] \quad \text{(4.DC.conC.longi)}$$

Equation (4.DC.conC.longi) indicates that when the source and detector are positioned only along the longitudinal direction, $\ln(\bar{\Psi}_{\mathrm{conC}} d^2)$ reduces versus d at a rate greater than $\bar{k}_0$. Along the azimuthal direction, termed *case-azi*, i.e., $\cos\alpha = 1$, $d_\perp = d$, we have

$$\left.\frac{\partial \ln(\bar{\Psi}_{\mathrm{conC}} d^2)}{\partial d}\right|_{\mathrm{azi}} = -\left\{\bar{k}_0 + \frac{1}{2\bar{k}_0 R_b(R_0-R_a)} - \left[\frac{2R_0-R_a+2R_b}{2R_0R_b(R_0-R_a)}\right]d\right\}. \quad \text{(4.DC.conC.azi)}$$

It can be demonstrated that the rate of the reduction of $\ln(\bar{\Psi}_{\mathrm{conC}} d^2)$ in Eq. (4.DC.conC.azi) versus d is actually smaller than $\bar{k}_0$. We also have from Eq. (4.DC.conC) that when the source and detector are positioned along a set of spiral paths defined by the following relationship

$$\cos\bar{\alpha}_{\mathrm{conC}} = \frac{1}{\bar{k}_0 d_\perp}\frac{R_0}{2R_0 - R_a + 2R_b}. \quad \text{(4.DC.conC.spiral)}$$

$\ln(\bar{\Psi}_{\mathrm{conC}} d^2)$ reduces versus d at a rate of $\bar{k}_0$, i.e., identical to the rate when evaluated along a straight line on a semi-infinite medium–applicator interface.

4. Source and Detector on a Convex Medium–Applicator Interface with Large Radius

On a convex interface with large radius, we have $\ln(\bar{\Psi}_{\mathrm{conV}} d^2)$ reducing versus d as [16]

$$\frac{\partial \ln(\bar{\Psi}_{\mathrm{conV}} d^2)}{\partial d} = -\left\{\bar{k}_0 - \frac{1}{2\bar{k}_0 R_b(R_0+R_a)} + \left[\frac{2R_0+R_a-2R_b}{2R_0R_b(R_0+R_a)}\right](\cos\alpha)d_\perp\right\}. \quad \text{(4.DC.conV)}$$

Along the longitudinal direction as in *case-longi*, i.e., $\cos\alpha = 0$, we have

$$\left.\frac{\partial \ln(\bar{\Psi}_{\mathrm{conV}} d^2)}{\partial d}\right|_{\mathrm{longi}} = -\left[\bar{k}_0 - \frac{1}{2\bar{k}_0 R_b(R_0+R_a)}\right]. \quad \text{(4.DC.conV.longi)}$$

Equation (4.DC.conV.longi) indicates that when the source and detector are positioned only along the longitudinal direction, $\ln(\bar{\Psi}_{\mathrm{conV}} d^2)$ reduces versus d at a rate smaller than $\bar{k}_0$. Along the azimuthal direction as in *case-azi*, i.e., $\cos\alpha = 1$, $d_\perp = d$, we have

$$\frac{\partial \ln(\bar{\Psi}_{\mathrm{convV}} d^2)}{\partial d}\bigg|_{\mathrm{azi}} = -\left\{\bar{k}_0 - \frac{1}{2\bar{k}_0 R_b(R_0+R_a)} + \left[\frac{2R_0+R_a-2R_b}{2R_0R_b(R_0+R_a)}\right]d\right\}. \tag{4.DC.conV.azi}$$

It can be demonstrated that the rate of the reduction of $\ln(\bar{\Psi}_{\mathrm{convV}} d^2)$ in Eq. (4.DC.conV.azi) versus d is actually greater than $\bar{k}_0$. We also have from Eq. (4.DC.conV) that when the source and detector are positioned along a set of spiral paths defined by the following relationship

$$\cos\bar{\alpha}_{\mathrm{conV}} = \frac{1}{\bar{k}_0 d_\perp}\frac{R_0}{2R_0+R_a-2R_b}. \tag{4.DC.conV.spiral}$$

$\ln(\bar{\Psi}_{\mathrm{convV}} d^2)$ reduces versus d at a rate of $\bar{k}_0$, i.e., identical to the rate when evaluated along a straight line on a semi-infinite medium–applicator interface.

B. Change of the Amplitude of AC Photon Fluence Rate with Respect to *d*

1. *Source and Detector in an Infinite Medium Geometry*

In an infinite geometry, we have $\ln(|\tilde{\Psi}_{\mathrm{inf}}|d)$ reducing versus d at a rate of $\tilde{k}_{\mathrm{amp}}$ as

$$\frac{\partial \ln(|\tilde{\Psi}_{\mathrm{inf}}|d)}{\partial d} = -\tilde{k}_{\mathrm{amp}}. \tag{4.AC.infi}$$

2. *Source and Detector on a Semi-Infinite Medium–Applicator Interface*

On a semi-infinite interface, we have $\ln(|\tilde{\Psi}_{\mathrm{semi}}|d^2)$ reducing versus d at a rate of $\tilde{k}_{\mathrm{amp}}$ as

$$\frac{\partial \ln(|\tilde{\Psi}_{\mathrm{semi}}|d^2)}{\partial d} = -\tilde{k}_{\mathrm{amp}}. \tag{4.AC.semi}$$

3. *Source and Detector on a Concave Medium–Applicator Interface with Large Radius*

On a concave interface with large radius, we have $\ln(|\tilde{\Psi}_{\mathrm{conC}}|d^2)$ reducing versus d as

$$\frac{\partial \ln(|\tilde{\Psi}_{\mathrm{conC}}|d^2)}{\partial d} = -\left\{\tilde{k}_{\mathrm{amp}} + \frac{\tilde{k}_{\mathrm{amp}}}{2(\tilde{k}_{\mathrm{amp}}^2+\tilde{k}_{\mathrm{phi}}^2)R_b(R_0-R_a)} - \left[\frac{2R_0-R_a+2R_b}{2R_0R_b(R_0-R_a)}\right](\cos\alpha)d_\perp\right\}. \tag{4.AC.conC}$$

Along the longitudinal direction as in *case-longi*, i.e., $\cos\alpha = 0$, we have

$$\frac{\partial \ln(|\tilde{\Psi}_{\mathrm{conC}}|d^2)}{\partial d}\bigg|_{\mathrm{longi}} = -\left[\tilde{k}_{\mathrm{amp}} + \frac{\tilde{k}_{\mathrm{amp}}}{2(\tilde{k}_{\mathrm{amp}}^2+\tilde{k}_{\mathrm{phi}}^2)R_b(R_0-R_a)}\right]. \tag{4.AC.conC.longi}$$

Equation (4.AC.conC.longi) indicates that when the source and detector are positioned only along the longitudinal direction, $\ln(|\tilde{\Psi}_{\mathrm{conC}}|d^2)$ reduces versus d at a rate greater than $\tilde{k}_{\mathrm{amp}}$. Along the azimuthal direction as in *case-azi*, i.e., $\cos\alpha = 1$, $d_\perp = d$, we have

$$\frac{\partial \ln(|\tilde{\Psi}_{\mathrm{conC}}|d^2)}{\partial d}\bigg|_{\mathrm{azi}} = -\left\{\tilde{k}_{\mathrm{amp}} + \frac{\tilde{k}_{\mathrm{amp}}}{2(\tilde{k}_{\mathrm{amp}}^2+\tilde{k}_{\mathrm{phi}}^2)R_b(R_0-R_a)} - \left[\frac{2R_0-R_a+2R_b}{2R_0R_b(R_0-R_a)}\right]d\right\}. \tag{4.AC.conC.azi}$$

It can be demonstrated that the rate of the reduction of $\ln(|\tilde{\Psi}_{\mathrm{conC}}|d^2)$ in Eq. (4.AC.conC.azi) versus d is actually smaller than $\tilde{k}_{\mathrm{amp}}$. We also have from Eq. (4.AC.conC) that when the source and detector are positioned along a set of spiral paths defined by the following relationship

$$\cos\tilde{\alpha}_{\mathrm{conC}} = \frac{\tilde{k}_{\mathrm{amp}}}{(\tilde{k}_{\mathrm{amp}}^2+\tilde{k}_{\mathrm{phi}}^2)d_\perp}\frac{R_0}{2R_0-R_a+2R_b}, \tag{4.AC.conC.spiral}$$

$\ln(|\tilde{\Psi}_{\mathrm{conC}}|d^2)$ reduces versus d at a rate of $\tilde{k}_{\mathrm{amp}}$, i.e., identical to the rate when evaluated along a straight line on a semi-infinite medium–applicator interface. Comparison of Eq. (4.AC.conC.spiral) with Eq. (4.DC.conC.spiral), however, reveals that the spiral paths associated with the amplitude of AC photon fluence rate should differ from that associated with DC photon fluence rate, and the difference should decrease as the modulation frequency decreases.

4. *Source and Detector on a Convex Medium–Applicator Interface with Large Radius*

On a convex interface with large radius, we have $\ln(|\tilde{\Psi}_{\mathrm{conV}}|d^2)$ reducing versus d as

$$\frac{\partial \ln(|\tilde{\Psi}_{\mathrm{conV}}|d^2)}{\partial d} = -\left\{\tilde{k}_{\mathrm{amp}} - \frac{\tilde{k}_{\mathrm{amp}}}{2(\tilde{k}_{\mathrm{amp}}^2+\tilde{k}_{\mathrm{phi}}^2)R_b(R_0+R_a)} + \left[\frac{2R_0+R_a-2R_b}{2R_0R_b(R_0+R_a)}\right](\cos\alpha)d_\perp\right\}. \tag{4.AC.conV}$$

Along the longitudinal direction as in *case-longi*, i.e., $\cos\alpha = 0$, we have

$$\frac{\partial \ln(|\tilde{\Psi}_{\mathrm{conV}}|d^2)}{\partial d}\bigg|_{\mathrm{longi}} = -\left[\tilde{k}_{\mathrm{amp}} - \frac{\tilde{k}_{\mathrm{amp}}}{2(\tilde{k}_{\mathrm{amp}}^2+\tilde{k}_{\mathrm{phi}}^2)R_b(R_0+R_a)}\right]. \tag{4.AC.conV.longi}$$

Equation (4.AC.conV.longi) indicates that when the source and detector are positioned only along the longitudinal direction, $\ln(|\tilde{\Psi}_{\mathrm{conV}}|d^2)$ reduces versus d at a rate smaller than $\tilde{k}_{\mathrm{amp}}$. Along the azimuthal direction as in *case-azi*, i.e., $\cos\alpha = 1$, $d_\perp = d$, we have

$$\frac{\partial \ln(|\tilde{\Psi}_{\mathrm{conV}}|d^2)}{\partial d}\bigg|_{\mathrm{azi}} = -\left\{\tilde{k}_{\mathrm{amp}} - \frac{\tilde{k}_{\mathrm{amp}}}{2(\tilde{k}_{\mathrm{amp}}^2+\tilde{k}_{\mathrm{phi}}^2)R_b(R_0+R_a)} + \left[\frac{2R_0+R_a-2R_b}{2R_0R_b(R_0+R_a)}\right]d\right\}. \tag{4.AC.conV.azi}$$

It can be demonstrated that the rate of the reduction of $\ln(|\tilde{\Psi}_{\mathrm{conV}}|d^2)$ in Eq. (4.AC.conV.azi) versus d is actually greater than $\tilde{k}_{\mathrm{amp}}$. We also have from Eq. (4.AC.conV) that when the source and detector are positioned along a set of spiral paths defined by the following relationship

$$\cos \tilde{\alpha}_{\mathrm{conV}} = \frac{\tilde{k}_{\mathrm{amp}}}{(\tilde{k}_{\mathrm{amp}}^2 + \tilde{k}_{\mathrm{phi}}^2) d_{\perp}} \frac{R_0}{2R_0 + R_a - 2R_b}. \tag{4.AC.conV.spiral}$$

$\ln(|\tilde{\Psi}_{\mathrm{conV}}|d^2)$ reduces versus d at a rate of $\tilde{k}_{\mathrm{amp}}$, i.e., identical to the rate when evaluated along a straight line on a semi-infinite medium–applicator interface. Comparison of Eq. (4.AC.conV.spiral) with Eq. (4.DC.conV.spiral) also reveals that the spiral paths associated with the amplitude of AC photon fluence rate should differ from that associated with DC photon fluence rate, and the difference should decrease as the modulation frequency decreases.

C. Change of Modulation Depth of Photon Fluence Rate with Respect to *d*

We evaluate the modulation depth $\mathrm{Mod} = |\tilde{\Psi}|/\bar{\Psi}$, which is the ratio of the amplitude of AC photon fluence rate to the DC photon fluence rate.

1. Source and Detector in an Infinite Medium Geometry

In an infinite geometry, we have $\ln(\mathrm{Mod}_{\mathrm{inf}})$ reducing versus d at a rate of $(\tilde{k}_{\mathrm{amp}} - \bar{k}_0)$ as

$$\frac{\partial[\ln(\mathrm{Mod}_{\mathrm{inf}})]}{\partial d} = -(\tilde{k}_{\mathrm{amp}} - \bar{k}_0). \tag{4.Mod.infi}$$

2. Source and Detector on a Semi-Infinite Medium–Applicator Interface

On a semi-infinite interface, we have $\ln(\mathrm{Mod}_{\mathrm{semi}})$ reducing versus d at a rate of $(\tilde{k}_{\mathrm{amp}} - \bar{k}_0)$ as

$$\frac{\partial[\ln(\mathrm{Mod}_{\mathrm{semi}})]}{\partial d} = -(\tilde{k}_{\mathrm{amp}} - \bar{k}_0). \tag{4.Mod.semi}$$

3. Source and Detector on a Concave Medium–Applicator Interface with Large Radius

On a concave interface with large radius, we have $\ln(\mathrm{Mod}_{\mathrm{conC}})$ reducing versus d as

$$\frac{\partial[\ln(\mathrm{Mod}_{\mathrm{conC}})]}{\partial d} = -\left\{(\tilde{k}_{\mathrm{amp}} - \bar{k}_0) - \frac{1}{2R_b(R_0 - R_a)}\left[\frac{1}{\bar{k}_0} - \frac{\tilde{k}_{\mathrm{amp}}}{\tilde{k}_{\mathrm{amp}}^2 + \tilde{k}_{\mathrm{phi}}^2}\right]\right\} \tag{4.Mod.conC}$$

for both *case-longi* and *case-azi*. Since $\tilde{k}_{\mathrm{amp}} > \bar{k}_0 > 0$, $\ln(\mathrm{Mod}_{\mathrm{conC}})$ reduces versus d at a rate smaller than $(\tilde{k}_{\mathrm{amp}} - \bar{k}_0)$, and the higher the modulation frequency is, the bigger the difference becomes with respect to $(\tilde{k}_{\mathrm{amp}} - \bar{k}_0)$. Thus on the concave medium–applicator interface there is not any spiral path inferred for the decay rate of modulation frequency.

4. Source and Detector on a Convex Medium–Applicator Interface with Large Radius

On a convex interface with large radius, we have $\ln(\mathrm{Mod}_{\mathrm{conV}})$ reducing versus d as

$$\frac{\partial[\ln(\mathrm{Mod}_{\mathrm{conV}})]}{\partial d} = -\left\{(\tilde{k}_{\mathrm{amp}} - \bar{k}_0) + \frac{1}{2R_b(R_0 + R_a)}\left[\frac{1}{\bar{k}_0} - \frac{\tilde{k}_{\mathrm{amp}}}{\tilde{k}_{\mathrm{amp}}^2 + \tilde{k}_{\mathrm{phi}}^2}\right]\right\} \tag{4.Mod.conV}$$

for both *case-longi* and *case-azi*. Since $\tilde{k}_{\mathrm{amp}} > \bar{k}_0 > 0$, the $\ln(\mathrm{Mod}_{\mathrm{conV}})$ reduces versus d at a rate greater than $(\tilde{k}_{\mathrm{amp}} - \bar{k}_0)$, and the higher the modulation frequency is, the bigger the difference becomes with respect to $(\tilde{k}_{\mathrm{amp}} - \bar{k}_0)$. Thus on the convex medium–applicator interface there is not any spiral path inferred for the decay rate of modulation frequency.

D. Change of Phase of AC Photon Fluence Rate with Respect to *d*

1. Source and Detector in an Infinite Medium Geometry

In an infinite geometry, the phase value $|\angle\tilde{\Psi}_{\mathrm{inf}}|$ increases versus d at a rate of $\tilde{k}_{\mathrm{phi}}$ as

$$\frac{\partial|\angle\tilde{\Psi}_{\mathrm{inf}}|}{\partial d} = \tilde{k}_{\mathrm{phi}}. \tag{4.Phi.infi}$$

2. Source and Detector on a Semi-Infinite Medium–Applicator Interface

On a semi-infinite interface, the phase value $|\angle\tilde{\Psi}_{\mathrm{semi}}|$ increases versus d as

$$\frac{\partial|\angle\tilde{\Psi}_{\mathrm{semi}}|}{\partial d} = \tilde{k}_{\mathrm{phi}}. \tag{4.Phi.semi}$$

3. Source and Detector on a Concave Medium–Applicator Interface with Large Radius

On a concave interface with large radius, the phase value $|\angle\tilde{\Psi}_{\mathrm{conC}}|$ increases versus d as

$$\frac{\partial|\angle\tilde{\Psi}_{\mathrm{conC}}|}{\partial d} = \tilde{k}_{\mathrm{phi}} - \frac{\tilde{k}_{\mathrm{phi}}}{2(\tilde{k}_{\mathrm{amp}}^2 + \tilde{k}_{\mathrm{phi}}^2)R_b(R_0 - R_a)} \tag{4.Phi.conC}$$

for both *case-longi* and *case-azi*. From Eq. (4.Phi.conC), $|\angle\tilde{\Psi}_{\mathrm{conC}}|$ increases versus d at a rate smaller than $\tilde{k}_{\mathrm{phi}}$, and the greater the modulation frequency is, the bigger the difference becomes with respect to $\tilde{k}_{\mathrm{phi}}$. Thus on the concave medium–applicator interface there are no spiral paths inferred for the phase changing rate of the AC photon fluence rate.

4. Source and Detector on a Convex Medium–Applicator Interface with Large Radius

On a concave interface with large radius, the phase value $|\angle\tilde{\Psi}_{\mathrm{conV}}|$ increases versus d as

$$\frac{\partial|\angle\tilde{\Psi}_{\mathrm{conV}}|}{\partial d} = \tilde{k}_{\mathrm{phi}} + \frac{\tilde{k}_{\mathrm{phi}}}{2(\tilde{k}_{\mathrm{amp}}^2 + \tilde{k}_{\mathrm{phi}}^2)R_b(R_0 + R_a)} \tag{4.Phi.conV}$$

for both *case-longi* and *case-azi*. From Eq. (4.Phi.conV), $|\angle\tilde{\Psi}_{\mathrm{conV}}|$ increases versus d at a rate greater than $\tilde{k}_{\mathrm{phi}}$, and the greater the modulation frequency is, the bigger the difference becomes with respect to $\tilde{k}_{\mathrm{phi}}$. Thus on the convex medium–applicator interface there are no spiral paths inferred for the phase changing rate of the AC photon fluence rate.

The above predictions based on analytical approximations are tabulated in Table 1. The influence of the shape of the medium–applicator interface on FD photon diffusion when compared with semi-infinite geometry is explicitly shown.

5. NUMERICAL EVALUATION OF THE CHARACTERISTICS OF FD PHOTON DIFFUSION VERSUS SOURCE–DETECTOR DISTANCE IN CONCAVE AND CONVEX GEOMETRIES OF SMALL RADIUS

The previous section has indicated the general behaviors of FD photon diffusion between a source and a detector aligned azimuthally or longitudinally on a concave or convex medium–applicator interface. Although the predictions are made for concave or convex geometry of very large radius, the qualitative patterns of FD photon diffusion, namely the rate of change of photon fluence versus the source–detector distance in comparison to that along a straight line on a semi-infinite medium–applicator interface, are expected to hold for concave or convex geometry of smaller radius. This section conducts numerical evaluations based on general analytical results given in Eqs. (3.1.1.AC) and (3.2.1.AC), and FEM, to examine the qualitative patterns of FD photon diffusion for concave or convex geometry of smaller radius.

From Subsections. 5.1 to 5.3, two specific cases, namely *case-azi* and *case-longi*, in concave or convex geometry are examined. In *case-azi* the source and detector are azimuthally aligned; thus $z = z'$ is applied to both Eq. (3.1.1.AC) and Eq. (3.2.1.AC). In *case-longi* the source and detector are longitudinally aligned; thus $\varphi = \varphi'$ is applied to both Eq. (3.1.1.AC) and Eq. (3.2.1.AC). In either Eq. (3.1.1.AC) or Eq. (3.2.1.AC), the limits of m in the summation and k in the integration are chosen following the criteria adopted in Part I [13] for numerical evaluation of the analytic results for CW photon diffusion. The limits of m and k are evaluated individually for each set of computations conducted in this study. Each plot of the numerical implementation of the analytical results to FD photon diffusion is also accompanied by FEM simulation using a package of near-infrared fluorescence and spectroscopy tomography [18]. For both concave and convex geometries, the FEM meshing volume is a cylinder of 40 cm in height and 10 cm in radial thickness. Denser meshes are placed along the mid azimuth plane on the medium–applicator interface for *case-azi*, and along the longitudinal direction for *case-longi*. The meshing volume for the semi-infinite geometry is a $16\ \text{cm} \times 8\ \text{cm} \times 8\ \text{cm}$ rectangle, and denser meshes are generated along the straight line whereupon the optodes are placed. In each set of computation for concave, convex, and semi-infinite geometries, the meshing volume is discretized into at least 50,000 tetrahedral elements with more than 10,000 nodes. Unless otherwise specified, the radius of the cylindrical applicator is 10 mm, the optical parameters are $\mu_a = 0.0025\ \text{mm}^{-1}$, $\mu_s' = 1\ \text{mm}^{-1}$, $A = 1.86$ [14], and the modulation frequency is 100 MHz.

Subsection 5.D is used to illustrate the set of spiral paths associated with the amplitude of AC photon fluence rate and the set corresponding to DC photon fluence rate, on both concave and convex medium–applicator interfaces. The profiling of the spiral paths for the amplitude of AC photon fluence rate is methodologically similar to that for DC photon fluence rate, based on a two-step procedure detailed in [15]. Briefly, a coarse rectangular grid with 0.1 mm length is first generated in the interested area along the concave or convex medium–applicator interface, by numerically evaluating Eq. (3.1.1.AC) or Eq. (3.2.1.AC), respectively, for concave or convex medium–applicator interface. The area of interest is determined by comparing the numerical evaluations of Eq. (3.1.1.AC) or Eq. (3.2.1.AC) with the semi-infinite analytic results of Eq. (2.1.AC). In the second step, a denser rectangular grid with 0.04 mm length is interpolated within the coarse grid. For the source located on the origin, the field point has three directions to move on the denser grid in each step: along the azimuthal direction, along the longitudinal direction, and along the diagonal of the previous two directions. For each direction, the difference of the amplitude of AC photon fluence rate originating from the source with respect to that detected along a straight line on a semi-infinite medium-applicator interface is calculated. The direction with the least difference is the direction to move the field point one step, which becomes the starting point for the next step. The trace of the moving field point forms the spiral profile.

Table 1. Summary of the Analytical Expressions Presented in Section 4

	Concave Geometry		Semi-infinite Geometry	Convex Geometry	
	Case-longi	*Case-azi*		*Case-longi*	*Case-azi*
Decay rate of DC amplitude $\frac{\partial \ln(\bar{\Psi}\cdot d^2)}{\partial d}$	$-\left[\bar{k}_0 + \frac{1}{2\bar{k}_0 R_b (R_0 - R_a)}\right]$	$-\left\{\bar{k}_0 + \frac{1}{2\bar{k}_0 R_b (R_0 - R_a)} - \left[\frac{2R_0 - R_a + 2R_b}{2R_0 R_b (R_0 - R_a)}\right] d\right\}$	$-\bar{k}_0$	$-\left[\bar{k}_0 - \frac{1}{2\bar{k}_0 R_b (R_0 + R_a)}\right]$	$-\left\{\bar{k}_0 - \frac{1}{2\bar{k}_0 R_b (R_0 + R_a)} + \left[\frac{2R_0 + R_a - 2R_b}{2R_0 R_b (R_0 + R_a)}\right] d\right\}$
Decay rate of AC amplitude $\frac{\partial \ln(\lvert\tilde{\Psi}\rvert\cdot d^2)}{\partial d}$	$-\left[\tilde{k}_{\text{amp}} + \frac{\tilde{k}_{\text{amp}}}{2(\tilde{k}_{\text{amp}}^2 + \tilde{k}_{\text{phi}}^2) R_b (R_0 - R_a)}\right]$	$-\left\{\tilde{k}_{\text{amp}} + \frac{\tilde{k}_{\text{amp}}}{2(\tilde{k}_{\text{amp}}^2 + \tilde{k}_{\text{phi}}^2) R_b (R_0 - R_a)} - \left[\frac{2R_0 - R_a + 2R_b}{2R_0 R_b (R_0 - R_a)}\right] d\right\}$	$-\tilde{k}_{\text{amp}}$	$-\left[\tilde{k}_{\text{amp}} - \frac{\tilde{k}_{\text{amp}}}{2(\tilde{k}_{\text{amp}}^2 + \tilde{k}_{\text{phi}}^2) R_b (R_0 + R_a)}\right]$	$-\left\{\tilde{k}_{\text{amp}} - \frac{\tilde{k}_{\text{amp}}}{2(\tilde{k}_{\text{amp}}^2 + \tilde{k}_{\text{phi}}^2) R_b (R_0 + R_a)} + \left[\frac{2R_0 + R_a - 2R_b}{2R_0 R_b (R_0 + R_a)}\right] d\right\}$
Change rate of modulation depth $\frac{\partial[\ln(\text{Mod})]}{\partial d}$	$-\left\{(\tilde{k}_{\text{amp}} - \bar{k}_0) - \frac{1}{2R_b (R_0 - R_a)} \left[\frac{1}{\bar{k}_0} - \frac{\tilde{k}_{\text{amp}}}{\tilde{k}_{\text{amp}}^2 + \tilde{k}_{\text{phi}}^2}\right]\right\}$		$-(\tilde{k}_{\text{amp}} - \bar{k}_0)$	$-\left\{(\tilde{k}_{\text{amp}} - \bar{k}_0) + \frac{1}{2R_b (R_0 - R_a)} \left[\frac{1}{\bar{k}_0} - \frac{\tilde{k}_{\text{amp}}}{\tilde{k}_{\text{amp}}^2 + \tilde{k}_{\text{phi}}^2}\right]\right\}$	
Change rate of phase $\frac{\partial \lvert\angle\tilde{\Psi}\rvert}{\partial d}$	$\tilde{k}_{\text{phi}} - \frac{\tilde{k}_{\text{phi}}}{2(\tilde{k}_{\text{amp}}^2 + \tilde{k}_{\text{phi}}^2) R_b (R_0 - R_a)}$		$\tilde{k}_{\text{phi}}$	$\tilde{k}_{\text{phi}} + \frac{\tilde{k}_{\text{phi}}}{2(\tilde{k}_{\text{amp}}^2 + \tilde{k}_{\text{phi}}^2) R_b (R_0 - R_a)}$	

A. Change of AC Amplitude with Respect to *d*

Figures 3(A) and 3(B) illustrate the changes of AC amplitude of photon fluence rate versus the source–detector distance in both concave and convex geometries. A vertical shift is incurred to the FEM results due to the difference of the source term from the one for numerical evaluation of the analytic results. As illustrated in Fig. 3(A) for concave geometry, the decay rate of AC amplitude is smaller in *case-azi* while greater in *case-longi* than that along a straight line on the semi-infinite interface for the same source–detector distance. Conversely for convex geometry, as illustrated in Fig. 3(B), the decay rate of AC amplitude is greater in *case-azi* while smaller in *case-longi* than that along a straight line on the semi-infinite interface for the same source–detector distance. These salient features indicate that a unique set of spiral profiles exists on the medium–applicator interface in both concave and convex geometries, as in the case of CW photon diffusion [15,16], along which the decay rate of AC amplitude could be modeled by that along a straight line on a semi-infinite medium–applicator interface.

It is observed from both Figs. 3(A) and 3(B) that the analytic results and FEM simulations agree well in the diffusion regime, i.e., the source–detector distance is greater than several times of the transport scattering length. However, within the subdiffusion regime, as also observed for DC amplitude in Part II [14], the two approaches deviate, mainly due to the different implements of the source definition [14]. In the analytic treatments the source is defined as a spatial impulse while in FEM the source is implemented as a spatially Gaussian shaped source. This difference has minimal effects upon photon fluence rate in the diffusion regime while noticeably affecting the photon fluence rate in the sub-diffusion regime. The deviation is also related to the boundary conditions, as in the analytic treatments the extrapolated boundary is assumed while in FEM the Robin-type boundary condition is employed. In Fig. 3(B), the amplitude of photon fluence rate in convex geometry in *case-azi* is only plotted for source–detector distance less than 32 mm, as for larger source–detector distance the modified Bessel functions in Eqs. (3.1.1.AC) and (3.2.1.AC) is beyond the smallest or the greatest number that can be accommodated by IEEE standard for floating-point arithmetic [19].

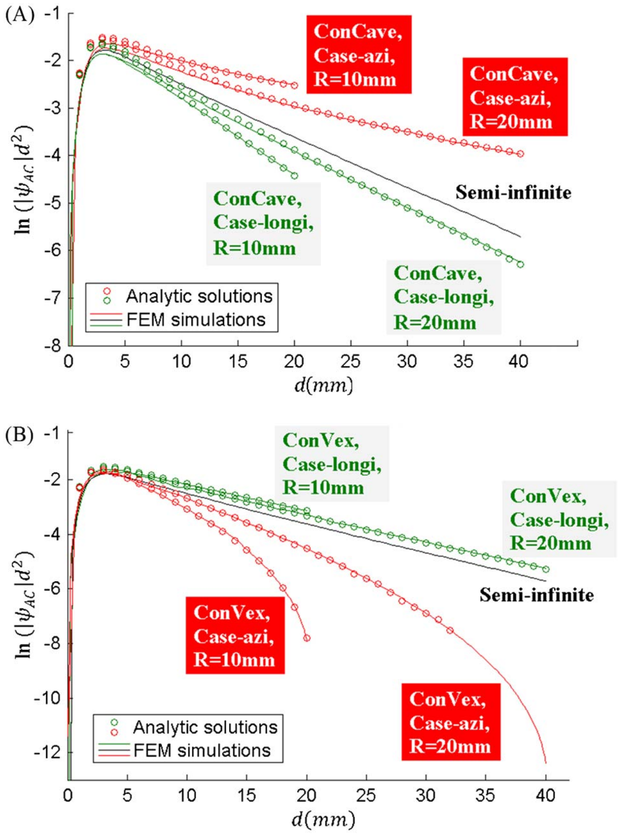

Fig. 3. (Color online) Changes of AC amplitude versus source-detector distance in both *case-azi* and *case-longi* configurations. (A) In concave geometry, the decay rate of AC amplitude is smaller in *case-azi* while greater in *case-longi* than that along a straight line on the semi-infinite interface. (B) In convex geometry, the decay rate of AC amplitude is greater in *case-azi* while smaller in *case-longi* than that along a straight line on the semi-infinite interface.

B. Changes of Modulation Depth versus Source–Detector Distance and Modulation Frequency

The changes of modulation depth at 100 MHz versus source–detector distance in concave and convex geometries are shown in Fig. 4(A). The changes of modulation depth at a fixed source–detector distance $d = 15$ mm versus modulation frequency in concave and convex geometries are depicted in Fig. 4(B). Figure 4 indicates that the reduction of modulation depth is smaller in concave geometry while greater in convex geometry than that along a straight line on the semi-infinite medium–applicator interface for the same modulation frequency. Therefore no spiral path occurring to DC or the amplitude of AC fluence rate is inferred for the modulation

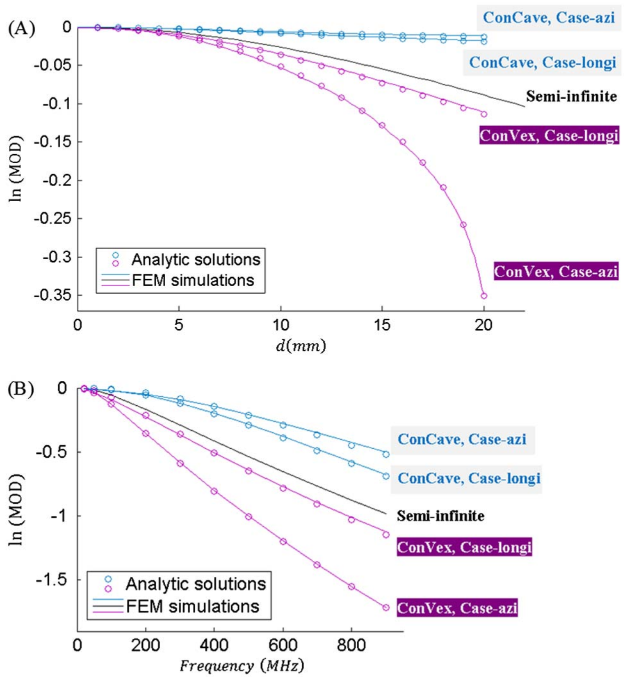

Fig. 4. (Color online) (A) Changes of modulation depth versus source–detector distance in the concave geometry and convex geometry at 100 MHz modulation frequency. (B) Changes of modulation depth versus modulation frequency in the concave geometry and convex geometry at a source–detector distance of $d = 15$ mm. In both (A) and (B), the reduction of the modulation depth is smaller in both *case-azi* and *case-longi* of concave geometry and greater in both *case-azi* and *case-longi* of convex geometry than that along a straight line on the semi-infinite interface, for the same source–detector distance.

depth. The modulation depth evaluated along the longitudinal direction, however, is always closer to that along a straight line on the semi-infinite interface than the one evaluated along the azimuthal direction is as follows.

C. Changes of Phase versus Source–Detector Distance and Modulation Frequency

The changes of phase at 100 MHz versus source–detector distance in concave and convex geometries are shown in Fig. 5(A). The changes of phase at a fixed source–detector distance $d = 15$ mm versus modulation frequency in concave and convex geometries are depicted in Fig. 5(B). Figure 5 indicates that the phase increases slower in concave geometry while greater in convex geometry than that along a straight line on the semi-infinite medium–applicator interface for the same modulation frequency. Therefore no spiral paths occurring to DC or the amplitude of AC fluence rate is inferred for the phase change of AC photon fluence rate. The phase evaluated along the longitudinal direction, however, is always closer to that along a straight line on the semi-infinite interface than the one evaluated along the azimuthal direction is as follows.

D. Spiral Paths for DC and the Amplitude of AC Photon Fluence Rates

The different spiral paths associated with DC and the amplitude of AC photon fluence rates are illustrated in Fig. 6(A) for concave medium–applicator interface and Fig. 6(B) for convex medium–applicator interface, respectively. The spiral paths are computed for only a specific set of parameters, including a cylinder radius of 10 mm, optical properties of $\mu_a = 0.002\ \text{mm}^{-1}$, $\mu_s' = 0.5\ \text{mm}^{-1}$, $A = 1.86$, and a modulation frequency of 100 MHz. It is shown that the spiral paths for are tilted more axially than that for DC photon fluence rate. The difference between these two sets of spiral paths seems to be greater on the convex medium–applicator interface than that on the concave medium–applicator interface.

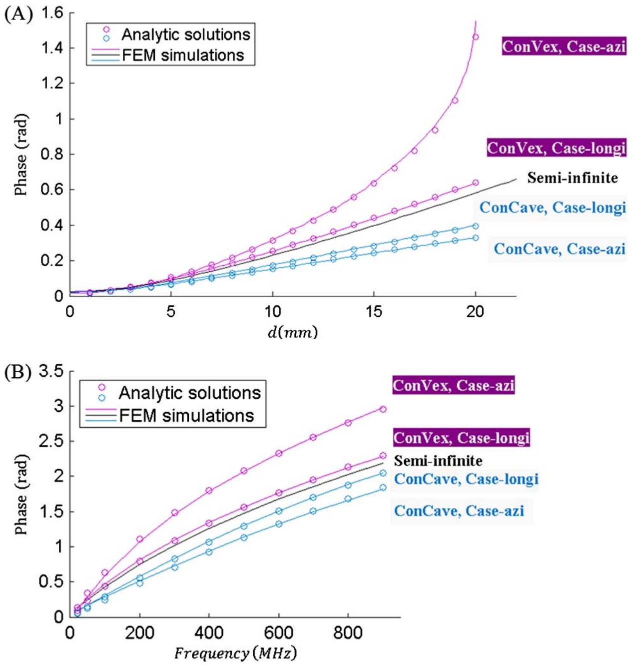

Fig. 5. (Color online) (A) Changes of phase versus source–detector distance in the concave geometry and convex geometry at 100 MHz modulation frequency. (B) Changes of phase versus modulation frequency in the concave geometry and convex geometry at a source–detector distance of $d = 15$ mm. In both (A) and (B), the increase of the phase is smaller in *case-azi* and *case-longi* of concave geometry and greater in both *case-azi* and *case-longi* of convex geometry than that along a straight line on the semi-infinite interface, for the same source–detector distance.

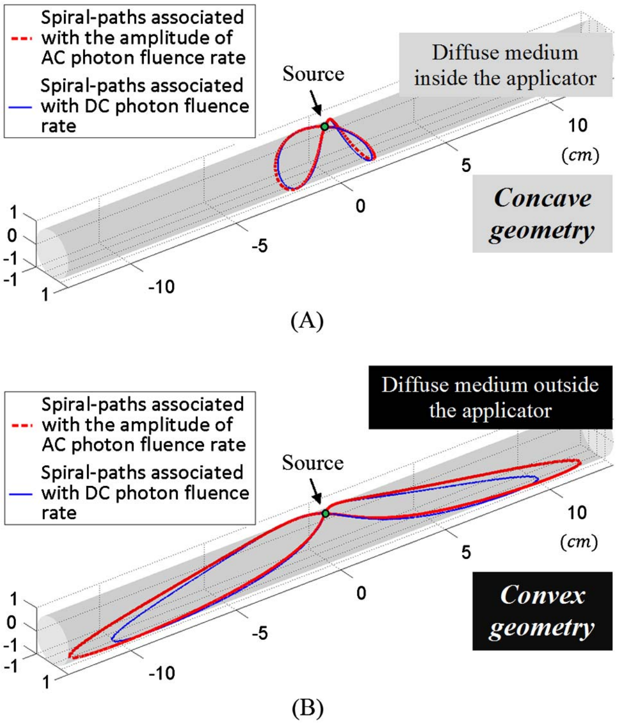

Fig. 6. (Color online) (A) Spiral paths associated with the amplitude of AC and DC photon fluence rate on the concave medium–applicator interface. (B) Spiral paths associated with the amplitude of AC and DC photon fluence rate on the convex medium–applicator interface. In both (A) and (B), the spiral paths for the amplitude of AC photon fluence rate tilt more axially than that for DC photon fluence rate. The difference between these two sets of spiral paths is more pronounced on the convex medium–applicator interface.

6. DISCUSSION

The existence of a phase offset at $d = 0$ mm is easily observed for all the investigated geometries in Fig. 5(A). This offset can be related directly to the term $\tan^{-1}(\tilde{k}_{\text{phi}}/\tilde{k}_{\text{amp}})$ appearing in the phase part of the FD photon fluence, as appearing in Eqs. (2.1.4.AC), (4.3.AC), and (4.6.AC). The existence of this phase offset can also be interpreted through the diffusion process, as a directional physical source is replaced by an isotropic source placed one transport scattering length inwards to the diffuse medium, and the approximation is valid only for source–detector distance greater than 3–5 times of transport scattering length. It is also observed that regardless of the geometry, the phase of photon fluence appears to be nearly linear to the modulation frequency below 200 MHz. As the modulation frequency goes higher beyond 200 MHz, the phase becomes smaller compared to the one projected linearly from sub-200 MHz ranges. These appearances of the phase are in agreement with the simulation [5] and experimental results of earlier studies [20,21] performed on semi-infinite medium–applicator interface.

The simplified analytic results presented in Section 4 for cylindrical applicators with large radius provide direct analytic representations of the effect of applicator's curvature when compared with semi-infinite geometry. The sets of Eqs. (4.DC.conC) and (4.AC.conC) for concave geometry and Eqs. (4.DC.conV) and (4.AC.conV) for convex geometry show that as $R_0 \to \infty$, the decay rates of both DC and AC amplitude of photon fluence reach those in semi-infinite geometry. The set of Eqs. (4.Mod.conC) and (4.Mod.conV) shows that as $R_0 \to \infty$, the changing rates of the modulation depth versus the source–detector distance in both concave and convex geometries reach those in semi-infinite geometry. A set of Eqs. (4.Phi.conC) and (4.Phi.conV) shows that as $R_0 \to \infty$, the changing rates of the phase of AC photon fluence versus the source–detector distance in both concave and convex geometries reach those in semi-infinite geometry. Since these qualitative features of FD photon diffusion were derived for cylindrical applicators with very large radius, they do not necessarily represent the exact quantitative features of FD photon diffusion for cylindrical applicator with small, such as at centimeter-order, radius. For instance, for cylindrical applicator with small radius, Fig. 4 indicates different rates of modulation-depth change versus the source–detector distance for *case-azi* and *case-longi* in both concave and convex geometries, while the rate-difference between *case-azi* and *case-longi* certainly would diminish as the radius of the cylindrical applicator becomes increasingly large. Similarly, Fig. 5 indicates different rates of phase change versus the source-detector distance for *case-azi* and *case-longi* in both concave and convex geometries for cylindrical applicator with small radius, while the rate-difference between *case-azi* and *case-longi* certainly would also diminish as the radius of the cylindrical applicator becomes increasingly large. It is worth to note that numerical evaluation of the general analytical results of Eqs. (3.1.1) or (3.2.1)for FD photon diffusion in concave or convex geometry of large radius is arithmetically challenging.

The numerical evaluations of the analytic results presented in Section 5 explicitly visualize perhaps some less appreciated aspects of the photon diffusion in both concave and convex geometries. The decay rate of AC amplitude of photon fluence rate and DC photon fluence [14] with respect to source-detector distance could be either greater in *case-azi* and smaller in *case-longi* or smaller in *case-azi* and greater in *case-longi* than that in the semi-infinite geometry. However, the change of modulation depth and phase with respect to source–detector distance uniquely reflect the applicator curvature when compared with that in the semi-infinite geometry. As indicated in Fig. 4, the changes of modulation depth with respect to source–detector distance are smaller in concave geometry and larger in convex geometry than that in the semi-infinite geometry, and the changes of phase with respect to source–detector distance show similar opposite trend as indicated in Fig. 5. As the photon fluence reaching the detector is an ensemble of many trajectories, it seems that the ensemble photon-path length is shorter in concave geometry whereas longer in convex geometry than that in semi-infinite geometry for the same source–detector distance. This also agrees with the observation in Fig. 5 regarding the phase changes of AC photon fluence rate versus the source–detector distance in the concave and convex geometries. Subsequently one may expect that, although the measurement in the convex geometry is subjected to smaller signal-to-noise ratio than in concave geometry (the signal-noise-ratio in a quasi-concave geometry analyzed by the more accurate radiative transfer approach is seen in [22]) as the modulation depth drops faster, it may render greater phase sensitivity than the measurement in the concave geometry.

The spiral paths, which render the convenience of treating photon fluence rate in either concave or convex geometry as if it is along a straight line on a semi-infinite medium–applicator interface, were proposed and demonstrated for CW photon diffusion [14–15]. This current study has shown that the spiral paths do exist to the amplitude of AC photon fluence rate; however they do not coincide with those occurring to DC photon fluence rate. Therefore no single spiral path can be found for FD photon diffusion that allows treating both the amplitude of AC and DC photon fluence rate as if they are along a straight line on a semi-infinite medium–applicator interface. On the other hand, when both AC amplitude and DC fluence rate are combined, the resulted modulation depth shows smaller changes in concave geometry and greater changes in convex geometry, when comparing with that evaluated along a straight line on a semi-infinite medium–applicator interface. This single-sided response of the modulation depth to the concave or convex curvature of the geometry, which is similar to that of phase, may support the notation that the DC information is indeed supplementary to the AC information for FD measurement [23].

7. CONCLUSIONS

This Part IV of the work studies the FD photon diffusion between a source and a detector on an infinitely long circular cylindrical applicator bounding internally or externally a homogeneous medium. The general analytic results for both concave and convex geometry cases are simplified at large radius to evaluate qualitatively the characteristics of FD photon diffusion, including the AC amplitude, modulation depth, and phase, with respect to source–detector distance and/or modulation frequency. The discoveries, substantiated by numerical evaluations based on analytical results and FEM at smaller centimeter-order radius, are (1) the decay rate of the AC amplitude of photon fluence rate versus the source–detector distance is greater in *case-azi* and smaller in *case-longi* on the concave medium–applicator interface, and conversely smaller in *case-azi* and greater in *case-longi* on the convex medium–applicator interface, than that along a straight line on the semi-infinite medium–applicator interface, (2) the reduction of modulation depth versus the source–detector distance is slower on the concave medium–applicator interface and faster on the convex medium–applicator interface than that along a straight line on the semi-infinite medium–applicator interface, and (3) the increase of the phase of AC photon fluence versus the source-detector distance is slower on the concave medium–applicator interface and faster on the convex medium–applicator interface than that along a straight line on the semi-infinite medium–applicator interface.

ACKNOWLEDGMENTS

This work has been supported by the Prostate Cancer Research Program of the U.S. Army Medical Research Acquisition Activity through Grant No. W81XWH-10-1-0836.

REFERENCES

1. A. Ishimaru, “Diffusion of light in turbid material,” Appl. Opt. **28**, 2210–2215 (1989).
2. A. H. Hielscher, A. Y. Bluestone, G. S. Abdoulaev, A. D. Klose, J. Lasker, M. Stewart, U. Netz, and J. Beuthan, “Near-infrared diffuse optical tomography,” Dis. Markers **18**, 313–337 (2002).
3. D. Piao, H. Xie, W. Zhang, J. S. Kransinski, G. Zhang, H. Dehghani, and B. W. Pogue, “Endoscopic, rapid near-infrared optical tomography,” Opt. Lett. **31**, 2876–2878 (2006).
4. S. Fantini, M. A. Franceschini, and E. Gratton, “Semi-infinite-geometry boundary problem for light migration in highly scattering media: a frequency-domain study in the diffusion approximation,” J. Opt. Soc. Am. B **11**, 2128–2138 (1994).
5. S. R. Arridge, M. Cope, and D. T. Delpy, “The theoretical basis for the determination of optical path lengths in tissue: temporal and frequency analysis,” Phys. Med. Biol. **37**, 1531–1560 (1992).
6. H. S. Carslaw and J. C. Jaeger, *Conduction of Heat in Solids*, 2nd ed. (Oxford, 1986).
7. B. W. Pogue and M. S. Patterson, “Frequency-domain optical absorption spectroscopy of finite tissue volumes using diffusion theory,” Phys. Med. Biol. **39**, 1157–1180 (1994).
8. R. C. Haskell, L. O. Svaasand, T. Tsay, T. Feng, M. S. McAdams, and B. J. Tromberg, “Boundary conditions for the diffusion equation in radiative transfer,” J. Opt. Soc. Am. A **11**, 2727–2741 (1994).
9. D. Contini, F. Martelli, and G. Zaccanti, “Photon migration through a turbid slab described by a model based on diffusion approximation. I. Theory,” Appl. Opt. **36**, 4587–4599 (1997).
10. A. Da Silva, M. Leabad, C. Driol, T. Bordy, M. Debourdeau, J. Dinten, P. Peltié, and P. Rizo, “Optical calibration protocol for an x-ray and optical multimodality tomography system dedicated to small-animal examination,” Appl. Opt. **48**, D151–D162 (2009).
11. A. Liemert and A. Kienle, “Light diffusion in a turbid cylinder. I. Homogeneous case,” Opt. Express **18**, 9456–9473 (2010).
12. A. Liemert and A. Kienle, “Light diffusion in a turbid cylinder. II. Layered case,” Opt. Express **18**, 9266–9279 (2010).
13. A. Zhang, D. Piao, C. F. Bunting, and B. W. Pogue, “Photon diffusion in a homogeneous medium bounded externally or internally by an infinitely long circular cylindrical applicator. I. Steady-state theory,” J. Opt. Soc. Am. A **27**, 648–662 (2010).
14. A. Zhang, G. Xu, C. Daluwatte, G. Yao, C. F. Bunting, B. W. Pogue, and D. Piao, “Photon diffusion in a homogeneous medium bounded externally or internally by an infinitely long circular cylindrical applicator. II. Quantitative examinations of the steady-state theory,” J. Opt. Soc. Am. A **28**, 66–75 (2011).
15. A. Zhang, D. Piao, G. Yao, C. F. Bunting, and Y. Jiang, “Diffuse photon remission along unique spiral paths on a cylindrical interface is modeled by photon remission along a straight line on a semi-infinite interface,” Opt. Lett. **36**, 654–656 (2011).
16. A. Zhang, D. Piao, and C. F. Bunting, “Photon diffusion in a homogeneous medium bounded externally or internally by an infinitely long circular cylindrical applicator. III. Synthetic-study of continuous-wave photon fluence rate along unique spiral-paths,” J. Opt. Soc. Am. A **29**, 545–558 (2012).
17. J. D. Jackson, “Expansion of Green functions in cylindrical coordinates,” in *Classical Electrodynamics*, 3rd ed. (Wiley, 1998), pp. 125–126.
18. H. Dehghani, M. E. Eames, P. K. Yalavarthy, S. C. Davis, S. Srinivasan, C. M. Carpenter, B. W. Pogue, and K. D. Paulsen, “Near infrared optical tomography using NIRFAST: algorithm for numerical model and image reconstruction,” Commun. Numer. Methods Eng. **25**, 711–732 (2009).
19. IEEE 754-2008 Standard for Floating-Point Arithmetic (IEEE, 2008).
20. B. J. Tromberg, L. O. Svaasand, T. Tsay, and R. C. Haskell, “Properties of photon density waves in multiple-scattering media,” Appl. Opt. **32**, 607–616 (1993).
21. I. V. Yaroslavsky, A. N. Yaroslavsky, V. V. Tuchin, and H. J. Schwarzmaier, “Effect of the scattering delay on time-dependent photon migration in turbid media,” Appl. Opt. **36**, 6529–38 (1997).
22. H. K. Kim, U. J. Netz, J. Beuthan, and A. H. Hielscher, “Optimal source-modulation frequencies for transport-theory-based optical tomography of small-tissue volumes,” Opt. Express **16**, 18082–18101 (2008).
23. G. Xu, D. Piao, C. F. Bunting, and H. Dehghani, “Direct-current-based image reconstruction versus direct-current included or excluded frequency-domain reconstruction in diffuse optical tomography,” Appl. Opt. **49**, 3059–3070 (2010).

Photon diffusion in a homogeneous medium bounded externally or internally by an infinitely long circular cylindrical applicator. V. Steady-state fluorescence

Daqing Piao,[1,*] Anqi Zhang,[1] and Guan Xu[2]

[1]*School of Electrical and Computer Engineering, Oklahoma State University, Stillwater, Oklahoma 74078, USA*
[2]*Department of Radiology, Medical School, University of Michigan, Ann Arbor, Michigan 48109, USA*
**Corresponding author: daqing.piao@okstate.edu*

Received January 3, 2013; revised February 16, 2013; accepted February 18, 2013;
posted February 22, 2013 (Doc. ID 182333); published March 29, 2013

As Part V in our series, this paper examines steady-state fluorescence photon diffusion in a homogenous medium that contains a homogenous distribution of fluorophores, and is enclosed by a "concave" circular cylindrical applicator or is enclosing a "convex" circular cylindrical applicator, both geometries being infinite in the longitudinal dimension. The aim is to predict by analytics and examine with the finite-element method the changing characteristics of the fluorescence-wavelength photon-fluence rate and the ratio (sometimes called the Born ratio) of it versus the excitation-wavelength photon-fluence rate, with respect to the source–detector distance. The analysis is performed for a source and a detector located on the medium–applicator interface and aligned either azimuthally or longitudinally in both concave and convex geometries. When compared to its steady-state counterparts on a semi-infinite medium–applicator interface with the same line-of-sight source–detector distance, the fluorescence-wavelength photon-fluence rate reduces faster along the longitudinal direction and slower along the azimuthal direction in the concave geometry, and conversely in the convex geometry. However, the Born ratio increases slower in both azimuthal and longitudinal directions in the concave geometry and faster in both directions in the convex geometry, respectively, when compared to that in the semi-infinite geometry. © 2013 Optical Society of America

OCIS codes: 170.3660, 170.5280, 170.6280, 170.6960, 170.7050.

1. INTRODUCTION

Diffuse optical tomography enhanced with fluorescence contrast [1–4] is an active area of optically rendered imaging that has the potential to achieve molecular sensitivity and high specificity in diagnosis. A surface measurement of the fluorescence photon to resolve the distribution of an endogenous [5] or exogenous [6,7] fluorophore usually involves an array of illumination and detection points at the medium–applicator interface. The medium–applicator interface, relevant to reflective-mode diffuse fluorescence measurements, may be idealized by three geometries: (1) a semi-infinite geometry whereby the medium bounds with an infinite planar applicator [8], (2) a "concave" geometry whereby the medium is enclosed by an infinitely long circularly curved applicator [9,10], and (3) a "convex" geometry whereby the medium encloses an infinitely long circularly curved applicator [11]. Photon propagation in any of these geometries could be modeled by diffusion as long as the measurement distance exceeds several times of the transport scattering scale [12,13]. Abundant numerical resources are available for forward quantization of the fluorescence photon diffusion in arbitrary geometries [1–7]. Yet analytical treatment is of fundamental interest in revealing the effect of a particular geometry on fluorescence photon diffusion. Examples of the analytical modeling of fluorescence photon diffusion for infinite and semi-infinite geometries can be found in [14–16], and for concave geometry in [17]; however, an analytical modeling of fluorescence photon diffusion in convex geometry is outstanding. It is appreciable for both concave and convex geometries that as the radius of the geometry becomes infinite, the associated reflective measurement must converge to the measurement associated with the semi-infinite geometry.

Analytical treatments to reflective measurement of photon diffusion applying to both concave and convex geometries that are infinite in the longitudinal direction have been developed recently [18]. The validity of the models in the diffusion regime was demonstrated by Monte Carlo and experimental methods for steady-state measurements [19], and by the finite-element method (FEM) for frequency-domain (FD) measurements [20]. The models illustrate that the DC and AC photon-fluence rates evaluated along the longitudinal and azimuthal directions of either concave or convex geometry have an opposite pattern of changes when compared to those along a straight line on a semi-infinite interface, with respect to the same source–detector distance. However, the pattern of opposite changes between along the longitudinal and azimuthal directions is not observed for the modulation depth and phase of FD measurement, indicating a "lumped" effect of the shape of the geometry upon the modulation depth and phase. Extrapolating these findings to fluorescence measurement, it is expectable that the fluorescence-wavelength photon-fluence rate might reveal an opposite pattern of changes along the longitudinal and azimuthal directions, and furthermore a parameter that represents the "lumped" effect of the shape of the geometry on fluorescence measurement could also be speculated. One term that is of interest is the so-called Born ratio [21–23], which refers to normalization of the photon fluence at the fluorescence wavelength to that at the excitation wavelength [24].

As Part V in our series, this paper investigates steady-state fluorescence photon diffusion, to study the effect of concave and convex shapes of the geometry when compared to the semi-infinite geometry on reflective measurements of a homogenous medium. The study is specific to having a uniform distribution of flurophores, as there is always some degree of background fluorescence due to intrinsic tissue fluorochromes (auto-fluorescence) or nonspecific bio-distribution of the fluorescence dye or fluorescence probe injected [24]. The analytical treatment employs the extrapolated zero-boundary condition [25–27] by implementing the "image" source method [28]. The solutions for each of the three bounded geometries contain three parts, the first one attributed to the physical source, the second one attributed to the mirror image of the physical source with respect to the boundary, and the third one representing a shell effect specific to the extrapolated boundary. Approximations at a large radius of either concave or convex geometry reveal that the changing pattern of the fluorescence-wavelength fluence rate with respect to the source–detector distance is similar to that of the excitation-wavelength fluence rate, in terms of the opposite trends along the longitudinal and azimuthal directions. However, the change of the Born ratio with respect to the same source–detector distance is always slower in concave and faster in convex geometries, compared to the semi-infinite geometry. FEM modeling is implemented for concave and convex geometries of practical dimensions to examine qualitatively the shape effect of the geometry on steady-state fluorescence photon diffusion.

2. STEADY-STATE FLUORESCENCE IN INFINITE AND SEMI-INFINITE GEOMETRIES

This section first formulates the analytics associated with an infinite medium containing a uniform distribution of fluorophores that amounts to the Born ratio derived in [23]. The analytics are then applied to the semi-infinite medium geometry, to provide a closed-form representation of the effect of the extrapolated boundary condition that was initially indicated in [14].

A. Infinite Geometry

Figure 1A depicts an infinite scattering medium that has a diffusion coefficient $D = [3(\mu_a + \mu_s')]^{-1}$, where μ_a is the absorption coefficient and μ_s' is the reduced scattering coefficient. We use $S^{\mathrm{ex}}(\vec{r}\,') = S \cdot \delta(\vec{r} - \vec{r}\,')$ to symbolize a CW isotropic point source of intensity S at the excitation wavelength that locates at $\vec{r}\,'$, and we use $\bullet\vec{r}^{\,\mathrm{fl}}$ to represent an infinitesimal fluorophore element located at $\vec{r}^{\,\mathrm{fl}}$, and define $\vec{r}$ as the field point or the detector. The CW photon-fluence rate at the excitation wavelength originating from $S^{\mathrm{ex}}(\vec{r}\,')$ and reaching $\vec{r}$ is represented by $\Psi^{\mathrm{ex}}(\vec{r}\,' \to \vec{r})$, and that reaching $\bullet\vec{r}^{\,\mathrm{fl}}$ is represented by $\Psi^{\mathrm{ex}}(\vec{r}\,' \to \bullet\vec{r}^{\,\mathrm{fl}})$. Under $\Psi^{\mathrm{ex}}(\vec{r}\,' \to \bullet\vec{r}^{\,\mathrm{fl}})$ the fluorophore element $\bullet\vec{r}^{\,\mathrm{fl}}$ becomes a secondary CW isotropic point source at the fluorescence wavelength [14], which is symbolized by

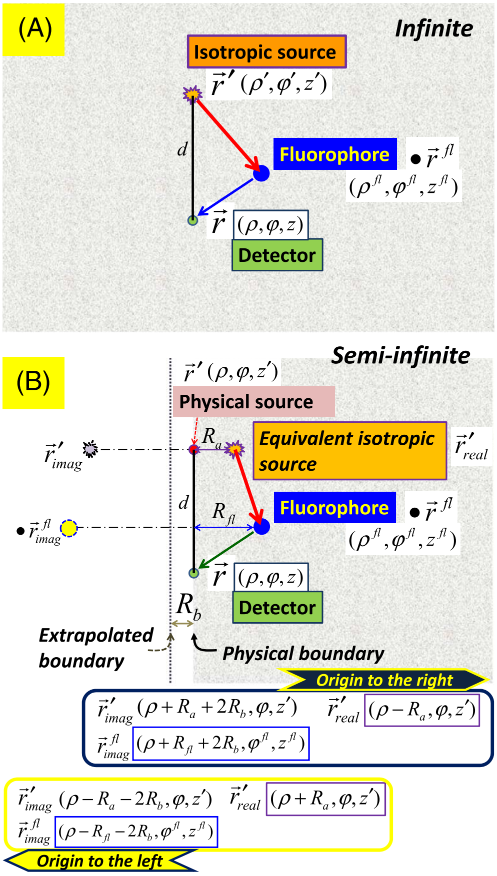

Fig. 1. (Color online) Illustrations of a medium of infinite geometry (A) and a medium of semi-infinite geometry (B). In the semi-infinite geometry, the directional source and the detector are positioned on the physical boundary of the medium, and it becomes convenient to assign the same radial and azimuthal coordinates to the source and detector. The implementation of the extrapolated zero-boundary condition introduces the image of the equivalent isotropic source and the image of the fluorophore element with respect to the extrapolated boundary.

$Q^{\mathrm{fl}}(\bullet\vec{r}^{\,\mathrm{fl}}) = \bullet Q^{\mathrm{fl}} \cdot \delta(\vec{r} - \vec{r}^{\,\mathrm{fl}})$ and has the following intensity:

$$\bullet Q^{\mathrm{fl}} = \eta\mu_a^{\mathrm{fl}}\Psi^{\mathrm{ex}}(\vec{r}\,' \to \bullet\vec{r}^{\,\mathrm{fl}}), \tag{1}$$

where μ_a^{fl} is the absorption coefficient of the fluorophore at the excitation wavelength, and η is the fluorescence quantum yield when ignoring the saturation effect and secondary pathways of fluorescence [14]. The CW Ψ^{fl} originating from $Q^{\mathrm{fl}}(\bullet\vec{r}^{\,\mathrm{fl}})$ and reaching $\vec{r}$ is symbolized as $\Psi^{\mathrm{fl}}(\bullet\vec{r}^{\,\mathrm{fl}} \Rightarrow \vec{r})$. The CW Ψ^{fl} originating from $Q^{\mathrm{fl}}(\bullet\vec{r}^{\,\mathrm{fl}})$ as a result of the excitation by $S^{\mathrm{ex}}(\vec{r}\,')$ and reaching $\vec{r}$ is expressed as $\Psi^{\mathrm{fl}}(\vec{r}\,' \to \bullet\vec{r}^{\,\mathrm{fl}} \Rightarrow \vec{r})$, and that originating from ***ALL*** (symbolized by "$\forall$") fluorophore elements in the medium being excited by $S^{\mathrm{ex}}(\vec{r}\,')$ and reaching $\vec{r}$ is represented by $\Psi^{\mathrm{fl}}(\vec{r}\,' \to \forall\vec{r}^{\,\mathrm{fl}} \Rightarrow \vec{r})$. Note that the "→" sign in Ψ refers to evaluation at the excitation wavelength, and the "⇒" sign at the fluorescence wavelength.

As our main goal is to assess the effect of the shape (either concave or convex) of the cylindrical curvature to Ψ^{fl} when compared to the semi-infinite planar geometry, including the mismatch of optical properties at fluorescence and excitation wavelengths would introduce additional variations that make the analytics less explicit [14,15,21–24]. We therefore suppose for all studied geometries that the optical properties of the fluorophore, as well as the background medium, are identical at the excitation and emission wavelengths. This hypothesis is actually largely justified in the near infrared [24]. As this study concerns a homogenous medium containing a homogenous distribution of the fluorophore, the effective attenuation coefficient is

$$k_0 = \sqrt{\frac{\mu_a^{\mathrm{total}}}{D^{\mathrm{total}}}}, \tag{2}$$

where μ_a^{total} and D^{total} are, respectively, the total absorption and diffusion coefficients of the medium containing the fluorophore, and will be represented by μ_a and D, respectively, hereafter. The CW photon-fluence rates Ψ^{ex} and Ψ^{fl} satisfy the following equations [14–17,21–24]:

$$\nabla^2\Psi_{\mathrm{inf}}^{\mathrm{ex}}(\vec{r}) - k_0^2\Psi_{\mathrm{inf}}^{\mathrm{ex}}(\vec{r}) = -\frac{S^{\mathrm{ex}}(\vec{r})}{D}, \tag{3}$$

$$\nabla^2\Psi_{\mathrm{inf}}^{\mathrm{fl}}(\vec{r}) - k_0^2\Psi_{\mathrm{inf}}^{\mathrm{fl}}(\vec{r}) = -\frac{Q^{\mathrm{fl}}(\vec{r})}{D}. \tag{4}$$

In cylindrical coordinates, we analyze Ψ^{ex} from the source $S^{\mathrm{ex}}(\vec{r}\,')$ at $\vec{r}\,'(\rho',\phi',z')$ to the fluorophore element $\bullet\vec{r}^{\,\mathrm{fl}}$ at $\vec{r}^{\,\mathrm{fl}}(\rho^{\mathrm{fl}},\phi^{\mathrm{fl}},z^{\mathrm{fl}})$, and the resulting Ψ^{fl} from the fluorescing source element $Q^{\mathrm{fl}}(\bullet\vec{r}^{\,\mathrm{fl}})$ at $\vec{r}^{\,\mathrm{fl}}(\rho^{\mathrm{fl}},\phi^{\mathrm{fl}},z^{\mathrm{fl}})$ to the detector at $\vec{r}\ (\rho,\phi,z)$, for the infinite geometry as well as for the other medium geometries investigated in this study.

B. Semi-Infinite Geometry

A medium of semi-infinite geometry with the physical source and the detector located on the medium boundary is depicted in Fig. 1B. In semi-infinite geometry, it becomes convenient to assign the same radial and azimuthal coordinates to the physical source and the detector. Then the physical source $S^{\mathrm{ex}}(\vec{r}\,')$ locates at $\vec{r}\,'(\rho,\phi,z')$ and the detector locates at $\vec{r}\ (\rho,\phi,z)$. The physical source $S^{\mathrm{ex}}(\vec{r}\,')$ launches the photon into the medium at an initial direction orthogonal to the medium–applicator interface, and is treated as an equivalent "real" isotropic point source located one step of transport scattering, $R_a = 1/\mu_s'$, into the medium [29]. The "real" isotropic source, denoted by $S^{\mathrm{ex}}(\vec{r}\,'_{\mathrm{real}}) = S\cdot\delta(\vec{r} - \vec{r}\,'_{\mathrm{real}})$, has the coordinates $\vec{r}\,'_{\mathrm{real}}(\rho - R_a,\phi,z')$ or $\vec{r}\,'_{\mathrm{real}}(\rho + R_a,\phi,z')$, respectively, for the origin at the medium side or opposite to the medium side. The effect of the medium–applicator interface on photon diffusion at the excitation wavelength may be modeled by an extrapolated zero-boundary condition [25–28], which sets zero Ψ^{ex} at an imaginary boundary located $R_b = 2AD$ off the physical boundary, where $A = (1 + R_{\mathrm{eff}})/(1 - R_{\mathrm{eff}})$ and R_{eff} is a coefficient [25,28] determined by the refractive index differences across the physical boundary. This extrapolated zero-boundary condition is accommodated by setting a sink or a negative "image" of the "real" isotropic source $S^{\mathrm{ex}}(\vec{r}\,'_{\mathrm{real}})$, with respect to the extrapolated boundary. This "image" source that produces a Ψ^{ex} to be "negated" at any field point is denoted by $S^{\mathrm{ex}}(\vec{r}\,'_{\mathrm{imag}}) = S\cdot\delta(\vec{r} - \vec{r}\,'_{\mathrm{imag}})$. The "image" source $S^{\mathrm{ex}}(\vec{r}\,'_{\mathrm{imag}})$ has the strength of the "real" isotropic source $S^{\mathrm{ex}}(\vec{r}\,'_{\mathrm{real}})$, and locates at $\vec{r}\,'_{\mathrm{imag}}(\rho + R_a + 2R_b,\phi,z')$ or $\vec{r}\,'_{\mathrm{imag}}(\rho - R_a - 2R_b,\phi,z')$, respectively, for the origin at the medium side or opposite to the medium side. Then on the extrapolated boundary Ω the following condition is satisfied:

$$\Psi_{\mathrm{semi}}^{\mathrm{ex}}(\vec{r}) = \Psi_{\mathrm{inf}}^{\mathrm{ex}}(\vec{r}\,'_{\mathrm{real}} \to \vec{r}) - \Psi_{\mathrm{inf}}^{\mathrm{ex}}(\vec{r}\,'_{\mathrm{imag}} \to \vec{r}) = 0 \quad \text{for } \vec{r} \in \Omega. \tag{5}$$

The distances from the "real" isotropic source $S^{\mathrm{ex}}(\vec{r}\,'_{\mathrm{real}})$ and its "image" $S^{\mathrm{ex}}(\vec{r}\,'_{\mathrm{imag}})$ to the detector at $\vec{r}$ are denoted by $l_{\mathrm{real}} = |\vec{r}\,'_{\mathrm{real}} - \vec{r}\,|$ and $l_{\mathrm{imag}} = |\vec{r}\,'_{\mathrm{imag}} - \vec{r}\,|$, respectively. The straight-line distance between the physical source $S^{\mathrm{ex}}(\vec{r}\,')$ and the detector, $d = |\vec{r}\,' - \vec{r}\,|$, is referred to as the "line-of-sight" source–detector distance, and is hereafter abbreviated as source–detector distance in all studied geometries. It is with respect to this source–detector distance d that the changing characteristics of Ψ^{fl} and $\Psi^{\mathrm{fl}}/\Psi^{\mathrm{ex}}$ are evaluated among different geometries.

In the semi-infinite geometry, the fluorescing source element $Q^{\mathrm{fl}}(\bullet\vec{r}^{\,\mathrm{fl}}) = \bullet Q^{\mathrm{fl}}\cdot\delta(\vec{r} - \vec{r}^{\,\mathrm{fl}})$ due to the excitation of the fluorophore element $\bullet\vec{r}^{\,\mathrm{fl}}$ locates at $\vec{r}^{\,\mathrm{fl}}(\rho - R_{\mathrm{fl}},\phi^{\mathrm{fl}},z^{\mathrm{fl}})$ or $\vec{r}^{\,\mathrm{fl}}(\rho + R_{\mathrm{fl}},\phi^{\mathrm{fl}},z^{\mathrm{fl}})$, respectively, for the origin at the medium side or opposite to the medium side. The effect of the medium–applicator interface on photon diffusion at the fluorescence wavelength may also be modeled by the extrapolated zero-boundary condition, by setting zero Ψ^{fl} on the same imaginary boundary located $R_b = 2AD$ off the physical boundary as that for the Ψ^{ex}, following the assumption of wavelength independence of D. This extrapolated zero-boundary condition is also accommodated by setting a sink or a negative "image" of the fluorescing source element $Q^{\mathrm{fl}}(\bullet\vec{r}^{\,\mathrm{fl}})$ with respect to the extrapolated boundary. This "image" fluorescing source element that produces a Ψ^{fl} to be "negated" at any field point is denoted by $Q^{\mathrm{fl}}(\bullet\vec{r}^{\,\mathrm{fl}}_{\mathrm{imag}})$. The "image" fluorescing source element $Q^{\mathrm{fl}}(\bullet\vec{r}^{\,\mathrm{fl}}_{\mathrm{imag}})$ has the strength of the "real" fluorescing source element $Q^{\mathrm{fl}}(\bullet\vec{r}^{\,\mathrm{fl}})$, and is located at $\vec{r}^{\,\mathrm{fl}}_{\mathrm{imag}}(\rho + R_{\mathrm{fl}} + 2R_b,\phi^{\mathrm{fl}},z^{\mathrm{fl}})$ or $\vec{r}^{\,\mathrm{fl}}_{\mathrm{imag}}(\rho - R_{\mathrm{fl}} - 2R_b,\phi^{\mathrm{fl}},z^{\mathrm{fl}})$, respectively, for the origin at the medium side or opposite to the medium side. Then the following condition is satisfied:

$$\Psi_{\mathrm{semi}}^{\mathrm{fl}}(\vec{r}) = \Psi_{\mathrm{inf}}^{\mathrm{fl}}(\bullet\vec{r}^{\,\mathrm{fl}} \to \vec{r}) - \Psi_{\mathrm{inf}}^{\mathrm{fl}}(\bullet\vec{r}^{\,\mathrm{fl}}_{\mathrm{imag}} \to \vec{r}) = 0 \quad \text{for } \vec{r} \in \Omega. \tag{6}$$

The distances from the "real" isotropic source $S^{\mathrm{ex}}(\vec{r}\,'_{\mathrm{real}})$ and the "image" source $S^{\mathrm{ex}}(\vec{r}\,'_{\mathrm{imag}})$ to the fluorophore element $\bullet\vec{r}^{\,\mathrm{fl}}$ are denoted by $l_{\mathrm{real}}^{\mathrm{ex}} = |\vec{r}\,'_{\mathrm{real}} - \vec{r}^{\,\mathrm{fl}}|$ and $l_{\mathrm{imag}}^{\mathrm{ex}} = |\vec{r}\,'_{\mathrm{imag}} - \vec{r}^{\,\mathrm{fl}}|$, respectively. The distances from the fluorescing source element $Q^{\mathrm{fl}}(\bullet\vec{r}^{\,\mathrm{fl}})$ and its "image" $Q^{\mathrm{fl}}(\bullet\vec{r}^{\,\mathrm{fl}}_{\mathrm{imag}})$ to the detector at $\vec{r}$ are denoted by $l_{\mathrm{real}}^{\mathrm{fl}} = |\vec{r}^{\,\mathrm{fl}} - \vec{r}\,|$ and $l_{\mathrm{imag}}^{\mathrm{fl}} = |\vec{r}^{\,\mathrm{fl}}_{\mathrm{imag}} - \vec{r}\,|$, respectively. These notations, $l_{\mathrm{real}}^{\mathrm{ex}}$, $l_{\mathrm{imag}}^{\mathrm{ex}}$, $l_{\mathrm{real}}^{\mathrm{fl}}$, and $l_{\mathrm{imag}}^{\mathrm{fl}}$, and the previously introduced l_{real} and l_{imag}, also apply to other studied medium geometries involving a boundary.

It is noted by Eqs. (5) and (6) that we treat $\Psi_{\mathrm{inf}}^{\mathrm{ex}}$ and $\Psi_{\mathrm{inf}}^{\mathrm{fl}}$ that satisfy the boundary condition as being always positive, and use the sign of "+" or "−" proceeding them to signify the contribution that a specific $\Psi_{\mathrm{inf}}^{\mathrm{ex}}$ or $\Psi_{\mathrm{inf}}^{\mathrm{fl}}$ makes at a field point. So the $\Psi_{\mathrm{semi}}^{\mathrm{fl}}$ at a physically existing field point will be the $\Psi_{\mathrm{inf}}^{\mathrm{fl}}$ by the "real" fluorescing source subtracting the $\Psi_{\mathrm{inf}}^{\mathrm{fl}}$ by the "image" fluorescing source. As will be shown in Section 2.C.2, it becomes imperative to evaluate the $\Psi_{\mathrm{inf}}^{\mathrm{ex}}$ by a "real" source or an "image" of it, upon a "real" field point (specifically the fluorophore element) or an "image" of it. These "real" or "image" sources and "real" or "image" field points result in four cases of $\Psi_{\mathrm{inf}}^{\mathrm{ex}}$ to be determined based on the "image-source" method: (1) one by a "real" source upon a physically existing field point, (2) one by an “image” source upon a physically existing field point, (3) one by a “real” source upon the “image” of a physically existing field point with respect to the extrapolated zero boundary, and (4) one by the “image” source upon the “image” of a physically existing field point with respect to the extrapolated zero boundary. Then the $\Psi^{\mathrm{ex}}_{\mathrm{semi}}$ at a physically existing field point is the $\Psi^{\mathrm{ex}}_{\mathrm{inf}}$ produced by the “real” source subtracting the $\Psi^{\mathrm{ex}}_{\mathrm{inf}}$ produced by the “image” source, whereas the $\Psi^{\mathrm{ex}}_{\mathrm{inf}}$ at an “image” field point is found as the $\Psi^{\mathrm{ex}}_{\mathrm{inf}}$ produced by the “image” source to be subtracted from the $\Psi^{\mathrm{ex}}_{\mathrm{inf}}$ produced by the “real” source.

C. Solutions in Spherical Coordinates to Steady-State Fluorescence Associated with a Homogenous Medium and a Uniform Distribution of the Fluorophore

1. Source and Detector in an Infinite Medium Geometry

The spherical-coordinates solution to Eq. (3) and $S^{\mathrm{ex}}(\vec{r}\,') = S\cdot\delta(\vec{r}-\vec{r}\,')$ is well known:

$$\Psi^{\mathrm{ex}}_{\mathrm{inf}}(\vec{r}\,'\to\vec{r}\,) = \frac{S}{4\pi D}\frac{\exp(-k_0|\vec{r}\,'-\vec{r}\,|)}{|\vec{r}\,'-\vec{r}\,|}. \tag{7}$$

Similarly, the spherical-coordinates solution to Eq. (4) and $Q^{\mathrm{fl}}(\vec{r}^{\,\mathrm{fl}}) = Q\cdot\delta(\vec{r}-\vec{r}^{\,\mathrm{fl}})$ is

$$\Psi^{\mathrm{fl}}_{\mathrm{inf}}(\vec{r}^{\,\mathrm{fl}}\Rightarrow\vec{r}\,) = \frac{Q}{4\pi D}\frac{\exp(-k_0|\vec{r}^{\,\mathrm{fl}}-\vec{r}\,|)}{|\vec{r}^{\,\mathrm{fl}}-\vec{r}\,|}. \tag{8}$$

The fluorophore element $\bullet\vec{r}^{\,\mathrm{fl}}$ due to excitation by $S^{\mathrm{ex}}(\vec{r}\,')$ becomes a fluorescing source element $Q^{\mathrm{fl}}(\bullet\vec{r}^{\,\mathrm{fl}})$ that has the following intensity:

$$\bullet Q^{\mathrm{fl}} = \eta\mu_a^{\mathrm{fl}}\Psi^{\mathrm{ex}}_{\mathrm{inf}}(\vec{r}\,'\to\bullet\vec{r}^{\,\mathrm{fl}}) = \frac{\eta\mu_a^{\mathrm{fl}}S}{4\pi D}\frac{\exp(-k_0|\vec{r}\,'-\vec{r}^{\,\mathrm{fl}}|)}{|\vec{r}\,'-\vec{r}^{\,\mathrm{fl}}|}. \tag{9}$$

Then $\Psi^{\mathrm{fl}}_{\mathrm{inf}}$ excited by $S^{\mathrm{ex}}(\vec{r}\,')$ upon the fluorophore element $\bullet\vec{r}^{\,\mathrm{fl}}$ and reaching $\vec{r}$ is expressed as

$$\begin{aligned}\Psi^{\mathrm{fl}}_{\mathrm{inf}}(\vec{r}\,'\to\bullet\vec{r}^{\,\mathrm{fl}}\Rightarrow\vec{r}\,) &= \frac{\bullet Q^{\mathrm{fl}}}{4\pi D}\frac{\exp(-k_0|\vec{r}^{\,\mathrm{fl}}-\vec{r}\,|)}{|\vec{r}^{\,\mathrm{fl}}-\vec{r}\,|}\\ &= \frac{\eta\mu_a^{\mathrm{fl}}S}{(4\pi D)^2}\frac{\exp(-k_0|\vec{r}\,'-\vec{r}^{\,\mathrm{fl}}|)}{|\vec{r}\,'-\vec{r}^{\,\mathrm{fl}}|}\frac{\exp(-k_0|\vec{r}^{\,\mathrm{fl}}-\vec{r}\,|)}{|\vec{r}^{\,\mathrm{fl}}-\vec{r}\,|}.\end{aligned} \tag{10}$$

For the medium containing a uniform distribution of the fluorophore, the $\Psi^{\mathrm{fl}}_{\mathrm{inf}}$ that is excited by $S^{\mathrm{ex}}(\vec{r}\,')$ upon ***ALL*** fluorophore elements and reaches the detector at $\vec{r}$ is

$$\begin{aligned}\Psi^{\mathrm{fl}}_{\mathrm{inf}}(\vec{r}\,'\to\forall\,\vec{r}^{\,\mathrm{fl}}\Rightarrow\vec{r}\,) &= \iiint\Psi^{\mathrm{fl}}_{\mathrm{inf}}(\vec{r}\,'\to\bullet\vec{r}^{\,\mathrm{fl}}\Rightarrow\vec{r}\,)\mathrm{d}^3\vec{r}^{\,\mathrm{fl}}\\ &= \frac{\eta\mu_a^{\mathrm{fl}}S}{8\pi k_0 D^2}\exp(-k_0|\vec{r}\,'-\vec{r}\,|),\end{aligned} \tag{11}$$

the derivation of which relies upon the following identity [14,23]:

$$\begin{aligned}&\iiint\frac{\exp(-k_0|\vec{r}\,'-\vec{r}^{\,\mathrm{fl}}|)}{|\vec{r}\,'-\vec{r}^{\,\mathrm{fl}}|}\frac{\exp(-k_0|\vec{r}^{\,\mathrm{fl}}-\vec{r}\,|)}{|\vec{r}^{\,\mathrm{fl}}-\vec{r}\,|}\mathrm{d}^3\vec{r}^{\,\mathrm{fl}}\\ &= \frac{2\pi}{k_0}\exp(-k_0|\vec{r}\,'-\vec{r}\,|).\end{aligned} \tag{12}$$

In Eq. (12) and other equations that involve integrating over ***ALL*** fluorophore elements of the given domain, i.e., $\iiint\mathrm{d}^3\vec{r}^{\,\mathrm{fl}} = \iiint\rho^{\mathrm{fl}}\mathrm{d}\rho^{\mathrm{fl}}\mathrm{d}\phi^{\mathrm{fl}}\mathrm{d}z^{\mathrm{fl}}$, the range of a specific integral dimension is omitted if performed over the entire space, unless otherwise becoming necessary to specify.

2. Source and Detector on a Semi-Infinite Medium–Applicator Interface

For a source and a detector located on a semi-infinite boundary to a homogenous medium, the solution in spherical coordinates to Eq. (3) in response to $S^{\mathrm{ex}}(\vec{r}\,') = S\cdot\delta(\vec{r}-\vec{r}\,')$ that satisfies the extrapolated zero-boundary condition (5) is

$$\begin{aligned}\Psi^{\mathrm{ex}}_{\mathrm{semi}}(\vec{r}\,'\to\vec{r}\,) &= \Psi^{\mathrm{ex}}_{\mathrm{inf}}(\vec{r}\,'_{\mathrm{real}}\to\vec{r}\,) - \Psi^{\mathrm{ex}}_{\mathrm{inf}}(\vec{r}\,'_{\mathrm{imag}}\to\vec{r}\,)\\ &= \frac{S}{4\pi D}\frac{\exp(-k_0|\vec{r}\,'_{\mathrm{real}}-\vec{r}\,|)}{|\vec{r}\,'_{\mathrm{real}}-\vec{r}\,|}\\ &\quad-\frac{S}{4\pi D}\frac{\exp(-k_0|\vec{r}\,'_{\mathrm{imag}}-\vec{r}\,|)}{|\vec{r}\,'_{\mathrm{imag}}-\vec{r}\,|}.\end{aligned} \tag{13}$$

Similarly the $\Psi^{\mathrm{ex}}_{\mathrm{semi}}$ evaluated at the fluorophore element $\bullet\vec{r}^{\,\mathrm{fl}}$ is

$$\begin{aligned}\Psi^{\mathrm{ex}}_{\mathrm{semi}}(\vec{r}\,'\to\bullet\vec{r}^{\,\mathrm{fl}}) &= \Psi^{\mathrm{ex}}_{\mathrm{inf}}(\vec{r}\,'_{\mathrm{real}}\to\bullet\vec{r}^{\,\mathrm{fl}}) - \Psi^{\mathrm{ex}}_{\mathrm{inf}}(\vec{r}\,'_{\mathrm{imag}}\to\bullet\vec{r}^{\,\mathrm{fl}})\\ &= \frac{S}{4\pi D}\frac{\exp(-k_0|\vec{r}\,'_{\mathrm{real}}-\vec{r}^{\,\mathrm{fl}}|)}{|\vec{r}\,'_{\mathrm{real}}-\vec{r}^{\,\mathrm{fl}}|}\\ &\quad-\frac{S}{4\pi D}\frac{\exp(-k_0|\vec{r}\,'_{\mathrm{imag}}-\vec{r}^{\,\mathrm{fl}}|)}{|\vec{r}\,'_{\mathrm{imag}}-\vec{r}^{\,\mathrm{fl}}|}.\end{aligned} \tag{14}$$

So the intensity of the fluorescing source element $Q^{\mathrm{fl}}(\bullet\vec{r}^{\,\mathrm{fl}})$ due to excitation by $S^{\mathrm{ex}}(\vec{r}\,')$ is

$$\begin{aligned}\bullet Q^{\mathrm{fl}} &= \eta\mu_a^{\mathrm{fl}}\Psi^{\mathrm{ex}}_{\mathrm{semi}}(\vec{r}\,'\to\bullet\vec{r}^{\,\mathrm{fl}})\\ &= \eta\mu_a^{\mathrm{fl}}[\Psi^{\mathrm{ex}}_{\mathrm{inf}}(\vec{r}\,'_{\mathrm{real}}\to\bullet\vec{r}^{\,\mathrm{fl}}) - \Psi^{\mathrm{ex}}_{\mathrm{inf}}(\vec{r}\,'_{\mathrm{imag}}\to\bullet\vec{r}^{\,\mathrm{fl}})].\end{aligned} \tag{15}$$

Then the spherical-coordinates solution to Eq. (4) in response to the fluorescing source element $Q^{\mathrm{fl}}(\bullet\vec{r}^{\,\mathrm{fl}})$ that satisfies the extrapolated zero-boundary condition (6) is

$$\begin{aligned}\Psi^{\mathrm{fl}}_{\mathrm{semi}}(\bullet\vec{r}^{\,\mathrm{fl}}\Rightarrow\vec{r}\,) &= \Psi^{\mathrm{fl}}_{\mathrm{inf}}(\bullet\vec{r}^{\,\mathrm{fl}}\Rightarrow\vec{r}\,) - \Psi^{\mathrm{fl}}_{\mathrm{inf}}(\bullet\vec{r}^{\,\mathrm{fl}}_{\mathrm{imag}}\Rightarrow\vec{r}\,)\\ &= \frac{\bullet Q^{\mathrm{fl}}}{4\pi D}\frac{\exp(-k_0|\vec{r}^{\,\mathrm{fl}}-\vec{r}\,|)}{|\vec{r}^{\,\mathrm{fl}}-\vec{r}\,|}\\ &\quad-\frac{\bullet Q^{\mathrm{fl}}_{\mathrm{imag}}}{4\pi D}\frac{\exp(-k_0|\vec{r}^{\,\mathrm{fl}}_{\mathrm{imag}}-\vec{r}\,|)}{|\vec{r}^{\,\mathrm{fl}}_{\mathrm{imag}}-\vec{r}\,|}.\end{aligned} \tag{16}$$

In the semi-infinite geometry, it is straightforward to obtain that

$$\begin{aligned}\bullet Q^{\mathrm{fl}}_{\mathrm{imag}} &= [\bullet Q^{\mathrm{fl}}]_{\mathrm{imag}} = \left[\eta\mu_a^{\mathrm{fl}}\Psi^{\mathrm{ex}}_{\mathrm{semi}}(\vec{r}\,'\to\bullet\vec{r}^{\,\mathrm{fl}})\right]_{\mathrm{imag}}\\ &= \eta\mu_a^{\mathrm{fl}}\left[\Psi^{\mathrm{ex}}_{\mathrm{inf}}(\vec{r}\,'_{\mathrm{real}}\to\bullet\vec{r}^{\,\mathrm{fl}}) - \Psi^{\mathrm{ex}}_{\mathrm{inf}}(\vec{r}\,'_{\mathrm{imag}}\to\bullet\vec{r}^{\,\mathrm{fl}})\right]_{\mathrm{imag}}\\ &= \eta\mu_a^{\mathrm{fl}}\left[\Psi^{\mathrm{ex}}_{\mathrm{inf}}(\vec{r}\,'_{\mathrm{imag}}\to\bullet\vec{r}^{\,\mathrm{fl}}_{\mathrm{imag}}) - \Psi^{\mathrm{ex}}_{\mathrm{inf}}(\vec{r}\,'_{\mathrm{real}}\to\bullet\vec{r}^{\,\mathrm{fl}}_{\mathrm{imag}})\right],\end{aligned} \tag{17}$$

where $\Psi^{\mathrm{ex}}_{\mathrm{inf}}(\vec{r}'_{\mathrm{imag}} \to \bullet\vec{r}^{\mathrm{fl}}_{\mathrm{imag}})$ is the $\Psi^{\mathrm{ex}}_{\mathrm{inf}}$ by the “image” source $S^{\mathrm{ex}}(\vec{r}'_{\mathrm{imag}})$ upon the “image” fluorophore element $\bullet\vec{r}^{\mathrm{fl}}_{\mathrm{imag}}$, and $\Psi^{\mathrm{ex}}_{\mathrm{inf}}(\vec{r}'_{\mathrm{real}} \to \bullet\vec{r}^{\mathrm{fl}}_{\mathrm{imag}})$ is the $\Psi^{\mathrm{ex}}_{\mathrm{inf}}$ by the “real” source $S^{\mathrm{ex}}(\vec{r}'_{\mathrm{real}})$ upon the “image” fluorophore element $\bullet\vec{r}^{\mathrm{fl}}_{\mathrm{imag}}$. Then $\Psi^{\mathrm{fl}}_{\mathrm{semi}}$ by the fluorophore element $\bullet\vec{r}^{\mathrm{fl}}$ due to the excitation of $S^{\mathrm{ex}}(\vec{r}')$ upon the detector at $\vec{r}$ is

$$\begin{aligned}
&\Psi^{\mathrm{fl}}_{\mathrm{semi}}(\vec{r}' \to \bullet\vec{r}^{\mathrm{fl}} \Rightarrow \vec{r})\\
&= \frac{\eta\mu_a^{\mathrm{fl}}}{4\pi D}\left[\Psi^{\mathrm{ex}}_{\mathrm{inf}}(\vec{r}'_{\mathrm{real}} \to \bullet\vec{r}^{\mathrm{fl}})\right]\frac{\exp(-k_0|\vec{r}^{\mathrm{fl}}-\vec{r}|)}{|\vec{r}^{\mathrm{fl}}-\vec{r}|}\\
&\quad - \frac{\eta\mu_a^{\mathrm{fl}}}{4\pi D}\left[\Psi^{\mathrm{ex}}_{\mathrm{inf}}(\vec{r}'_{\mathrm{imag}} \to \bullet\vec{r}^{\mathrm{fl}})\right]\frac{\exp(-k_0|\vec{r}^{\mathrm{fl}}-\vec{r}|)}{|\vec{r}^{\mathrm{fl}}-\vec{r}|}\\
&\quad - \frac{\eta\mu_a^{\mathrm{fl}}}{4\pi D}\left[\Psi^{\mathrm{ex}}_{\mathrm{inf}}(\vec{r}'_{\mathrm{imag}} \to \bullet\vec{r}^{\mathrm{fl}}_{\mathrm{imag}})\right]\frac{\exp(-k_0|\vec{r}^{\mathrm{fl}}_{\mathrm{imag}}-\vec{r}|)}{|\vec{r}^{\mathrm{fl}}_{\mathrm{imag}}-\vec{r}|}\\
&\quad + \frac{\eta\mu_a^{\mathrm{fl}}}{4\pi D}\left[\Psi^{\mathrm{ex}}_{\mathrm{inf}}(\vec{r}'_{\mathrm{real}} \to \bullet\vec{r}^{\mathrm{fl}}_{\mathrm{imag}})\right]\frac{\exp(-k_0|\vec{r}^{\mathrm{fl}}_{\mathrm{imag}}-\vec{r}|)}{|\vec{r}^{\mathrm{fl}}_{\mathrm{imag}}-\vec{r}|}\\
&= \Psi^{\mathrm{fl}}_{\mathrm{inf}}(\vec{r}'_{\mathrm{real}} \to \bullet\vec{r}^{\mathrm{fl}} \Rightarrow \vec{r}) - \Psi^{\mathrm{fl}}_{\mathrm{inf}}(\vec{r}'_{\mathrm{imag}} \to \bullet\vec{r}^{\mathrm{fl}} \Rightarrow \vec{r})\\
&\quad + \Psi^{\mathrm{fl}}_{\mathrm{inf}}(\vec{r}'_{\mathrm{real}} \to \bullet\vec{r}^{\mathrm{fl}}_{\mathrm{imag}} \Rightarrow \vec{r}) - \Psi^{\mathrm{fl}}_{\mathrm{inf}}(\vec{r}'_{\mathrm{imag}} \to \bullet\vec{r}^{\mathrm{fl}}_{\mathrm{imag}} \Rightarrow \vec{r}), \qquad (18)
\end{aligned}$$

where $\Psi^{\mathrm{fl}}_{\mathrm{inf}}(\vec{r}'_{\mathrm{real}} \to \bullet\vec{r}^{\mathrm{fl}} \Rightarrow \vec{r})$ is the $\Psi^{\mathrm{fl}}_{\mathrm{inf}}$ associated with $\bullet\vec{r}^{\mathrm{fl}}$ due to an excitation by $S^{\mathrm{ex}}(\vec{r}'_{\mathrm{real}})$ and reaching $\vec{r}$, $\Psi^{\mathrm{fl}}_{\mathrm{inf}}(\vec{r}'_{\mathrm{imag}} \to \bullet\vec{r}^{\mathrm{fl}} \Rightarrow \vec{r})$ is the $\Psi^{\mathrm{fl}}_{\mathrm{inf}}$ associated with $\bullet\vec{r}^{\mathrm{fl}}$ due to an excitation by $S^{\mathrm{ex}}(\vec{r}'_{\mathrm{imag}})$ and reaching $\vec{r}$, $\Psi^{\mathrm{fl}}_{\mathrm{inf}}(\vec{r}'_{\mathrm{real}} \to \bullet\vec{r}^{\mathrm{fl}}_{\mathrm{imag}} \Rightarrow \vec{r})$ is the $\Psi^{\mathrm{fl}}_{\mathrm{inf}}$ associated with $\bullet\vec{r}^{\mathrm{fl}}_{\mathrm{imag}}$ due to an excitation by $S^{\mathrm{ex}}(\vec{r}'_{\mathrm{real}})$ and reaching $\vec{r}$, and $\Psi^{\mathrm{fl}}_{\mathrm{inf}}(\vec{r}'_{\mathrm{imag}} \to \bullet\vec{r}^{\mathrm{fl}}_{\mathrm{imag}} \Rightarrow \vec{r})$ is the $\Psi^{\mathrm{fl}}_{\mathrm{inf}}$ associated with $\bullet\vec{r}^{\mathrm{fl}}_{\mathrm{imag}}$ due to an excitation by $S^{\mathrm{ex}}(\vec{r}'_{\mathrm{imag}})$ and reaching $\vec{r}$.

For the medium containing a uniform distribution of the fluorophore, the $\Psi^{\mathrm{fl}}_{\mathrm{semi}}$ reaching the detector at $\vec{r}$ that accounts for ***ALL*** fluorophore elements due to excitation by $S^{\mathrm{ex}}(\vec{r}')$, with the origin opposite to the medium side, is

$$\begin{aligned}
&\Psi^{\mathrm{fl}}_{\mathrm{semi}}(\vec{r}' \to \forall\,\vec{r}^{\mathrm{fl}} \Rightarrow \vec{r})\\
&\quad = \iint_{\rho^{\mathrm{fl}}=\rho}^{\infty}\int \Psi^{\mathrm{fl}}_{\mathrm{semi}}(\vec{r}' \to \bullet\vec{r}^{\mathrm{fl}} \Rightarrow \vec{r})\mathrm{d}^3\vec{r}^{\mathrm{fl}}\\
&\quad = \iint_{\rho^{\mathrm{fl}}=\rho}^{\infty}\int \Psi^{\mathrm{fl}}_{\mathrm{inf}}(\vec{r}'_{\mathrm{real}} \to \bullet\vec{r}^{\mathrm{fl}} \Rightarrow \vec{r})\mathrm{d}^3\vec{r}^{\mathrm{fl}}\\
&\qquad - \iint_{\rho^{\mathrm{fl}}=\rho}^{\infty}\int \Psi^{\mathrm{fl}}_{\mathrm{inf}}(\vec{r}'_{\mathrm{imag}} \to \bullet\vec{r}^{\mathrm{fl}} \Rightarrow \vec{r})\mathrm{d}^3\vec{r}^{\mathrm{fl}}\\
&\qquad + \iint_{\rho^{\mathrm{fl}}=\rho}^{\infty}\int \Psi^{\mathrm{fl}}_{\mathrm{inf}}(\vec{r}'_{\mathrm{real}} \to \bullet\vec{r}^{\mathrm{fl}}_{\mathrm{imag}} \Rightarrow \vec{r})\mathrm{d}^3\vec{r}^{\mathrm{fl}}\\
&\qquad - \iint_{\rho^{\mathrm{fl}}=\rho}^{\infty}\int \Psi^{\mathrm{fl}}_{\mathrm{inf}}(\vec{r}'_{\mathrm{imag}} \to \bullet\vec{r}^{\mathrm{fl}}_{\mathrm{imag}} \Rightarrow \vec{r})\mathrm{d}^3\vec{r}^{\mathrm{fl}}. \qquad (19)
\end{aligned}$$

The first integral of Eq. (19) decomposes into three parts, one over the entire space as symbolized by $\rho^{\mathrm{fl}} = (-\infty, \infty)$ that becomes $\Psi^{\mathrm{fl}}_{\mathrm{inf}}(\vec{r}'_{\mathrm{real}} \to \forall\,\vec{r}^{\mathrm{fl}} \Rightarrow \vec{r})$, one over the mirrored space of the medium with respect to the extrapolated boundary as symbolized by $\rho^{\mathrm{fl}} = (-\infty, \rho - 2R_b)$, and one over the shell region dissected by the extrapolated boundary as symbolized by $\rho^{\mathrm{fl}} = (\rho - 2R_b, \rho)$, resulting in the following equation:

$$\begin{aligned}
&\iint_{\rho^{\mathrm{fl}}=\rho}^{\infty}\int \Psi^{\mathrm{fl}}_{\mathrm{inf}}(\vec{r}'_{\mathrm{real}} \to \bullet\vec{r}^{\mathrm{fl}} \Rightarrow \vec{r})\mathrm{d}^3\vec{r}^{\mathrm{fl}}\\
&\quad = \Psi^{\mathrm{fl}}_{\mathrm{inf}}(\vec{r}'_{\mathrm{real}} \to \forall\,\vec{r}^{\mathrm{fl}} \Rightarrow \vec{r})\\
&\qquad - \iint_{\rho^{\mathrm{fl}}=\rho-2R_b}^{\rho}\int \Psi^{\mathrm{fl}}_{\mathrm{inf}}(\vec{r}'_{\mathrm{real}}\\
&\qquad \to \bullet\vec{r}^{\mathrm{fl}} \Rightarrow \vec{r})\mathrm{d}^3\vec{r}^{\mathrm{fl}}\\
&\qquad - \iint_{\rho^{\mathrm{fl}}=-\infty}^{\rho-2R_b}\int \Psi^{\mathrm{fl}}_{\mathrm{inf}}(\vec{r}'_{\mathrm{real}}\\
&\qquad \to \bullet\vec{r}^{\mathrm{fl}} \Rightarrow \vec{r})\mathrm{d}^3\vec{r}^{\mathrm{fl}}. \qquad (20)
\end{aligned}$$

Similarly, the second integral of Eq. (19) becomes

$$\begin{aligned}
&\iint_{\rho^{\mathrm{fl}}=\rho}^{\infty}\int \Psi^{\mathrm{fl}}_{\mathrm{inf}}(\vec{r}'_{\mathrm{imag}} \to \bullet\vec{r}^{\mathrm{fl}} \Rightarrow \vec{r})\mathrm{d}^3\vec{r}^{\mathrm{fl}}\\
&\quad = \Psi^{\mathrm{fl}}_{\mathrm{inf}}(\vec{r}'_{\mathrm{imag}} \to \forall\,\vec{r}^{\mathrm{fl}} \Rightarrow \vec{r})\\
&\qquad - \iint_{\rho^{\mathrm{fl}}=\rho-2R_b}^{\rho}\int \Psi^{\mathrm{fl}}_{\mathrm{inf}}(\vec{r}'_{\mathrm{imag}} \to \bullet\vec{r}^{\mathrm{fl}} \Rightarrow \vec{r})\mathrm{d}^3\vec{r}^{\mathrm{fl}}\\
&\qquad - \iint_{\rho^{\mathrm{fl}}=-\infty}^{\rho-2R_b}\int \Psi^{\mathrm{fl}}_{\mathrm{inf}}(\vec{r}'_{\mathrm{imag}} \to \bullet\vec{r}^{\mathrm{fl}} \Rightarrow \vec{r})\mathrm{d}^3\vec{r}^{\mathrm{fl}}. \qquad (21)
\end{aligned}$$

Substituting Eqs. (20) and (21) into (19), we have

$$\begin{aligned}
&\Psi^{\mathrm{fl}}_{\mathrm{semi}}(\vec{r}' \to \forall\,\vec{r}^{\mathrm{fl}} \Rightarrow \vec{r})\\
&\quad = \Psi^{\mathrm{fl}}_{\mathrm{inf}}(\vec{r}'_{\mathrm{real}} \to \forall\,\vec{r}^{\mathrm{fl}} \Rightarrow \vec{r}) - \Psi^{\mathrm{fl}}_{\mathrm{inf}}(\vec{r}'_{\mathrm{imag}} \to \forall\,\vec{r}^{\mathrm{fl}} \Rightarrow \vec{r})\\
&\qquad - \iint_{\rho^{\mathrm{fl}}=\rho-2R_b}^{\rho}\int \Psi^{\mathrm{fl}}_{\mathrm{inf}}(\vec{r}'_{\mathrm{real}} \to \bullet\vec{r}^{\mathrm{fl}} \Rightarrow \vec{r})\mathrm{d}^3\vec{r}^{\mathrm{fl}}\\
&\qquad - \iint_{\rho^{\mathrm{fl}}=-\infty}^{\rho-2R_b}\int \Psi^{\mathrm{fl}}_{\mathrm{inf}}(\vec{r}'_{\mathrm{real}} \to \bullet\vec{r}^{\mathrm{fl}} \Rightarrow \vec{r})\mathrm{d}^3\vec{r}^{\mathrm{fl}}\\
&\qquad + \iint_{\rho^{\mathrm{fl}}=\rho-2R_b}^{\rho}\int \Psi^{\mathrm{fl}}_{\mathrm{inf}}(\vec{r}'_{\mathrm{imag}} \to \bullet\vec{r}^{\mathrm{fl}} \Rightarrow \vec{r})\mathrm{d}^3\vec{r}^{\mathrm{fl}}\\
&\qquad + \iint_{\rho^{\mathrm{fl}}=-\infty}^{\rho-2R_b}\int \Psi^{\mathrm{fl}}_{\mathrm{inf}}(\vec{r}'_{\mathrm{imag}} \to \bullet\vec{r}^{\mathrm{fl}} \Rightarrow \vec{r})\mathrm{d}^3\vec{r}^{\mathrm{fl}}\\
&\qquad + \iint_{\rho^{\mathrm{fl}}=\rho}^{\infty}\int \Psi^{\mathrm{fl}}_{\mathrm{inf}}(\vec{r}'_{\mathrm{real}} \to \bullet\vec{r}^{\mathrm{fl}}_{\mathrm{imag}} \Rightarrow \vec{r})\mathrm{d}^3\vec{r}^{\mathrm{fl}}\\
&\qquad - \iint_{\rho^{\mathrm{fl}}=\rho}^{\infty}\int \Psi^{\mathrm{fl}}_{\mathrm{inf}}(\vec{r}'_{\mathrm{imag}} \to \bullet\vec{r}^{\mathrm{fl}}_{\mathrm{imag}} \Rightarrow \vec{r})\mathrm{d}^3\vec{r}^{\mathrm{fl}}. \qquad (22)
\end{aligned}$$

We note that in Eq. (22), as the integration variable r^{fl} moves over the mirrored space of the real medium with respect to the extrapolated boundary, $r^{\mathrm{fl}}_{\mathrm{imag}}$ moves over the space of the real medium, the sixth integral is identical to the fourth integral, and the second integral is identical to the fifth integral in Eq. (22). Then Eq. (22) simplifies to

$$\begin{aligned}
&\Psi^{\mathrm{fl}}_{\mathrm{semi}}(\vec{r}' \to \forall\,\vec{r}^{\mathrm{fl}} \Rightarrow \vec{r})\\
&= \Psi^{\mathrm{fl}}_{\mathrm{inf}}(\vec{r}'_{\mathrm{real}} \to \forall\,\vec{r}^{\mathrm{fl}} \Rightarrow \vec{r}) - \Psi^{\mathrm{fl}}_{\mathrm{inf}}(\vec{r}'_{\mathrm{imag}} \to \forall\,\vec{r}^{\mathrm{fl}} \Rightarrow \vec{r})\\
&\quad - \iint_{\rho^{\mathrm{fl}}=\rho-2R_b}^{\rho}\int [\Psi^{\mathrm{fl}}_{\mathrm{inf}}(\vec{r}'_{\mathrm{real}} \to \bullet\vec{r}^{\mathrm{fl}} \Rightarrow \vec{r})\\
&\quad - \Psi^{\mathrm{fl}}_{\mathrm{inf}}(\vec{r}'_{\mathrm{imag}} \to \bullet\vec{r}^{\mathrm{fl}} \Rightarrow \vec{r})]\mathrm{d}^3\vec{r}^{\mathrm{fl}}. \qquad (23)
\end{aligned}$$

The integral term in Eq. (23) corresponds to the “real” and “image” sources exciting the hypothetical fluorophore uniformly distributed within a $2R_b$ shell off the physical boundary, in order to satisfy the extrapolated zero-boundary condition necessary for reaching the solutions in the physical domain of the fluorophore. The existence of this term, called a "$2R_b$-shell" term in this study, was first discussed in [14], which did not provide a closed form of it and ignored it when computing $\Psi^{\text{fl}}_{\text{semi}}$ using the other two terms in Eq. (23).

3. STEADY-STATE FLUORESCENCE ASSOCIATED WITH "CONCAVE" AND "CONVEX" GEOMETRIES OF INFINITE LONGITUDINAL DIMENSION

A. Concave Geometry

The "concave" geometry as shown in Fig. 2A refers to a diffusive medium ***enclosed*** by an infinitely long cylindrical medium–applicator interface. The radius of the cylinder is R_0, a detector on the interface locates at $\vec{r}(R_0,\phi,z)$, and a directional source $S^{\text{ex}}(\vec{r}\,')$ on the interface locates at $\vec{r}\,'(R_0,\phi',z')$. The geometric symmetry requires that the directional source $S^{\text{ex}}(\vec{r}\,')$ is modeled by a "real" isotropic point source $S^{\text{ex}}(\vec{r}\,'_{\text{real}}) = S\cdot\delta(\vec{r}-\vec{r}\,'_{\text{real}})$ positioned ***inward*** along the radial direction of $\vec{r}\,'$ at a distance of $R_a = 1/\mu_s'$, i.e., at $\vec{r}\,'_{\text{real}}(R_0-R_a,\phi',z')$. The effect of the medium–applicator interface on photon diffusion at the excitation wavelength is modeled by setting zero $\Psi^{\text{ex}}_{\text{semi}}$ on a boundary that is concentric with and at a radial distance of $R_b = 2AD$ ***outward*** from the physical boundary [18]. This boundary condition is accommodated by setting a sink or a negative "image" of the "real" isotropic source $S^{\text{ex}}(\vec{r}\,'_{\text{real}})$, with respect to the extrapolated boundary. The "image" source that produces a "negating" Ψ^{ex} is denoted by $S^{\text{ex}}(\vec{r}\,'_{\text{imag}}) = S^*\cdot\delta(\vec{r}-\vec{r}\,'_{\text{imag}})$, whose strength reaches that of $S^{\text{ex}}(\vec{r}\,'_{\text{real}})$ as $R_0\to\infty$, and locates at $\vec{r}\,'_{\text{imag}}(\rho^?,\phi',z')$, of which the radial coordinate $\rho^?$ reaches R_a+2R_b outward from the boundary as $R_0\to\infty$. Then on the extrapolated boundary $\vec{r}\in\Omega$ or $\rho\in R_0+R_b$, the condition of Eq. (5) is satisfied.

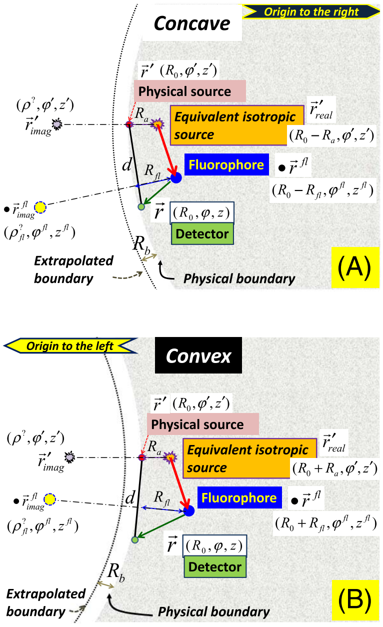

Fig. 2. (Color online) Illustrations of a medium of concave geometry (A) and a medium of convex geometry (B). In both geometries, the directional source and the detector are positioned on the physical boundary of the medium. The implementation of extrapolated zero-boundary condition introduces the image of the equivalent isotropic source along the radial direction of the source, and the image of the fluorophore element along the radial direction of the element.

In the concave geometry, the fluorescing source element $Q^{\text{fl}}(\bullet\vec{r}^{\,\text{fl}}) = \bullet Q^{\text{fl}}\cdot\delta(\vec{r}-\vec{r}^{\,\text{fl}})$ due to excitation of the fluorophore element $\bullet\vec{r}^{\,\text{fl}}$ locates at $\vec{r}^{\,\text{fl}}(R_0-R_{\text{fl}},\phi^{\text{fl}},z^{\text{fl}})$. The effect of the medium–applicator interface on photon diffusion at the fluorescence wavelength is modeled by setting zero $\Psi^{\text{fl}}_{\text{semi}}$ on the same extrapolated boundary of $\Psi^{\text{ex}}_{\text{semi}}$. This boundary condition is also accommodated by setting a sink or a negative "image" of the fluorescing source element $Q^{\text{fl}}(\bullet\vec{r}^{\,\text{fl}})$, with respect to the extrapolated boundary. This "image" fluorescing source element that produces a "negating" Ψ^{fl} is denoted by $Q^{\text{fl}}(\bullet\vec{r}^{\,\text{fl}}_{\text{imag}}) = *Q^{\text{fl}}_{\text{imag}}\cdot\delta(\vec{r}-\vec{r}^{\,\text{fl}}_{\text{imag}})$, whose strength reaches that of $Q^{\text{fl}}(\bullet\vec{r}^{\,\text{fl}})$ as $R_0\to\infty$, and locates at $\vec{r}^{\,\text{fl}}_{\text{imag}}(\rho^?_{\text{fl}},\phi^{\text{fl}},z^{\text{fl}})$, of which the radial coordinate $\rho^?_{\text{fl}}$ reaches R_a+2R_b outward from the boundary as $R_0\to\infty$. Then on the extrapolated boundary $\vec{r}\in\Omega$ or $\rho\in R_0+R_b$, the condition of Eq. (6) is satisfied.

For a source–detector pair located on a concave boundary to a homogenous medium, the cylindrical-coordinates solution to Eqs. (3), (5), and $S^{\text{ex}}(\vec{r}\,') = S\cdot\delta(\vec{r}-\vec{r}\,')$ is [18]

$$\begin{aligned}\Psi^{\text{ex}}_{\text{conC}}(\vec{r}\,'\to\vec{r}) &= \Psi^{\text{ex}}_{\text{inf}}(\vec{r}\,'_{\text{real}}\to\vec{r}) - \Psi^{\text{ex}}_{\text{inf}}(\vec{r}\,'_{\text{imag}}\to\vec{r})\\ &= \frac{S}{4\pi^2 D}\int_{-\infty}^{\infty}\mathrm{d}k\left\{e^{ik(z'-z)}\sum_{m=-\infty}^{\infty} I_m[k_{\text{eff}}(R_0-R_a)]\right.\\ &\quad\left.\times K_m(k_{\text{eff}}R_0)e^{im(\phi'-\phi)}\right\}\\ &\quad-\frac{S}{4\pi^2 D}\int_{-\infty}^{\infty}\mathrm{d}k\left\{e^{ik(z'-z)}\sum_{m=-\infty}^{\infty} I_m[k_{\text{eff}}(R_0-R_a)]\right.\\ &\quad\left.\times I_m(k_{\text{eff}}R_0)\frac{K_m[k_{\text{eff}}(R_0+R_b)]}{I_m[k_{\text{eff}}(R_0+R_b)]}e^{im(\phi'-\phi)}\right\},\end{aligned}\tag{24}$$

where

$$k_{\text{eff}} = \sqrt{k^2+k_0^2}.\tag{25}$$

As the $\Psi^{\text{ex}}_{\text{conC}}$ reaching the fluorophore element $\bullet\vec{r}^{\,\text{fl}}$ is

$$\Psi^{\text{ex}}_{\text{conC}}(\vec{r}\,'\to\bullet\vec{r}^{\,\text{fl}}) = \Psi^{\text{ex}}_{\text{inf}}(\vec{r}\,'_{\text{real}}\to\bullet\vec{r}^{\,\text{fl}}) - \Psi^{\text{ex}}_{\text{inf}}(\vec{r}\,'_{\text{imag}}\to\bullet\vec{r}^{\,\text{fl}}),\tag{26}$$

the intensity of the fluorescing source element $Q^{\text{fl}}(\bullet\vec{r}^{\,\text{fl}})$ due to excitation by $S^{\text{ex}}(\vec{r}\,')$ is

$$\begin{aligned}\bullet Q^{\text{fl}} &= \eta\mu_a^{\text{fl}}\Psi^{\text{ex}}_{\text{conC}}(\vec{r}\,'\to\bullet\vec{r}^{\,\text{fl}})\\ &= \eta\mu_a^{\text{fl}}[\Psi^{\text{ex}}_{\text{inf}}(\vec{r}\,'_{\text{real}}\to\bullet\vec{r}^{\,\text{fl}}) - \Psi^{\text{ex}}_{\text{inf}}(\vec{r}\,'_{\text{imag}}\to\bullet\vec{r}^{\,\text{fl}})].\end{aligned}\tag{27}$$

The cylindrical-coordinates solution to Eq. (4) due to the fluorescing source element $Q^{\text{fl}}(\bullet\vec{r}^{\,\text{fl}})$ that satisfies the extrapolated boundary condition (6) is

$$\begin{aligned}\Psi^{\mathrm{fl}}_{\mathrm{conC}}(\bullet\vec{r}^{\,\mathrm{fl}} \Rightarrow \vec{r}) &= \Psi^{\mathrm{fl}}_{\mathrm{inf}}(\bullet\vec{r}^{\,\mathrm{fl}} \Rightarrow \vec{r}) - \Psi^{\mathrm{fl}}_{\mathrm{inf}}(\bullet\vec{r}^{\,\mathrm{fl}}_{\mathrm{imag}} \Rightarrow \vec{r})\\ &= \frac{\bullet Q^{\mathrm{fl}}}{4\pi^2 D}\int_{-\infty}^{\infty}\mathrm{d}k\left\{e^{ik(z^{\mathrm{fl}}-z)}\sum_{m=-\infty}^{\infty} I_m[k_{\mathrm{eff}}(R_0-R_{\mathrm{fl}})]\right.\\ &\quad\left.\times K_m(k_{\mathrm{eff}}R_0)e^{im(\phi^{\mathrm{fl}}-\phi)}\right\}\\ &\quad-\frac{\bullet Q^{\mathrm{fl}}}{4\pi^2 D}\int_{-\infty}^{\infty}\mathrm{d}k\left\{e^{ik(z^{\mathrm{fl}}-z)}\sum_{m=-\infty}^{\infty} I_m[k_{\mathrm{eff}}(R_0-R_{\mathrm{fl}})]\right.\\ &\quad\left.\times I_m(k_{\mathrm{eff}}R_0)\frac{K_m[k_{\mathrm{eff}}(R_0+R_b)]}{I_m[k_{\mathrm{eff}}(R_0+R_b)]}e^{im(\phi^{\mathrm{fl}}-\phi)}\right\}.\end{aligned} \tag{28}$$

In concave geometry, it can be shown that (see Appendix A)

$$\Psi^{\mathrm{ex}}_{\mathrm{inf}}(\vec{r}'_{\mathrm{imag}} \to \bullet\vec{r}^{\,\mathrm{fl}}) = \Psi^{\mathrm{ex}}_{\mathrm{inf}}(\vec{r}'_{\mathrm{real}} \to \bullet\vec{r}^{\,\mathrm{fl}}_{\mathrm{imag}}) \quad \text{and}$$
$$\Psi^{\mathrm{ex}}_{\mathrm{inf}}(\vec{r}'_{\mathrm{real}} \to \bullet\vec{r}^{\,\mathrm{fl}}) = \Psi^{\mathrm{ex}}_{\mathrm{inf}}(\vec{r}'_{\mathrm{imag}} \to \bullet\vec{r}^{\,\mathrm{fl}}_{\mathrm{imag}}), \tag{29}$$

where the two terms $\Psi^{\mathrm{ex}}_{\mathrm{inf}}(\vec{r}'_{\mathrm{real}} \to \bullet\vec{r}^{\,\mathrm{fl}}_{\mathrm{imag}})$ and $\Psi^{\mathrm{ex}}_{\mathrm{inf}}(\vec{r}'_{\mathrm{imag}} \to \bullet\vec{r}^{\,\mathrm{fl}}_{\mathrm{imag}})$ are similar in definition to those in Section 2.C.2. Based on Eqs. (26)–(29), we can find the $\Psi^{\mathrm{fl}}_{\mathrm{conC}}$ associated with $\bullet\vec{r}^{\,\mathrm{fl}}$ due to excitation by $S^{\mathrm{ex}}(\vec{r}\,')$ and reaching $\vec{r}$ as

$$\begin{aligned}&\Psi^{\mathrm{fl}}_{\mathrm{conC}}(\vec{r}\,' \to \bullet\vec{r}^{\,\mathrm{fl}} \Rightarrow \vec{r})\\ &= \Psi^{\mathrm{fl}}_{\mathrm{inf}}(\vec{r}'_{\mathrm{real}} \to \bullet\vec{r}^{\,\mathrm{fl}} \Rightarrow \vec{r}) - \Psi^{\mathrm{fl}}_{\mathrm{inf}}(\vec{r}'_{\mathrm{imag}} \to \bullet\vec{r}^{\,\mathrm{fl}} \Rightarrow \vec{r})\\ &\quad + \Psi^{\mathrm{fl}}_{\mathrm{inf}}(\vec{r}'_{\mathrm{real}} \to \bullet\vec{r}^{\,\mathrm{fl}}_{\mathrm{imag}} \Rightarrow \vec{r}) - \Psi^{\mathrm{fl}}_{\mathrm{inf}}(\vec{r}'_{\mathrm{imag}} \to \bullet\vec{r}^{\,\mathrm{fl}}_{\mathrm{imag}} \Rightarrow \vec{r}),\end{aligned} \tag{30}$$

where the four terms $\Psi^{\mathrm{fl}}_{\mathrm{inf}}(\vec{r}\,'_{\mathrm{real}} \to \bullet\vec{r}^{\,\mathrm{fl}} \Rightarrow \vec{r})$, $\Psi^{\mathrm{fl}}_{\mathrm{inf}}(\vec{r}\,'_{\mathrm{imag}} \to \bullet\vec{r}^{\,\mathrm{fl}} \Rightarrow \vec{r})$, $\Psi^{\mathrm{fl}}_{\mathrm{inf}}(\vec{r}'_{\mathrm{real}} \to \bullet\vec{r}^{\,\mathrm{fl}}_{\mathrm{imag}} \Rightarrow \vec{r})$, and $\Psi^{\mathrm{fl}}_{\mathrm{inf}}(\vec{r}'_{\mathrm{imag}} \to \bullet\vec{r}^{\,\mathrm{fl}}_{\mathrm{imag}} \Rightarrow \vec{r})$ are similar in definition to those in Section 2.C.2.

For the medium containing a uniform distribution of the fluorophore, the $\Psi^{\mathrm{fl}}_{\mathrm{conC}}$ reaching $\vec{r}$ that accounts for ***ALL*** fluorophore elements due to excitation by $S^{\mathrm{ex}}(\vec{r}\,')$ is

$$\begin{aligned}&\Psi^{\mathrm{fl}}_{\mathrm{conC}}(\vec{r}\,' \to \forall\,\vec{r}^{\,\mathrm{fl}} \Rightarrow \vec{r})\\ &= \iint_{\rho^{\mathrm{fl}}=0}^{R_0}\int \Psi^{\mathrm{fl}}_{\mathrm{conC}}(\vec{r}\,' \to \bullet\vec{r}^{\,\mathrm{fl}} \Rightarrow \vec{r})\mathrm{d}^3\vec{r}^{\,\mathrm{fl}}\\ &= \iint_{\rho^{\mathrm{fl}}=0}^{R_0}\int \Psi^{\mathrm{fl}}_{\mathrm{inf}}(\vec{r}'_{\mathrm{real}} \to \bullet\vec{r}^{\,\mathrm{fl}} \Rightarrow \vec{r})\mathrm{d}^3\vec{r}^{\,\mathrm{fl}}\\ &\quad - \iint_{\rho^{\mathrm{fl}}=0}^{R_0}\int \Psi^{\mathrm{fl}}_{\mathrm{inf}}(\vec{r}'_{\mathrm{imag}} \to \bullet\vec{r}^{\,\mathrm{fl}} \Rightarrow \vec{r})\mathrm{d}^3\vec{r}^{\,\mathrm{fl}}\\ &\quad + \iint_{\rho^{\mathrm{fl}}=0}^{R_0}\int \Psi^{\mathrm{fl}}_{\mathrm{inf}}(\vec{r}'_{\mathrm{real}} \to \bullet\vec{r}^{\,\mathrm{fl}}_{\mathrm{imag}} \Rightarrow \vec{r})\mathrm{d}^3\vec{r}^{\,\mathrm{fl}}\\ &\quad - \iint_{\rho^{\mathrm{fl}}=0}^{R_0}\int \Psi^{\mathrm{fl}}_{\mathrm{inf}}(\vec{r}'_{\mathrm{imag}} \to \bullet\vec{r}^{\,\mathrm{fl}}_{\mathrm{imag}} \Rightarrow \vec{r})\mathrm{d}^3\vec{r}^{\,\mathrm{fl}}.\end{aligned} \tag{31}$$

In Eq. (31), the first integral can be decomposed to three parts, including one over $\rho^{\mathrm{fl}} = (0,\infty)$ to become $\Psi^{\mathrm{fl}}_{\mathrm{inf}}(\vec{r}'_{\mathrm{real}} \to \forall\,\vec{r}^{\,\mathrm{fl}} \Rightarrow \vec{r})$, one over $\rho^{\mathrm{fl}} = (R_0, R_0 + 2R_b)$, and one over $\rho^{\mathrm{fl}} = (R_0 + 2R_b, \infty)$ as follows:

$$\begin{aligned}&\iint_{\rho^{\mathrm{fl}}=0}^{R_0}\int \Psi^{\mathrm{fl}}_{\mathrm{inf}}(\vec{r}\,'_{\mathrm{real}} \to \bullet\vec{r}^{\,\mathrm{fl}} \Rightarrow \vec{r})\mathrm{d}^3\vec{r}^{\,\mathrm{fl}}\\ &= \Psi^{\mathrm{fl}}_{\mathrm{inf}}(\vec{r}\,'_{\mathrm{real}} \to \forall\,\vec{r}^{\,\mathrm{fl}} \Rightarrow \vec{r})\\ &\quad - \iint_{\rho^{\mathrm{fl}}=R_0}^{R_0+2R_b}\int \Psi^{\mathrm{fl}}_{\mathrm{inf}}(\vec{r}\,'_{\mathrm{real}} \to \bullet\vec{r}^{\,\mathrm{fl}} \Rightarrow \vec{r})\mathrm{d}^3\vec{r}^{\,\mathrm{fl}}\\ &\quad - \iint_{\rho^{\mathrm{fl}}=R_0+2R_b}^{\infty}\int \Psi^{\mathrm{fl}}_{\mathrm{inf}}(\vec{r}\,'_{\mathrm{real}} \to \bullet\vec{r}^{\,\mathrm{fl}} \Rightarrow \vec{r})\mathrm{d}^3\vec{r}^{\,\mathrm{fl}}.\end{aligned} \tag{32}$$

In Eq. (31), the second integral can also be decomposed into three parts as follows:

$$\begin{aligned}&\iint_{\rho^{\mathrm{fl}}=0}^{R_0}\int \Psi^{\mathrm{fl}}_{\mathrm{inf}}(\vec{r}\,'_{\mathrm{imag}} \to \bullet\vec{r}^{\,\mathrm{fl}} \Rightarrow \vec{r})\mathrm{d}^3\vec{r}^{\,\mathrm{fl}}\\ &= \Psi^{\mathrm{fl}}_{\mathrm{inf}}(\vec{r}\,'_{\mathrm{imag}} \to \forall\,\vec{r}^{\,\mathrm{fl}} \Rightarrow \vec{r})\\ &\quad - \iint_{\rho^{\mathrm{fl}}=R_0}^{R_0+2R_b}\int \Psi^{\mathrm{fl}}_{\mathrm{inf}}(\vec{r}\,'_{\mathrm{imag}} \to \bullet\vec{r}^{\,\mathrm{fl}} \Rightarrow \vec{r})\mathrm{d}^3\vec{r}^{\,\mathrm{fl}}\\ &\quad - \iint_{\rho^{\mathrm{fl}}=R_0+2R_b}^{\infty}\int \Psi^{\mathrm{fl}}_{\mathrm{inf}}(\vec{r}\,'_{\mathrm{imag}} \to \bullet\vec{r}^{\,\mathrm{fl}} \Rightarrow \vec{r})\mathrm{d}^3\vec{r}^{\,\mathrm{fl}}.\end{aligned} \tag{33}$$

Substituting Eqs. (32) and (33) into (31), we have

$$\begin{aligned}&\Psi^{\mathrm{fl}}_{\mathrm{conC}}(\vec{r}\,' \to \forall\,\vec{r}^{\,\mathrm{fl}} \Rightarrow \vec{r})\\ &= \Psi^{\mathrm{fl}}_{\mathrm{inf}}(\vec{r}\,'_{\mathrm{real}} \to \forall\,\vec{r}^{\,\mathrm{fl}} \Rightarrow \vec{r}) - \Psi^{\mathrm{fl}}_{\mathrm{inf}}(\vec{r}\,'_{\mathrm{imag}} \to \forall\,\vec{r}^{\,\mathrm{fl}} \Rightarrow \vec{r})\\ &\quad - \iint_{\rho^{\mathrm{fl}}=R_0}^{R_0+2R_b}\int \Psi^{\mathrm{fl}}_{\mathrm{inf}}(\vec{r}\,'_{\mathrm{real}} \to \bullet\vec{r}^{\,\mathrm{fl}} \Rightarrow \vec{r})\mathrm{d}^3\vec{r}^{\,\mathrm{fl}}\\ &\quad - \iint_{\rho^{\mathrm{fl}}=R_0+2R_b}^{\infty}\int \Psi^{\mathrm{fl}}_{\mathrm{inf}}(\vec{r}\,'_{\mathrm{real}} \to \bullet\vec{r}^{\,\mathrm{fl}} \Rightarrow \vec{r})\mathrm{d}^3\vec{r}^{\,\mathrm{fl}}\\ &\quad + \iint_{\rho^{\mathrm{fl}}=R_0}^{R_0+2R_b}\int \Psi^{\mathrm{fl}}_{\mathrm{inf}}(\vec{r}\,'_{\mathrm{imag}} \to \bullet\vec{r}^{\,\mathrm{fl}} \Rightarrow \vec{r})\mathrm{d}^3\vec{r}^{\,\mathrm{fl}}\\ &\quad + \iint_{\rho^{\mathrm{fl}}=R_0+2R_b}^{\infty}\int \Psi^{\mathrm{fl}}_{\mathrm{inf}}(\vec{r}\,'_{\mathrm{imag}} \to \bullet\vec{r}^{\,\mathrm{fl}} \Rightarrow \vec{r})\mathrm{d}^3\vec{r}^{\,\mathrm{fl}}\\ &\quad + \iint_{\rho^{\mathrm{fl}}=0}^{R_0}\int \Psi^{\mathrm{fl}}_{\mathrm{inf}}(\vec{r}\,'_{\mathrm{real}} \to \bullet\vec{r}^{\,\mathrm{fl}}_{\mathrm{imag}} \Rightarrow \vec{r})\mathrm{d}^3\vec{r}^{\,\mathrm{fl}}\\ &\quad - \iint_{\rho^{\mathrm{fl}}=0}^{R_0}\int \Psi^{\mathrm{fl}}_{\mathrm{inf}}(\vec{r}\,'_{\mathrm{imag}} \to \bullet\vec{r}^{\,\mathrm{fl}}_{\mathrm{imag}} \Rightarrow \vec{r})\mathrm{d}^3\vec{r}^{\,\mathrm{fl}}.\end{aligned} \tag{34}$$

Notice that in Eq. (34) the second integral is in fact identical to the fifth integral, and the fourth integral is in fact identical to the sixth integral. Canceling these four integrals makes Eq. (33) as

$$\begin{aligned}&\Psi^{\mathrm{fl}}_{\mathrm{conC}}(\vec{r}\,' \to \forall\,\vec{r}^{\,\mathrm{fl}} \Rightarrow \vec{r})\\ &= \Psi^{\mathrm{fl}}_{\mathrm{inf}}(\vec{r}\,'_{\mathrm{real}} \to \forall\,\vec{r}^{\,\mathrm{fl}} \Rightarrow \vec{r}) - \Psi^{\mathrm{fl}}_{\mathrm{inf}}(\vec{r}\,'_{\mathrm{imag}} \to \forall\,\vec{r}^{\,\mathrm{fl}} \Rightarrow \vec{r})\\ &\quad - \iint_{\rho^{\mathrm{fl}}=R_0}^{R_0+2R_b}\int [\Psi^{\mathrm{fl}}_{\mathrm{inf}}(\vec{r}\,'_{\mathrm{real}} \to \bullet\vec{r}^{\,\mathrm{fl}} \Rightarrow \vec{r})\\ &\quad - \Psi^{\mathrm{fl}}_{\mathrm{inf}}(\vec{r}\,'_{\mathrm{imag}} \to \bullet\vec{r}^{\,\mathrm{fl}} \Rightarrow \vec{r})]\mathrm{d}^3\vec{r}^{\,\mathrm{fl}}.\end{aligned} \tag{35}$$

B. Convex Geometry

The "convex" geometry as shown in Fig. 2B refers to a diffusive medium ***enclosing*** an infinitely long cylindrical medium–applicator interface. The radius of the cylinder is R_0, a detector on the interface locates at $\vec{r}\,(R_0, \phi, z)$, and a directional source $S^{\mathrm{ex}}(\vec{r}\,')$ on the interface locates at $\vec{r}\,'(R_0, \phi', z')$. The geometric symmetry requires that the directional source $S^{\mathrm{ex}}(\vec{r}\,')$ is modeled by a "real" isotropic point source $S^{\mathrm{ex}}(\vec{r}'_{\mathrm{real}}) =$

$S \cdot \delta(\vec{r} - \vec{r}'_{\text{real}})$ positioned ***outward*** along the radial direction of $\vec{r}'$ at a distance of $R_a = 1/\mu_s'$, i.e., at $\vec{r}'_{\text{real}}(R_0 + R_a, \phi', z')$. The effect of the medium–applicator interface on photon diffusion at the excitation wavelength is modeled by setting zero $\Psi^{\text{ex}}_{\text{semi}}$ on a boundary that is concentric with and at a radial distance of $R_b = 2AD$ ***inward*** from the physical boundary [18]. This boundary condition is accommodated by setting a sink or a negative "image" of the "real" isotropic source $S^{\text{ex}}(\vec{r}'_{\text{real}})$, with respect to the extrapolated boundary. The "image" source that produces a "negating" Ψ^{ex} is denoted by $S^{\text{ex}}(\vec{r}'_{\text{imag}}) = S^* \cdot \delta(\vec{r} - \vec{r}'_{\text{imag}})$, whose strength reaches that of $S^{\text{ex}}(\vec{r}'_{\text{real}})$ as $R_0 \to \infty$, and locates at $\vec{r}'_{\text{imag}}(\rho^?, \phi', z')$, of which the radial coordinate $\rho^?$ reaches $R_a + 2R_b$ inward from the boundary as $R_0 \to \infty$. Then on the extrapolated boundary $\vec{r} \in \Omega$ or $\rho \in R_0 - R_b$, the condition of Eq. (5) is satisfied.

For a source–detector pair located on the convex boundary of a homogenous medium, the cylindrical-coordinates solution to Eqs. (3), (5), and $S^{\text{ex}}(\vec{r}') = S \cdot \delta(\vec{r} - \vec{r}')$ is derived by following the analytics of Section 3.A as

$$\begin{aligned}
&\Psi^{\text{ex}}_{\text{conV}}(\vec{r}' \to \vec{r}) \\
&= \Psi^{\text{ex}}_{\text{inf}}(\vec{r}'_{\text{real}} \to \vec{r}) - \Psi^{\text{ex}}_{\text{inf}}(\vec{r}'_{\text{imag}} \to \vec{r}) \\
&= \frac{S}{4\pi^2 D}\int_{-\infty}^{\infty} \mathrm{d}k \Bigg\{ e^{ik(z'-z)} \sum_{m=-\infty}^{\infty} I_m(k_{\text{eff}} R_0) \\
&\quad \times K_m[k_{\text{eff}}(R_0 + R_a)] e^{im(\phi'-\phi)} \Bigg\} \\
&\quad - \frac{S}{4\pi^2 D}\int_{-\infty}^{\infty} \mathrm{d}k \Bigg\{ e^{ik(z'-z)} \sum_{m=-\infty}^{\infty} \frac{I_m[k_{\text{eff}}(R_0 - R_b)]}{K_m[k_{\text{eff}}(R_0 - R_b)]} K_m(k_{\text{eff}} R_0) \\
&\quad \times K_m[k_{\text{eff}}(R_0 + R_a)] e^{im(\phi'-\phi)} \Bigg\}. \qquad (36)
\end{aligned}$$

In the convex geometry, the fluorescing source element $Q^{\text{fl}}(\bullet\vec{r}^{\,\text{fl}}) = \bullet Q^{\text{fl}} \cdot \delta(\vec{r} - \vec{r}^{\,\text{fl}})$ due to excitation of the fluorophore element $\bullet\vec{r}^{\,\text{fl}}$ locates at $\vec{r}^{\,\text{fl}}(R_0 + R_{\text{fl}}, \phi^{\text{fl}}, z^{\text{fl}})$. The effect of the medium–applicator interface on photon diffusion at the fluorescence wavelength is modeled by setting zero $\Psi^{\text{fl}}_{\text{semi}}$ on the same extrapolated boundary of $\Psi^{\text{ex}}_{\text{semi}}$. This boundary condition is also accommodated by setting a sink or a negative "image" of the fluorescing source element $Q^{\text{fl}}(\bullet\vec{r}^{\,\text{fl}})$, with respect to the extrapolated boundary. This "image" fluorescing source element that produces a "negating" Ψ^{fl} is denoted by $Q^{\text{fl}}(\bullet\vec{r}^{\,\text{fl}}_{\text{imag}}) = *Q^{\text{fl}}_{\text{imag}} \cdot \delta(\vec{r} - \vec{r}^{\,\text{fl}}_{\text{imag}})$, whose strength reaches that of $Q^{\text{fl}}(\bullet\vec{r}^{\,\text{fl}})$ as $R_0 \to \infty$, and locates at $\vec{r}^{\,\text{fl}}_{\text{imag}}(\rho^?_{\text{fl}}, \phi^{\text{fl}}, z^{\text{fl}})$, of which the radial coordinate $\rho^?_{\text{fl}}$ reaches $R_a + 2R_b$ inward from the boundary as $R_0 \to \infty$. Then on the extrapolated boundary $\vec{r} \in \Omega$ or $\rho \in R_0 - R_b$, the condition of Eq. (6) is satisfied.

For a source–detector pair located on a convex boundary of a homogenous medium of a homogenous fluorophore distribution, the solution in cylindrical coordinates to Eqs. (4), 6)), and $S^{\text{ex}}(\vec{r}') = S \cdot \delta(\vec{r} - \vec{r}')$ is derived by following the analytics of Section 3.A as

$$\begin{aligned}
&\Psi^{\text{fl}}_{\text{conV}}(\vec{r}' \to \forall\, \vec{r}^{\,\text{fl}} \Rightarrow \vec{r}) \\
&= \Psi^{\text{fl}}_{\text{inf}}(\vec{r}'_{\text{real}} \to \forall\, \vec{r}^{\,\text{fl}} \Rightarrow \vec{r}) - \Psi^{\text{fl}}_{\text{inf}}(\vec{r}'_{\text{imag}} \to \forall\, \vec{r}^{\,\text{fl}} \Rightarrow \vec{r}) \\
&\quad - \iint_{\rho^{\text{fl}}=R_0-2R_b}^{R_0} \int [\Psi^{\text{fl}}_{\text{inf}}(\vec{r}'_{\text{real}} \to \bullet\vec{r}^{\,\text{fl}} \Rightarrow \vec{r}) \\
&\quad - \Psi^{\text{fl}}_{\text{inf}}(\vec{r}'_{\text{imag}} \to \bullet\vec{r}^{\,\text{fl}} \Rightarrow \vec{r})]\mathrm{d}^3\vec{r}^{\,\text{fl}}. \qquad (37)
\end{aligned}$$

4. STEADY-STATE FLUORESCENCE VERSUS SOURCE–DETECTOR DISTANCE IN CONCAVE AND CONVEX GEOMETRIES OF LARGE RADIUS

As the radius of either concave or convex geometry reaches infinity, the reflective measurement associated with either geometry must converge to that associated with the semi-infinite geometry. To illustrate the effect of concave or convex shape on Ψ^{fl} in comparison to the semi-infinite geometry, the following analysis is based on the assumption that the radius of the concave or convex geometry is much greater than the source–detector distance, which is also in the diffusion regime, i.e., $R_0 \gg d \gg R_a, R_b$. For completeness, the case of infinite geometry is also presented.

A. Excitation- and Fluorescence-Wavelength Photon-Fluence Rates with Respect to d

1. *Infinite Geometry*

For the case of an infinite homogenous medium of a uniform fluorophore distribution, we have

$$\Psi^{\text{ex}}_{\text{inf}}(\vec{r}' \to \vec{r}) = \frac{S}{4\pi D}\frac{\exp(-k_0 d)}{d}, \qquad (38)$$

$$\Psi^{\text{fl}}_{\text{inf}}(\vec{r}' \to \forall\, \vec{r}^{\,\text{fl}} \Rightarrow \vec{r}) = \frac{\eta\mu_a^{\text{fl}} S}{8\pi k_0 D^2}\exp(-k_0 d), \qquad (39)$$

2. *Semi-Infinite Geometry*

For a source and a detector located on a semi-infinite boundary of a homogenous medium containing a uniform distribution of the fluorophore, we have

$$\begin{aligned}
|\vec{r}'_{\text{real}} - \vec{r}\,| &= l_{\text{real}} = d\sqrt{1 + \frac{R_a^2}{d^2}}; \\
|\vec{r}'_{\text{imag}} - \vec{r}\,| &= l_{\text{imag}} = d\sqrt{1 + \frac{(R_a + 2R_b)^2}{d^2}}. \qquad (40)
\end{aligned}$$

Then the condition of $d \gg R_a, R_b$, or equivalently $k_0 d \gg 1$, approximates Eq. (13) to

$$\Psi^{\text{ex}}_{\text{semi}}(\vec{r}' \to \vec{r}) = \frac{S}{2\pi D}\frac{\exp(-k_0 d)}{d^2} k_0 R_b (R_a + R_b). \qquad (41)$$

In Eq. (23) the remaining integration term changes to (see Appendix B)

$$\begin{aligned}
&\iint_{\rho^{\text{fl}}=\rho-2R_b}^{\rho} \int [\Psi^{\text{fl}}_{\text{inf}}(\vec{r}'_{\text{real}} \to \bullet\vec{r}^{\,\text{fl}} \Rightarrow \vec{r}) \\
&\quad - \Psi^{\text{fl}}_{\text{inf}}(\vec{r}'_{\text{imag}} \to \bullet\vec{r}^{\,\text{fl}} \Rightarrow \vec{r})]\mathrm{d}^3\vec{r}^{\,\text{fl}} \\
&= \frac{\eta\mu_a^{\text{fl}} S}{8\pi k_0 D^2}\frac{\exp(-k_0 l_{\text{real}})}{l_{\text{real}}} k_0 R_b^2. \qquad (42)
\end{aligned}$$

Then Eq. (23) can be approximated to

$$\begin{aligned}&\Psi^{\mathrm{fl}}_{\mathrm{semi}}(\vec{r}' \to \forall r^{\mathrm{fl}} \Rightarrow \vec{r})\\ &= \frac{\eta\mu_a^{\mathrm{fl}}S}{8\pi k_0 D^2}\left[\exp(-k_0 l_{\mathrm{real}}) - \exp(-k_0 l_{\mathrm{imag}}) - \frac{\exp(-k_0 l_{\mathrm{real}})}{l_{\mathrm{real}}}k_0 R_b^2\right]\\ &= \frac{\eta\mu_a^{\mathrm{fl}}S}{4\pi D^2}R_b(R_a+R_b)\frac{\exp(-k_0 d)}{d}\left[1 - \frac{R_b}{2(R_a+R_b)}\left(1 - \frac{1}{2}k_0 d\frac{R_a^2}{d^2}\right)\right].\end{aligned} \tag{43}$$

3. *Source and Detector on a Concave Medium–Applicator Interface with Large Radius*

For a source and a detector located on an infinitely long concave boundary of a homogenous medium containing a uniform distribution of the fluorophore, we have

$$l_{\mathrm{real}} = d\sqrt{\left[1 + \frac{R_a^2}{d^2} - \frac{R_a}{R_0}(\cos\alpha)^2\right]};$$
$$l_{\mathrm{imag}} = d\sqrt{\left[1 + \frac{(R_a+2R_b)^2}{d^2} + \frac{R_a+2R_b}{R_0}(\cos\alpha)^2\right]}, \tag{44}$$

where α is the acute angle formed by $(\vec{r} - \vec{r}')$ and the azimuthal plane. At large R_0, Eq. (24) approximates to

$$\begin{aligned}&\Psi^{\mathrm{ex}}_{\mathrm{conC}}(\vec{r}' \to \vec{r})\\ &= \frac{S}{4\pi D}\frac{\exp(-k_0 l_{\mathrm{real}})}{l_{\mathrm{real}}} - \frac{S}{4\pi D}\frac{\exp(-k_0 l_{\mathrm{imag}})}{l_{\mathrm{imag}}}\sqrt{\frac{R_0+R_a+2R_b}{R_0-R_a}}\\ &= \frac{S}{2\pi D}[k_0 R_b(R_a+R_b)]\frac{1}{d^2}\\ &\quad\times\exp\left\{-\left[k_0 d + \frac{d}{2k_0 R_b(R_0-R_a)} - \frac{2R_0-R_a+2R_b}{4R_0R_b(R_0-R_a)}(\cos\alpha)^2 d^2\right]\right\}.\end{aligned} \tag{45}$$

In deriving Eq. (45) and hereafter, a term [20] of $\exp\{(R_a+2R_b)^2/[4R_b(R_0-R_a)]\}$ is omitted for analytical simplicity as it has a negligible effect on the results due to $R_a,\ R_b \ll d \ll R_0$. In Eq. (35), the finite integral term approximates to (see Appendix B)

$$\begin{aligned}&\iint_{\rho^{\mathrm{fl}}=R_0}^{R_0+2R_b}\int[\Psi^{\mathrm{fl}}_{\mathrm{inf}}(\vec{r}'_{\mathrm{real}} \to \bullet\vec{r}^{\mathrm{fl}} \Rightarrow \vec{r}) - \Psi^{\mathrm{fl}}_{\mathrm{inf}}(\vec{r}'_{\mathrm{imag}} \to \bullet\vec{r}^{\mathrm{fl}} \Rightarrow \vec{r})]\mathrm{d}^3\vec{r}^{\mathrm{fl}}\\ &= \frac{\eta\mu_a^{\mathrm{fl}}S}{8\pi k_0 D^2}\frac{\exp(-k_0 l_{\mathrm{real}})}{l_{\mathrm{real}}}k_0 R_b^2,\end{aligned} \tag{46}$$

and the unresolved term associated with the image source approximates to (derivation similar to Eq. (3.3.conC) of [18])

$$\begin{aligned}&\Psi^{\mathrm{fl}}_{\mathrm{inf}}(\vec{r}'_{\mathrm{imag}} \to \forall\,\vec{r}^{\mathrm{fl}} \Rightarrow \vec{r})\\ &= \frac{\eta\mu_a^{\mathrm{fl}}S}{8\pi^2 k_0 D}\exp\left(-k_0|\vec{r}'_{\mathrm{imag}} - \vec{r}|_{\mathrm{semi}}\sqrt{\frac{R_0-R_a}{R_0+R_a+2R_b}}\right),\end{aligned} \tag{47}$$

where $|\vec{r}'_{\mathrm{imag}} - \vec{r}|_{\mathrm{semi}}$ is the distance between the detector and the image of the "real" isotropic source with respect to an imaginary semi-infinite plane that is tangential to the concave geometry at the point of the physical source. We than have the following results:

$$\begin{aligned}&\Psi^{\mathrm{fl}}_{\mathrm{conC}}(\vec{r}' \to \forall\,\vec{r}^{\mathrm{fl}} \Rightarrow \vec{r})\\ &= \frac{\eta\mu_a^{\mathrm{fl}}S}{8\pi k_0 D^2}\left[\exp(-k_0 l_r) - \exp\left(-k_0 l_i\sqrt{\frac{R_0-R_a}{R_0+R_a+2R_b}}\right)\right.\\ &\qquad\left.- \frac{\exp(-k_0 l_r)}{l_r}k_0 R_b^2\right]\\ &= \frac{\eta\mu_a^{\mathrm{fl}}S}{4\pi D^2}R_b(R_a+R_b)\frac{1}{d}\exp\left\{-\left[k_0 d + \frac{d^2}{2R_b\left(R_0+R_a+2R_b\right)}\right.\right.\\ &\qquad\left.\left.- \frac{2\left(R_0+R_a+2R_b\right) + (R_a+2R_b)k_0 d}{4R_0R_b\left(R_0+R_a+2R_b\right)}\left(\cos\alpha\right)^2 d^2\right]\right\}\\ &\qquad- \frac{\eta\mu_a^{\mathrm{fl}}S}{4\pi D^2}R_b(R_a+R_b)\frac{\exp(-k_0 d)}{d}\frac{R_b}{2(R_a+R_b)}\\ &\qquad\times\left(1 - \frac{1}{2}k_0 d\left[\frac{R_a^2}{d^2} - \frac{R_a}{R_0}(\cos\alpha)^2\right]\right).\end{aligned} \tag{48}$$

4. *Source and Detector on a Convex Medium–Applicator Interface with Large Radius*

For a source and a detector located on an infinitely long convex boundary of a homogenous medium containing a uniform distribution of the fluorophore, we have

$$l_{\mathrm{real}} = d\sqrt{\left[1 + \frac{R_a^2}{d^2} + \frac{R_a}{R_0}(\cos\alpha)^2\right]};$$
$$l_{\mathrm{imag}} = d\sqrt{\left[1 + \frac{(R_a+2R_b)^2}{d^2} - \frac{R_a+2R_b}{R_0}(\cos\alpha)^2\right]}, \tag{49}$$

where α is the acute angle formed by $(\vec{r} - \vec{r}')$ and the azimuthal plane. At large R_0, Eq. (36) approximates to

$$\begin{aligned}&\Psi^{\mathrm{ex}}_{\mathrm{conV}}(\vec{r}' \to \vec{r})\\ &= \frac{S}{4\pi D}\frac{\exp(-k_0 l_{\mathrm{real}})}{l_{\mathrm{real}}} - \frac{S}{4\pi D}\frac{\exp(-k_0 l_{\mathrm{imag}})}{l_{\mathrm{imag}}}\sqrt{\frac{R_0-R_a-2R_b}{R_0+R_a}}\\ &= \frac{S}{2\pi D}[k_0 R_b(R_a+R_b)]\frac{1}{d^2}\\ &\quad\times\exp\left\{-\left[k_0 d - \frac{d}{2k_0 R_b(R_0+R_a)}\right.\right.\\ &\quad\left.\left.+ \frac{2R_0+R_a-2R_b}{4R_0R_b(R_0+R_a)}(\cos\alpha)^2 d^2\right]\right\}.\end{aligned} \tag{50}$$

In deriving Eq. (50) and hereafter, a term [20] of $\exp\{-(R_a+2R_b)^2/[4R_b(R_0+R_a)]\}$ is omitted for analytical simplicity as it has a negligible effect on the results due to $R_a,\ R_b \ll d \ll R_0$. In Eq. (37), the finite integral term approximates to

$$\int_{\rho^{\mathrm{fl}}=R_0-2R_b}^{R_0}\int[\Psi_{\mathrm{inf}}^{\mathrm{fl}}(\vec{r}'_{\mathrm{real}}\rightarrow\bullet\vec{r}^{\,\mathrm{fl}}\Rightarrow\vec{r}\,)-\Psi_{\mathrm{inf}}^{\mathrm{fl}}(\vec{r}'_{\mathrm{imag}}\rightarrow\bullet\vec{r}^{\,\mathrm{fl}}\Rightarrow\vec{r}\,)]\mathrm{d}^3\vec{r}^{\,\mathrm{fl}} = \frac{\eta\mu_a^{\mathrm{fl}}S}{8\pi k_0D^2}\frac{\exp(-k_0l_{\mathrm{real}})}{l_{\mathrm{real}}}k_0R_b^2, \tag{51}$$

and the unresolved term associated with the image source approximates to

$$\Psi_{\mathrm{inf}}^{\mathrm{fl}}(\vec{r}'_{\mathrm{imag}}\rightarrow\forall\,\vec{r}^{\,\mathrm{fl}}\Rightarrow\vec{r}\,) = \frac{\eta\mu_a^{\mathrm{fl}}S}{8\pi^2k_0D}\exp\left(-k_0|\vec{r}'_{\mathrm{imag}}-\vec{r}\,|_{\mathrm{semi}}\sqrt{\frac{R_0+R_a}{R_0-R_a-2R_b}}\right), \tag{52}$$

where $|\vec{r}'_{\mathrm{imag}}-\vec{r}\,|_{\mathrm{semi}}$ is the distance between the detector and the image of the "real" isotropic source with respect to an imaginary semi-infinite plane that is tangential to the convex geometry at the point of the physical source. We then have the following results:

$$\begin{aligned}
&\Psi_{\mathrm{conV}}^{\mathrm{fl}}(\vec{r}\,'\rightarrow\forall\,\vec{r}^{\,\mathrm{fl}}\Rightarrow\vec{r}\,)\\
&=\frac{\eta\mu_a^{\mathrm{fl}}S}{8\pi k_0D^2}\left[\exp(-k_0l_r)-\exp\left(-k_0l_i\sqrt{\frac{R_0+R_a}{R_0-R_a-2R_b}}\right)\right.\\
&\quad\left.-\frac{\exp(-k_0l_r)}{l_r}k_0R_b^2\right]=\frac{\eta\mu_a^{\mathrm{fl}}S}{4\pi D^2}R_b(R_a+R_b)\frac{1}{d}\\
&\quad\times\exp\left\{-\left[k_0d-\frac{d^2}{2R_b\left(R_0-R_a-2R_b\right)}\right.\right.\\
&\quad\left.\left.+\frac{2\left(R_0-R_a-2R_b\right)-(R_a+2R_b)k_0d}{4R_0R_b\left(R_0-R_a-2R_b\right)}\left(\cos\alpha\right)^2d^2\right]\right\}\\
&\quad-\frac{\eta\mu_a^{\mathrm{fl}}S}{4\pi D^2}R_b(R_a+R_b)\frac{\exp(-k_0d)}{d}\frac{R_b}{2(R_a+R_b)}\\
&\quad\times\left(1-\frac{1}{2}k_0d\left[\frac{R_a^2}{d^2}+\frac{R_a}{R_0}(\cos\alpha)^2\right]\right).
\end{aligned}\tag{53}$$

The above equations characterize the changes of Ψ^{ex} and Ψ^{fl} versus the source–detector distance $d=|\vec{r}-\vec{r}\,'|$ in a homogeneous medium containing a uniformly distributed fluorophore.

B. Changing Characteristics of Excitation- and Fluorescence-Wavelength Photon-Fluence Rates along the Longitudinal and Azimuthal Directions with Respect to *d*

1. Source and Detector on a Concave Medium–Applicator Interface with Large Radius

On a concave interface of large R_0, we have along the longitudinal direction (termed *case-longi*), i.e., $\phi'=\phi$, the following results:

$$\begin{aligned}
&\Psi_{\mathrm{conC}}^{\mathrm{ex}}(\vec{r}\,'\rightarrow\vec{r}\,)\\
&=\frac{S}{2\pi D}[k_0R_b(R_a+R_b)]\frac{1}{d^2}\exp\left\{-\left[k_0d+\frac{d}{2k_0R_b(R_0-R_a)}\right]\right\},
\end{aligned}\tag{54}$$

$$\begin{aligned}
&\Psi_{\mathrm{conC}}^{\mathrm{fl}}(\vec{r}\,'\rightarrow\forall\,\vec{r}^{\,\mathrm{fl}}\Rightarrow\vec{r}\,)\\
&=\frac{\eta\mu_a^{\mathrm{fl}}S}{4\pi D^2}R_b(R_a+R_b)\frac{1}{d}\exp\left\{-\left[k_0d+\frac{d^2}{2R_b(R_0+R_a+2R_b)}\right]\right\}\\
&\quad-\frac{\eta\mu_a^{\mathrm{fl}}S}{4\pi D^2}R_b(R_a+R_b)\frac{\exp(-k_0d)}{d}\frac{R_b}{2(R_a+R_b)}\left(1-\frac{1}{2}k_0d\left[\frac{R_a^2}{d^2}\right]\right).
\end{aligned}\tag{55}$$

It can be shown by comparing the above two equations with Eqs. (41) and (43) that both $\Psi_{\mathrm{conC}}^{\mathrm{ex}}$ and $\Psi_{\mathrm{conC}}^{\mathrm{fl}}$ decay faster along the longitudinal direction on a concave interface than their counterparts along a straight line on a semi-infinite interface, versus the same *d*. However, the deviation of the concave case-longi $\Psi_{\mathrm{conC}}^{\mathrm{fl}}$ from its semi-infinite counterpart is greater than that of the concave case-longi $\Psi_{\mathrm{conC}}^{\mathrm{ex}}$ from its semi-infinite counterpart.

Similarly we have along the azimuthal direction (termed *case-azi*), i.e., $z'=z$, the following:

$$\begin{aligned}
\Psi_{\mathrm{conC}}^{\mathrm{ex}}(\vec{r}\,'\rightarrow\vec{r}\,)&=\frac{S}{2\pi D}[k_0R_b(R_a+R_b)]\frac{1}{d^2}\\
&\quad\times\exp\left\{-\left[k_0d+\frac{2R_0d-(2R_0-R_a+2R_b)d\cdot k_0d}{4k_0R_bR_0(R_0-R_a)}\right]\right\},
\end{aligned}\tag{56}$$

$$\begin{aligned}
&\Psi_{\mathrm{conC}}^{\mathrm{fl}}(\vec{r}\,'\rightarrow\forall\,\vec{r}^{\,\mathrm{fl}}\Rightarrow\vec{r}\,)\\
&=\frac{\eta\mu_a^{\mathrm{fl}}S}{4\pi D^2}R_b(R_a+R_b)\frac{1}{d}\\
&\quad\times\exp\left\{-\left[k_0d-\frac{(R_a+2R_b)(2+k_0d)d^2}{4R_bR_0\left(R_0+R_a+2R_b\right)}\right]\right\}\\
&\quad-\frac{\eta\mu_a^{\mathrm{fl}}S}{4\pi D^2}R_b(R_a+R_b)\frac{\exp(-k_0d)}{d}\frac{R_b}{2(R_a+R_b)}\\
&\quad\times\left(1-\frac{1}{2}k_0d\left[\frac{R_a^2}{d^2}-\frac{R_a}{R_0}\right]\right).
\end{aligned}\tag{57}$$

It can be shown by comparing the above two equations with Eqs. (41) and (43) in the region of $k_0d\gg1$ that both $\Psi_{\mathrm{conC}}^{\mathrm{ex}}$ and $\Psi_{\mathrm{conC}}^{\mathrm{fl}}$ decay slower along the azimuthal direction on a concave interface than their counterparts along a straight line on a semi-infinite interface, versus the same *d*. However, the deviation of the case-azi $\Psi_{\mathrm{conC}}^{\mathrm{fl}}$ from its semi-infinite counterpart is smaller than that of the case-azi $\Psi_{\mathrm{conC}}^{\mathrm{ex}}$ from its semi-infinite counterpart. The opposite trends of the decay of case-longi $\Psi_{\mathrm{conC}}^{\mathrm{fl}}$ and case-azi $\Psi_{\mathrm{conC}}^{\mathrm{fl}}$ indicate that a unique set of spiral paths should exist on the concave interface, along which $\Psi_{\mathrm{conC}}^{\mathrm{fl}}$ reduces at the same rate versus *d* as along a straight line on a semi-infinite interface.

2. Source and Detector on a Convex Medium–Applicator Interface with Large Radius

On a convex interface of large R_0, we have along the following *case-longi* results:

$$\Psi^{\mathrm{ex}}_{\mathrm{conV}}(\vec{r}\,' \to \vec{r}\,') = \frac{S}{2\pi D}[k_0 R_b(R_a + R_b)]\frac{1}{d^2}\exp\left\{-\left[k_0 d - \frac{d}{2k_0 R_b(R_0 + R_a)}\right]\right\}, \tag{58}$$

$$\begin{aligned}\Psi^{\mathrm{fl}}_{\mathrm{conV}}(\vec{r}\,' \to \forall\, \vec{r}^{\,\mathrm{fl}} \Rightarrow \vec{r}\,) &= \frac{\eta\mu_a^{\mathrm{fl}} S}{4\pi D^2} R_b(R_a + R_b)\frac{1}{d}\exp\left\{-\left[k_0 d - \frac{d^2}{2R_b(R_0 - R_a - 2R_b)}\right]\right\} \\ &\quad - \frac{\eta\mu_a^{\mathrm{fl}} S}{4\pi D^2} R_b(R_a + R_b)\frac{\exp(-k_0 d)}{d}\frac{R_b}{2(R_a + R_b)}\left(1 - \frac{1}{2}k_0 d\left[\frac{R_a^2}{d^2}\right]\right).\end{aligned} \tag{59}$$

It can be shown by comparing the above two equations with Eqs. (41) and (43) that both $\Psi^{\mathrm{ex}}_{\mathrm{conV}}$ and $\Psi^{\mathrm{fl}}_{\mathrm{conV}}$ decay slower along the longitudinal direction on a convex interface than their counterparts along a straight line on a semi-infinite interface, versus the same d. However, the deviation of the convex case-longi $\Psi^{\mathrm{fl}}_{\mathrm{conC}}$ from its semi-infinite counterpart is greater than that of the convex case-longi $\Psi^{\mathrm{ex}}_{\mathrm{conC}}$ from its semi-infinite counterpart.

Similarly we have the following *case-azi* results:

$$\begin{aligned}\Psi^{\mathrm{ex}}_{\mathrm{conV}} &= \frac{S}{2\pi D}[k_0 R_b(R_a + R_b)]\frac{1}{d^2} \\ &\quad \times \exp\left\{-\left[k_0 d - \frac{2R_0 d - (2R_0 + R_a - 2R_b)d \cdot k_0 d}{4k_0 R_b R_0(R_0 + R_a)}\right]\right\},\end{aligned} \tag{60}$$

$$\begin{aligned}\Psi^{\mathrm{fl}}_{\mathrm{conV}}&(\vec{r}\,' \to \forall\, \vec{r}^{\,\mathrm{fl}} \Rightarrow \vec{r}\,) \\ &= \frac{\eta\mu_a^{\mathrm{fl}} S}{4\pi D^2} R_b(R_a + R_b)\frac{1}{d} \\ &\quad \times \exp\left\{-\left[k_0 d + \frac{(R_a + 2R_b)(2 + k_0 d)d^2}{4R_b R_0\left(R_0 - R_a - 2R_b\right)}\right]\right\} \\ &\quad - \frac{\eta\mu_a^{\mathrm{fl}} S}{4\pi D^2} R_b(R_a + R_b)\frac{\exp(-k_0 d)}{d}\frac{R_b}{2(R_a + R_b)} \\ &\quad \times \left(1 - \frac{1}{2}k_0 d\left[\frac{R_a^2}{d^2} + \frac{R_a}{R_0}\right]\right).\end{aligned} \tag{61}$$

It can be shown by comparing the above two equations with Eqs. (41) and (43) in the region of $k_0 d \gg 1$ that both $\Psi^{\mathrm{ex}}_{\mathrm{conV}}$ and $\Psi^{\mathrm{fl}}_{\mathrm{conV}}$ decay faster along the azimuthal direction on a convex interface than their counterparts along a straight line on a semi-infinite interface, versus the same d. However, the deviation of the case-azi $\Psi^{\mathrm{fl}}_{\mathrm{conV}}$ from its semi-infinite counterpart is smaller than that of the case-azi $\Psi^{\mathrm{ex}}_{\mathrm{conV}}$ from its semi-infinite counterpart. The opposite trends of the decay of case-longi $\Psi^{\mathrm{fl}}_{\mathrm{conV}}$ and case-azi $\Psi^{\mathrm{fl}}_{\mathrm{conV}}$ indicate that a unique set of spiral paths should exist on the convex interface, along which $\Psi^{\mathrm{fl}}_{\mathrm{conC}}$ reduces at the same rate versus d as along a straight line on a semi-infinite interface.

C. Photon-Fluence Rate at the Fluorescence Wavelength Normalized to the Photon-Fluence Rate at the Excitation Wavelength

For a source and a detector located in an infinite homogenous medium containing a uniform distribution of the fluorophore, the normalized Born ratio has been derived as [23]

$$\begin{aligned}\Re_{\mathrm{inf}}(\vec{r}\,' \to \vec{r}\,) &= \frac{\Psi^{\mathrm{fl}}_{\mathrm{inf}}(\vec{r}\,' \to \forall\, \vec{r}^{\,\mathrm{fl}} \Rightarrow \vec{r}\,)}{\Psi^{\mathrm{ex}}_{\mathrm{inf}}(\vec{r}\,' \to \vec{r}\,)} \\ &= \frac{\eta\mu_a^{\mathrm{fl}}}{2k_0 D}|\vec{r}\,' - \vec{r}\,| = \frac{\eta\mu_a^{\mathrm{fl}}}{2k_0 D}d,\end{aligned} \tag{62}$$

which increases versus d. For a source and a detector located on a semi-infinite boundary of a homogenous medium containing a uniform distribution of the fluorophore, Eqs. (41) and (43) lead to the following normalized Born ratio:

$$\begin{aligned}\Re_{\mathrm{semi}}(\vec{r}\,' \to \vec{r}\,) &= \frac{\Psi^{\mathrm{fl}}_{\mathrm{semi}}(\vec{r}\,' \to \forall\, \vec{r}^{\,\mathrm{fl}} \Rightarrow \vec{r}\,)}{\Psi^{\mathrm{ex}}_{\mathrm{semi}}(\vec{r}\,' \to \vec{r}\,)} \\ &= \frac{\eta\mu_a^{\mathrm{fl}}}{2k_0 D}d\left[1 - \frac{R_b}{2(R_a + R_b)}\left(1 - \frac{1}{2}k_0\frac{R_a^2}{d}\right)\right].\end{aligned} \tag{63}$$

It is observed that the Born ratio of the semi-infinite geometry is smaller versus d when compared to Eq. (62), and as d increases the difference between the Born ratio of semi-infinite geometry and that of infinite geometry reaches a constant multiplying d.

1. Source and Detector on a Concave Medium–Applicator Interface with Large Radius

For a source–detector pair on an infinitely long concave interface bounding a homogenous medium containing a uniform distribution of the fluorophore, the normalized Born ratio is

$$\begin{aligned}\Re_{\mathrm{conC}}(\vec{r}\,' \to \vec{r}\,) &= \frac{\Psi^{\mathrm{fl}}_{\mathrm{conC}}(\vec{r}\,' \to \forall\, \vec{r}^{\,\mathrm{fl}} \Rightarrow \vec{r}\,)}{\Psi^{\mathrm{ex}}_{\mathrm{conC}}(\vec{r}\,' \to \vec{r}\,)} \\ &= \frac{\eta\mu_a^{\mathrm{fl}}}{2k_0 D}d\left\{A_{\mathrm{conC}} - \frac{R_b}{2(R_a + R_b)}\right. \\ &\quad \left.\times\left(1 - \frac{1}{2}k_0 d\left[\frac{R_a^2}{d^2} - \frac{R_a}{R_0}(\cos\alpha)^2\right]\right)B_{\mathrm{conC}}\right\},\end{aligned} \tag{64}$$

where as $R_0 \to \infty$, both A_{conC} and B_{conC} converge to 1, and Eq. (64) reaches Eq. (63). It can be shown that the Born ratio given by Eq. (64) is generally smaller than the one given by Eq. (63), and the Born ratio of case-longi ($\cos\alpha = 0$) is closer to the semi-infinite case than the Born ratio of case-azi ($\cos\alpha = 1$).

2. Source and Detector on a Convex Medium–Applicator Interface with Large Radius

For a source–detector pair on an infinitely long convex interface bounding a homogenous medium containing a uniform distribution of the fluorophore, the normalized Born ratio is

$$\begin{aligned}\mathfrak{R}_{\mathrm{conV}}(\vec{r}\,' \to \vec{r}) &= \frac{\Psi^{\mathrm{fl}}_{\mathrm{conV}}(\vec{r}\,' \to \forall\, \vec{r}^{\,\mathrm{fl}} \Rightarrow \vec{r})}{\Psi^{\mathrm{ex}}_{\mathrm{conV}}(\vec{r}\,' \to \vec{r})} \\ &= \frac{\eta \mu_a^{\mathrm{fl}}}{2k_0 D} d \left\{ A_{\mathrm{conV}} - \frac{R_b}{2(R_a + R_b)} \right. \\ &\quad \left. \times \left(1 - \frac{1}{2} k_0 d \left[\frac{R_a^2}{d^2} - \frac{R_a}{R_0} (\cos\,\alpha)^2 \right] \right) B_{\mathrm{conV}} \right\}, \end{aligned} \tag{65}$$

where as $R_0 \to \infty$, both A_{conV} and B_{conV} converge to 1, and Eq. (65) reaches Eq. (63). It can be shown that the Born ratio given by Eq. (65) is generally greater than the one given by Eq. (63), and the Born ratio of case-longi ($\cos\,\alpha = 0$) is closer to the semi-infinite case than the Born ratio of case-azi ($\cos\,\alpha = 1$).

The analyses in Sections 3 and 4 indicate the general behaviors of CW fluorescence-wavelength photon diffusion between a source and a detector aligned azimuthally or longitudinally on a concave or convex medium–applicator interface when the medium contains a uniform distribution of the fluorophore. It is straightforward to conclude that the changing patterns of Ψ^{fl} and $\Psi^{\mathrm{fl}}/\Psi^{\mathrm{ex}}$ predicted for concave or convex geometry of very large radius asymptotically reach the patterns of semi-infinite geometry for the same line-of-sight source–detector distance. It has been demonstrated in [18,19] that the relative patterns of Ψ^{ex} for concave or convex geometry of smaller radius quantified by either numerical implementation of the general (nonsimplified) analytical results or FEM solution to the equation of photon diffusion are the same as the relative patterns predicted by the simplified analytics. However, it is worth noting that numerical implementation of the general analytical results of Eqs. (35) or (37) for CW fluorescence photon diffusion in concave or convex geometry is arithmetically challenging, because the second term in either of the equations that corresponds to free-space excitation by the image source involves two integrations and two summations. Therefore quantization of the changing patterns of Ψ^{fl} and $\Psi^{\mathrm{fl}}/\Psi^{\mathrm{ex}}$ for concave or convex geometry of smaller practical radius is performed by FEM only in the next section using the simulation tool-box near-infrared fluorescence and spectroscopy tomography [30] employed for the studies in [18,19].

5. NUMERICAL EVALUATION OF THE CHARACTERISTICS OF STEADY-STATE FLUORESCENCE PHOTON DIFFUSION VERSUS SOURCE–DETECTOR DISTANCE IN CONCAVE AND CONVEX GEOMETRIES OF SMALL RADIUS

In this section, we examine *case-azi* and *case-longi* measurements in concave or convex geometry, in comparison to the straight line in semi-infinite geometry. The *case-azi* measurement corresponds to $z = z'$ in Eqs. (24), (35), (36), and (37). The *case-longi* measurement corresponds to $\phi = \phi'$ in Eqs. (24), (35), (36), and (37). For both concave and convex geometries, the FEM meshing volume is a cylinder 40 cm in height [20]. Denser meshes are placed along the mid-azimuthal plane on the medium–applicator interface for *case-azi*, and along the longitudinal direction for *case-longi*. The meshing volume for the semi-infinite geometry is a 16 cm × 8 cm × 8 cm rectangle, and denser meshes are generated along the straight line whereupon the optodes are placed. In each set of computation for concave, convex, and semi-infinite geometries, the meshing volume is discretized into at least 50,000 tetrahedral elements with more than 10,000 nodes. The radius of the concave geometry and the inner radius of the convex geometry are both 10 mm, the outer radius of the convex geometry is 40 mm, and the optical parameters are $\mu_a = 0.0025\ \mathrm{mm}^{-1}$, $\mu_s' = 1\ \mathrm{mm}^{-1}$, $\mu_a = 0.005\ \mathrm{mm}^{-1}$, $\eta = 0.1$, and $A = 1.86$ [19].

Figures 3A and 3B illustrate the changes of CW photon fluence at the excitation wavelength and the fluorescence wavelength versus d in both concave and convex geometries. As illustrated in Fig. 3A for concave geometry, the CW fluorescence-wavelength photon fluence reduces slower in *case-azi* and faster in *case-longi* than that along a straight line on the semi-infinite interface for the same d. Conversely, for convex geometry, as illustrated in Fig. 3B, the CW fluorescence-wavelength photon fluence reduces faster in *case-azi* and slower in *case-longi* than that along a straight line on the semi-infinite interface for the same d. These features agree with the predictions of Section 4.B. The changes of the Born ratio versus d in concave and convex geometries in comparison to semi-infinite geometry are shown in Fig. 3C. With respect to the same d, the Born ratio increases slower in concave geometry and faster in convex geometry when compared to that along a straight line on the semi-infinite interface. The Born ratio evaluated along the longitudinal direction is closer to that along a straight line on the semi-infinite interface than the Born ratio evaluated along the azimuthal direction. These features agree with the predictions of Section 4.C.

6. DISCUSSION

The analysis in Section 4 for concave or convex geometry includes the approximations made at a large radius, and offers insight into the effect of the applicator's curvature on the fluorescence-wavelength photon diffusion when compared to semi-infinite geometry. The analytics agree with the physical aspect that as $R_0 \to \infty$, the changing characteristics of the CW photon-fluence rate at both excitation wavelength and fluorescence wavelength, as well as the Born ratio, of concave and convex geometries must reach their counterparts in semi-infinite geometry. Any rate difference between the changes along *case-azi* and *case-longi* certainly would also diminish as the radius of the cylindrical applicator becomes increasingly large. These qualitatively expected predictions by analytical approximations are validated by FEM simulation. The decay of CW fluorescence-wavelength photon-fluence rate with respect to d reveals opposite trends in *case-azi* and in *case-longi* when compared to that in the semi-infinite geometry. However, the change in the Born ratio in concave or convex geometry with respect to d uniquely reflects the shape of the applicator curvature when compared to the Born ratio in the semi-infinite geometry. The changes in the Born ratio with respect to d are smaller in concave geometry and greater in convex geometry than those in the semi-infinite geometry, indicating that the Born ratio represents the "lumped" effect of a cylindrical shape of the boundary on florescence photon diffusion. Subsequently, it will be interesting to investigate in future studies the change to the Born ratio by a perturbation to the uniform fluorescence distribution in concave and convex geometries

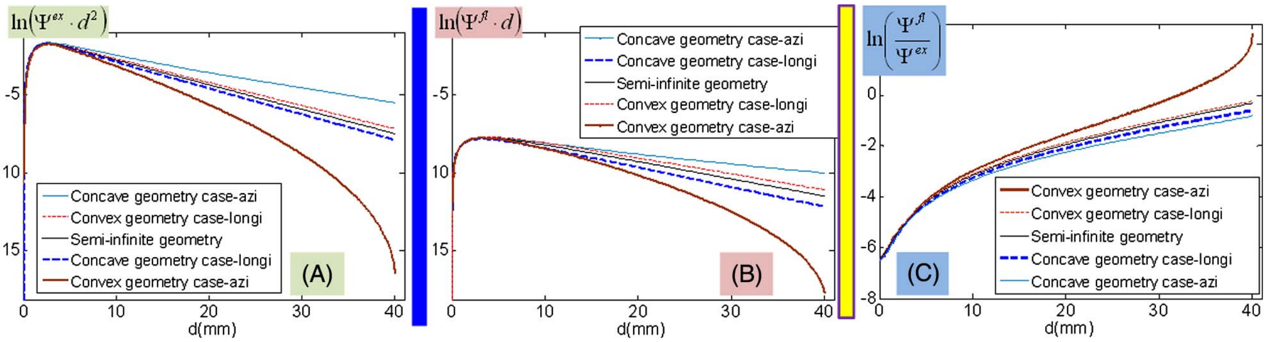

Fig. 3. (Color online) FEM results of the changes of CW photon-fluence rates at excitation wavelength (A), fluorescence wavelength (B), and Born ratio (C), in concave and convex geometries in comparison to semi-infinite geometry. In concave geometry, the CW photon-fluence rates at both the excitation wavelength and the fluorescence wavelength reduce more slowly in case-azi and more quickly in case-longi than those along a straight line on the semi-infinite interface. In convex geometry, the CW photon-fluence rates at both the excitation wavelength and the fluorescence wavelength reduce more quickly in case-azi and more slowly in case-longi than those along a straight line on the semi-infinite interface. Note that the dominant slopes of the excitation-wavelength and fluorescence-wavelength lines associated with the semi-infinite medium are identical. We also note that the lines associated with the fluorescence wavelength have a slower change than the lines associated with the excitation wavelength in the concave geometry, and conversely in the convex geometry. In concave geometry, the changes in the Born ratio in both case-azi and case-longi are smaller than those along a straight line on the semi-infinite interface. In convex geometry, the changes in the Born ratio in both case-azi and case-longi are greater than those along a straight line on the semi-infinite interface.

with respect to the change in semi-infinite geometry, as that relates to the sensitivity of the fluorescence measurement.

In terms of the "largeness" of the radius of the concave or convex geometry to apply the simplified analytics in Section 4, one can consider that d greater than 10 times of the larger one of R_a and R_b satisfies the condition $d \gg \{R_a, R_b\}$, and R_0 greater than 10 times of d satisfies the condition of applying the asymptotic expressions of I_m and K_m. Then the general parameters, $\mu_s' = 1.0\ \mathrm{mm}^{-1}$ corresponding to $R_a = 1.0$ mm and $\mu_a = 0.01\ \mathrm{mm}^{-1}$ and $A = 1.86$ [19] corresponding to $R_b = 1.23$ mm, result in $R_0 = 12.3$ cm being considered large. The scale of this radius may be close to that of a slightly curved external applicator but is not in any sense comparable to that of an internal applicator, which at most could have a radius of 1.5 cm. Therefore, although the simplified analytics of this work present a "qualitative" examination of the patterns of CW fluorescence photon diffusion in concave and convex geometries, the quantitative patterns of CW fluorescence photon diffusion, in particular the convex geometry of practical dimension, have to be studied using appropriate numerical methods.

7. CONCLUSION

This paper (Part V) examines steady-state fluorescence photon diffusion in a homogenous medium that contains a homogenous distribution of fluorophores. The geometries of the medium include a semi-infinite geometry, a "concave" geometry for the medium being enclosed by a circular cylindrical applicator of infinite length, and a "convex" geometry for the medium enclosing a circular cylindrical applicator of infinite length. The aim of this paper (Part V) is to investigate the changing characteristics of Ψ^{fl} and the ratio (sometimes called the Born ratio) of it versus Ψ^{ex}, with respect to the line-of-sight source–detector distance as applied to reflective measurements. Generalized analytical representations are derived and approximated for larger radius condition, and further analysis is performed for azimuthally or longitudinally aligned source–detector pairs in both concave and convex geometries. Numerical evaluations of the fluorescence photon diffusion in concave and convex geometries of a practical radius are carried out, and the revealed qualitative characteristics agree with the analytical predictions. When compared to the steady-state counterparts on a semi-infinite medium–applicator interface with the same line-of-sight source–detector distance, Ψ^{fl} reduces faster along the longitudinal direction and slower along the azimuthal direction, respectively, in the concave geometry, and conversely in the convex geometry. However, the Born ratio always increases slower in the concave geometry and faster in the convex geometry, respectively, when compared to that in the semi-infinite geometry.

APPENDIX A: DEVELOPMENT OF EQ. (29) FOR THE CONCAVE GEOMETRY

In concave geometry, $\vec{r}\,'_{\mathrm{imag}}$ is farther from the origin than $\bullet\vec{r}^{\,\mathrm{fl}}$, and $\vec{r}\,'_{\mathrm{real}}$ is closer to the origin than $\bullet\vec{r}^{\,\mathrm{fl}}_{\mathrm{imag}}$; therefore we have

$$\Psi^{\mathrm{ex}}_{\mathrm{inf}}(\vec{r}\,'_{\mathrm{imag}} \to \bullet\vec{r}^{\,\mathrm{fl}}) = \frac{S}{4\pi^2 D}\int \mathrm{d}k \cdot e^{ik(z'-z^{\mathrm{fl}})} \sum e^{im(\phi'-\phi^{\mathrm{fl}})} \eta_m^* I_m(k_{\mathrm{eff}}\rho^{\mathrm{fl}}) K_m(k_{\mathrm{eff}}\rho^{?}), \tag{A1}$$

$$\Psi^{\mathrm{ex}}_{\mathrm{inf}}(\vec{r}\,'_{\mathrm{real}} \to \bullet\vec{r}^{\,\mathrm{fl}}_{\mathrm{imag}}) = \frac{S}{4\pi^2 D}\int \mathrm{d}k \cdot e^{ik(z'-z^{\mathrm{fl}})} \sum e^{im(\phi'-\phi^{\mathrm{fl}})} \eta_m^{\mathrm{fl}} I_m[k_{\mathrm{eff}}(R_0 - R_a)] K_m(k_{\mathrm{eff}}\rho^{?}_{\mathrm{fl}}). \tag{A2}$$

Based on the boundary conditions defined by Eqs. (5) and (6), we have

$$\eta_m^* K_m(k_{\mathrm{eff}}\rho^{?}) = I_m[k_{\mathrm{eff}}(R_0 - R_a)] \frac{K_m[k_{\mathrm{eff}}(R_0 + R_b)]}{I_m[k_{\mathrm{eff}}(R_0 + R_b)]} \quad \text{and}$$
$$\eta_m^{\mathrm{fl}} K_m(k_{\mathrm{eff}}\rho^{?}_{\mathrm{fl}}) = I_m(k_{\mathrm{eff}}\rho^{\mathrm{fl}}) \frac{K_m[k_{\mathrm{eff}}(R_0 + R_b)]}{I_m[k_{\mathrm{eff}}(R_0 + R_b)]}, \tag{A3}$$

which changes the right-hand sides of Eqs. (A1) and (A2) to the following:

$$\frac{S}{4\pi^2 D}\int \mathrm{d}k\cdot e^{ik(z'-z^{\mathrm{fl}})}\sum e^{im(\phi'-\phi^{\mathrm{fl}})}I_m[k_{\mathrm{eff}}(R_0-R_a)]\times I_m(k_{\mathrm{eff}}\rho^{\mathrm{fl}})\frac{K_m[k_{\mathrm{eff}}(R_0+R_b)]}{I_m[k_{\mathrm{eff}}(R_0+R_b)]}. \tag{A4}$$

So the first identity of Eq. (29), $\Psi^{\mathrm{ex}}_{\mathrm{inf}}(\vec{r}\,'_{\mathrm{imag}}\to\bullet\vec{r}^{\,\mathrm{fl}}) = \Psi^{\mathrm{ex}}_{\mathrm{inf}}(\vec{r}\,'_{\mathrm{real}}\to\bullet\vec{r}^{\,\mathrm{fl}}_{\mathrm{imag}})$, is proved.

In terms of the second identity of Eq. (29), $\Psi^{\mathrm{ex}}_{\mathrm{inf}}(\vec{r}\,'_{\mathrm{real}}\to\bullet\vec{r}^{\,\mathrm{fl}}) = \Psi^{\mathrm{ex}}_{\mathrm{inf}}(\vec{r}\,'_{\mathrm{imag}}\to\bullet\vec{r}^{\,\mathrm{fl}}_{\mathrm{imag}})$, we provide in the following a heuristic proof of it, by using an alternative and more convenient set of notations: $\hat{S}$ represents the source element at $\vec{r}\,'_{\mathrm{real}}$, $\hat{D}$ represents the field element at $\bullet\vec{r}^{\,\mathrm{fl}}$, $\hat{S}'$ represents the element that is the image of $\hat{S}$, and $\hat{D}'$ represents the element that is the image of $\hat{D}$. Assume that the second identity of Eq. (29) is not held, i.e., $\Psi^{\mathrm{ex}}_{\mathrm{inf}}(\hat{S}'\to\hat{D}')\neq\Psi^{\mathrm{ex}}_{\mathrm{inf}}(\hat{S}\to\hat{D})$. Then we can define a "secondary" source (in the sense that this source is not an independent source) $\hat{S}''\neq\hat{S}'$, located at the position of $\hat{S}'$, that satisfies the condition $\Psi^{\mathrm{ex}}_{\mathrm{inf}}(\hat{S}''\to\hat{D}')=\Psi^{\mathrm{ex}}_{\mathrm{inf}}(\hat{S}\to\hat{D})$. Now if we reverse the signs of both $\hat{S}$ and $\hat{S}''$ so they become $-\hat{S}$ and $-\hat{S}''$, respectively, the fluence rates reaching $\hat{D}$ and $\hat{D}'$, respectively, by $-\hat{S}$ and $-\hat{S}''$ will become $\Psi^{\mathrm{ex}}_{\mathrm{inf}}(\langle-\hat{S}''\rangle\to\hat{D}')=-\Psi^{\mathrm{ex}}_{\mathrm{inf}}(\hat{S}''\to\hat{D}')=-\Psi^{\mathrm{ex}}_{\mathrm{inf}}(\hat{S}\to\hat{D})=\Psi^{\mathrm{ex}}_{\mathrm{inf}}(\langle-\hat{S}\rangle\to\hat{D})$. Now let us combine a source $\hat{S}$ and another source $-\hat{S}$ at the location of $\hat{S}$. Then what the combination of $\hat{S}$ and $-\hat{S}$ at the location of $\hat{S}$ does to $\hat{D}$ will be equivalent to what the combination of $\hat{S}'$ and the secondary $-\hat{S}''$ at the location of $\hat{S}'$ does to $\hat{D}'$. Apparently the resulting combined source intensity at the location of $\hat{S}$ is zero, indicating net-zero energy, so the fluence rate at $\hat{D}$ must be zero, i.e., $\Psi^{\mathrm{ex}}_{\mathrm{inf}}(\langle\hat{S},-\hat{S}\rangle\to\hat{D}')=0$. This net-zero-energy condition has to transform to the combined image and secondary source intensity at the location of $\hat{S}'$, which results in zero fluence rate at $\hat{D}'$, i.e., $\Psi^{\mathrm{ex}}_{\mathrm{inf}}(\langle\hat{S}',-\hat{S}''\rangle\to\hat{D}')=0$, which is not possible unless $\hat{S}''=\hat{S}'$. Therefore the previous assumption of $\Psi^{\mathrm{ex}}_{\mathrm{inf}}(\hat{S}'\to\hat{D}')\neq\Psi^{\mathrm{ex}}_{\mathrm{inf}}(\hat{S}\to\hat{D})$ is invalid; i.e., the second identity of Eq. (29), $\Psi^{\mathrm{ex}}_{\mathrm{inf}}(\vec{r}\,'_{\mathrm{real}}\to\bullet\vec{r}^{\,\mathrm{fl}})=\Psi^{\mathrm{ex}}_{\mathrm{inf}}(\vec{r}\,'_{\mathrm{imag}}\to\bullet\vec{r}^{\,\mathrm{fl}}_{\mathrm{imag}})$, is justified.

APPENDIX B: 2Rb-SHELL TERM OF EQ. (35)

We derive the 2Rb-shell term in Eq. (35) for the concave geometry. Similar procedures can be developed for the semi-infinite and convex geometries, and are not repeated here:

$$\begin{aligned}
&\iint_{\rho^{\mathrm{fl}}=R_0}^{R_0+2R_b}\int[\Psi^{\mathrm{fl}}_{\mathrm{inf}}(\vec{r}\,'_{\mathrm{real}}\to\bullet\vec{r}^{\,\mathrm{fl}}\Rightarrow\vec{r})-\Psi^{\mathrm{fl}}_{\mathrm{inf}}(\vec{r}\,'_{\mathrm{imag}}\to\bullet\vec{r}^{\,\mathrm{fl}}\Rightarrow\vec{r})]\mathrm{d}^3\vec{r}^{\,\mathrm{fl}}\\
&=\frac{\eta\mu_a^{\mathrm{fl}}S}{(4\pi D)^2}\frac{1}{\pi^2}\int\mathrm{d}z^{\mathrm{fl}}\int\mathrm{d}\phi^{\mathrm{fl}}\int_{\rho^{\mathrm{fl}}=R_0}^{R_0+2R_b}\rho^{\mathrm{fl}}d\rho^{\mathrm{fl}}\int\mathrm{d}k^{\mathrm{ex}}e^{ik^{\mathrm{ex}}(z'-z^{\mathrm{fl}})}\sum e^{im(\phi'-\phi^{\mathrm{fl}})}I_m[k^{\mathrm{ex}}_{\mathrm{eff}}(R_0-R_a)]K_m(k^{\mathrm{ex}}_{\mathrm{eff}}\rho^{\mathrm{fl}})\\
&\quad\times\int\mathrm{d}k^{\mathrm{fl}}e^{ik^{\mathrm{fl}}(z^{\mathrm{fl}}-z)}\sum e^{in(\phi^{\mathrm{fl}}-\phi)}I_m(k^{\mathrm{fl}}_{\mathrm{eff}}R_0)K_m(k^{\mathrm{fl}}_{\mathrm{eff}}\rho^{\mathrm{fl}})\\
&\quad-\frac{\eta\mu_a^{\mathrm{fl}}S}{(4\pi D)^2}\frac{1}{\pi^2}\int\mathrm{d}z^{\mathrm{fl}}\int\mathrm{d}\phi^{\mathrm{fl}}\int_{\rho^{\mathrm{fl}}=R_0}^{R_0+2R_b}\rho^{\mathrm{fl}}\mathrm{d}\rho^{\mathrm{fl}}\int\mathrm{d}k^{\mathrm{ex}}e^{ik^{\mathrm{ex}}(z'-z^{\mathrm{fl}})}\sum e^{im(\phi'-\phi^{\mathrm{fl}})}I_m[k^{\mathrm{ex}}_{\mathrm{eff}}(R_0-R_a)]I_m(k^{\mathrm{ex}}_{\mathrm{eff}}R_0)\\
&\quad\times\frac{K_m[k^{\mathrm{ex}}_{\mathrm{eff}}(R_0+R_b)]}{I_m[k^{\mathrm{ex}}_{\mathrm{eff}}(R_0+R_b)]}\int\mathrm{d}k^{\mathrm{fl}}e^{ik^{\mathrm{fl}}(z^{\mathrm{fl}}-z)}\sum e^{in(\phi^{\mathrm{fl}}-\phi)}I_m(k^{\mathrm{fl}}_{\mathrm{eff}}R_0)K_m(k^{\mathrm{fl}}_{\mathrm{eff}}\rho^{\mathrm{fl}})\\
&=\frac{\eta\mu_a^{\mathrm{fl}}S}{(4\pi D)^2}\int\mathrm{d}k\cdot e^{ik(z'-z)}\sum e^{im(\phi'-\phi)}I_m[k_{\mathrm{eff}}(R_0-R_a)]I_m(k_{\mathrm{eff}}R_0)\int_{\rho^{\mathrm{fl}}=R_0}^{R_0+2R_b}\rho^{\mathrm{fl}}[K_m(k_{\mathrm{eff}}\rho^{\mathrm{fl}})]^2\mathrm{d}\rho^{\mathrm{fl}}\\
&\quad-\frac{\eta\mu_a^{\mathrm{fl}}S}{(4\pi D)^2}\int\mathrm{d}k\cdot e^{ik(z'-z)}\sum e^{im(\phi'-\phi)}I_m[k_{\mathrm{eff}}(R_0-R_a)]I_m(k_{\mathrm{eff}}R_0)\frac{K_m[k_{\mathrm{eff}}(R_0+R_b)]}{I_m[k_{\mathrm{eff}}(R_0+R_b)]}\int_{\rho^{\mathrm{fl}}=R_0}^{R_0+2R_b}\rho^{\mathrm{fl}}I_m(k_{\mathrm{eff}}\rho^{\mathrm{fl}})K_m(k_{\mathrm{eff}}\rho^{\mathrm{fl}})\mathrm{d}\rho^{\mathrm{fl}}\\
&=\frac{\eta\mu_a^{\mathrm{fl}}S}{(4\pi D)^2}\int\mathrm{d}k\cdot e^{ik(z'-z)}\sum e^{im(\phi'-\phi)}I_m[k_{\mathrm{eff}}(R_0-R_a)]K_m(k_{\mathrm{eff}}R_0)\\
&\quad\times\frac{I_m(k_{\mathrm{eff}}R_0)}{K_m(k_{\mathrm{eff}}R_0)}\int_{\rho^{\mathrm{fl}}=R_0}^{R_0+2R_b}\rho^{\mathrm{fl}}\left\{[K_m(k_{\mathrm{eff}}\rho^{\mathrm{fl}})]^2-\frac{K_m[k_{\mathrm{eff}}(R_0+R_b)]}{I_m[k_{\mathrm{eff}}(R_0+R_b)]}I_m(k_{\mathrm{eff}}\rho^{\mathrm{fl}})K_m(k_{\mathrm{eff}}\rho^{\mathrm{fl}})\right\}\mathrm{d}\rho^{\mathrm{fl}}.
\end{aligned}$$

Using the asymptotic representation of I_m and K_m at large argument due to large R_0, we have

$$\begin{aligned}
&\iint_{\rho^{\mathrm{fl}}=R_0}^{R_0+2R_b}\int[\Psi^{\mathrm{fl}}_{\mathrm{inf}}(\vec{r}\,'_{\mathrm{real}}\to\bullet\vec{r}^{\,\mathrm{fl}}\Rightarrow\vec{r})-\Psi^{\mathrm{fl}}_{\mathrm{inf}}(\vec{r}\,'_{\mathrm{imag}}\to\bullet\vec{r}^{\,\mathrm{fl}}\Rightarrow\vec{r})]\mathrm{d}^3\vec{r}^{\,\mathrm{fl}}\\
&=\frac{\eta\mu_a^{\mathrm{fl}}S}{(4\pi D)^2}\int\mathrm{d}k\cdot e^{ik(z'-z)}\sum e^{im(\phi'-\phi)}I_m[k_{\mathrm{eff}}(R_0-R_a)]K_m(k_{\mathrm{eff}}R_0)\frac{e^{2k_{\mathrm{eff}}R_0}}{2k_{\mathrm{eff}}}\int_{\rho^{\mathrm{fl}}=R_0}^{R_0+2R_b}[e^{-2k_{\mathrm{eff}}\rho^{\mathrm{fl}}}-e^{-2k_{\mathrm{eff}}(R_0+R_b)}]\mathrm{d}\rho^{\mathrm{fl}}\\
&=\frac{\eta\mu_a^{\mathrm{fl}}S}{(4\pi D)^2}\int\mathrm{d}k\cdot e^{ik(z'-z)}\sum e^{im(\phi'-\phi)}I_m[k_{\mathrm{eff}}(R_0-R_a)]K_m(k_{\mathrm{eff}}R_0)\left[\frac{1}{(2k_{\mathrm{eff}})^2}-\frac{e^{-4k_{\mathrm{eff}}R_b}}{(2k_{\mathrm{eff}})^2}-\frac{R_b}{k_{\mathrm{eff}}}e^{-2k_{\mathrm{eff}}R_b}\right]\\
&\approx\frac{\eta\mu_a^{\mathrm{fl}}S}{(4\pi D)^2}\int\mathrm{d}k\cdot e^{ik(z'-z)}\sum e^{im(\phi'-\phi)}I_m[k_{\mathrm{eff}}(R_0-R_a)]K_m(k_{\mathrm{eff}}R_0)[2(R_b)^2]\\
&=\frac{\eta\mu_a^{\mathrm{fl}}S}{8\pi k_0 D^2}\frac{\exp(-k_0|\vec{r}\,'_{\mathrm{real}}-\vec{r}\,'|)}{|\vec{r}\,'_{\mathrm{real}}-\vec{r}\,'|}[k_0(R_b)^2].
\end{aligned}\tag{B1}$$

ACKNOWLEDGMENTS

We thank the anonymous reviewer for painstakingly examining the analytics of this work. This work has been supported by the Prostate Cancer Research Program of the U.S. Army Medical Research Acquisition Activity through grant no. W81XWH-10-1-0836.

REFERENCES

1. V. Ntziachristos, C. Bremer, and R. Weissleder, "Fluorescence imaging with near-infrared light: new technological advances that enable *in vivo* molecular imaging," Eur. J. Radiol. **13**, 195–208 (2003).
2. R. Roy and E. M. Sevick-Muraca, "Truncated Newton's optimization scheme for absorption and fluorescence optical tomography: part I theory and formulation," Opt. Express **4**, 353–371 (1999).
3. A. B. Milstein, S. Oh, K. J. Webb, C. A. Bouman, Q. Zhang, D. A. Boas, and R. P. Millane, "Fluorescence optical diffusion tomography," Appl. Opt. **42**, 3081–3094 (2003).
4. Y. Lin, H. Gao, O. Nalcioglu, and G. Gulsen, "Fluorescence diffuse optical tomography with functional and anatomical a priori information: feasibility study," Phys. Med. Biol. **52**, 5569–5585 (2007).
5. D. S. Kepshire, S. L. Gibbs-Strauss, J. A. O'Hara, M. Hutchins, N. Mincu, F. Leblond, M. Khayat, H. Dehghani, S. Srinivasan, and B. W. Pogue, "Imaging of glioma tumor with endogenous fluorescence tomography," J. Biomed. Opt. **14**, 030501 (2009).
6. A. Liebert, H. Wabnitz, H. Obrig, R. Erdmann, M. Möller, R. Macdonald, H. Rinneberg, A. Villringer, and J. Steinbrink, "Noninvasive detection of fluorescence from exogenous chromophores in the adult human brain," NeuroImage **31**, 600–608 (2006).
7. A. Corlu, R. Choe, T. Durduran, M. A. Rosen, M. Schweiger, S. R. Arridge, M. D. Schnall, and A. G. Yodh, "Three-dimensional in vivo fluorescence diffuse optical tomography of breast cancer in humans," Opt. Express **15**, 6696–6716 (2007).
8. A. Godavarty, A. B. Thompson, R. Roy, M. Gurfinkel, M. J. Eppstein, C. Zhang, and E. M. Sevick-Muraca, "Diagnostic imaging of breast cancer using fluorescence-enhanced optical tomography: phantom studies," J. Biomed. Opt. **9**, 488–496 (2004).
9. Y. Tan and H. Jiang, "DOT guided fluorescence molecular tomography of arbitrarily shaped objects," Med. Phys. **35**, 5703–5707 (2008).
10. X. Intes, J. Ripoll, Y. Chen, S. Nioka, A. G. Yodh, and B. Chance, "In vivo continuous-wave optical breast imaging enhanced with indocyanine green," Med. Phys. **30**, 1039–1047 (2003).
11. J. Boutet, L. Herve, M. Debourdeau, L. Guyon, P. Peltie, J.-M. Dinten, L. Saroul, F. Duboeuf, and D. Vray, "Bimodal ultrasound and fluorescence approach for prostate cancer diagnosis," J. Biomed. Opt. **14**, 064001 (2009).
12. C. Li, R. Liengsawangwong, H. Choi, and R. Cheung, "Using a priori structural information from magnetic resonance imaging to investigate the feasibility of prostate diffuse optical tomography and spectroscopy: a simulation study," Med. Phys. **34**, 266–274 (2007).
13. A. Ishimaru, "Diffusion of light in turbid material," Appl. Opt. **28**, 2210–2215 (1989).
14. X. D. Li, M. A. O'Leary, D. A. Boas, B. Chance, and A. G. Yodh, "Fluorescent diffuse photon density waves in homogeneous and heterogeneous turbid media: analytic solutions and applications," Appl. Opt. **35**, 3746–3758 (1996).
15. F. Martelli, S. Del Bianco, and P. Di Ninni, "Perturbative forward solver software for small localized fluorophores in tissue," Biomed. Opt. Express **3**, 26–36 (2012).
16. M. Sadoqi, P. Riseborough, and S. Kumar, "Analytical models for time-resolved fluorescence spectroscopy in tissues," Phys. Med. Biol. **46**, 2725–2743 (2001).
17. J. B. Domínguez and Y. Bérubé-Lauzière, "Light propagation from fluorescent probes in biological tissues by coupled time-dependent parabolic simplified spherical harmonics equations," Biomed. Opt. Express **2**, 817–837 (2011).
18. A. Zhang, D. Piao, C. F. Bunting, and B. W. Pogue, "Photon diffusion in a homogeneous medium bounded externally or internally by an infinitely long circular cylindrical applicator. I. Steady-state theory," J. Opt. Soc. Am. A **27**, 648–662 (2010).
19. A. Zhang, G. Xu, C. Daluwatte, G. Yao, C. F. Bunting, B. W. Pogue, and D. Piao, "Photon diffusion in a homogeneous medium bounded externally or internally by an infinitely long circular cylindrical applicator. II. Quantitative examinations of the steady-state theory," J. Opt. Soc. Am. A **28**, 66–75 (2011).
20. A. Zhang and D. Piao, "Photon diffusion in a homogeneous medium bounded externally or internally by an infinitely long circular cylindrical applicator. IV. Frequency-domain analysis," J. Opt. Soc. Am. A **29**, 1445–1458 (2012).
21. M. Gao, G. Lewis, G. M. Turner, A. Soubret, and V. Ntziachristos, "Effects of background fluorescence in fluorescence molecular tomography," Appl. Opt. **44**, 5468–5474 (2005).
22. V. Ntziachristos, G. Turner, J. Dunham, S. Windsor, A. Soubret, J. Ripoll, and H. A. Shih, "Planar fluorescence imaging using normalized data," J. Biomed. Opt. **10**, 064007 (2005).
23. A. Soubret and V. Ntziachristos, "Fluorescence molecular tomography in the presence of background fluorescence," Phys. Med. Biol. **51**, 3983–4001 (2006).
24. J. F. Abascal, J. Aguirre, J. Chamorro-Servent, M. Schweiger, S. Arridge, J. Ripoll, J. J. Vaquero, and M. Desco, "Influence of absorption and scattering on the quantification of fluorescence diffuse optical tomography using normalized data," J. Biomed. Opt. **17**, 036013 (2012).
25. R. C. Haskell, L. O. Svaasand, T. Tsay, T. Feng, M. S. McAdams, and B. J. Tromberg, "Boundary conditions for the diffusion equation in radiative transfer," J. Opt. Soc. Am. A **11**, 2727–2741 (1994).
26. D. Contini, F. Martelli, and G. Zaccanti, "Photon migration through a turbid slab described by a model based on diffusion approximation. I. Theory," Appl. Opt. **36**, 4587–4599 (1997).
27. A. Da Silva, M. Leabad, C. Driol, T. Bordy, M. Debourdeau, J. Dinten, P. Peltié, and P. Rizo, "Optical calibration protocol for an x-ray and optical multimodality tomography system dedicated to small-animal examination," Appl. Opt. **48**, D151–D162 (2009).
28. R. Aronson, "Boundary conditions for diffusion of light," J. Opt. Soc. Am. A **12**, 2532–2539 (1995).
29. M. Schweiger, S. R. Arridge, M. Hiraoka, and D. T. Delpy, "The finite element method for the propagation of light in scattering media: boundary and source conditions," Med. Phys. **22**, 1779–1792 (1995).
30. H. Dehghani, M. E. Eames, P. K. Yalavarthy, S. C. Davis, S. Srinivasan, C. M. Carpenter, B. W. Pogue, and K. D. Paulsen, "Near infrared optical tomography using NIRFAST: algorithm for numerical model and image reconstruction," Commun. Numer. Methods Eng. **25**, 711–732 (2009).

A geometric-sensitivity-difference based algorithm improves object depth-localization for diffuse optical tomography in a circular-array outward-imaging geometry

Guan Xu
Department of Radiology, Medical School, University of Michigan, Ann Arbor, Michigan 48109

Daqing Piao[a)]
School of Electrical and Computer Engineering, Oklahoma State University, Stillwater, Oklahoma 74078

(Received 11 June 2012; revised 8 November 2012; accepted for publication 27 November 2012; published 27 December 2012)

Purpose: To improve object depth-localization for diffuse optical tomography (DOT) in a circular-array outward-imaging geometry that is subjected to strong sensitivity variation with respect to imaging depth.
Methods: The authors introduce an alternative DOT image reconstruction approach that optimizes the data-model fit based on the *paired* measurements corresponding to two pairs of source-detector that share either the source or the detector, in comparison to the conventional method that optimizes the data-model fit based on the *unpaired* measurements corresponding to individual pairs of source-detector. This alternative approach, namely, geometric-sensitivity-difference (GSD) method, effectively reduces the variation of the reconstruction sensitivity with respect to imaging depth. The DOT image reconstruction based on GSD-scheme applied to same-source source-detector pairs is demonstrated using simulated and experimental continuous-wave measurements in a circular-array outward-imaging geometry, of which the native sensitivity varies strongly with respect to the depth. The outcomes of GSD-based image reconstruction are compared to those of two other methods: one is the conventional baseline method that utilizes the native sensitivity but does not involve depth-compensating scheme; and the other is a reference-compensation approach that employs active and depth-adapted compensation scheme to counteract the dependence of the reconstruction sensitivity with respect to imaging depth.
Results: The GSD method generally outperforms the other two methods in localizing the depth of single object, resolving two objects that are azimuthally separated, and estimating the optical property of single object or azimuthally separated dual objects. The GSD method, however, demands more computations due to an increase of the element size of the resulted sensitivity matrix and more matrix multiplications.
Conclusions: The GSD method improves the depth localization in the circular-array outward-imaging geometry, by taking advantage of the paired measurements of two source-sharing source-detector-pairs to passively and effectively homogenize the sensitivity of the reconstruction with respect to imaging depth. © *2013 American Association of Physicists in Medicine*. [http://dx.doi.org/10.1118/1.4771957]

Key words: image reconstruction, diffuse optical tomography, sensitivity, photon migration in tissue

I. INTRODUCTION

Diffuse optical tomography (DOT) is inherently prone to spatially dependent sensitivity,[1–4] due to scattering-dominated photon propagation in biological tissue.[5] The spatial dependence of DOT sensitivity is also specific to the geometry of the interface between the medium and the array of optodes. The optode-array of DOT usually has one- or two-dimensional symmetry[2,6–9] that gives rise to a sensitivity distribution that is mostly uniform along the direction of the symmetry except at locations close to the optodes. For example, the spatial sensitivity of a circular array[8,9] that has evenly distributed optodes along the circumference is azimuthally invariant, and the spatial sensitivity of a near-planar array whereupon the optodes are orderly distributed[3,7] changes insignificantly over the lateral dimension of the array. However, at the directions orthogonal to the symmetry of the optode configuration, specifically along the depth into the medium, the spatial sensitivity varies, generally, with a pronounced peak in the proximity of the medium-array interface, as exemplified by the thinner solid curve in Fig. 1(a) (detailed description of Fig. 1 is referred to Sec. II.A). Such variation of the sensitivity causes depth-dependent reconstruction of the contrast and resolution. More severely, it may cause objects of different depths to be recovered at approximately the same depth, the position at which the radial profile of the sensitivity peaks.[1–3,7,8] The depth-dependence of the sensitivity is thus a common issue to be negotiated in many DOT applications, including those to brain,[7,10] to breast using planar remission geometry,[1] and to prostate via endorectal probing for either sagittal[3] or axial[9] imaging, etc. Among these DOT applications, the endorectal axial-imaging geometry is subjected to

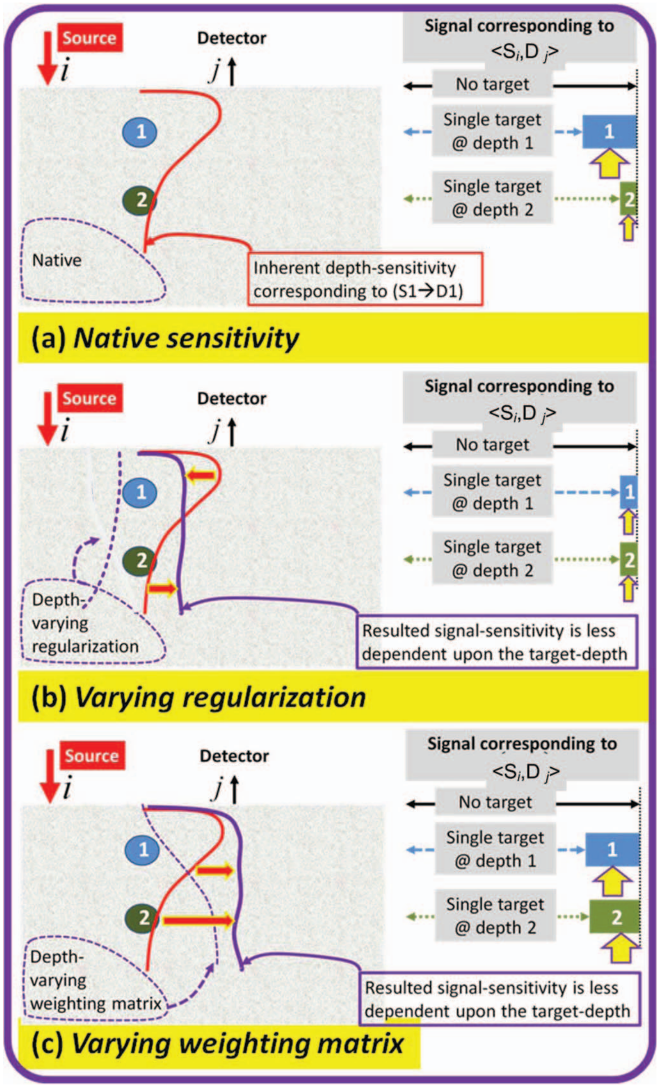

FIG. 1. Illustration of conventional DOT image reconstruction approaches that utilize the measurements of individual source-detector-pairs. The thinner solid curve represents the native sensitivity profile, the thicker solid curve represents the modified sensitivity profile, and the dashed curve indicates the regularization or compensation with respect to imaging depth. The boxes pointed by framed arrows represent the signal responses to an object at position 1 and 2, respectively. (a) The signal responses to an object located at different depths are different due to the spatial variations of the native sensitivity. (b) Spatially varying regularization factors suppresses the stronger intensity of the natural sensitivity during the sensitivity matrix inversion to even the recovery of the object contrast with respect to imaging depth. (c) Spatially varying weighting magnifies the weak sensitivity in deeper regions and to even the recovery of the object contrast with respect to imaging depth.

arguably the strongest variation of the sensitivity with respect to imaging depth, due to the rapid reduction of photon fluence versus the source-detector distance when compared with the geometries involving a planar interface or a curved interface that encloses the medium.[11] As will be shown, localizing the depth of an object of interest in such circular-array outward-imaging geometry is challenging.

Robust localization of an object in the depth direction along which the sensitivity varies significantly has to rely upon establishing a reconstruction scheme in which the updating of the medium optical properties is insensitive to the imaging depth. Methods demonstrated to suppress the sensitivity of reconstruction to the imaging depth can be coarsely classified into two categories. The first category, as conceptually illustrated in Fig. 1(b), applies stronger regularization to regions with higher native sensitivity to damp the response of the reconstruction to the same amount of the update to the optical properties. For a circular-array inward-imaging geometry of which the spatial sensitivity tends to be azimuthally uniform but decreases toward the center of the imaging geometry, Pogue *et al.* applied a radially varying regularization parameter that had a greater magnitude near the sources but smaller magnitude in the interior of the geometry.[8] This method, called spatially variant regularization (SVR), noticeably improved the reconstruction, as the artifacts near the optode array were suppressed and the contrast and resolution across the image were equalized. However, artifacts could appear at the center of the circular image, and the parameters determining the radial variation of the regularization were required to be optimized for a particular imaging geometry and a specific object size. It is also noted that the spatial sensitivity of the circular-array inward-imaging geometry utilized by Pogue *et al.*[8] decreases only mildly versus the depth from the medium-boundary, when compared to that of the circular-array outward-imaging geometry to be investigated in this study. The second category of methods, as conceptually illustrated in Fig. 1(c), implements a spatially resolved weighting scheme to the native depth-dependent sensitivity in the iteration process. For a near-planar geometry of which the variation of the spatial sensitivity with respect to depth was stronger than that of the inward-imaging geometries of Ref. 8, Culver *et al.* employed spatially varied contrast-to-noise-ratio weighting to the reconstruction, after the data were corrected for optode mispositioning, to improve both the point-spread-function and the object-localization in depth.[10] For geometries that were similar to the near-planar one in Ref. 10, Niu *et al.*,[2] Huang and Zhu,[1] and Zhao *et al.*[4] embedded depth-dependent weighting matrices in the iterative process to counterbalance the depth-variations of the respective native spatial sensitivities. The methods[1,2,4] of the second category effectively elevated the response of the objective functions to the same amount of the update to the optical properties in deeper depths; however, the spatially varied weighting to the sensitivity profiles, such as that introduced by the depth-compensation-algorithm (DCA),[2] naturally has to be optimized case-by-case.

These previously demonstrated methods, all making the reconstruction less sensitive to the object depth, may be different in terms of how the native sensitivity profile was compensated or counteracted. As in some the actions were imposed indirectly by the regularization but in others were applied directly to the sensitivity function; however, all these methods were similar, in terms of fitting the calculated data to the individual measurements taken by individual source-detector-pairs. This study introduces an alternative method of optimizing the data-model fit, which is to fit the calculated data to the paired measurements taken by two source-detector-pairs that share either the source or the detector. An intuitive explanation of this method is that, although the sensitivity of one pair of source-detector with respect to an object could vary significantly over the depth of the object, the relative response between two pairs of source-detector that share one optode could vary substantially less over the depth with respect to the same object, and hypothetically the image reconstruction based on this relative or paired response could be more robust in localizing the object than that based on the response of individual pairs of source-detector. The relative response between two optode-sharing source-detector-pairs to a given medium heterogeneity is related to the positioning (i.e., geometric) difference of the heterogeneity with respect to the two source-detector-pairs, therefore, the reconstruction scheme that takes advantage of such relative or paired response is called a geometric-sensitivity-difference (GSD) based reconstruction. The objective of this study is to demonstrate that the GSD method effectively evens the reconstruction updating sensitivity with respect to imaging depth and consequently improves DOT depth-localization. The GSD differs from previously investigated depth-compensation reconstruction method in that it does not involve depth-adapted or to-be-optimized parameters in order to reduce the variation of the reconstruction sensitivity with respect to imaging depth.

The rest of the paper is arranged as follows. Section II presents the analytical formations of GSD method as it applies to DOT image reconstruction in the context of Levenberg–Marquardt (LM) minimization,[12] using paired continuous-wave (CW) measurements from source-sharing source-detector-pairs. Section III outlines the circular-array axial outward-imaging geometry to be studied, of which the native sensitivity with respect to imaging depth varies significantly more than those of planar or circular-array inward-imaging geometries of previous studies. Section III also describes two reconstruction approaches against which the GSD method will be evaluated: one is a conventional or baseline method that applies a spatially invariant regulation in the LM minimization;[13] and the other is a reference-compensation approach which is similar in methodology to the DCA method but is more robust than the original DCA method for the circular-array outward-imaging geometry of this study. Section IV details simulation and experimental methods used for evaluating the three reconstruction methods. The simulation and experimental results in Sec. V demonstrate that the GSD method generally outperforms the baseline and reference-compensation methods, in terms of localizing the depth of single object, resolving two azimuthally separated objects, and estimating the optical property of single object or azimuthally separated dual objects in the circular-array outward-imaging geometry. As all three methods involve a step-specific regularization scheme in the iterations, the same step-specific regularization factor optimal to the reference-compensation method is applied to the baseline reconstruction and the GSD based reconstruction. A step-specific regularization factor optimal to the baseline method for the studied geometry was found difficult to determine, because the baseline method performs very poorly in the studied geometry, as to impair the evaluation of the outcomes at different choices of the step-specific regularization factors. The step-specific regularization factor optimal to the reference-compensation method is not necessarily optimal to the GSD method. An outperformance of the GSD method over the baseline method is unsurprising at all, because the effective sensitivity profile of the former method is much more uniform with respect to the imaging depth than that of the latter method. The outperformance of the GSD method over the reference-compensation method shall relate to the pairing measurements by the former method versus the unpaired measurements by the latter method. Section VI discusses how the GSD operation may be implemented to Tikhonov minimization and the general-least-square (GLS) minimization.[13]

II. THE GEOMETRIC-SENSITIVITY-DIFFERENCE METHOD

The model of frequency-domain (FD) photon propagation in turbid media by using a diffusion approximation to the Boltzmann transport equation results in the following Helmholtz type equation:

$$-\nabla \cdot [D(\vec{r})\nabla\Phi(\vec{r},\omega)] + \mu_a(\vec{r})\Phi(\vec{r},\omega) = q_0(\vec{r},\omega), \tag{1}$$

where $\Phi(\vec{r},\omega)$ is the photon fluence rate at a position $\vec{r}$, $D = 1/[3(\mu_a + \mu'_s)]$ is the diffusion coefficient, μ_a is the absorption coefficient, μ'_s is the scattering coefficient, ω is the angular modulation frequency, and $q_0(\vec{r},\omega)$ is the source term. A Robin-type condition applies to the medium-applicator interface $\vec{r}_0$ as

$$\Phi(\vec{r}_0,\omega) + 2D(\vec{r}_0)A\hat{n}_0 \cdot \nabla\Phi(\vec{r}_0,\omega) = 0, \tag{2}$$

where $\hat{n}_0$ is the unit outward-pointing vector normal to the interface and A is a coefficient determined by the reflective index mismatch across the boundary. By a phasor notation, $\Phi(\vec{r},\omega) = Ie^{j\theta}$, where I and θ are the magnitude and phase of the photofluence rate, respectively, $\Phi(\vec{r},\omega)$ can be implemented in logarithm as[14]

$$\log[\Phi(\vec{r},\omega)] = \log(I) + j\theta \tag{3}$$

to yield a better scaled inverse problem for the reconstructions.[15] An alternative form of Eq. (3), $\Psi(\vec{r},\omega) = \{\log(I),\theta\}$, will be used for the following analytics.

II.A. Image reconstruction based on the measurements taken by individual source-detector-pairs

We use $\langle S_i, D_j\rangle$ to denote a source-detector pair consisting of a source i and a detector j on the medium boundary, and $\{\langle S_i, D_j\rangle\}$ to indicate the ensemble of all pairs of source-detector. The conventional objective function of the DOT inverse problem is thereby[13]

$$\|\chi\|^2 = \|[\Psi_{\{\langle S_i,D_j\rangle\}}]_m - [\Psi_{\{\langle S_i,D_j\rangle\}}(\mu)]_c\|^2, \tag{4}$$

where μ specifies μ_a and D, the subscripts m and c represent, respectively, the "measurement" and the "calculation," and χ is the data-model misfit. The objective function in Eq. (4) is iteratively minimized by updating the calculated photon fluence rate using the following form, which ignores the higher order terms (order ≥2) in Taylor series expansion around the μ values of the previous iteration:

$$[\Psi(\mu_n)]_c \approx [\Psi(\mu_{n-1})]_c + J\delta\mu_n, \tag{5}$$

where the subscripts n and $n-1$ are the iteration numbers, and δ is the difference between the referred value at current and the previous iterations as $\delta\mu_n = \mu_n - \mu_{n-1}$. The J in Eq. (5) is the Jacobian, or called the sensitivity matrix, which is the first order derivative of the measurement quantities with respect to the optical properties.

Rearranging Eq. (4) using Eq. (5) gives

$$\begin{aligned}\chi_n &= \Psi_m - \Psi_c(\mu_n) \approx \Psi_m - \Psi_c(\mu_{n-1}) - J\delta\mu_n\\ &= \chi_{n-1} - J\delta\mu_n.\end{aligned} \tag{6}$$

The reconstruction process, which is to iteratively compute the change of the objective function with respect to the change of the optical property until the change of the former reaches a predetermined stopping criterion, is equivalent to solving

$$\frac{\partial(\chi)^2}{\partial\mu} = \frac{\partial(\Psi_m - \Psi_c)^2}{\partial\mu} = -2\left(\frac{\partial\Psi_c}{\partial\mu}\right)\chi = -2\cdot J^T\chi = 0. \tag{7}$$

Substituting Eq. (6) to Eq. (7) at the nth iteration gives

$$J^T\cdot(\chi_{n-1} - J\cdot\delta\mu_n) = 0. \tag{8a}$$

Therefore, the update of the optical properties at the nth iteration is

$$\delta\mu_n = (J^TJ)^{-1}J^T\chi_{n-1}. \tag{8b}$$

To facilitate a better conditioning of the inversion of J^TJ in Eq. (8b), a Levenberg–Marquardt scheme implements a diagonal regularization factor λ in the form of

$$\delta\mu_n = (J^TJ + \lambda I)^{-1}J^T\chi_{n-1}. \tag{8c}$$

The λ value is typically step-wisely adjusted,[13] i.e., the λ value at each step of iteration is reduced with respect to that in the immediate previous step (an empirical damping factor of 1.78 is used in this work).

We denote N as the total number of the spatial elements for which the updating of the optical properties is performed, "NoS" as the number of source channels, and "NoD" as the number of detector channels. Then the complete Jacobian matrix, of FD measurements, amounts to the form of

$$J_{[\mathrm{NoD}*\mathrm{NoS}*2]\times[\mathrm{N}*2]} = \begin{bmatrix} \left[\dfrac{\partial\log(I)}{\partial\mu_a}\right]_{[\mathrm{NoD}*\mathrm{NoS}]\times\mathrm{N}} & \left[\dfrac{\partial\log(I)}{\partial D}\right]_{[\mathrm{NoD}*\mathrm{NoS}]\times\mathrm{N}} \\ \left[\dfrac{\partial\theta}{\partial\mu_a}\right]_{[\mathrm{NoD}*\mathrm{NoS}]\times\mathrm{N}} & \left[\dfrac{\partial\theta}{\partial D}\right]_{[\mathrm{NoD}*\mathrm{NoS}]\times\mathrm{N}} \end{bmatrix}, \tag{9a}$$

wherein each of the four blocks of the right-hand-side has (NoD*NoS) rows and N columns. In the following analytics, however, we will consider only the upper-left block of the Jacobian of Eq. (9a) for compactness. The upper-left block of the Jacobian may conform to the simplest case of recovering the absorption coefficients by using intensity information as could be rendered by CW measurements. However, the analytical formulations of the GSD method discussed for the CW case can be straightforwardly extended to recovering both absorption and scattering properties, which is not impractical by using only CW measurements,[16–18] or to recovering both absorption and scattering properties by using FD measurements that include phase information. The extensions involve either doubling the numbers of columns or doubling the numbers of both columns and rows.

In the remaining analytics, as we will consider $J = [\partial\log(I)/\partial\mu_a]_{[\mathrm{NoD}*\mathrm{NoS}]\times\mathrm{N}}$, $\log(I)$ is to be replaced by ψ, and μ_a by μ, for clarity. The remaining analytics will also specify that NoS = 8 and NoD = 8, to conform to the geometry (Fig. 3) involved later in the simulation and experimental studies. With these customizations, the Jacobian matrix becomes

$$J^{\Diamond} = \left[\frac{\partial\psi}{\partial\mu^{\Diamond}}\right]_{64\times N} = [\,J^1\;J^2\;\ldots\ldots\;J^N\,], \tag{9b}$$

where $J^{\Diamond}$ and $\mu^{\Diamond}$, $\Diamond = \{1\colon N\}$, are, respectively, the sub-matrix of J and the μ associated with the "$\Diamond$th" spatial element. $J^{\Diamond}$ has a matrix dimension of 64 × 1, and is shown explicitly as

$$J^{\Diamond} = \left[J^{\Diamond}_{\langle S_1,D_1\rangle}\ldots\ldots J^{\Diamond}_{\langle S_1,D_8\rangle}J^{\Diamond}_{\langle S_2,D_1\rangle}\ldots\ldots J^{\Diamond}_{\langle S_2,D_8\rangle}\ldots\ldots\ldots\ldots J^{\Diamond}_{\langle S_8,D_1\rangle}\ldots\ldots J^{\Diamond}_{\langle S_8,D_8\rangle}\right]^T, \tag{10a}$$

where

$$J^{\Diamond}_{\langle S_i,D_j\rangle} = \frac{\partial\Psi_{\langle S_i,D_j\rangle}}{\partial\mu^{\Diamond}} \quad i = \{1,2,\ \ldots\ldots 8\}\,;\, j = \{1,2,\ \ldots\ldots 8\}\,;\, \Diamond = \{1:N\} \tag{10b}$$

is the sensitivity of the measurement by the source-detector-pair $\langle S_i, D_j\rangle$ with respect to the "$\Diamond$th" spatial element.

The DOT measurement corresponding to an individual source-detector-pair is conceptually illustrated in Fig. 1. Figure 1(a) shows the measurement by the pair of source-detector $\langle S_i, D_j\rangle$ in response to a single object with a positive absorption contrast over the background at varied depths (either depth 1 or 2). The thinner solid curve within the medium indicates the hypothetical depth-dependence of the measurement sensitivity, i.e., $J^{\Diamond}_{\langle S_i,D_j\rangle}$ of Eq. (10b) evaluated for all $\Diamond$

elements located along the specific depth direction. The solid boxes at the right edge and pointed by the framed arrows represent the change of the measurements between without the object and with the object at the two depths. The signal change corresponding to the object at depth 1 would be greater than that corresponding to the identical object at depth 2, owing to the variation of the measurement sensitivity with respect to depth. Figure 1(b) illustrates the effect of applying a series of regularization factors that decreases in strength along the depth (dashed curve), such as the one achieved by SVR approach.[8] The outcome of this depth-adapted "regularization" is equivalent to suppressing the change of the data-model misfit with respect to the same amount of update to the optical property at regions of higher measurement sensitivity. The regularization results in an overall reconstruction response (the thicker solid curve) that varies less with respect to the depth. On the other hand, Fig. 1(c) illustrates the effect of applying a sensitivity-weighting matrix that increases in strength along the depth (dashed curve), as is reported by the DCA approach.[2] The outcome of this "weighting" approach is to elevate the change of the data-model misfit with respect to the same amount of update to the optical property in regions with less measurement sensitivity, which also results in an overall reconstruction response (the thicker solid curve) of varying less upon the depth.

II.B. Image reconstruction based on paired measurements taken by source-sharing source-detector-pairs

Figure 2 conceptually illustrates the measurements taken by two source-detector-pairs that share the source. The solid curve and the dashed curve represent hypothetical depth-sensitivities of the measurements by $\langle S_i, D_j\rangle$ and $\langle S_i, D_{j+k}\rangle$, respectively, and k is the difference between the serial numbers of the detectors in the two source-detector-pairs. These sensitivity values are $J^{\lozenge}_{\langle S_i,D_j\rangle}$ and $J^{\lozenge}_{\langle S_i,D_{j+k}\rangle}$, respectively, evaluated for the same set of $\lozenge$ elements located along the specific depth direction. The solid boxes at the right edge and pointed by the framed arrows represent the change of the respective measurements by $\langle S_i, D_j\rangle$ and $\langle S_i, D_{j+k}\rangle$ without and with the object at the two depths. The signal change corresponding to either $\langle S_i, D_j\rangle$ and $\langle S_i, D_{j+k}\rangle$ for the object at depth 1 would be greater than that at depth 2 for the sensitivities varying with respect to depth as shown; however, the relative sensitivity between $\langle S_i, D_j\rangle$ and $\langle S_i, D_{j+k}\rangle$ for the same object at different depths varies much less than the individual sensitivity of $\langle S_i, D_j\rangle$ or $\langle S_i, D_{j+k}\rangle$ does. For the special case of the detector D_j and D_{j+k} being symmetric to the source S_i, and an object located at a position symmetric to the detector D_j and D_{j+k}, the relative sensitivity between $\langle S_i, D_j\rangle$ and $\langle S_i, D_{j+k}\rangle$ will be the same with respect to the depth of the object, regardless of the depth-variation of the individual sensitivities of $\langle S_i, D_j\rangle$ or $\langle S_i, D_{j+k}\rangle$, for the object in an otherwise homogenous medium. These hypothetical analyses suggest that the objective function using the paired measurements taken by source-sharing source-detector-pairs could be insensitive to the depth of the object to be recovered, when comparing to the objective function using the unpaired measurements taken by individual source-detector-pairs.

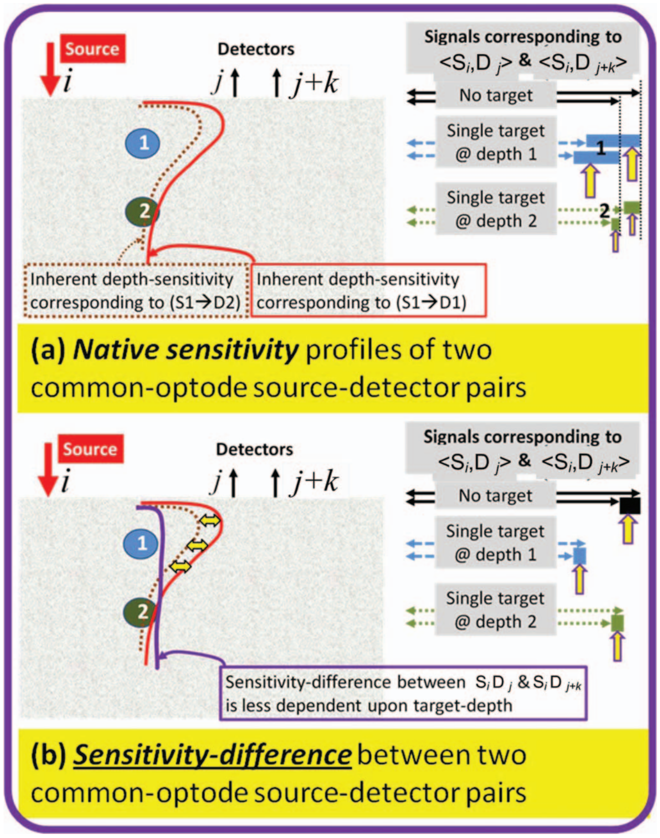

FIG. 2. Illustration of DOT image reconstruction approaches that utilizes the paired measurements from two source-sharing source-detector-pairs. The solid curve represents the native sensitivity profile of $\langle S_i, D_j\rangle$, the dashed curve represents the native sensitivity profile of $\langle S_i, D_{j+k}\rangle$. The framed dual-ended arrows indicate the difference between the sensitivity of the two source-detector-pairs. The framed arrows indicate the difference between the signal responses measured between the two source-detector-pairs. (a) The signal responses by either of the two same-source source-detector pairs $\langle S_i, D_j\rangle$ and $\langle S_i, D_{j+k}\rangle$ to an object located at different depths are different; (b) The relative differences between the signal responses of $\langle S_i, D_j\rangle$ and $\langle S_i, D_{j+k}\rangle$ to the same object at different depths are different, yet the difference between the sensitivity profiles of the two source-detector-pairs are less depth-dependent.

We analyze the forward-pairing between two source-sharing source-detector pairs, i.e., $\langle S_i, D_j\rangle$ and $\langle S_i, D_m\rangle$ with $j < m$. The relative sensitivity of the measurements by $\langle S_i, D_j\rangle$ and $\langle S_i, D_m\rangle$ with respect to the $\lozenge$th element is

$$\frac{\partial[\Psi_{\langle S_i,D_j\rangle}-\Psi_{\langle S_i,D_m\rangle}]}{\partial\mu^{\lozenge}} = \frac{\partial\Psi_{\langle S_i,D_j\rangle}}{\partial\mu^{\lozenge}} - \frac{\partial\Psi_{\langle S_i,D_m\rangle}}{\partial\mu^{\lozenge}} = J^{\lozenge}_{\langle S_i,D_j\rangle} - J^{\lozenge}_{\langle S_i,D_m\rangle} = \tilde{J}^{\lozenge}_{\langle S_i,D_j,D_m\rangle}. \tag{11a}$$

The complete forward-pairing with respect to $\langle S_1, D_1\rangle$ composes $\tilde{J}^{\lozenge}_{\langle S_i,D_j,D_m\rangle}$ with $i = 1, j = 1, m = \{2{:}8\}$, which has the following explicit form:

$$\begin{bmatrix} \tilde{J}^{\Diamond}_{\langle S_1,D_1,D_2\rangle} \\ \tilde{J}^{\Diamond}_{\langle S_1,D_1,D_3\rangle} \\ \tilde{J}^{\Diamond}_{\langle S_1,D_1,D_4\rangle} \\ \tilde{J}^{\Diamond}_{\langle S_1,D_1,D_5\rangle} \\ \tilde{J}^{\Diamond}_{\langle S_1,D_1,D_6\rangle} \\ \tilde{J}^{\Diamond}_{\langle S_1,D_1,D_7\rangle} \\ \tilde{J}^{\Diamond}_{\langle S_1,D_1,D_8\rangle} \end{bmatrix} = \begin{bmatrix} 1 & -1 & 0 & 0 & 0 & 0 & 0 & 0 \\ 1 & 0 & -1 & 0 & 0 & 0 & 0 & 0 \\ 1 & 0 & 0 & -1 & 0 & 0 & 0 & 0 \\ 1 & 0 & 0 & 0 & -1 & 0 & 0 & 0 \\ 1 & 0 & 0 & 0 & 0 & -1 & 0 & 0 \\ 1 & 0 & 0 & 0 & 0 & 0 & -1 & 0 \\ 1 & 0 & 0 & 0 & 0 & 0 & 0 & -1 \end{bmatrix} \begin{bmatrix} J^{\Diamond}_{\langle S_1,D_1\rangle} \\ J^{\Diamond}_{\langle S_1,D_2\rangle} \\ J^{\Diamond}_{\langle S_1,D_3\rangle} \\ J^{\Diamond}_{\langle S_1,D_4\rangle} \\ J^{\Diamond}_{\langle S_1,D_5\rangle} \\ J^{\Diamond}_{\langle S_1,D_6\rangle} \\ J^{\Diamond}_{\langle S_1,D_7\rangle} \\ J^{\Diamond}_{\langle S_1,D_8\rangle} \end{bmatrix}. \tag{11b}$$

Equation (11b) can be simplified to the form of

$$\left[\tilde{J}^{\Diamond}_{\{\langle S_1,D_1,D_{2:8}\rangle\}}\right]_{7\times 1} = \left[\mathrm{Diff}^{\Diamond}_{\langle S_1,D_1,D_{2:8}\rangle}\right]_{7\times 8} \times \left[\, J^{\Diamond}_{\langle S_1,D_1\rangle} \;\; J^{\Diamond}_{\langle S_1,D_2\rangle} \;\; \ldots\ldots \;\; J^{\Diamond}_{\langle S_1,D_8\rangle} \,\right]^T, \tag{11c}$$

where the [Diff] matrix performing the forward-pairing differentiation of the native sensitivity values is called the GSD operation matrix. The [Diff] matrix of Eq. (11c) that is associated with $\langle S_1, D_1\rangle$ has a dimension of 7 × 8, whereas similar complete forward-pairing GSD operations to $\langle S_1, D_j\rangle$, $j = \{2{:}7\}$, will generate respective [Diff] matrix that has a dimension of $(8 - j) \times 8$, as explicitly listed in Table I. Note that none of the empty blocks in Table I contribute to the differentiation (i.e., they are the "zero" elements in the [Diff] matrix). Each set of the blocks in Table I associated with the same starting source-detector-pair $\langle S_1, D_\mathrm{j}\rangle$, $j = \{1{:}7\}$, in the forward-pairing GSD operation, can be expressed in a general form of

$$\left[\tilde{J}^{\Diamond}_{\{\langle S_1,D_j,D_{(j+1):8}\rangle\}}\right]_{(8-j)\times 1} = \left[\mathrm{Diff}^{\Diamond}_{\langle S_1,D_j,D_{(j+1):8}\rangle}\right]_{(8-j)\times 8} \times \left[\, J^{\Diamond}_{\langle S_1,D_1\rangle} \;\; J^{\Diamond}_{\langle S_1,D_2\rangle} \;\; \ldots\ldots \;\; J^{\Diamond}_{\langle S_1,D_8\rangle} \,\right]^T \Big|_{j=\{1:7\}}. \tag{12a}$$

The complete set of the blocks in Table I represents the forward-pairing GSD operation on all source-detector-pairs that share the source 1. The complete forward-pairing GSD operation on all source-detector-pairs that share each of the other seven sources will have a structure identical to the one shown in Table I, with only a change in the source channel. Therefore, the complete set of forward-pairing GSD operations to all source-detector-pairs that share the source S_i, $i = \{1{:}8\}$, can be represented by $\tilde{J}^{\Diamond}_{\{\langle S_i,D_j,D_m\rangle\}}$, or simplified as $\tilde{J}^{\Diamond}_{\{S_i\}}$ of the following:

$$\left[\tilde{J}^{\Diamond}_{\{S_i\}}\right]_{28\times 1} = \left[\mathrm{Diff}^{\Diamond}_{\{S_i\}}\right]_{28\times 8} \times \left[\, J^{\Diamond}_{\langle S_i,D_1\rangle} \;\; J^{\Diamond}_{\langle S_i,D_2\rangle} \;\; \ldots\ldots \;\; J^{\Diamond}_{\langle S_i,D_8\rangle} \,\right]^T \Big|_{i=\{1:8\}}. \tag{12b}$$

The complete $[\tilde{J}^{\Diamond}_{\{S_i\}}]_{28\times 1}$ for $i = \{1{:}8\}$ are presented in Table II, of which each block along the diagonal is identical to Table I in terms of the structure except a change to the source number i. Table II follows the matrix form of

$$[\tilde{J}^{\Diamond}]_{224\times 1} = [\mathrm{Diff}^{\Diamond}]_{224\times 64}[J^{\Diamond}]_{64\times 1}. \tag{12c}$$

It is worthy to present the counterparts to Eqs. (12a)–(12c) for general NoS and NoD:

$$\left[\tilde{J}^{\Diamond}_{\{\langle S_1,D_j,D_{(j+1):\mathrm{NoD}}\rangle\}}\right]_{(\mathrm{NoD}-j)\times 1} = \left[\mathrm{Diff}^{\Diamond}_{\langle S_1,D_j,D_{(j+1):\mathrm{NoD}}\rangle}\right]_{(\mathrm{NoD}-j)\times \mathrm{NoD}} \left[\, J^{\Diamond}_{\langle S_1,D_1\rangle} \;\; J^{\Diamond}_{\langle S_1,D_2\rangle} \;\; \ldots\ldots \;\; J^{\Diamond}_{\langle S_1,D_{\mathrm{NoD}}\rangle} \,\right]^T \Big|_{j=\{1:(\mathrm{NoD}-1)\}}, \tag{13a}$$

$$\left[\tilde{J}^{\Diamond}_{\{S_i\}}\right]_{[(\mathrm{NoD}-1)*\mathrm{NoD}/2]\times 1} = \left[\mathrm{Diff}^{\Diamond}_{\{S_i\}}\right]_{[(\mathrm{NoD}-1)*\mathrm{NoD}/2]\times \mathrm{NoD}} \left[\, J^{\Diamond}_{\langle S_i,D_1\rangle} \;\; J^{\Diamond}_{\langle S_i,D_2\rangle} \;\; \ldots\ldots \;\; J^{\Diamond}_{\langle S_i,D_{\mathrm{NoD}}\rangle} \,\right]^T \Big|_{i=\{1:\mathrm{NoS}\}}, \tag{13b}$$

$$[\tilde{J}^{\Diamond}]_{[(\mathrm{NoD}-1)*\mathrm{NoD}/2*\mathrm{NoS}]\times 1} = [\mathrm{Diff}^{\Diamond}]_{[(\mathrm{NoD}-1)*\mathrm{NoD}/2*\mathrm{NoS}]\times[\mathrm{NoD}*\mathrm{NoS}]}[J^{\Diamond}]_{[\mathrm{NoD}*\mathrm{NoS}]\times 1}. \tag{13c}$$

By applying Eqs. (12c) or (13c) to all N spatial elements, a matrix transformation to the native sensitivity J by a complete and nonredundant forward-pairing GSD-operator [Diff] follows as

$$\tilde{J} = [\mathrm{Diff}]J, \tag{14}$$

where the dimension of $\tilde{J}$ is [(NoD − 1)*NoD/2*NoS] × 1 × N, that of [Diff] is [(NoD − 1)*NoD/2* NoS] × [NoS*NoD] × N, and that of J is [NoS*NoD] × 1 × N. It is noticed that the matrix multiplication in Eq. (14) is performed for the first two dimensions of the three matrices. The third dimension N indicates that the matrix multiplication described by Eq. (13) is repeated for each of the N elements. Therefore, the native Jacobian matrix is presented in the form of [NoS*NoD] × 1 × N rather than its original form of [NoS*NoD] × N.

By using the GSD-operation of Eq. (14), the objective function for reconstruction changes from the one of Eq. (4) to

$$\|\tilde{\chi}\|^2 = \left\|[\tilde{\Psi}]_m - [\tilde{\Psi}]_c\right\|^2 = \|[Diff]\,[\Psi]_m - [Diff]\,[\Psi]_c\|^2 = [\Psi_m - \Psi_c]^T[Diff]^T[Diff][\Psi_m - \Psi_c]. \tag{15}$$

TABLE I. Illustration of the iterative assembly of the geometric-difference of the sensitivities associated with source-detector channels sharing the source channel 1. Note: the blank cells are zeros. The **bold** ***italic*** characters indicate the sign flipping. The bold numbers will cancel the bold italic numbers during the column summation, leaving only the rows highlighted in green.

Forward-paring with respect to	**For the ◊th element**	$J_{\langle S_1,D_1\rangle}$	$J_{\langle S_1,D_2\rangle}$	$J_{\langle S_1,D_3\rangle}$	$J_{\langle S_1,D_4\rangle}$	$J_{\langle S_1,D_5\rangle}$	$J_{\langle S_1,D_6\rangle}$	$J_{\langle S_1,D_7\rangle}$	$J_{\langle S_1,D_8\rangle}$
$\langle S_1, D_1\rangle$ 7 rows	$\tilde{J}_{\langle S_1,D_1,D_2\rangle}$	**1**	**−1**						
	$\tilde{J}_{\langle S_1,D_1,D_3\rangle}$	**1**		**−1**					
	$\tilde{J}_{\langle S_1,D_1,D_4\rangle}$	**1**			**−1**				
	$\tilde{J}_{\langle S_1,D_1,D_5\rangle}$	1				−1			
	$\tilde{J}_{\langle S_1,D_1,D_6\rangle}$	***1→ (−1)***					***−1→(1)***		
	$\tilde{J}_{\langle S_1,D_1,D_7\rangle}$	***1→(−1)***						***−1→(1)***	
	$\tilde{J}_{\langle S_1,D_1,D_8\rangle}$	***1→(−1)***							***−1→(1)***
$\langle S_1, D_2\rangle$ 6 rows	$\tilde{J}_{\langle S_1,D_2,D_3\rangle}$		**1**	**−1**					
	$\tilde{J}_{\langle S_1,D_2,D_4\rangle}$		**1**		**−1**				
	$\tilde{J}_{\langle S_1,D_2,D_5\rangle}$		**1**			**−1**			
	$\tilde{J}_{\langle S_1,D_2,D_6\rangle}$		1				−1		
	$\tilde{J}_{\langle S_1,D_2,D_7\rangle}$		***1→(−1)***					***−1→(1)***	
	$\tilde{J}_{\langle S_1,D_2,D_8\rangle}$		***1→(−1)***						***−1→(1)***
$\langle S_1, D_3\rangle$ 5 rows	$\tilde{J}_{\langle S_1,D_3,D_4\rangle}$			**1**	**−1**				
	$\tilde{J}_{\langle S_1,D_3,D_5\rangle}$			**1**		**−1**			
	$\tilde{J}_{\langle S_1,D_3,D_6\rangle}$			**1**			**−1**		
	$\tilde{J}_{\langle S_1,D_3,D_7\rangle}$			1				−1	
	$\tilde{J}_{\langle S_1,D_3,D_8\rangle}$			***1→(−1)***					***−1→(1)***
$\langle S_1, D_4\rangle$ 4 rows	$\tilde{J}_{\langle S_1,D_4,D_5\rangle}$				**1**	**−1**			
	$\tilde{J}_{\langle S_1,D_4,D_6\rangle}$				**1**		**−1**		
	$\tilde{J}_{\langle S_1,D_4,D_7\rangle}$				**1**			**−1**	
	$\tilde{J}_{\langle S_1,D_4,D_8\rangle}$				1				−1
$\langle S_1, D_5\rangle$ 3 rows	$\tilde{J}_{\langle S_1,D_5,D_6\rangle}$					**1**	**−1**		
	$\tilde{J}_{\langle S_1,D_5,D_7\rangle}$					**1**		**−1**	
	$\tilde{J}_{\langle S_1,D_5,D_8\rangle}$					**1**			**−1**
$\langle S_1, D_6\rangle$ 2 rows	$\tilde{J}_{\langle S_1,D_6,D_7\rangle}$						**1**	**−1**	
	$\tilde{J}_{\langle S_1,D_6,D_8\rangle}$						**1**		**−1**
$\langle S_1, D_7\rangle$ 1 row	$\tilde{J}_{\langle S_1,D_7,D_8\rangle}$							**1**	**−1**

Both $\tilde{\Psi}$ and $\tilde{\chi}$ are now column vectors that have [NoS*NoD*(NoD − 1)/2] rows. Accordingly, Eq. (8b) transforms to

$$\delta\mu_n = (\tilde{J}^T\tilde{J})^{-1} \times \tilde{J}^T \times \tilde{\chi}_{n-1}$$
$$= (J^T[\text{Diff}]^T[\text{Diff}]J)^{-1} \times J^T[\text{Diff}]^T \times [\text{Diff}]\chi_{n-1} \tag{16a}$$

and Eq. (8c) transforms to

$$\delta\mu_n = (\tilde{J}^T\tilde{J} + \lambda I)^{-1} \times \tilde{J}^T \times \tilde{\chi}_{n-1}. \tag{16b}$$

III. GEOMETRY AND METHODS OF RECONSTRUCTION INVOLVED

III.A. The geometry studied and the depth-dependence of the native sensitivity

In this study we use a circular-array outward-imaging geometry as is shown in Fig. 3. This imaging geometry has an inner radius of 10 mm and an outer radius of 50 mm, with eight sources and eight detectors evenly interspersed along the inner boundary. Note that the outer boundary of the reconstruction domain is not a physical boundary as is the inner boundary. However, the depth of the

TABLE II. Assembly of all source-detector pairs. Parameters in Table I are repeated for the $J_{\{\langle S_i,D_j\rangle\}}$ and $J_{\{\langle S_i,D_j,D_{j+k}\rangle\}}$. Note: blank cells are zeros.

For the ◊th element	$J_{\{\langle S_1,D_j\rangle\}}$	$J_{\{\langle S_2,D_j\rangle\}}$	$J_{\{\langle S_3,D_j\rangle\}}$	$J_{\{\langle S_4,D_j\rangle\}}$	$J_{\{\langle S_5,D_j\rangle\}}$	$J_{\{\langle S_6,D_j\rangle\}}$	$J_{\{\langle S_7,D_j\rangle\}}$	$J_{\{\langle S_8,D_j\rangle\}}$
$\tilde{J}_{\{S_1\}}\|_{28\times 1}$	Table I							
$\tilde{J}_{\{S_2\}}\|_{28\times 1}$		Table I						
$\tilde{J}_{\{S_3\}}\|_{28\times 1}$			Table I					
$\tilde{J}_{\{S_4\}}\|_{28\times 1}$				Table I				
$\tilde{J}_{\{S_5\}}\|_{28\times 1}$					Table I			
$\tilde{J}_{\{S_6\}}\|_{28\times 1}$						Table I		
$\tilde{J}_{\{S_7\}}\|_{28\times 1}$							Table I	
$\tilde{J}_{\{S_8\}}\|_{28\times 1}$								Table I

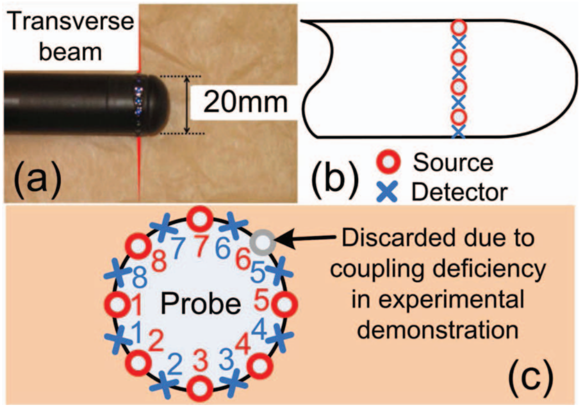

FIG. 3. Imaging geometry. (a) Photograph of the 20 mm diameter outward-imaging DOT applicator; (b) side-view; and (c) axial front view of the source-detector layout.

reconstruction domain warrants that treating the outer boundary as a physical one has minimal interference to the photon fluence rate in the useful imaging region proximal to the inner boundary. For this circular outward-imaging array what we concerned was reconstructing objects in the plane of the optode array as occurring to axial endorectal imaging; therefore, the introduced GSD method is evaluated primarily in a two-dimensional geometry. Nonetheless, an example of applying GSD method to a simple three-dimensional geometry is also presented. The two-dimensional annular imaging domain applying to the geometry of Fig. 3 was discretized to a finite element mesh including 7708 evenly distributed nodes and 15 040 elements. The display of the sensitivity distributions, the forward, and inverse computations were realized based on NIRFAST.[14]

The potential of GSD method in alleviating the sensitivity variation with respect to the imaging depth may be graphically appreciated by comparing the difference between the sensitivity profiles of two neighboring source-sharing source-detector-pairs as those shown in Fig. 4. Figures 4(a) and 4(b) display the native sensitivity distributions corresponding to $\langle S_1, D_2\rangle$ and $\langle S_1, D_3\rangle$, respectively. Plotted in Figs. 4(c)–4(f) are the sensitivity values along the four radial directions within the overlapping area of the two sensitivity profiles. The two radial sensitivity profiles in all four directions within their common decaying-region are nearly parallel to each other in terms of the slopes of depth-degradation. The relatively even change of the two radial profiles over the decaying-region manifests that differentiating the two radial profiles will not produce a peak as prominent as presented by the individual radial profile. Note that at one place over the entire depth range the two radial profiles cross each other as shown in Figs. 4(d)–4(f), indicating that the differentiation of the two radial profiles could encounter a sign change across a specific radial position. This sign change, however, is to be accompanied by the differentiation of the measurements by the two corresponding source-detector pairs when applying the GSD method, so the resulted product in Eq. (16) between the sensitivity and the measurement terms is likely to remain positive. Therefore, the crossing pattern that could occur in the GSD implementation does not necessarily cause the reversing of the contrast to be recovered, as will be demonstrated in Secs. IV–VI. Since the same principles apply to source-detector-pairs that share the detector, the remaining demonstrations are limited to source-detector-pairs that share the source.

III.B. Choice of methods to which the GSD method is compared

It is straightforward to evaluate the outcome of GSD-based DOT image reconstruction to that of a baseline method of DOT reconstruction that uses the native sensitivity profiles

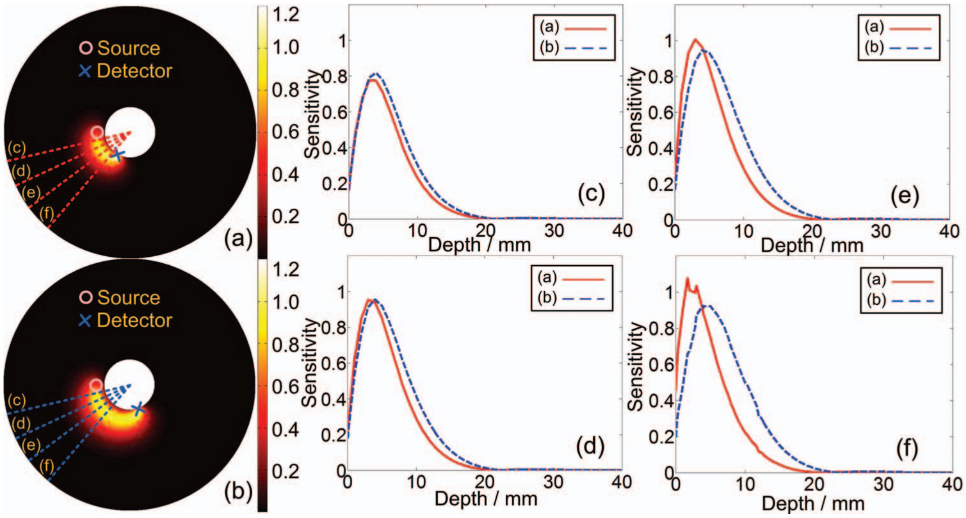

FIG. 4. The difference between the sensitivity profiles of two source-sharing source-detector-pairs in the imaging geometry corresponding to Fig. 3. (a) and (b) are the two-dimensional sensitivity profiles between two source-sharing source-detector-pairs. (c)–(f) include the sensitivity profiles along the marked directions for both source-detector-pairs. The two radial sensitivity profiles in all four directions within their common decaying-region are shown nearly parallel to each other in terms of the depth-degradation.

but does not involve a depth-compensating scheme. On the other hand, it becomes imperative to compare the outcome of GSD method with that of methods including SVR or DCA that involves active compensation of the depth variation of the update function. Niu *et al.*[19] have suggested that SVR method is not as robust as DCA method is in improving the image quality for deep objects in a planar-geometry. It is, therefore, anticipated that the SVR method would be less effective than the DCA method in dealing with the studied circular-array outward-imaging geometry of which the variation of the sensitivity with respect to imaging depth is much stronger than that of a planar geometry. The DCA method in Ref. 2 modifies the sensitivity matrix by a weighting scheme of $J_R = M^\gamma J$ to achieve an update function of the following:

$$\delta\mu = [[J_R]^T J_R + \lambda I]^{-1}[J_R]^T \chi. \quad (17)$$

The weighting implemented in J_R is $M = \{\mathrm{diag}[\mathrm{MSV}(J_l), \mathrm{MSV}(J_{l-1}), \ldots, \mathrm{MSV}(J_2), \mathrm{MSV}(J_1)]\}$, where $\mathrm{MSV}(J_l)$ stands for the maximum singular value of the sensitivity terms in J_l, the subscripts $\{1, 2, \ldots, l\}$ denote the subgroups of J in an artificially stratified layer l over the depth, and γ is a power factor. In Eq. (17) there are two parameters to optimize, the total number of layers l and the power factor γ. We have tested this DCA method for the studied circular-array outward-imaging geometry in Appendix A, and concluded that the variation of the sensitivity with respect to the imaging depth of the studied geometry appears to be too strong for the DCA method to effectively compensate to the extent as having been demonstrated for the planar-geometry.[2] We hereby implement a reference-compensation method, which can be viewed as an enhanced DCA method, against which the GSD method will be evaluated. The update equation of this reference-compensation method is identical to Eq. (17) except that $J_R = M^{\mathrm{SVR}} J$, where M^{SVR} is a sensitivity compensation matrix that is exponentially regulated according to the radial depth of the spatial element, and is a square matrix that has all nonzero terms (totaling N) located along its diagonal. For the studied circular-array outward-imaging geometry with an inner radius of 10 mm the diagonal elements of M^{SVR} are calculated for each of the N spatial elements with respect to their distance (ρ) from the center of the geometry as

$$M^{\mathrm{SVR}}(i,j) = \begin{cases} 500\exp^{(\rho_i-10)/(R-10)} & \text{if}(i=j,\ \text{i.e., diagonal element}) \\ 0 & \text{else} \end{cases}, \quad (18)$$

where i and j are the row and column indices of the M^{SVR} matrix, respectively.

III.C. The effective sensitivity distributions and the optimization of the regularization parameters

The effective sensitivity distribution over the entire imaging domain can be evaluated by summing the sensitivity terms corresponding to the same spatial element $\diamondsuit$ and associated with all source-detector-pairs, i.e., $\sum[J^{\diamondsuit}_{\{\langle S_i,D_j\rangle\}}]$ for the baseline method [Fig. 5(a)], $\sum[J^{\diamondsuit}_{R_{\{\langle S_i,D_j\rangle\}}}]$ for the reference-compensation method [Fig. 5(b)], and $\sum[\tilde{J}^{\diamondsuit}_{\{\langle S_i,D_j,D_m\rangle\}}]$ for the GSD method [Fig. 5(c)]. The effective sensitivity distribution shown in Fig. 5(c) may appear rotationally asymmetric; however, the appearing asymmetry does not impair the actual rotational symmetry of the effective sensitivity. This can be illustrated by the following analysis that involves a slight rearrangement of the terms of GSD sensitivity matrix. Taking the sensitivity terms in Table I, for example, if the signs of all $\tilde{J}_{\{\langle S_i,D_j,D_m\rangle\}}$ terms that satisfy $m - j > 4$ are reversed, the rows containing paired blocks with **bold *italic*** numbers such as "***1***" and "***−1***" will incur a sign change to the paired blocks, denoted by "***1 → (−1)***" and "***−1 → (1)***", i.e., the reversing of the order of $J_{\langle S_i,D_j\rangle\}}$ and $J_{\langle S_i,D_m\rangle\}}$ in $\tilde{J}_{\{\langle S_i,D_j,D_m\rangle\}}$. Then if we perform a column-wise summation of all terms of Table I, those individual sensitivity terms of each column corresponding to the blocks containing bold numbers will cancel with the blocks containing bold Italic numbers. The uncancelled terms will contribute as the total effective sensitivity distribution imposed by S_1:

$$\sum[\tilde{J}^{\diamondsuit}_{\{\langle S_i,D_j,D_m\rangle\}}]\Big|_{i=1} = \tilde{J}_{\langle S_1,D_1,D_5\rangle} + \tilde{J}_{\langle S_1,D_2,D_6\rangle} + \tilde{J}_{\langle S_1,D_3,D_7\rangle} + \tilde{J}_{\langle S_1,D_4,D_8\rangle}. \quad (19a)$$

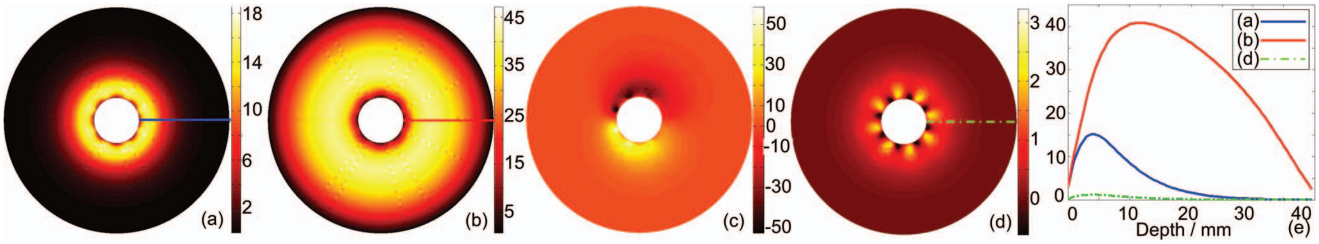

FIG. 5. Effective sensitivity [$\partial\log(I)/\partial\mu_a$] distributions evaluated for the entire imaging domain. (Unit: dB/mm^{-1}) (a) The one corresponding to J of the baseline method and Eq. (6). (b) The one corresponding to J_R of the reference compensation method and Eq. (17). (c) The one corresponding to $\tilde{J}$ of the GSD method and Eq. (12). (d) The one corresponding to rearranged $\tilde{J}$ of the GSD method and Table III. The radial profiles of the effective sensitivity distributions of (a), (b), and (d) are plotted together in (e).The effective sensitivity of the baseline method varies greatly with respect to the depth and peaks at an approximate depth of 4 mm. The reference-compensation method elevates the effective sensitivity in the entire depth and shifts the apparent peak of it to an approximate depth of 10 mm, a much greater depth than that of baseline method. The effective sensitivity by the GSD method varies negligibly with respect to the depth and is negligibly small in strength comparing to the other two methods.

TABLE III. Rearranged GSD matrix resulting in the effective sensitive profile of the one shown in Fig. 5(d). Bold italic numbers indicate the sign flippings.

Forward-paring with respect to	**For the ◊-th element**	$J_{\langle S_1,D_1\rangle}$	$J_{\langle S_1,D_2\rangle}$	$J_{\langle S_1,D_3\rangle}$	$J_{\langle S_1,D_4\rangle}$	$J_{\langle S_1,D_5\rangle}$	$J_{\langle S_1,D_6\rangle}$	$J_{\langle S_1,D_7\rangle}$	$J_{\langle S_1,D_8\rangle}$
$\langle S_1\rangle$ 4 rows	$\tilde{J}_{\langle S_1,D_1,D_5\rangle}$	1				−1			
	$\tilde{J}_{\langle S_1,D_2,D_6\rangle}$		1				−1		
	$\tilde{J}_{\langle S_1,D_3,D_7\rangle}$			1				−1	
	$\tilde{J}_{\langle S_1,D_4,D_8\rangle}$				1				−1
$\langle S_2\rangle$ 4 rows	$-\tilde{J}_{\langle S_2,D_1,D_5\rangle}$	***1→(−1)***				***−1→(1)***			
	$\tilde{J}_{\langle S_2,D_2,D_6\rangle}$		1				−1		
	$\tilde{J}_{\langle S_2,D_3,D_7\rangle}$			1				−1	
	$\tilde{J}_{\langle S_2,D_4,D_8\rangle}$				1				−1
$\langle S_3\rangle$ 4 rows	$-\tilde{J}_{\langle S_3,D_1,D_5\rangle}$	***1→(−1)***				***−1→(1)***			
	$-\tilde{J}_{\langle S_3,D_2,D_6\rangle}$		***1→(−1)***				***−1→(1)***		
	$\tilde{J}_{\langle S_3,D_3,D_7\rangle}$			1				−1	
	$\tilde{J}_{\langle S_3,D_4,D_8\rangle}$				1				−1
$\langle S_4\rangle$ 4 rows	$-\tilde{J}_{\langle S_4,D_1,D_5\rangle}$	***1→(−1)***				***−1→(1)***			
	$-\tilde{J}_{\langle S_4,D_2,D_6\rangle}$		***1→(−1)***				***−1→(1)***		
	$-\tilde{J}_{\langle S_4,D_3,D_7\rangle}$			***1→(−1)***				***−1→(1)***	
	$\tilde{J}_{\langle S_4,D_4,D_8\rangle}$				1				−1
$\langle S_5\rangle$ 4 rows	$-\tilde{J}_{\langle S_5,D_1,D_5\rangle}$	***1→(−1)***				***−1→(1)***			
	$-\tilde{J}_{\langle S_5,D_2,D_6\rangle}$		***1→(−1)***				***−1→(1)***		
	$-\tilde{J}_{\langle S_5,D_3,D_7\rangle}$			***1→(−1)***				***−1→(1)***	
	$-\tilde{J}_{\langle S_5,D_4,D_8\rangle}$				***1→(−1)***				***−1→(1)***
$\langle S_6\rangle$ 4 rows	$\tilde{J}_{\langle S_6,D_1,D_5\rangle}$	1				−1			
	$-\tilde{J}_{\langle S_6,D_2,D_6\rangle}$		***1→(−1)***				***−1→(1)***		
	$-\tilde{J}_{\langle S_6,D_3,D_7\rangle}$			***1→(−1)***				***−1→(1)***	
	$-\tilde{J}_{\langle S_6,D_4,D_8\rangle}$				***1→(−1)***				***−1→(1)***
$\langle S_7\rangle$ 4 rows	$\tilde{J}_{\langle S_7,D_1,D_5\rangle}$	1				−1			
	$\tilde{J}_{\langle S_7,D_2,D_6\rangle}$		1				−1		
	$-\tilde{J}_{\langle S_7,D_3,D_7\rangle}$			***1→(−1)***				***−1→(1)***	
	$-\tilde{J}_{\langle S_7,D_4,D_8\rangle}$				***1→(−1)***				***−1→(1)***
$\langle S_8\rangle$ 4 rows	$\tilde{J}_{\langle S_8,D_1,D_5\rangle}$	1				−1			
	$\tilde{J}_{\langle S_8,D_2,D_6\rangle}$		1				−1		
	$\tilde{J}_{\langle S_8,D_3,D_7\rangle}$			1				−1	
	$-\tilde{J}_{\langle S_8,D_4,D_8\rangle}$				***1→(−1)***				***−1→(1)***

Repeating the forward-paring GSD operation for all sources, and reversing the signs of every associated $\tilde{J}_{\{\langle S_i,D_j,D_m\rangle\}}$ terms that satisfy $m-j>4$ as exemplified in Table I, the resulted complete effective sensitivity distribution becomes

$$\begin{aligned}\sum[\tilde{J}^{\diamondsuit}_{\{\langle S_i,D_j,D_m\rangle\}}]\Big|_{i=1:8} &= \tilde{J}_{\{\langle S_i,D_1,D_5\rangle\}}+\tilde{J}_{\{\langle S_i,D_2,D_6\rangle\}}+\tilde{J}_{\{\langle S_i,D_3,D_7\rangle\}}+\tilde{J}_{\{\langle S_i,D_4,D_8\rangle\}}\Big|_{i=1:8}\\ &= [J_{\{\langle S_i,D_1\rangle\}}-J_{\{\langle S_i,D_5\rangle\}}]+[J_{\{\langle S_i,D_2\rangle\}}-J_{\{\langle S_i,D_6\rangle\}}]\\ &\quad+[J_{\{\langle S_i,D_3\rangle\}}-J_{\{\langle S_i,D_7\rangle\}}]+[J_{\{\langle S_i,D_4\rangle\}}-J_{\{\langle S_i,D_8\rangle\}}]\Big|_{i=1:8}.\end{aligned} \tag{19b}$$

Note that the sensitivity terms related to the detectors 1 to 4 are positive in the summation in Eq. (19b), whereas those related to detectors 5 to 8 are negative. Equation (19b) can effectively explain the asymmetry appeared in Fig. 5(c): (1) stronger sensitivity from 8 o'clock position counterclockwise to 4 o'clock position corresponds to the positive terms related to detectors 1 to 4; and (2) the weaker sensitivity from 2 o'clock position counterclockwise to 10 o'clock position corresponds to the negative terms related to detectors 5 to 8. It should be noted that, all the sign-reversing or pair-flipping operations needed for reaching Eq. (19b) are linear. Therefore, the sign-reversing or pair-flipping of the sensitivity terms, and the corresponding measurement terms, does not alter the native rotational symmetry of the reconstruction. We thereby could further rearrange the sensitivity terms in Eq. (19b), by following the bolded sign-reversals detailed in Table III, to generate what is appearing to be a rotationally symmetric effective sensitivity distribution as that shown in Fig. 5(d). It should be clarified that these aforementioned rearranging operations to $\tilde{J}$ are presented only to demonstrate that the GSD operation does not alter the original symmetry of the measurement sensitivity, which for this studied geometry is a rotational-symmetry. The actual $\tilde{J}$ implemented to the simulations and experiments of Secs. IV–VI take the form of that specified by Eq. (13). Figure 5(e) then compares the effective distribution profiles of the native sensitivity J, the reference-compensating applied sensitivity J_R, and the rearranged GSD-operated sensitivity $\tilde{J}$, along the marked depth direction. It can be appreciated that the effective sensitivity profile of GSD method is nearly depth-invariant and insignificant comparing to the other two methods, whereas the effective sensitivity profile of the reference-compensation method peaks at a significantly increased depth

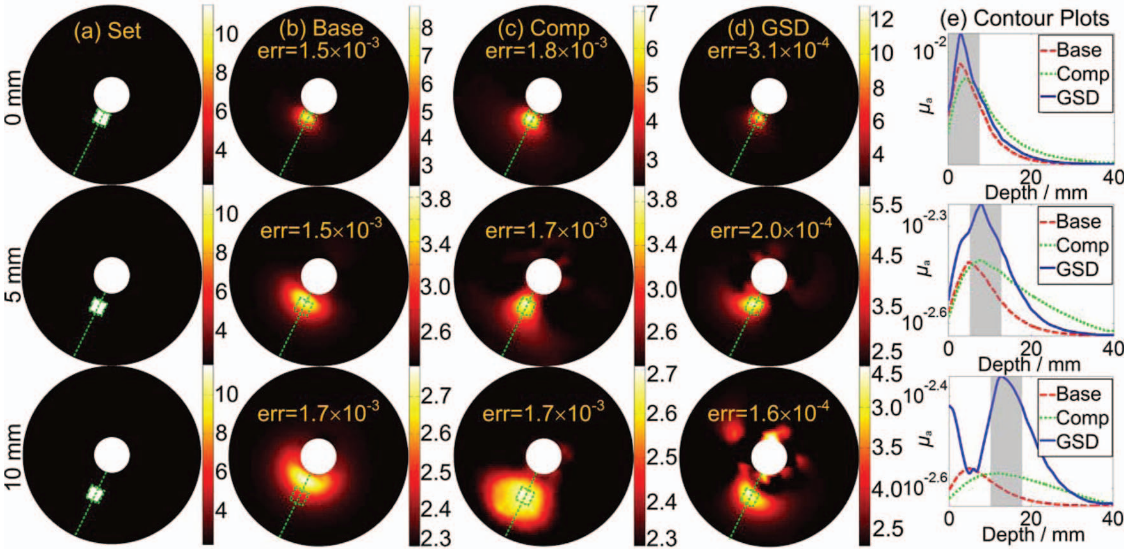

FIG. 6. Simulation results for single-object cases [unit used for columns (a)–(d): 10^{-3} mm^{-1}, unit used for column (e): mm^{-1}]. Column (a) set values; column (b) reconstruction based on the baseline method; column (c) reconstruction based on the reference-compensation method; column (d) reconstruction based on the GSD method; column (e) contour plots along the dotted lines marked in columns (b)–(d). The shaded areas in column (d) indicate the object locations corresponding to those marked in column (a). The "err"s in subfigures of columns (b)–(d) represent the standard deviation of the reconstruction errors averaged by the number of components in the objective function. Columns (c) and (d) show better depth-localization than (b). Column (d) has the best overall estimation of domain optical properties, albeit there are artifacts appearing in the case of 10 mm object-depth.

and is significantly stronger when comparing to that of the baseline method.

The strategy to step-wisely adjust the regularization factor λ of Eq. (17) for the reference-compensation method is detailed in Appendix B. The tests have shown that an initial value of $\lambda = 100$ and a step-wise damping rate of 1.78 are optimal for the reference-compensation method. The regularization factors λ of Eq. (8c) for the baseline method should have been optimized individually; however, as the baseline method performs very poorly in the studied geometry as to impair the evaluation of the outcomes at different choices of the factor λ, the step-wise adjusting of the λ for the reference-compensation method is applied directly to the baseline method. In all reconstructions the iteration stops when the change of the projection error between consecutive steps is less than 2%.

IV. SIMULATION AND EXPERIMENTAL METHODS

IV.A. Simulation setup

The optical heterogeneities employed for the simulation study were either a single cube that has a 7.5 mm side-length and $\mu_a = 0.0115$ mm^{-1} (five times of contrast over the background) or two such identical cubes separated azimuthally by 90°. The cubic-shaped objects were preferred for the fabrication handiness in the following experimental studies, on the other hand, a cube or sphere of 7.5 mm size may be insignificantly different to the experimental DOT system as its spatial resolution was low, of the order of 5 millimeters. The array-facing-edges of the cubic objects were placed 0, 5, and 10 mm away from the optical array, as shown in the column (a) of Figs. 6 and 8–10. Gaussian noise of 1% was added to this set and all other sets of forward computation unless otherwise specified. The reconstructions based on the baseline method, the reference-compensation method, and the GSD method are presented side-by-side in the respective sections.

IV.B. Experimental system and the actual number of optodes

A DOT system rendering CW measurements[21] was used to experimentally test the GSD method. The system to obtain the CW measurements contained a 4 mW wavelength-swept light source (Superlum BS-840-02) with a sweeping range of 838–853 nm. The light was coupled to a 500 mm focal-length spectrometer (SpectroPro 500i, Princeton Instrument) with a grating of 1200 grooves/mm. The spectral-sweeping of the light was transformed to a spatial scanning of the light beam at the exit port of the spectrometer for sequential coupling to the 8 source-fiber channels of the circular-array outward-imaging DOT applicator of 20 mm in diameter. The light re-emitting from the medium and reaching the 8 detector-fiber channels was acquired by a CCD mounted on another spectrometer (PIXIS 512 and SpectroPro 2300i, Princeton Instrument). The wavelength-sweeping was synchronized with the CCD exposure, at a data acquisition rate of 0.5 frame/s for the axial-imaging optical applicator to be placed in 1% intralipid solution ($\mu_a = 0.0023$ mm^{-1} and $\mu_s{}' = 1$ mm^{-1}). The details of the method for calibrating the raw data can be found in Ref. 21.

The 20 mm applicator photographed in Fig. 3(a) was designed to house 8 source and 8 detector channels; however, one of the source channels suffered from missalignment of the micro-optical components and consequently very low coupling efficiency [marked in Fig. 3(c)] comparing to the rest 7 source channels. The measurements corresponding to this low-efficiency source channel had to be discarded. Accordingly, the simulated or experimental measurements were conducted on 7 source channels and 8 detector channels. The cubic-shaped object inclusions used for the experimental measurements were identical in sizes to those for simulations. However, the inclusions were made from black plastic materials of which the absorption contrast over the background was considerably higher than that in the simulation. The use of stronger-contrast object was found necessary to generate measureable signal change from the low power level (4 mW) of the light source, especially when the targets were deep.

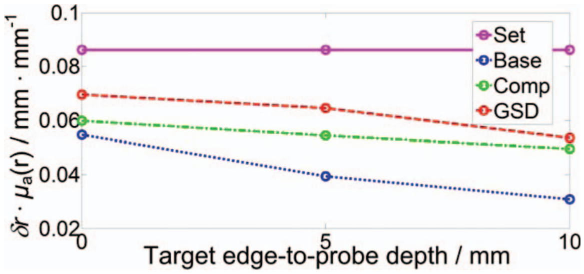

FIG. 7. Recovered object volume vs object depth. The curves represent the area covered by FWHM of the curves in column (e) in Fig. 6. Although all three methods show decreased area-within-the-FWHM profile as the depth increases, the change is the least by the GSD method, and the most by the baseline method.

IV.C. A simulation of applying the GSD method to a simple three-dimensional geometry

A simple three-dimensional planar reflectance geometry shown in Fig. 11 is used to exemplify the application of GSD method beyond the two-dimensional geometry of the aforementioned simulation and experimental studies. This example is conducted by simulation only, and involved the GSD method with respect to only the baseline method. The imaging geometry contains 18 sources and 18 detectors orderly arranged to the side of the medium, and the cubic imaging domain was discretized to 6466 nodes and 33 591 elements. The optical properties of the background were $\mu_a = 0.0023$ mm^{-1} and $\mu_s' = 1$ mm^{-1}, and a spherical inclusion of 5 mm in radius with $\mu_a = 0.006$ mm^{-1} and $\mu_s' = 1.1$ mm^{-1} was located at a center depth of 10–30 mm, at a step size of 5 mm. The reconstruction algorithms and other parameters were identical to those used in the simulations in Sec. IV.A and IV.B.

V. RESULTS

V.A. Simulation for single-object cases

The simulation results of resolving single object by using the three reconstruction methods are shown in Figs. 6(b)–6(e) along with the standard deviations of the reconstruction errors averaged by the number of components in the objective functions. The values and radial positions of the maximum recovered absorption coefficients in the object regions, as well as the mismatch between the set and reconstructed absorption distribution, are listed, respectively, for each simulation set in Table IV. It is observable in Figs. 6(b)–6(d) that the contours of the object are overestimated more in the azimuthal direction than in the radial direction. We thereby also included in Fig. 7 the areas covered by the full width at half maximum (FWHM) of the peak optical property of the recovered objects by the three methods.

By the baseline method the objects at three different depths are recovered at the same depth close to the optical array. By both the reference-compensation and GSD methods the objects are recovered at approximately the true depths, and it is appreciable that the azimuthal FWHM and the volume of the object resolved by the GSD method are closer to the set values than those by the reference-compensation method. The object optical properties were underestimated at greater depths by all three methods; however, the underestimation was the least by the GSD method. It is observed that artifacts do appear in GSD group at the 10 mm case. This is

TABLE IV. Simulation and experimental results for the reconstruction of single object. "Comp" stands for "reference-compensation.

Object-edge-depth and other relevant parameters		Set	Base	Comp	GSD
0 mm	Maximum μ_a (mm^{-1})	0.0115	0.0088	0.0071	0.013
	Radial position of maximum μ_a (mm)		3.0	5.0	3.0
	Azimuthal FWHM (mm)	7.5	9.7	11.3	7.0
	Averaged absorption map mismatch (mm^{-1})	0	1.89×10^{-5}	1.87×10^{-5}	1.80×10^{-5}
5 mm	Maximum μ_a (mm^{-1})	0.0115	0.0039	0.0039	0.0059
	Radial position of maximum μ_a (mm)		5.0	8.0	8.0
	Azimuthal FWHM (mm)	7.5	20.0	19.6	14.4
	Averaged absorption map mismatch (mm^{-1})	0	1.81×10^{-5}	1.74×10^{-5}	1.72×10^{-5}
10 mm	Maximum μ_a (mm^{-1})	0.0115	0.0028	0.0027	0.0044
	Radial position of maximum μ_a (mm)		5.0	11.0	12.0
	Azimuthal FWHM (mm)	7.5	26.6	32.9	19.7
	Averaged absorption map mismatch (mm^{-1})	0	1.87×10^{-5}	1.81×10^{-5}	1.69×10^{-5}

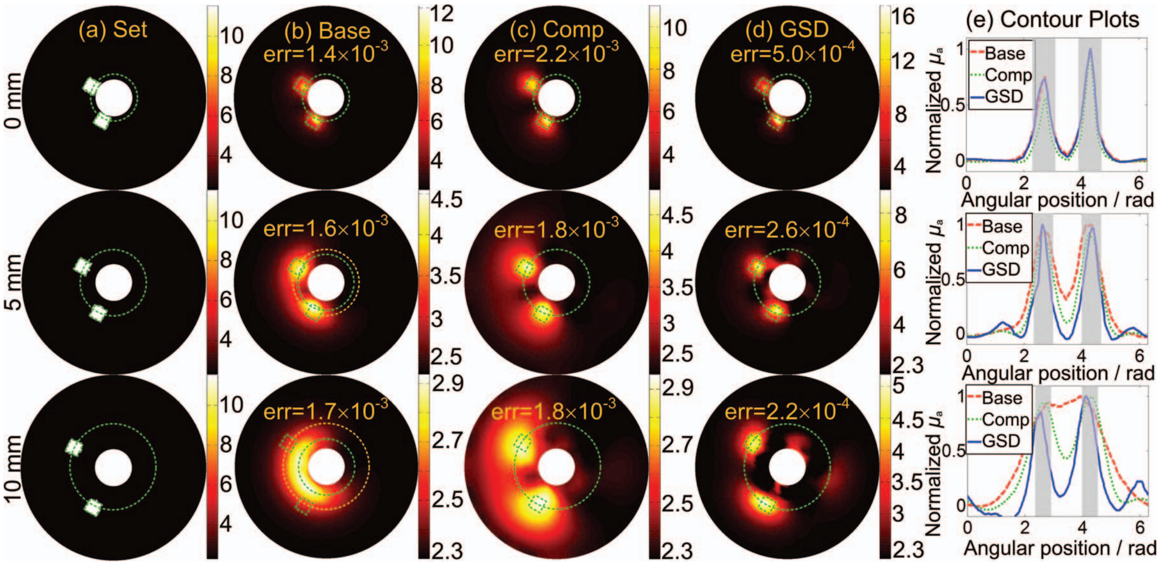

FIG. 8. Simulation results for dual-object cases [unit used for columns (a)–(d): 10^{-3} mm^{-1}]. Column (a) set values; column (b) reconstruction based on the baseline method; column (c) reconstruction based on the reference-compensation method; column (d) reconstruction based on the GSD method; column (e) normalized contour plots along the dotted loops marked in columns (b)–(d). The shaded areas in column (e) indicate the object locations corresponding to those marked in column (a). Note that although the widths of the object remain constant for all three depth, the radial expansion represented by the shaded areas in column (d) decreases with respect to imaging depth. The dotted circles in column (d) indicate the object locations corresponding to those marked in column (a). The "err"s in subfigures of columns (b)–(d) represent the standard deviation of the reconstruction errors averaged by the number of components in the objective function. Column (d) has the best overall resolution of the two objects and the most accurate estimation of domain optical properties.

not unexpected, because as the native measurement sensitivity diminishes significantly with respect to the depth, the effectiveness of GSD at that depth is also going to be mitigated. Nonetheless, the object recovery by the GSD method is of better quality than by the other two methods, as analyzed in Table IV and Fig. 7. The area-within-the-FWHM decreases as the depth increases, suggesting degradation of the reconstruction quality, by all three methods, yet the degradation in the GSD method is the least. In the rest of studies results similar to Table IV and Fig. 7 were observed and not separately presented.

V.B. Simulation for two-target cases

The objects as aforementioned were two identical cubes with a 7.5 mm side-length and were azimuthally separated by 90°, as illustrated in Fig. 8(a). The imaging results are given in Figs. 8(b)–8(e). The μ_a values along the azimuthal contours across the recovered objects are displayed in column (e) of Fig. 8. By the baseline method the objects at three different depths were recovered at almost the same depth close to the optical array, and the two objects at the 10 mm depth were not distinguished. By both the reference-compensation and GSD methods the objects were recovered at the set positions, but the contour plots of Fig. 8(e) show that the GSD method outperforms the other one in terms of the object size, the distinguishing of the two objects, and the estimations of the object optical properties. These profiles also suggest the outperformance of the GSD method over the other two methods.

V.C. Experimental results for single-object cases

The experimental results for single-object cases are given in Figs. 9(b)–9(d). It is observable that the array-facing edges of the targets were recovered by all three methods, however, unlike in the simulations the object body could not be resolved because no light should have propagated through it. Despite of that, the outcomes by the three methods were different. For the 0 and 5 mm cases, the array-facing edge of the object was identified by the baseline method and the reference-compensation method at positions more proximal to the set positions, but not as sharp as by the GSD method. For 10 mm cases, artifacts were noticeable in all three methods, but the distortion to the object by the localized artifacts was the least in the GSD method.

V.D. Experimental results for two-object cases

The reconstruction results given in Figs. 10(b)–10(e) are similar to those in Fig. 8, except that for the 10 mm case the baseline method was able to resolve the two targets, but the depth was not recovered correctly. The GSD method slightly outperforms the other two methods in terms of resolving the location, dimension, and the optical properties of the two azimuthally separated targets.

V.E. Simulation results of the simple three-dimensional imaging geometry

Figure 11(c) displays the images reconstructed by using the baseline and the GSD approaches. By the baseline method the objects at different depths were recovered at depths closer

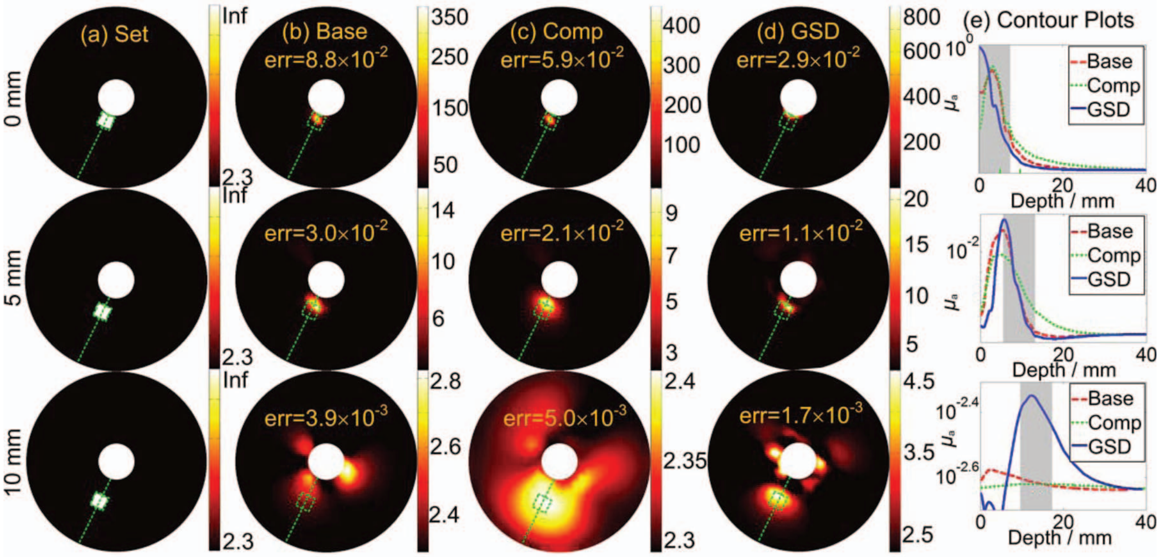

FIG. 9. Experimental results for single-object cases [unit used for columns (a)–(d): 10^{-3} mm^{-1}, unit used for column (e): mm^{-1}]. Column (a) set values; column (b) reconstruction based on the baseline method; column (c) reconstruction based on the reference-compensation method; column (d) reconstruction based on the GSD method; column (e) contour plots along the dotted lines marked in columns (b)–(d). The shaded areas in column (e) indicate the object locations corresponding to those marked in column (a). The "err"s in subfigures of columns (b)–(d) represent the standard deviation of the reconstruction errors averaged by the number of components in the objective function. Artifacts appeared for the object at 10 mm-depth by all three methods. Column (d) has the best overall estimation of object location and domain optical properties.

to the optical array than the true values. At the depth of 30 mm, the object was overwhelmed by the artifacts appearing close to the optical array when recovered by using the baseline method, in comparison, the depths and sizes of the object recovered by the GSD method were closer to the true values.

VI. DISCUSSION

The layered DCA (Ref. 2) method was not directly implemented to the comparisons in this study, as a set of trials detailed in Appendix A indicated that the layered DCA method in its original form as in Ref. 2 was ineffective in

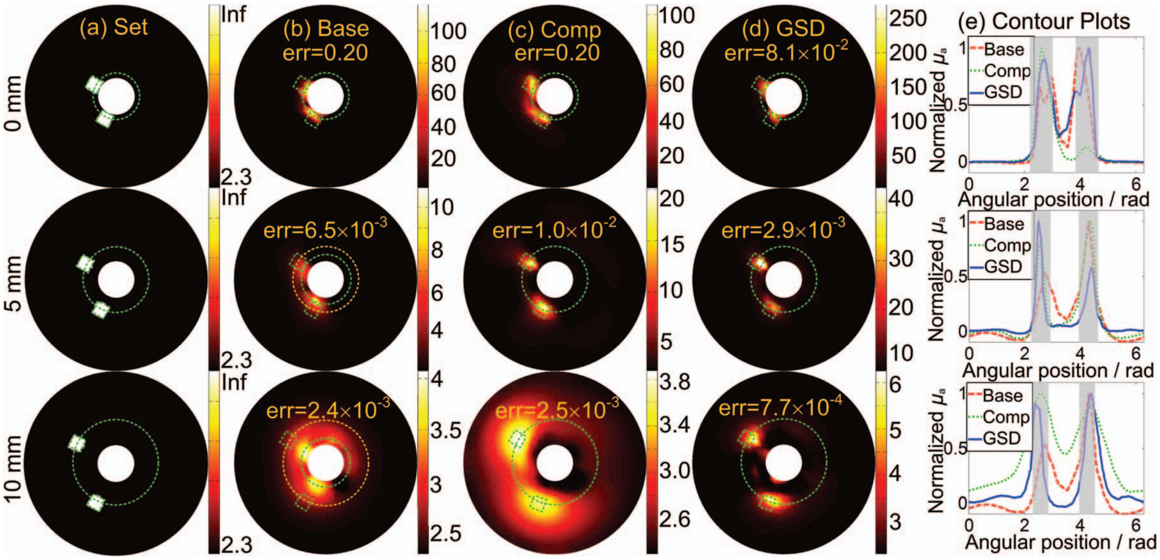

FIG. 10. Experimental results for dual-object cases [unit used for columns (a)–(d): 10^{-3} mm^{-1}]. Column (a) set values; column (b) reconstruction based on the baseline; column (c) reconstruction based on the reference-compensation method; column (d) reconstruction based on the GSD method; column (e) normalized contour plots along the dotted loops marked in columns (b)–(d). The shaded areas in column (e) indicate the object locations corresponding to those marked in column (a). Note that although the widths of the object remain constant for all three depths, the radial expansion represented by the shaded areas in column (d) decreases with respect to imaging depth. The gold circles in column (d) indicate the object locations corresponding to those marked in column (a). The "err"s in subfigures of columns (b)–(d) represent the standard deviation of the reconstruction errors averaged by the number of components in the objective function. Column (d) has the best overall resolution of the two objects and the most accurate estimation of domain optical properties with minimal level of artifacts.

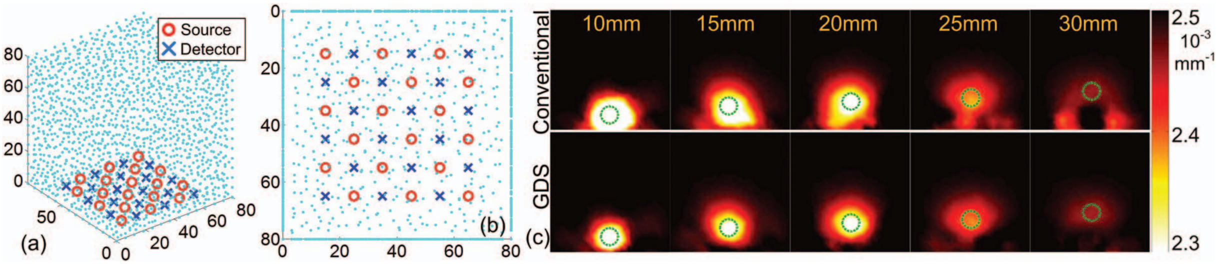

FIG. 11. Simulation results on recovering a single object in a planar reflectance imaging geometry. (a) 3D view of the simulating volume; (b) geometry of the optical array; (c) results of reconstruction based on the baseline and GSD methods. The objects are better resolved by GSD method.

the studied circular-array outward-imaging geometry. We argue that more robust suppression of the significant sensitivity decay of the studied geometry by using DCA method is feasible, should the resolution of the depth-layers be made comparable to or even finer than the radial resolution of the finite elements. We thus developed a piece-wise[8] DCA-based reference-compensation method as detailed in Appendix B, and since this enhanced DCA method better balances between object localization and artifact suppression it is adopted as the reference-compensation method to facilitate the evaluation of GSD method.

The reference-compensation method localized the objects but generally underestimated the optical contrasts and overestimated the azimuthal FWHM of the objects, resulting in an ambiguous differentiation of two azimuthally separated objects. As to the baseline method that reconstructs using the native sensitivity distribution, it failed to resolve two objects at 10 mm depth with 5 folds of absorption contrast over the background [Fig. 8, row 3, column (b)]. However, in the corresponding experiment [Fig. 10, row 3, column (b)], the two black plastic objects placed at 10 mm depth were resolved by the baseline method. The better resolution of the two objects in the experiment than in the simulation was indeed the result of stronger signal change in the experiment than in the simulation due to the use of black materials for the objects in the experiments. The averaged errors of the reconstruction by the reference-compensation and baseline methods were nearly an order greater than those achieved by the GSD method. It is also observable that lesser artifacts arouse in the two target cases (Fig. 8 and Fig. 10) than in one target cases (Fig. 6 and Fig. 9) by the GSD-method. This may also have been related to the stronger signal change occurring to more source-detector pairs by two targets than that by one target, but it favorably indicates that the GSD method is robust in recovering multiple objects. It is also cautiously observed that the deeper the object is located, the less accurate the optical contrast is recovered, even for the GSD method. This implies that the effectiveness of how GSD performs, in terms of passive sensitivity compensation, diminishes as the measurement sensitivity deteriorates. More enhancement to the recovery of deeply embedded target by the GSD method is feasible, should the source power or signal to noise ratio become stronger.

One limitation of the experimental study regarding recovering two-objects is that the two objects were placed azimuthally at the same imaging depth, as the optode array was primarily designed for transrectal prostate cancer imaging, where the malignant tissues could be multifocal and usually occurring close to the optode array. Moreover, for the endoscopic imaging geometry in Fig. 3, because of the dimensions of the object tested, placing two objects of the shown sizes along the same radial direction, and not stacking them against each other for them to be reasonably resolved by the reconstruction, would need to place most of the distal object in a region beyond what could be measured by the experimental system, regardless of how the sensitivity variation would be managed. Using objects much smaller than those implemented should facilitate testing the GSD operations to radially separated objects in the shown geometry; however, the experimental system at the given low level of the source power would be much less sensitive to the smaller objects and the resulted poor signal-to-noise ratio would likely make any comparisons inconclusive.

The GSD method reduces the depth-variance of the resulted sensitivity at a cost of increasing the number of rows of the sensitivity matrix by (NOD-1)/2 folds, for source-sharing GSD operation. The increase of the number of rows of the sensitivity matrix, however, does not degrade the rank of the matrix to be inverted, since $\tilde{J}^T\tilde{J}$ has a N × N dimension as J^TJ does. The increase in the computation time, approximately 40% in this study, is solely caused by the [Diff] operation in Eq. (14) and the corresponding multiplication of matrices of more elements. A sensitivity distribution that is more depth-invariant than the GSD sensitivity distribution investigated in this study could be achievable by hierarchical pairing of the GSD-resulted sensitivity profiles, but the cost in computation and complexity would likely outweigh the benefits.

It is noted that the linear conversion from the J to $\tilde{J}$ retains the full dynamic range of the measurements as is $\{\max(\Psi) - \min(\Psi)\}$. The differentiated objective function in Eq. (15) can also be considered belonging to the scheme involving a surrogate objective function,[22] as is demonstrated by Xu *et al.*[23] for DOT image reconstruction using a spectral derivative method. The spectral derivative method is based on the assumption that the boundary modeling errors are multiplicative to system measurements in normal scale[24] and can be modeled as additive in logarithm. The GSD method is similar to the spectral derivative methods in partially and passively cancelling out the modeling or system errors measured by two optode-sharing source-detector-pairs.

This study implemented the GSD operation in the LM scheme. It is known that the LM scheme is a special case of the Tikhonov regularization method, and the Tikhonov regularization itself is a special case of a generalized-least-square GLS approach.[13,25] Because the operation on the J by GSD method is linear, we expect that the GSD method is extendable to the Tikhonov and GLS minimization schemes. The GSD-operated update function in a Tikhonov minimization would become

$$\delta\mu = (\tilde{J}^T\tilde{J} + \lambda I)^{-1} \times [\tilde{J}^T\tilde{\chi} - \lambda(\mu - \mu_0)] \tag{20}$$

and the GSD-operated update function in a GLS minimization would become

$$\begin{aligned}\delta\mu = {} & [\tilde{J}^T W_{\tilde{\chi}}\tilde{J} + W_{\mu-\mu_0}]^{-1} \\ & \times [\tilde{J}^T W_{\tilde{\chi}}\tilde{\chi} - W_{\mu-\mu_0}(\mu - \mu_0)],\end{aligned} \tag{21}$$

where $W_{\tilde{\chi}}$ is the inverse of the covariance of the GSD-operated objective function $\tilde{\chi}$ and $W_{\mu-\mu_0}$ is the inverse of the covariance of the optical properties.

The effectiveness of the GSD method is apparently related to the extent of the spatial variations of the measurement sensitivity. The more uniform the native measurement sensitivity is with respect to the imaging depth, the less improvement the GSD method could impose to the object localization in the depth. On the other hand, the effectiveness of the GSD operation can be evaluated from Eq. (13) that it depends upon the geometric symmetry or antisymmetry of all source-detector-pairs. The circular-array imaging geometry as the one shown in Fig. 3 renders the geometric symmetry of $\langle S_i, D_j\rangle$ versus $\langle S_i, D_{9-j}\rangle$ for $i = \{1, 5\}, j = \{1{:}8\}$; and the geometric antisymmetry of the pairing of $[\langle S_i, D_j\rangle - \langle S_i, D_{9-j}\rangle]$ versus the pairing of $[\langle S_{10-i}, D_j\rangle - \langle S_{10-i}, D_{9-j}\rangle]$ for $i = \{2{:}4\}; j = \{1{:}4\}$. These symmetries indicate that the spatial variation of the sensitivity of measurements introduced by an individual source-detector-pair $\langle S_i, D_j\rangle$ may be cancelled or partially compensated by other source-detector-pair. The circular-imaging geometry with evenly interspersed source and detector renders complete rotational symmetry in either directions of the circumference; therefore, it would be the geometry for which the application of the GSD operation would be the most effective. The simple three-dimensional geometry simulated in Secs. IV.D and IV.E has a lateral symmetry with respect to the two middle-sectioning planes, but the symmetry is not complete for all source-detector-pairs. Therefore, the GSD method to this geometry is not as effective as is to the circular-array outward-imaging geometry. The simulations performed on the simple three-dimensional geometry, nonetheless, demonstrate that GSD operation is generally applicable, and as such we anticipate that DOT reconstructions that relies upon more complex data, such as frequency domain, time domain, multispectral, or fluorescence measurements, may become the future subjects for implementing GSD-operation, should the correct localization of an object depth without a spatial *prior* become a concern.

VII. CONCLUSION

This study demonstrated an alternative DOT image reconstruction approach that optimizes the data-model fit based on the paired measurements corresponding to two source-sharing source-detector-pairs, in comparison to the conventional DOT image reconstruction approach that optimizes the data-model fit based on the measurements corresponding to individual source-detector-pairs. This alternative method, conceptually called the GSD method, effectively and passively suppresses the spatial variance of the detection sensitivity with respect to imaging depth by taking advantage of the relative changes of the measurements between two optode-sharing source-detector-pairs. It is demonstrated that this GSD approach improves the object depth-localization for DOT in a circular-array outward-imaging geometry that is subjected to strong variation of the native measurement sensitivity with respect to the imaging depth. This GSD operation pairs the native sensitivity profiles corresponding to two source-sharing source-detector-pairs and effectively evens the responses of the updating function with respect to the imaging depth. Simulated and experimental studies based on CW measurements are used to evaluate the image reconstructions based on the GSD-method versus that on two other methods: one is the baseline method using the native sensitivity that does not involve a depth-compensating scheme, and the other is a reference-compensation approach that involves active depth-dependent compensating scheme. The GSD method is shown generally outperforming the other two methods in terms of localizing the depth of single object, resolving two azimuthally separated objects, as well as estimating the optical property of single object or azimuthally separated dual objects. The GSD method, however, is more computationally demanding due to increasing of the matrix elements as well as involving more matrix multiplications, and the effectiveness of it is associated with the symmetry of the optode-array.

ACKNOWLEGMENT

This work is a result of a U.S. Army Medical Research Acquisition Activity Grant No. W81XWH-10-1-0836.

APPENDIX A: LAYERED DCA METHOD APPLIED TO THE CIRCULAR-ARRAY OUTWARD-IMAGING GEOMETRY

This section tests the DCA method in the form originally presented in Ref. 2 to the studied circular-array outward-imaging geometry. The DCA method actually introduces a compensation matrix similar to the weight matrix in the GLS method.[13] The structure of the compensation matrix M is represented using the notations consistent with this study as

$$\begin{aligned}M = {} & \{\mathrm{diag}[\mathrm{MSV}(J_l), \mathrm{MSV}(J_{l-1}), \ldots, \\ & \mathrm{MSV}(J_2), \mathrm{MSV}(J_1)]\}^{\gamma},\end{aligned} \tag{A1}$$

where MSV stands for the maximum singular values, J_l is the sensitivity terms in the layer l, and γ is an exponential factor to be empirically optimized for a specific geometry. The

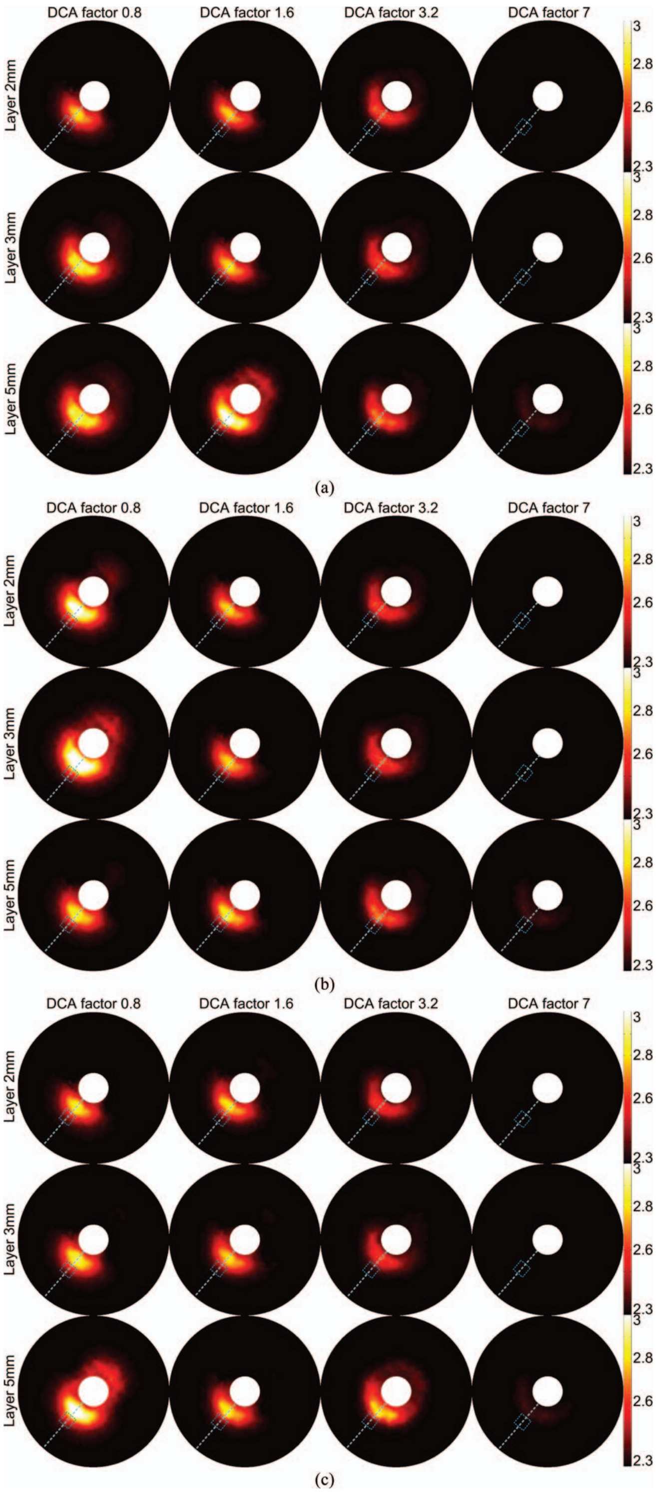

FIG. 12. Investigation on the performance of DCA method in the circular-array outward-imaging geometry (units 10^{-3} mm^{-1}). The object contour and location are marked by blue dotted lines. Simulation setup in Sec. III.B for single object was used. (a)–(c) Simulation results produced with regularization factor value of 50, 100, and 200, respectively. The DCA method in its original form as in Ref. 2 was ineffective in the studied circular-array outward-imaging geometry.

gradient-based iterative solver as that shown in Ref. 2 is implemented in the inverse problem by using the compensation sensitivity matrix MJ. Note that M is a square matrix and can be categorized to the GLS method.

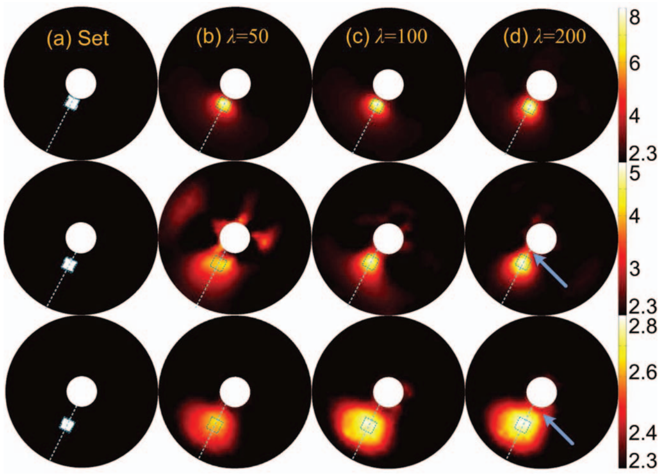

FIG. 13. Performance of the reference compensation method with varied regularization factors (units 10^{-3} mm^{-1}). The object contour and location are marked by dotted lines. When the object was close to the probe surface, reconstruction results are not significantly affected by the regularization factor. At deeper locations, either more artifacts appear or the object contrast is more severely underestimated in the column of $\lambda = 50$. The columns of $\lambda = 100$ and $\lambda = 200$ are only slightly different; however, the target size seems to be slightly overestimated by $\lambda = 200$ than by $\lambda = 100$. The arrows indicate the overestimations of the optical properties of the medium region between the object and the applicator.

Three parameters were tested. The first parameter was the thickness of the layer that was chosen to be 2, 3, and 5 mm, receptively, based on the 1 mm radial resolution of the mesh in this simulation and the 5 mm step of changing the object depth in Sec. IV. The second parameter was the exponential factor. Niu *et al.*[2] tested that $\gamma = 1.6$ was optimal for the planar reflectance imaging geometry specific to their study. In the circular-array outward imaging geometry of this study a series of γ values between 0 and 10 were tested, yet only the reconstruction results produced with γ values of $\{0.8, 1.6, 3.2, 7\}$ were presented in this section. The γ values were chosen greater than those used in Ref. 2, which was found necessary to counteract the more severe decay of the sensitivity with respect to imaging depth. The third parameter was the regularization factor λ that is critical to the convergence of the inverse problem, and the λ values of $\{50,100, 200\}$ were tested.

The test simulation shown in Fig. 12 is conducted for single cubic object identical to the one in Fig. 6 and its proximal-edge located at a depth of 10 mm. The objects in all cases were recovered at depths much closer to the probe surface than the true values, indicating the inadequacy of the DCA method in the tested or the originally presented form for the studied geometry. Implementing the DCA method in a piece-wise exponential weighting scheme is found to produce better results, as shown in Appendix B and Sec. V.

APPENDIX B: DETERMINATION OF THE INITIAL REGULARIZATION VALUE USED FOR STEP-WISE ADJUSTMENT

Because of the poor depth-localization of the baseline reconstruction in the studied geometry, the λ value to be step-wisely adjusted[13] was actually determined based on the reference compensation methods of Eq. (17), and the same stepwise-adjusting of the λ value was applied to the baseline method. A wide range of λ values were examined, for the single object case identical to that in Sec. IV.A, and those shown in Fig. 13 were the results of using three representative λ values of $\{50, 100, 200\}$. It is clear that in the column of $\lambda = 50$ either there are more artifacts or the object contrast is more severely underestimated. The columns of $\lambda = 100$ and $\lambda = 200$ are not significantly different; however, $\lambda = 200$ slightly overestimates the target size than $\lambda = 100$ does; therefore, a λ value of 100 is chosen.

[a] Author to whom correspondence should be addressed. Electronic mail: daqing.piao@okstate.edu

[1] M. Huang and Q. Zhu, "Dual-mesh optical tomography reconstruction method with a depth correction that uses a priori ultrasound information," Appl. Opt. **43**(8), 1654–1662 (2004).

[2] H. Niu, F. Tian, Z.-J. Lin, and H. Liu, "Development of a compensation algorithm for accurate depth localization in diffuse optical tomography," Opt. Lett. **35**(3), 429–431 (2010).

[3] G. Xu, D. Piao, C. H. Musgrove, C. F. Bunting, and H. Dehghani, "Trans-rectal ultrasound-coupled near-infrared optical tomography of the prostate, Part I: Simulation," Opt. Express **16**(22), 17484–17504 (2008).

[4] Q. Zhao, L. Ji, and T. Jiang, "Improving depth resolution of diffuse optical tomography with a layer-based sigmoid adjustment method," Opt. Express **15**(7), 4018–4029 (2007).

[5] S. R. Arridge, "Optical tomography in medical imaging," Inverse Probl. **15**(2), R41–R93 (1999).

[6] D. S. Kepshire, S. C. Davis, H. Dehghani, K. D. Paulsen, and B. W. Pogue, "Subsurface diffuse optical tomography can localize absorber and fluorescent objects but recovered image sensitivity is nonlinear with depth," Appl. Opt. **46**(10), 1669–1678 (2007).

[7] F. Tian, G. Alexandrakis, and H. Liu, "Optimization of probe geometry for diffuse optical brain imaging based on measurement density and distribution," Appl. Opt. **48**(13), 2496–2504 (2009).

[8] B. W. Pogue, T. O. McBride, J. Prewitt, U. L. Österberg, and K. D. Paulsen, "Spatially variant regularization improves diffuse optical tomography," Appl. Opt. **38**(13), 2950–2961 (1999).

[9] D. Piao, H. Xie, C. Musgrove, C. F. Bunting, W. Zhang, G. Zhang, E. B. Domnick-Davidsion, K. E. Bartels, G. R. Holyoak, S. N. Vemulapalli, H. Dehghani, and B. W. Pogue, *Near-Infrared Optical Tomography: Endoscopic Imaging Approach, Proc. SPIE 6431*, Multimodal Biomedical Imaging II, 643103 (2007).

[10] J. P. Culver, A. M. Siegel, J. J. Stott, and D. A. Boas, "Volumetric diffuse optical tomography of brain activity," Opt. Lett. **28**(21), 2061–2063 (2003).

[11] A. Zhang, D. Piao, C. F. Bunting, and B. W. Pogue, "Photon diffusion in a homogeneous medium bounded externally or internally by an infinitely long circular cylindrical applicator. I. Steady-state theory," J. Opt. Soc. Am. A **27**(3), 648–662 (2010).

[12] D. W. Marquardt, "An algorithm for least-squares estimation of nonlinear parameters," J. Soc. Ind. Appl. Math. **11**(2), 431–441 (1963).

[13] P. K. Yalavarthy, B. W. Pogue, H. Dehghani, and K. D. Paulsen, "Weight-matrix structured regularization provides optimal generalized least-squares estimate in diffuse optical tomography," Med. Phys. **34**(6), 2085–2098 (2007).

[14] H. Dehghani, M. E. Eames, P. K. Yalavarthy, S. C. Davis, S. Srinivasan, C. M. Carpenter, B. W. Pogue, and K. D. Paulsen, "Near infrared optical tomography using NIRFAST: Algorithm for numerical model and image reconstruction," Commun. Numer. Methods Eng. **25**(6), 711–732 (2009).

[15] A. Corlu, R. Choe, T. Durduran, K. Lee, M. Schweiger, S. R. Arridge, E. M. C. Hillman, and A. G. Yodh, "Diffuse optical tomography with spectral constraints and wavelength optimization," Appl. Opt. **44**(11), 2082–2093 (2005).

[16] H. Bastian, "On uniqueness in diffuse optical tomography," Inverse Probl. **25**(5), 055010 (14pp) (2009).

[17] Y. Xu, X. Gu, T. Khan, and H. Jiang, "Absorption and scattering images of heterogeneous scattering media can be simultaneously reconstructed by use of dc data," Appl. Opt. **41**(25), 5427–5437 (2002).

[18] G. Xu, D. Piao, C. F. Bunting, and H. Dehghani, "Direct-current-based image reconstruction versus direct-current included or excluded frequency-domain reconstruction in diffuse optical tomography," Appl. Opt. **49**(16), 3059–3070 (2010).

[19] H. Niu, Z.-J. Lin, F. Tian, S. Dhamne, and H. Liu, "Comprehensive investigation of three-dimensional diffuse optical tomography with depth compensation algorithm," J. Biomed. Opt. **15**(4), 046005–046009 (2010).

[20] V. Ntziachristos, A. G. Yodh, M. Schnall, and B. Chance, "Concurrent MRI and diffuse optical tomography of breast after indocyanine green enhancement," Proc. Natl. Acad. Sci. U.S.A. **97**(6), 2767–2772 (2000).

[21] G. Xu and D. Piao, *Feasibility of Rapid Near-Infrared Diffuse Optical Tomography by Swept-Spectral-Encoded Sequential Light Delivery, Proc. SPIE 7896*, Optical Tomography and Spectroscopy of Tissue IX, 78961W (2011).

[22] K. Lange, D. R. Hunter, and Y. Ilsoon, "Optimization transfer using surrogate objective functions," J. Comput. Graph. Stat. **9**(1), 1–20 (2000).

[23] H. Xu, B. W. Pogue, R. Springett, and H. Dehghani, "Spectral derivative based image reconstruction provides inherent insensitivity to coupling and geometric errors," Opt. Lett. **30**(21), 2912–2914 (2005).

[24] M. Schweiger, I. Nissilä, D. A. Boas, and S. R. Arridge, "Image reconstruction in optical tomography in the presence of coupling errors," Appl. Opt. **46**(14), 2743–2756 (2007).

[25] P. K. Yalavarthy, D. R. Lynch, B. W. Pogue, H. Dehghani, and K. D. Paulsen, "Implementation of a computationally efficient least-squares algorithm for highly under-determined three-dimensional diffuse optical tomography problems," Med. Phys. **35**(5), 1682–1697 (2008).